Micromechanical constitutive models for cementitious composite materials

PhD Thesis

Iulia C. MIHAI

School of Engineering, Cardiff University

2012

Declaration

This work has not previously been accepted in substance for any degree and is not concurrently submitted in candidature for any other higher degree.

Signed:.....(Candidate) Date: **22/12/2011**

Statement 1

This thesis is being submitted in partial fulfilment of the requirements for the degree of .....(insert as appropriate PhD, MPhil, EngD)

Signed:.....(Candidate) Date: **22/12/2011**

Statement 2

This thesis is the result of my own independent work/investigation, except where otherwise stated. Other sources are acknowledged by explicit references.

Signed:.....(Candidate) Date: **22/12/2011**

Statement 3

I hereby give consent for my thesis, if accepted, to be available for photocopying, inter-library loan and for the title and summary to be made available to outside organisations.

Signed:.....(Candidate) Date: **22/12/2011**

Abstract

A micromechanical constitutive model for concrete is proposed in which microcrack initiation, in the interfacial transition zone between aggregate particles and cement matrix, is governed by an exterior-point Eshelby solution. The model assumes a two-phase elastic composite, derived from an Eshelby solution and the Mori-Tanaka homogenization method, to which circular microcracks are added. A multi-component rough crack contact model is employed to simulate normal and shear behaviour of rough microcrack surfaces. It is shown, based on numerical predictions of uniaxial, biaxial and triaxial behaviour that the model captures key characteristics of concrete behaviour. An important aspect of the approach taken in this work is the adherence to a mechanistic modelling philosophy. In this regard the model is distinctly more rigorously mechanistic than its more phenomenological predecessors.

Following this philosophy, a new more comprehensive crack-plane model is described which could be applied to crack-planes in the above model. In this model the crack surface is idealised as a series of conical teeth and corresponding recesses of variable height and slope. Based on this geometrical characterization, an effective contact function is derived to relate the contact stresses on the sides of the teeth to the net crack-plane stresses. Plastic embedment and frictional sliding are simulated using a local plasticity model in which the plastic surfaces are expressed in terms of the contact surface function. Numerical simulations of several direct shear tests indicate a good performance of the model. The incorporation of this crack-plane model in the overall constitutive model is the next step in the development of the latter.

Computational aspects such as contact related numerical instability and accuracy of spherical integration rules employed in the constitutive model are also discussed. A smoothed contact state function is proposed to remove spurious contact chatter behaviour at a constitutive level.

Finally, an initial assessment of the performance of the micromechanical model when implemented in a finite element program is presented. This evaluation clearly demonstrates the capability of the proposed model to simulate the behaviour of plain and reinforced concrete structural elements as well as demonstrating the potential of the micromechanical approach to achieve a robust and comprehensive model for concrete.

Acknowledgements

The following project would not have been possible without the funding from the finite element company LUSAS and their support is gratefully acknowledged. In particular I would like to thank Prof. Paul Lyons for his encouragement and enthusiasm for the work.

I especially thank my supervisor Tony Jefferson who provided me with the greatest assistance and guidance. Tony, when I was sweating blood over my work, your constant encouragement, enthusiasm and faith in my research helped me sustain my motivation and sanity. I extend my thanks and gratitude to the other members in the research group: Bob Lark, Diane Gardner, Chris Joseph, Ben Isaacs, Simon Chan, Andi Hoffman, Simon Dunn, Adriana Chitez, Rob Davies and Toby Hazelwood for their help, advice and for creating and maintaining a very enjoyable work environment.

Special thanks to my wonderful parents and brothers for their extraordinary love, support and encouragement through good and not so good times. You are the best!

Finally, I thank my friends Katie, Eley, Debbie, Nancy, Dave and Cheryl, Katie and James, Saskia and James, Lydia, Annie and Richard for cheering me on and helping me keep things in perspective.

List of symbols

α, ζ, ρ	Cylindrical coordinates
$\boldsymbol{\gamma}$	Shear strain component
$\boldsymbol{\varepsilon}$	Strain tensor
$\overline{\boldsymbol{\varepsilon}}$	Average strain tensor
$\boldsymbol{\varepsilon}_0$	Far-field strain
ε_0	Strain at the end of softening curve
$\boldsymbol{\varepsilon}_\alpha$	Local additional strain tensor due to microcracking
$\boldsymbol{\varepsilon}_a$	Total additional strain tensor due to microcracking
$\boldsymbol{\varepsilon}_c$	Constrained strain
$\boldsymbol{\varepsilon}_m$	Matrix strain tensor
$\boldsymbol{\varepsilon}_{m\Omega}$	Strain in the matrix, outside an inclusion
ε_{tm}	Matrix strain at first uniaxial damage
$\boldsymbol{\varepsilon}_\tau$	Inhomogeneity-induced eigenstrain
$\boldsymbol{\varepsilon}_\Omega$	Strain in the inclusion
ζ	Effective local strain parameter
λ	Normalised asperity height
λ	Plastic multiplier
λ_{cl}, λ_{int}	Interpolation functions in the smoothed contact state function
μ	Coefficient of friction
ρ	Normalised distance parameter
$\boldsymbol{\sigma}$	Stress tensor
$\overline{\boldsymbol{\sigma}}$	Average stress tensor
$\boldsymbol{\sigma}_0$	Far-field stress
$\boldsymbol{\sigma}_c$	Contact stress

$\boldsymbol{\sigma}_m$	Matrix stress tensor
$\boldsymbol{\sigma}_{m\Omega}$	Stress in the matrix, outside an inclusion
$\boldsymbol{\sigma}_{\Omega}$	Stress in the inclusion
τ_L	Local shear stress component
υ	Poisson's ratio
υ_m	Poisson's ratio for matrix phase
υ_{Ω}	Poisson's ratio for inclusion phase
φ	Angle of friction
ω	Damage parameter
ϕ_{cl}	Closed surface function
ϕ_{int}	Interlock surface function
$\boldsymbol{\Phi}$, $\boldsymbol{\Phi}_d$, $\boldsymbol{\Phi}_g$	Contact matrices
a	Radius of a spherical inclusion
c_f	Effective contact function
d_{max}	Maximum aggregate size
f	Crack density parameter
f_c	Compressive strength
f_m	Volume fraction of matrix phase
f_{Ω}	Volume fraction of inclusion phase
f_t	Tensile strength
f_{ti}	Tensile strength of the ITZ
f_{tm}	Tensile strength of the matrix phase
$\mathbf{g}$	Gap strain
$\mathbf{g}_e$, $\mathbf{g}_{ne}$, $\mathbf{g}_{me}$	Total, normal and tangential elastic gap vectors
h_t	Height of asperities
k_n, k_m	Elastic normal and shear stiffness per unit area
m_g	Slope of asperities
$\hat{\mathbf{n}}$ and $\hat{\mathbf{m}}$	Unit normal and tangent vectors relative to the tooth surface
p	Contact proportion
$\mathbf{r}$, $\mathbf{s}$, $\mathbf{t}$	Local coordinate system
$\mathbf{s}$	Local stress
$\mathbf{s}_r$	Local recovered stress
$\mathbf{s}_u$	Local stress on undamaged material

$\mathbf{t}_c$	Total wall (contact) traction vector
$\mathbf{t}_{cn}$, $\mathbf{t}_{cm}$	Normal and tangential traction vectors
$\mathbf{u}(\alpha) = \begin{bmatrix} u_\zeta \\ u_\rho(\alpha) \end{bmatrix}$	Tooth displacement vector in cylindrical coordinates
$\mathbf{u}_c$	Stress free displacement vector
$\mathbf{u}_p$	Plastic displacement vector
u_0	Crack opening at the end of softening curve
w	Crack opening
$\mathbf{x}$	Position vector relative to the centre of an inclusion
$\bar{\mathbf{x}}$	Unit position vector
A_b	Base area of a conical asperity
A_c	Contact surface area
$\mathbf{C}_{add}$	Total added compliance
$\mathbf{C}_{c\alpha}$	Local added compliance
$\mathbf{C}_L$	Local elastic compliance tensor
$\mathbf{D}$	Elasticity matrix
$\mathbf{D}_L$	Local elasticity matrix
$\mathbf{D}_m$	Elasticity tensor for matrix phase
$\mathbf{D}_s$	Secant stiffness
$\mathbf{D}_t$	Tangent stiffness
$\mathbf{D}_\Omega$	Elasticity tensor for inclusion phase
$\mathbf{D}_{m\Omega}$	Effective elasticity tensor of a two-phase composite
E	Young's modulus
E_m	Young's modulus for matrix phase
E_Ω	Young's modulus for inclusion phase
F_n	Yield function for plastic embedment
F_s	Yield surface for frictional sliding
F_s	Damage surface
F_{sf}	Yield surface for frictional sliding for flat component
F_ζ	Local damage (microcracking) function
G	Shear modulus
G_f	Fracture energy
H	Heaviside function

H_f	Contact reduction function
$\mathbf{I}^{2s}$	Second order identity tensor
$\mathbf{I}^{4s}$	Fourth order identity tensor
$\mathbf{N}$	Transformation tensor
$\mathbf{S}$	Eshelby tensor
$\mathbf{S}_E$	Exterior point Eshelby tensor
$\mathbf{U}$	Relative displacement vector

Contents

Declaration ii

Abstract iii

Acknowledgements iv

List of symbols v

1 Introduction 1

1.1 A brief history of concrete modelling 2

1.2 Scope and outline of thesis 11

1.3 List of publications 13

2 Micromechanical constitutive model 15

2.1 Literature review. Micromechanics based concrete models 15

2.2 Theoretical components of the model 27

2.3 Summary and concluding remarks 41

3 Damage initiation and evolution. Numerical predictions 42

3.1 Damage initiation and evolution criteria in micromechanical models . 42

3.2 Exterior point Eshelby based microcrack initiation criterion 45

3.3 Discussion on EPE based crack initiation criterion and rough microcrack characteristics 52

3.4 Summary of micromechanical constitutive model 62

3.5 Numerical implementation 62

3.6 Model parameters and numerical simulations 64
3.7 Concluding remarks 73
4 Multi-asperity plastic-contact crack plane model 74
4.1 Introduction 74
4.2 Constitutive model 77
4.3 Stress computation algorithm..... 86
4.4 Model parameters 89
4.5 Numerical results..... 90
4.6 Concluding remarks 100
5 Miscellaneous computational aspects 101
5.1 Contact chatter 101
5.2 Numerical integration rules 118
5.3 Rate formulation. Tangent stiffness 121
5.4 Concluding remarks 126
6 Finite element analysis 127
6.1 Simplified 2D constitutive model 127
6.2 Implementation in LUSAS 130
6.3 Numerical examples 133
6.4 Summary and concluding remarks 149
7 Discussion and conclusions. Recommendations for future work 150
7.1 Discussion and conclusions 150
7.2 Recommendations for future work 154

Bibliography 156

Annex 1..... 172

Annex 2..... 173

Chapter 1

Introduction

In the age of nanocomposites, concrete could be regarded as a low-tech and well understood material. With an impressive amount of research having been carried out over the last century in order to understand the phenomena and mechanisms that govern its complex behaviour one would indeed think that all is known that can be known about this material. However, it has been the author's experience that this is far from true. In fact, today there is still plenty of scope for exploring the fundamental nature of concrete and its behaviour. As will be explained later in this chapter, current mathematical models are as yet incapable of reproducing the mechanical and transient behaviour of this material in an accurate manner. Furthermore, only now is the true nanostructure of concrete being discovered (Jennings and Bullard, 2011) which should reveal the true mechanisms that control its complex behaviour.

This does not mean that all research has ceased on the development of the basic material itself. To the contrary, there are now major research initiatives at making concrete more sustainable which come from both industry and environmentally motivated efforts to produce a 'greener' and more durable type of concrete with less embodied energy and less CO_2 emissions in its production (The Concrete Centre, 2010). This need for a more sustainable type of concrete has given birth to new, or revitalised, fields of research, engaging experimental as well as numerical investigations (Ulm, 2010); from 'green' cement replacements (Vandeperre et. al, 2008; Komnitsas and

Zaharaki, 2007) to manufactured and recycled aggregates (Nanthagopalan and Santhanam, 2011; Huang et al, 2012;), from fibre-reinforced (Farhat et al., 2007; Deeb et al, 2011; Sakulich and Li, 2011) to self-healing concrete (Wiktor and Jonkers, 2011; Wu et al., 2012)

Nevertheless, as mentioned earlier, long-standing issues remain to this day that have not been addressed to a satisfactory conclusion. One such aspect is modelling the mechanical behaviour of concrete. The lack of a well-accepted, robust and accurate mathematical model for the mechanical behaviour of concrete is preventing the more widespread use of non-linear analysis of concrete structures in practice and may also be a hindrance to the development of the new research areas mentioned above.

1.1 A brief history of concrete modelling

Extensive research has been carried out over the last few decades in order to explain and model damage phenomena in quasi-brittle materials such as concrete. It is generally accepted that the heterogeneous structure of such materials observed at nano, micro and meso levels determines their complex macroscopic behaviour and failure mechanisms (van Mier 1997).

The beginnings of research on numerical models for plain and reinforced concrete is marked by the two notable papers published in the late 1960s by Ngo and Scordelis (1967) and Rashid (1968) in which the “discrete” and “smeared” approaches for simulating cracks in finite element applications were introduced.

The short review presented in this section draws heavily on a number of previous reviews (Mazars and Pijaudier-Cabot, 1989; de Borst, 2002; Nguyen, 2005; Jefferson, 2010) and focuses on constitutive formulations, although it is recognised that in the case of modelling the mechanical behaviour of concrete, constitutive aspects are strongly linked to the computational issues related to scaling and fracture associated size effects as pointed out by Jefferson (2010).

Concrete modelling at a constitutive level can be classified in two main categories: macroscopic models that follow a phenomenological approach and models based on micromechanical solutions. Phenomenological models generally employ theories based on plasticity and /or damage mechanics in order to simulate the macroscopic behaviour

and their formulation often makes use of functions obtained by fitting experimental data (e.g. uniaxial tension and compression curves, strength envelopes). On the other hand micromechanical models aim to relate the microstructure of concrete, and the physical mechanisms that govern its evolution, to the macroscopic behaviour observed in experiments.

1.1.1. Plasticity models

In essence, plasticity theory, and therefore models based upon it, has the following main ingredients, a yield surface, a flow rule and a hardening function –or plastic evolution equation. Additionally, for the small strain case, plasticity models assume an additive decomposition or split of the total strain into the elastic strain and the plastic strain respectively and a constitutive relationship for the elastic part. The yield surface, defined by a yield function, initially bounds the elastic domain in the stress space and its evolution (i.e. the way it expands or contracts in the stress or strain space) is controlled by the hardening function. Finally, the flow rule governs the evolution of the plastic strain. The yield criterion is generally expressed as:

$$F(\boldsymbol{\sigma}, \kappa) \leq 0 \tag{1.1}$$

where $\boldsymbol{\sigma}$ is the stress tensor and κ denotes the hardening variable.

In general, yield surfaces have been proposed based upon biaxial and/or triaxial failure envelopes for concrete obtained experimentally. Willam and Warnke (1975) proposed such a yield surface which has since been widely applied in various models for concrete. The *failure surface* has an open shape, as indicated directly by experiments. In contrast, observations of the non-linear behaviour of concrete show that the *initial yield surface* should be "capped" to account for the plastic deformations which take place under hydrostatic compression. Therefore, as pointed out by Han and Chen (1985), yield surfaces prescribed as scaled down failure surfaces, although appealing, are inadequate.

In addition, many authors have considered it necessary to use non-associated flow rules, based upon a plastic potential different from the yield function, in order to capture the volumetric dilatancy of concrete under compression (Kang and Willam, 1999).

Other notable plasticity based models for concrete are those by Feenstra and de Borst (1995) and Grassl et al. (2002).

1.1.2. Damage models

The roots of damage theory date back to 1958 with the definition of a scalar damage variable by Kachanov, although Hult was the first to introduce the term "continuum damage mechanics" in 1972 (Lemaitre and Desmorat, 2005). The early developments of damage mechanics concepts, largely attributed to the French school, took place in the context of modelling cracks in reinforced concrete (Mazars, 1984; Mazars and Pijaudier-Cabot, 1989; de Borst, 2002).

Formulations based on continuum damage mechanics describe the progressive degradation of stiffness resulting from the propagation of microcracks. The degree of degradation is characterised by damage parameters that can be scalars, a family of vectors (Krajcinovic and Fonseka, 1981) or in the most general case a fourth-order tensor (Chaboche, 1979). Somewhat similar to plasticity theory, damage mechanics theory employs a damage function that controls the initiation of damage and evolution functions that govern the manner in which the damage function progresses with the damage parameter. These equations are generally written in terms of strains, stresses or energy based variables derived within a thermodynamic framework.

The fundamental concepts of damage mechanics are best illustrated by a simple isotropic damage model (Eq. 1.2) which employs a simplifying assumption that the degradation of stiffness is isotropic. With an additional assumption that the Poisson's ratio remains unaffected, damage can be characterised by a single scalar parameter.

$$\boldsymbol{\sigma} = (1-\omega)\mathbf{D}_{el} : \boldsymbol{\varepsilon} \tag{1.2}$$

where ':' denotes tensor contraction. $\boldsymbol{\sigma}$ and $\boldsymbol{\varepsilon}$ represent the macroscopic stress and strain tensor respectively, $\mathbf{D}_{el}$ is the elasticity tensor of the undamaged material and ω is the damage parameter generally defined such that it grows from 0 for an undamaged state to 1 for a fully damaged state.

While the formulation of such a model is appealing, it is unable to describe the difference between tensile and compressive behaviour of concrete. To account for this

discrepancy, Mazars (1986) assumed the damage parameter to comprise two components; one relating to tensile damage and governed by a tensile evolution function (ω_t) and the other relating to compressive damage and controlled by a compressive evolution law (ω_c). The overall damage parameter was then expressed as:

$$\omega = \alpha_t \omega_t + \alpha_c \omega_c \tag{1.3}$$

where α_t and α_c are parameters that depend upon the degree of tension and compression respectively in a multiaxial loading case.

Other significant isotropic damage models for concrete that employ two scalar damage parameters for tension and compression were proposed by Faria et al. (1998), Comi and Perego (2001), Marfia et al. (2004).

Damage in concrete, however, is not an isotropic process and models based on the isotropic damage assumption in general experience a number of deficiencies; in particular they are unable to capture the volumetric expansion (dilatancy) observed in uniaxial compression experimental tests and for large tensile strains applied in one direction the stiffness is completely lost in the loading direction and unrealistically reduced in lateral directions. In order to overcome these drawbacks, formulations have been explored and proposed that take into account the damage induced anisotropy. These anisotropic formulations however have a higher level of complexity as they usually employ second (Desmorat et. al, 2007) or even fourth-order tensors (Chaboche, 1979) to characterize damage and as mentioned by Contrafatto and Cuomo (2006) they exhibit serious convergence problems when implemented in finite element codes. These drawbacks often cause the simplified although unrealistic assumption of isotropic damage to be preferred and employed over the anisotropic damage assumption (Jirásek and Zimmermann, 1998; Salari et al, 2004; Contrafatto and Cuomo, 2006).

The reduction of stiffness and strength of concrete comes as a direct result of the onset and propagation of microcracking. Nevertheless, stress states do exist for which this effect diminishes or can disappear altogether. For instance when a previously open crack – that contributed to the stiffness reduction – is subsequently subjected to compressive stresses normal to the crack plane, it closes and the crack faces regain contact. The compressive stresses can thus be transferred across the crack plane although the damage state does not change (the damage parameter does not reduce).

These phenomena are referred to as unilateral or crack closure effects, damage deactivation or stiffness recovery. A very basic illustration of the abovementioned concepts is given for a one-dimensional damage model in Eq. (1.4) in which the deactivation of damage is taken into account by the introduction of a Heaviside function H that is 0 for negative (compressive) strains and 1 for positive (tensile) strains.

$$\sigma = \left[1 - \omega \cdot H(\varepsilon)\right] \cdot E \cdot \varepsilon \tag{1.4}$$

where E denotes Young's modulus. Extending the formulation to multiaxial models is not straightforward even for the case of isotropic damage models since a sudden deactivation of a damage parameter that multiplies a tensor can result in discontinuities. In these cases the formulations need to additionally satisfy a stress continuity condition.

Damage mechanics based models are generally developed within the thermodynamic framework of irreversible processes which controls the formulation of the damage criterion and evolution law. Lemaitre and Desmorat (2005) summarised this in three steps: 1) the definition of state variables (i.e. damage variable), 2) the definition of a state potential (generally expressed as the free energy potential) based on which the damage function is derived and 3) the definition of a dissipation potential, in turn employed in obtaining the evolution law of the state variable associated with the dissipative mechanism. The thermodynamic admissibility of the formulation is then assessed by checking that the second law of thermodynamics, conveniently expressed as the Clausius-Duhem inequality, is satisfied for any evolution. It is worth noting that the convexity of the dissipation potential function ensures the fulfilment of the second law (Lemaitre and Desmorat, 2005).

1.1.3. Plastic-damage models

Formulations of constitutive models for concrete that combine plasticity and damage theory have been proposed (Simo and Ju, 1987a,b; Lee and Fenves, 1998; Jefferson, 2003; Contrafatto and Cuomo, 2006; Cicekli et al., 2007) based on the argument that plasticity or damage theory employed on their own were not sufficient to capture key characteristics of the overall behaviour. As discussed by Contrafatto and Cuomo (2006), plasticity theory is not able to address properly the stiffness degradation due to microcracking whereas models based on continuum damage theory alone cannot

capture other important facets of concrete behaviour such as permanent deformations and inelastic volumetric expansion in compression. Moreover, Jefferson (2010) suggested, based on observations of the behaviour of concrete in tension and compression cyclic tests, that on one hand the tensile behaviour with an approximately secant unloading path is better reproduced by damage theory and on the other hand behaviour in compression, which follows a relatively elastic unloading path, is captured better by pure plasticity. In general, plastic-damage models combine isotropic hardening with either isotropic damage (Lee and Fenves, 1998; Lubliner et al., 1989) or anisotropic damage (Ortiz, 1985; Cicekli et al., 2007).

1.1.4. Microplane models

The microplane model, developed by Bažant and co-workers since the mid 1980s, was originally inspired by micromechanics (Bažant and Oh, 1984; Bažant and Prat, 1988), however it differs from the more mechanistic micromechanical models discussed in Chapter 2 as it was subsequently developed along a more phenomenological path (Bažant and Caner, 2005).

The first generalised microplane model employed an idea initially proposed by Taylor (1938) and subsequently applied by Batdorf and Budianski (1949) in a constitutive model for polycrystalline metals. According to Taylor (1938) the stress-strain relationship of a material can be defined in an independent manner on planes of various orientations – in this context called microplanes – by assuming either a static constraint (i.e. the stresses on a microplane are the resolved components of the macroscopic stress) or a kinematic constraint (i.e. the strains on a microplane are the resolved components of the microscopic strain tensor). The kinematic constraint was adopted by Bažant and Prat (1988) since it enabled, unlike the static constraint, a stable response during strain softening. On each microplane the strain vector comprised a normal and a shear component and the normal component was subsequently split into volumetric and deviatoric parts. Several assumptions were additionally employed. The volumetric, deviatoric and shear responses were assumed to be mutually independent and therefore each microplane was characterised by three decoupled, phenomenologically determined constitutive relations. Moreover, on each microplane these constitutive equations were assumed path independent for monotonic loading,

although the overall response displayed significant path dependence. Finally, the macroscopic stress tensor was obtained from the microplane stresses by employing the principle of virtual work.

The basic formulation presented by Bažant and Prat (1988) was extended in several ensuing versions. Carol et al. (1992) kept the fundamental assumptions from Bažant and Prat (1988) and mainly addressed computational issues with the aim of obtaining a more efficient numerical algorithm. In Ožbolt and Bažant (1992) and Hasegawa and Bažant (1993) cyclic loading and rate effects (i.e. the sensitivity to the deformation rate of the strength, stiffness and ductility of concrete) were introduced and the nonlocal formulation proposed by Bažant and Ožbolt (1990) was implemented to address the spurious mesh sensitivity problems related to strain localization. Furthermore, the model of Hasegawa and Bažant (1993) did not employ the volumetric-deviatoric split of the microplane normal strain. The thermodynamic validity of the microplane theory was assessed in Carol et al. (2001) and it was concluded that this was not guaranteed for the versions applying the split of the normal strain.

The more recent version of the microplane models (Bažant et al., 2000; Caner and Bažant, 2000; Bažant and Caner, 2005a, b) followed an even more phenomenological route in an attempt to fit a wide range of experimental data.

One of the impressive aspects of these developments is the range of experimental data used to calibrate the functions and to validate the model. However, one of the major drawbacks of the microplane model is the large number of model parameters used which do not have clear physical meanings. For example, Qiu (1999) reported that the microplane model proposed by Hasegawa and Bažant (1993) required a total of 39 parameters and from a practical point of view this represented a significant problem since no clear guidance was given with respect to the calibration of these parameters. In fact this is a common issue for macroscopic models: they have, in general, a large set of parameters, the majority of which having no physical interpretation. This is a direct consequence of the phenomenological or data-fitting approach.

1.1.5. Alternative approaches

Many macroscopic models based on damage and plasticity theories have been proposed and implemented in commercial FE codes with varying degrees of success

however, as mentioned earlier, they often use parameters that are difficult to determine and thus far no one model has been able to fully simulate all aspects of the complex behaviour of concrete. Therefore the development of an accurate and robust constitutive model remains a challenge.

In recent years, alternative approaches to modelling the mechanical behaviour of concrete have been proposed such as micromechanical and multi-scale models. In contrast to the phenomenological approach employed by more established macroscopic models, micromechanical models aim to capture the macroscopic behaviour observed in experiments by considering simple physical mechanisms modelled at micro and meso scales. These models will be presented in more detail in Chapter 2.

In the multi-scale approach, concrete is simulated by separately discretizing its components observed at a meso-level: aggregate particles, mortar and aggregate-mortar interfaces (Lopez et al., 2007; Gitman, 2006; Gitman et al., 2008).

Gitman et al. (2007) and Gitman (2006) used a multiscale approach to explore the existence of an RVE for concrete in both the undamaged and damaged state, concluding that once damage has progressed to a certain point, the concept of an RVE ceases to have meaning for quasi-brittle materials such as concrete.

The formulation proposed by Lopez et al. (2007) for the analysis of concrete specimens in 2D was able to predict realistic uniaxial and biaxial responses however such models can be expensive when large structures are analysed.

1.1.6. Computational aspects

The work presented in this thesis focuses on modelling the behaviour of quasi-brittle materials such as concrete at a constitutive level. Nevertheless, it is recognised that for a complete and reliable approach, computational issues related to the application of the constitutive model within a finite element code such as stress locking, mesh dependency of strain softening models, numerical efficiency (Feenstra and de Borst, 1995; Jefferson, 2010) need to be addressed likewise.

Spurious mesh-sensitivity is a problem common to strain softening models in which damage tends to localise in a zone of single element width and the energy

dissipated when opening the crack by a certain amount becomes a function of the element size. Moreover, with mesh refinement, the energy dissipation that causes failure converges to zero which is physically unrealistic (Pijaudier-Cabot and Bažant, 1987).

Several regularisation solutions have been proposed in order to address this issue. Bažant and Oh (1983) developed the crack-band theory based on the fundamental hypothesis that in the softening region damage localises to a band of single element width. The theory tends to be successful in situations where a discrete crack forms and thus the strains do localise to a defined fracture zone of one element width. However, it does not deal with the gradual development of a fracture process zone of changing width or mesh orientation bias (Jefferson, 2010). Strain softening related stability problems are not solved either.

Alternative techniques proposed to address mesh sensitivity, mesh bias and stability issues are the integral (Pijaudier-Cabot and Bažant, 1987; Bažant and Pijaudier-Cabot, 1988) and gradient (Peerlings et al., 1996 and 1998) nonlocal theories. It is interesting to note that after some years of following separate paths it was shown that the two approaches were effectively equivalent (Peerlings et al., 2001). The fundamental idea of integral nonlocal theory was explained for a simple isotropic damage model by Pijaudier-Cabot and Bažant (1987). The local damage parameter at a point was replaced by a nonlocal parameter that in turn was a function of a weighted average strain energy release rate over a representative volume centred on the given point. A general integral equation in strain terms reads:

$$\bar{\boldsymbol{\varepsilon}}(\mathbf{x}) = \frac{1}{V}\int_V g(\boldsymbol{\xi})\boldsymbol{\varepsilon}(\mathbf{x}+\boldsymbol{\xi})dV \tag{1.5}$$

where $\bar{\boldsymbol{\varepsilon}}$ denotes the non-local strain, $\mathbf{x}$ is the position vector of the given material point, g(ξ) is a weight function with $\frac{1}{V}\int_V g(\boldsymbol{\xi})dV = 1$ and ξ denotes the relative position pointing to the infinitesimal volume *dV*. The size of the representative volume is defined by a characteristic length (l_{ch}). The gradient formulation is obtained by expanding the local strain into a Taylor series and introducing it, with higher order terms neglected, into the nonlocal strain definition. The governing equation becomes (see also Ru and Aifantis, 1993 and Askes and Aifantis, 2002):

$$\bar{\boldsymbol{\varepsilon}} - {l_{ch}}^2\nabla^2\bar{\boldsymbol{\varepsilon}} = \boldsymbol{\varepsilon} \tag{1.6}$$

in which ∇^2 denotes the Laplacian operator.

The nonlocal approaches successfully address mesh sensitivity and bias but tend to be computationally expensive and their implementation can be problematic for complex constitutive models (Jefferson, 2010).

In recent years, techniques to simulate the development of cracks within a finite element framework in which strong discontinuities (i.e. jumps in the displacement field) are embedded at the element level have been proposed (Belytschko and Black, 1999; Moes et al., 1999; Belytschko et al, 2001, Oliver et al., 2002; Oliver and Husepe, 2003). These methods have proved to be powerful and convenient tools for simulating cracking (Karihaloo and Xiao, 2003) however additional research is required to address issues such as tracking multiple cracks in 3D (Oliver et al., 2004; Oliver and Husepe, 2004). Nevertheless, there seems to be an increasing sense that the strong discontinuity approach should be included for a complete solution to modelling concrete structures (Wells and Sluys, 2001).

1.2. Scope and outline of thesis

As indicated in the brief review presented in the previous section, considerable research has been carried out since the late 1960's for developing models and techniques to simulate the mechanisms leading to failure of quasi-brittle materials such as concrete. Although the progress achieved during this time is considerable, as yet, no one model has been able to fully capture all facets of the complex mechanical behaviour of concrete. The work of this thesis aims to address this issue and to demonstrate the potential of micromechanical models to finally achieve a fully robust and comprehensive model for concrete. The author does not claim to have developed the definitive model but the work to be presented in the remainder of this thesis does, in the author's opinion, clearly demonstrate the potential of the models developed and also does represent a significant step forward in the use of micro-mechanical theories in the constitutive modelling of concrete.

A particular focus is dedicated to the development of a micromechanical constitutive model which employs the essential ideas described in Jefferson and Bennett (2007 and 2010). However the present model adopts a more mechanistic approach in

that a number of phenomenological aspects of the previous formulations have been replaced with mechanistic components. The author also considers that a generally more rigorous and comprehensive approach to the model developed has been adopted for the present work.

In the first part of Chapter 2, a review of micromechanics based constitutive models for concrete is presented. The second part of Chapter 2 then provides details of three theoretical solutions employed in the formulation of the constitutive model. A two-phase composite elasticity theory based on the classic Eshelby inclusion solution is adopted to simulate a composite material comprising an elastic matrix -to simulate the mortar- and spherical inclusions -to model the coarse aggregate particles. Microcracking in the elastic matrix is addressed by evaluating the added compliance from a distribution of cracks with various orientations. The third solution presented deals with crack closure effects in a multi-asperity rough crack component.

In Chapter 3 a microcrack initiation criterion is proposed employing the exterior point Eshelby solution which captures tensile stress concentrations in the vicinity of the matrix-inclusion boundary. Microcracks can therefore be assumed to initiate in the interfacial transition between coarse aggregate particles and mortar. Numerical predictions compared against experimental results are presented for a range of uniaxial, biaxial and triaxial simulations in order to assess the performance of the proposed model at a constitutive level.

A new 3D multi-asperity plastic-friction-contact mechanistic crack plane model is described in Chapter 4 with the intention of being incorporated in the overall constitutive model, although this has yet to be achieved. Nevertheless the formulation presented in Chapter 4 is a model in its own right which can be applied to simulate the characteristic crack-plane behaviour of micro, meso and macrocracks in a range of quasi-brittle geomaterials. The mechanistic components which include simulating crushing and frictional sliding on the sides of conical asperities and the derivation of an effective contact function to relate the contact stresses that develop on the sides of the teeth to the net stresses on a crack plane are presented followed by a study on the geometrical quantification of the morphology of a rough crack surface. Simulations of several experimental tests are then carried out in order to validate the model.

Chapter 5 deals with several computational issues namely; a smoothed contact state function is proposed to address rough contact related instability problems or 'chatter', a study of integration rules is presented to assess the accuracy of such methods in the context of the micromechanical constitutive model and the derivation of the consistent tangent stiffness is given.

In Chapter 6, details regarding the implementation of a 2D simplified version of the micromechanical model into the finite element commercial code LUSAS followed by a set of numerical simulations of experimental tests which show the potential of such a model are presented.

Finally, Chapter 7 presents the overall conclusions and gives indications towards future work.

1.3. List of publications

Part of the work presented in this study is featured in a number of journal articles as follows:

Mihai I.C., Jefferson A.D., 2011. A numerical model for cementitious composite materials with an exterior point Eshelby microcrack initiation criterion. *International Journal of Solids and Structures* 48(24), 3312-3325. (This paper covers the work detailed in Chapters 2 and 3)

Mihai I.C., Jefferson A.D., 2012. A multi-asperity plastic-contact crack plane model for geomaterials. *International Journal for Numerical and Analytical Methods in Geomechanics.* Accepted. DOI: 10.1002/nag.2094 (This paper presents the crack plane model formulated in Chapter 4)

Mihai I.C., Jefferson A.D. Smoothed contact in a micromechanical model for cement bound materials. *Computers and Structures.* Invited paper. Submitted for review and possible publication. (This paper presents the study on rough crack contact related instability problems)

Additionally, the developments of the micromechanical constitutive model were systematically presented at national and international conferences:

Mihai I., Jefferson T., 2009. A constitutive model for cementitious composites

based on micromechanical solutions. *Proceedings of the 17 thUK Conference on Computational Mechanics (ACME), Nottingham*

Jefferson T., Mihai I., Lyons P. 2009. A model for concrete based on micromechanical solutions. *Proceedings of the X International Conference on Computational Plasticity (COMPLAS X), Barcelona, Spain*

Mihai I.C., Jefferson A.D. 2010. The simulation of microcracking and micro-contact in a constitutive model for concrete. *Computational Modelling of Concrete Structures. Proceedings of EURO-C, Rohrmoos-Schladming, Austria*

Mihai I., Jefferson T., 2011. An interface failure criterion in a micromechanical model for concrete. *Proceedings of the 19 thUK Conference on Computational Mechanics (ACME), Edinburgh*

Mihai I., Jefferson T., 2011. Microcrack initiation criterion in a micromechanical model for concrete. *XI International Conference on Computational Plasticity (COMPLAS XI), Barcelona, Spain*

Chapter 2

Micromechanical constitutive model

2.1. Literature review. Micromechanics based concrete models

In the context of applied mechanics, micromechanical analysis -or in short *micromechanics*- provides the mechanical and mathematical framework in which the *overall* or *macroscopic properties* and *macroscopic behaviour* of a composite or heterogeneous material are examined based on a priori knowledge regarding its *microstructure* and *microscopic properties*. In modelling composite or heterogeneous materials, a particular focus is given to evaluating their *effective* or *homogenized properties* and this can be achieved through various micromechanics-based *homogenization* or *averaging schemes*.

A number of textbooks have been published over the years that provide details of the established micromechanical solutions as well as of the more recent advances in the field, notably the works of Mura (1987), Nemat-Nasser and Hori (1993) and more recently Dormieux et al. (2006) and Li and Wang (2008). It is noted that the aforementioned list is not by any means exhaustive.

Micromechanical solutions have been employed extensively during the last few decades in modelling composite materials, in particular metal matrix composites (Ju and Chen, 1994; Ju and Tseng, 1996; Ju and Lee, 2001; Ju and Sun, 2001). In more recent years, work has been carried out on the application of micromechanics based solutions

to modelling various other materials with heterogeneous structures such as wood (Hofstetter et al., 2005), bones (Hellmich et al, 2004), fibre-reinforced composites (Kim and Lee, 2009), cementitious materials or rocks (Zhu et al. 2008; Xie et al, 2011). In the case of cement based materials, micromechanical solutions have been used to model a wide range of aspects; initially, work concentrated on the mechanical behaviour (Penseé et al., 2002; Penseé and Kondo, 2003; Zhu et al., 2008; 2009; 2011; Gambarotta, 2004) but more recently investigations have explored formulations for modelling early age properties (Bernard et al., 2003; Pichler et al., 2009a,b; Pichler and Hellmich, 2011) or shrinkage (Pichler et al, 2007; Zhang et al., 2012).

This section presents a review of the micromechanics based constitutive models for simulating the mechanical behaviour of mature concrete. As the micromechanical approach is relatively recent in concrete modelling considerably fewer constitutive models have been proposed than those based on phenomenological theories. Three main research groups with significant contributions in this area can be identified; however, the author recognizes that this is not a strict classification: the group of Kondo, Shao and co-workers, the group of Gambarotta and co-workers and the group of Pichler and co-workers, which are discussed in Sections 2.1.1, 2.1.2 and 2.1.3 respectively.

Generally, the aim with micromechanical models is to capture the macroscopic mechanical behaviour observed in experiments by simulating simple physical mechanisms at micro and mesoscale. This is in contrast with the phenomenological macroscopic models for which uniaxial compression, uniaxial tension functions and strength envelope equations are generally prescribed directly. The mechanistic micromechanical models combine individual mechanistic components to predict a response which is not pre-prescribed. This means that the prediction of behaviour as apparently simple as the uniaxial compressive response of concrete, with the near peak associated dilatancy, becomes a significant challenge. This challenge is, however, worth addressing because, as alluded to in the introduction chapter, all present macroscopic models have shortcomings.

2.1.1. Work of Kondo, Shao and co-workers

Kondo, Dormieux, Shao, Pensée and Zhu conducted a detailed investigation of a number of micromechanical solutions applicable to quasi-brittle materials (Pensée et al.,

2002, Pensée and Kondo, 2003, Zhu et al, 2008). Based on this study a number of models for concrete (Zhu et al, 2009, Zhu et al, 2011) and rocks (Xie et al, 2011) were proposed.

In Pensée et al. (2002) two equivalent approaches for deriving the homogenised properties of a solid weakened by penny-shaped microcracks were investigated. Crack closure (unilateral effect) was also included in the study. This analysis, which in part represents a 3D generalization of the framework proposed by Andrieux et al. (1986), employed two assumptions, namely: *i)* the interaction between microcracks can be neglected and *ii)* the density of microcracks is dilute (i.e. volume fraction of microcracks ≤ 0.05).

In the first approach presented by Pensée et al. (2002), also referred to as the direct approach, the homogenised properties (i.e. the effective elasticity tensor relating macroscopic stresses to macroscopic strains) were obtained from a closed form expression of the free energy (effective potential). The free energy was in turn derived following a decomposition in which the macrostrain was split into an elastic homogeneous component and a 'fracture' strain component due to the presence of penny-shaped microcracks. The latter was obtained by employing the solution presented in Nemat-Nasser and Hori (1993) in which the normal and tangential components of the crack opening displacement were derived and then integrated over the crack surface and averaged over the crack volume to give the additional strains due to a family of cracks with the same orientation. In the derivation of the free energy, two cases of open microcracks and frictionless closed microcracks were explicitly considered and based on the dilute microcrack density assumption a strain-based opening/closure criterion was also derived.

The homogenized properties were alternatively derived by employing the Eshelby inclusion approach in which the microcracks were modelled as flat ellipsoidal inclusions. The open cracks were characterized by null normal and shear stiffness whereas in the frictionless closed microcracks the normal stiffness was recovered.

The formulation was then generalized in order to obtain the homogenized properties for a solid weakened by randomly distributed microcracks. The generalised macroscopic free energy was subsequently expressed as the integral of the free energy associated with each family of microcracks (microcracks that have the same

orientation). To account for the fact that the microcracks can occur in any direction, the integration is performed over a unit sphere and is evaluated numerically using an integration rule with 33 integration directions with associated weights, distributed over the upper hemisphere.

Both methods made use of a crack density parameter *d* associated with the considered microcrack family (originally introduced by Budiansky and O'Connell, 1976) and this parameter constituted a convenient internal damage variable. For a given microcrack family, a damage yield function in the form of Eq. (2.1) was proposed in which F^{d^i} is a thermodynamic force or a strain energy release rate associated with the *i*th microcrack and *R(d)* represents a crack resistance curve which was assumed to be a linear function in *d*.

$$f(F^{d^i}, d^i) = F^{d^i} - R(d^i) \tag{2.1}$$

in which the thermodynamic force F^{d^i} is defined based on the free energy W^i as $F^{d^i} = -\frac{\partial W^i}{\partial d^i}$.

Finally, the evolution of damage was obtained by employing the normality rule. The damage formulation has an intrinsic anisotropic nature given by the dependence of the damage variable on the microcrack orientation.

As discussed in Pensée et al. (2002) each of these equivalent approaches have unique advantages that facilitate the expansion of the formulation. On one hand, due to the fact that in the direct approach the normal and tangential crack opening displacements can easily be evaluated frictional sliding on closed microcrack faces can be incorporated in a straightforward manner. On the other hand, the Eshelby approach can be readily extended to account for microcrack interaction. These two issues are subsequently explored in the study of Zhu et al. (2008).

In Pensée and Kondo (2003) an alternative stress-based formulation to the strain-based anisotropic damage model of Pensée et al. (2002) was proposed. Following the direct method the homogenised compliance tensor was derived from a stress-based expression of the macroscopic free enthalpy or (Gibbs energy) – which is related to the free energy by the Legendre transform. Furthermore, a microcrack closure condition stating that open cracks become closed when the normal stress cancels was assumed.

This is not strictly equivalent to the strain-based criterion in Pensée et al. (2002) since the latter employs a dilute crack density assumption. The damage yield function associated with a microcrack family was kept in the form of Eq. (2.1); however, the thermodynamic force was defined based on the free enthalpy W^{*i} as $F^{d^i} = \frac{\partial W^{*i}}{\partial d^i}$ and under a non-interacting microcracks assumption represented the strain energy release rate.

The comparative analysis of the predictive capabilities of the strain-based (Pensée et al., 2002) and stress-based (Pensée and Kondo, 2003) formulations under uniaxial tensile and compressive loading lead to the following conclusions:

- For lower stress or damage levels the predictions obtained with the two formulations are similar
- For higher stress levels predictions are significantly different
- The strain based formulations is able to predict a peak whereas the stress based formulations does not seem to. Pensée and Kondo (2003) suggested that the strain based formulations should be used in their future work.

The study of micromechanical solutions for modelling quasi-brittle materials was continued by Zhu et al. (2008) with the analysis of homogenizations schemes that take into account the interaction between microcracks and their spatial distribution. Frictional sliding on closed crack lips was also introduced into the formulation.

The Eshelby inclusion approach presented in Pensée et al. (2002) was extended and the homogenised stiffness for a solid weakened by a single family of penny-shaped microcracks was derived for three homogenization schemes: the dilute scheme (equivalent to the formulation in Pensée et al., 2002), the Mori-Tanaka (MT) scheme and the Ponte-Castaneda and Willis (PCW) scheme. In the dilute scheme microcrack interactions are ignored and whilst the formulation is kept simple –essentially this is equivalent to the solution for a inclusion in an infinite elastic media- this assumption can be unrealistic for moderate and high concentrations of microcracks. A frequently used method that takes into account crack interaction effects is the Mori-Tanaka scheme. However, it was argued by Zhu et al. (2008) that because it requires only the shape of the inclusions, i.e. microcracks, and does not take into account their spatial distribution, the effects of microcrack interaction are not thoroughly captured by the Mori-Tanaka

scheme. To address this limitation they proposed the scheme developed by Ponte-Castaneda and Willis (1995) as a more rigorous homogenisation method. This makes use of two Hill-type tensors, one that characterizes the shape of the inclusions and the other being associated to their spatial distribution.

The formulation was further extended by the coupling between damage evolution and frictional sliding on closed crack faces. The framework based on the strain energy release rate proposed by Pensée et al. (2002) was employed to model damage evolution and for the case of closed microcracks this was coupled with Coulomb based friction. The friction yield criterion was formulated in the form:

$$g = \left|\mathbf{F}^{\gamma}\right| + \mu_c F^{\beta} = 0 \tag{2.2}$$

where μ_c represented the coefficient of friction on the crack faces and the thermodynamic forces $\boldsymbol{F}^{\gamma}$ and F^{β} were defined as:

$$\begin{aligned} \mathbf{F}^{\gamma} &= -\frac{\partial W}{\partial \boldsymbol{\gamma}} = -\frac{\partial W}{\partial \mathbf{E}^{c}}\frac{\partial \mathbf{E}^{c}}{\partial \boldsymbol{\gamma}}, \\ F^{\beta} &= -\frac{\partial W}{\partial \beta} = -\frac{\partial W}{\partial \mathbf{E}^{c}}\frac{\partial \mathbf{E}^{c}}{\partial \beta} \end{aligned} \tag{2.3}$$

W denotes the overall free energy and $\mathbf{E}^{c}$ represents the macroscopic inelastic strain due to microcracks. $\boldsymbol{\gamma}$ and β were originally introduced in Pensée et al. (2002) as kinematic variables that characterize the crack displacement jump; β is a scalar variable that represents the crack opening and characterizes the crack opening-closure state and $\boldsymbol{\gamma}$ is a vector that quantifies the sliding along the crack plane. The flow rule or the evolution of sliding vector $\boldsymbol{\gamma}$ was next postulated as follows:

$$\dot{\boldsymbol{\gamma}} = \dot{\lambda}^{\gamma}\frac{\mathbf{F}^{\gamma}}{\left|\mathbf{F}^{\gamma}\right|} \tag{2.4}$$

An extensive comparative analysis of the predictions from the three homogenization schemes was carried out. In uniaxial tensile simulations the responses predicted by the three methods vary significantly. The dilute scheme produces a very brittle and unstable response, the response obtained when employing the Mori-Tanaka scheme resembles an elastic-perfectly plastic response with elastic unloading whereas the Ponte-Castaneda and Willis scheme leads to a strain softening behaviour. Friction

without damage evolution and friction coupled with damage were considered in a shear test under monotonous and cyclic loading paths. The simulation was in effect performed on a crack plane on which a compressive normal stress was pre-applied to ensure crack closure. In general, the model employing the MT scheme tended to predict strain hardening behaviour whilst both the dilute scheme and the PCW scheme led to a strain softening response, with the response predicted with the dilute scheme being considerably more brittle than with the PCW scheme. In this formulation dilatancy was directly addressed by the evolution of variable β and this component improved substantially the volumetric response in comparison with the formulations proposed by Pensée et al. (2002) and Pensée and Kondo (2003). However, it was observed that the (overall) response predicted with dilatant cracks was somewhat more brittle than for the non-dilatant crack case (in which the evolution of β was restrained).

Based on the results of the investigations carried out by Pensée et al. (2002), Pensée and Kondo (2003) and Zhu et al. (2008) two distinct comprehensive constitutive models were subsequently proposed in Zhu et al. (2009) and Zhu et al. (2011) and their performance assessed against experimental data.

In Zhu et al. (2009) an anisotropic damage model based on a homogenization procedure that made use of the Eshelby inclusion solution and Ponte-Castaneda and Willis scheme was proposed. The thermodynamics framework described at microscopic level by Pensée et al. (2002) for damage evolution with an energy release rate based damage criterion was employed. The model therefore simulated a solid material comprising a homogeneous matrix and a non-dilute distribution of penny-shaped microcracks with various orientations. Each microcrack family is characterised by a local (microscopic) damage yield surface and the overall (macroscopic) yield surface is the envelope of all individual surfaces. The model does not take into account frictional sliding on closed microcracks. It is also noted that crack initiation is not specifically addressed through a crack initiation criterion but it is merely and, in a somewhat simplified way, addressed by assuming an initial isotropic distribution of microcracks with a pre-set initial value of the crack density parameter variable in each direction. This rather simplified approach was employed by the authors due to the lack of significant information on the microstructure.

As mentioned before, the Ponte-Castaneda and Willis homogenization scheme considers crack interaction effects and takes into account both the shape of the cracks and their spatial distribution. Moreover the formulation of the model allows microcrack interaction to be also considered in both the damage criterion and in the crack opening-closure condition by making use of a tensor that couples the damage induced effect on stiffness from all microcrack families. Zhu et al. (2009) argued that physically, crack propagation in a certain direction alters the distribution of local fields and this in turn influences the damage evolution in other directions.

A noteworthy aspect of this model is its limited number of parameters; only four parameters, each with clear physical meaning, were employed: the elastic properties, i.e., Young's modulus and Poisson's ratio and two parameters involved in the damage criterion, which appear in the linear expression of the resistance curve R in Eq. (2.1). The latter parameters are, in fact, the primary means of calibrating the model.

Numerical predictions were subsequently compared with experimental data from various tests performed on concrete in order to evaluate the capabilities of the model. In general the numerical results compared well against experimental data from uniaxial tension and compression tests. A slight tendency for over-ductile post peak predicted responses could be observed, however the pre-peak responses as well as the tensile and compressive strengths were successfully captured. The performance of the model in biaxial simulations was not as effective; the predicted biaxial compressive strength was lower than the experimental one and occurred for a lower level of strain. The authors argued that this underestimation of the biaxial strength was due to the frictionless closed microcrack assumption. It should be mentioned that biaxial simulations were presented only for one relatively low level of confinement and therefore only limited conclusions could be drawn in this case. No information is provided regarding predictions of triaxial response.

More recently Zhu et al. (2011) proposed an isotropic damage model incorporating crack closure and friction effects. The homogenization scheme based on the Eshelby inclusion solution and the Ponte-Castaneda and Willis estimate proposed by Zhu et al. (2008) was employed and simplified for an isotropic case (although the dilute estimate and the Mori-Tanaka estimate could readily be obtained as particular cases of the Ponte-Castaneda and Willis estimate). The spatial distribution of damage was

therefore assumed to be uniform in all directions and hence the discrete damage variable, each one of them associated to a microcrack family (i.e. that was previously dependent on microcrack orientation), became a global damage variable that characterized the state of damage for all microcrack families. This led to the evaluation of the homogenized stiffness tensor for isotropic damage. Next, the thermodynamic framework proposed by Zhu et al. (2008) for damage evolution and the coupling of damage and frictional sliding on closed microcracks is employed and essentially modified for isotropic damage. Subsequently, the damage criterion using the strain energy release rate with the normality rule based damage evolution was formulated and the macroscopic stress-based and strain-based conditions for crack closure were also derived. For modelling frictional sliding on closed microcracks the mean-deviatoric split of the macroscopic stress and of the total inelastic strain were employed. In this way generalized Coulomb type and von Mises type yield criteria could easily and conveniently be implemented as friction criteria and investigated. It was found however that the von Mises criterion does not satisfy the requirement of continuity of stresses and free energy and therefore the Coulomb based friction criterion and an associated flow rule were adopted in the final model. Only results from simulations of uniaxial compression tests and compression under plane-strain conditions were presented in Zhu et al. (2011) although the authors recognized that this constituted merely the first phase of validation. Generally the numerical predictions compared well against experimental data.

2.1.2. Work of Gambarotta and co-workers

Another significant contribution to micromechanics-based modelling of concrete was made by the group led by Luigi Gambarotta at the University of Genova (Gambarotta and Lagomarsino, 1993, Brencich and Gambarotta, 2001, Gambarotta 2004).

The formulations proposed by Gambarotta present similarities in terms of fundamental concepts with the models proposed by Zhu et al. (2008, 2009, 2011); concrete was modelled as a linear elastic matrix weakened by microcracks and in the case of closed microcracks (i.e. when compressive stresses act on the crack planes) frictional sliding is introduced. The detailed derivation of the models has however significant differences.

The stated objective in the work of Gambarotta and co-workers (Gambarotta and Lagomarsino, 1993; Brencich and Gambarotta, 2001; Gambarotta, 2004) was to develop a constitutive model for concrete with a reduced number of internal variables and complexity that would capture the main aspects of the observed response: different responses under compressive and tensile loading regarding the strength and the shape of the stress-strain curve, energy dissipation at constant damage. Two fundamental simplifying assumptions were employed consequently: the effects of interaction between microcracks were ignored and the distribution of the microcracks at the natural state was assumed isotropic. Based on these assumptions the normal and tangential components of the added overall strains due to normal and tangential displacement discontinuities across the microcrack faces respectively were derived (Gambarotta and Lagomarsino, 1993, Brencich and Gambarotta, 2001). Two inelastic compliance scalar parameters -normal and tangential- whose values were assumed to be evaluated phenomenologically (i.e. from experimental data) appeared in these expressions as well as a damage variable ω defined as a measure of the relative microcrack size that varied with orientation. Due to the assumption of isotropy at natural state the normal and tangential compliance parameters were considered to take the same value for each orientation defined by the normal **n**.

Brencich and Gambarotta (2001) employed a further simplifying assumption in which damage was considered isotropic throughout the whole deformation process and therefore the damage variable was assumed to have the same value on every damage plane. In this way damage was described by a single scalar variable as an overall measure of microcrack size. A damage criterion and evolution function, similar in form to the damage formulation proposed by the French group, was employed in a global sense:

$$\Phi_d = Y(\omega, \boldsymbol{\sigma}) - R(\omega) \leq 0 \tag{2.5}$$

where Y was introduced as the energy release rate corresponding to the infinitesimal damage evolution $\dot{\omega}$, $\boldsymbol{\sigma}$ represents the mean stress tensor and R was a phenomenologically determined monotonically increasing function representing the overall measure of the material fracture toughness, i.e., as an average value over all orientations **n**.

The microcrack opening/closing conditions were defined employing two symmetric second-order tensors **P** and **F´** (with tr **P** ≤ 0 and tr **F´** = 0) interpreted as the average of the normal and tangential contact tractions over all orientations. Therefore a case of open cracks in all directions was defined for a tensile stress field (**P=0**) and a partially closed or fully closed microcracks state was considered when compressive stresses act on at least one direction (**P** ≠ **0** and tr **P** < 0). It was argued in Brencich and Gambarotta (2001) that in the open crack case, frictional sliding cannot be expected and therefore only damage evolution was considered. Frictional sliding was introduced and coupled with damage on the closed microcracks by employing a global Drucker-Prager friction criterion:

$$\Phi_s = |\mathbf{F}'| + \mu \cdot \mathrm{tr}\mathbf{P} \leq 0 \tag{2.6}$$

where μ denoted the global coefficient of friction.

The performance of the model was assessed against experimental data for a set of uniaxial biaxial and triaxial simulations. Given the assumption of isotropic damage, Brencich and Gambarotta (2001) noted that the model's domain of validity was up to peak load which represented the limit for homogeneous damage. Therefore the numerical predictions were compared to experimental data up to peak load. A generally good agreement was found between the experimental data of Maekawa and Okamura (1983) and numerical results predicted for loading-unloading uniaxial compression paths when employing an expression for the toughness function *R* similar to the type proposed by Ouyang et al. (1990). In the loading phase the predicted pre-peak nonlinearity is slightly overestimated. The experimental data shows a somewhat progressive evolution of the instantaneous unloading compliance in the unloading phase and permanent deformations due to frictional sliding on crack faces. These features are not properly captured by the proposed model due to the isotropic damage (with a single crack resistance curve) assumption and the global description of the friction mechanism that excluded progressive sliding. However the model was rather successful in predicting biaxial strength envelopes that compared well against experimental data. Less accuracy was found in triaxial compressive simulations where the strength was underestimated.

The formulation was extended for anisotropic damage in Gambarotta (2004) in order to improve the performance of the aforementioned model. Damage was therefore

characterised by a second order damage tensor evolving from a natural isotropic state and the crack closure and frictional sliding mechanisms were described by a contact and a friction second order tensor respectively. Whilst the anisotropic form of the model is more comprehensive, it seems -from the limited simulations presented and from the lack of any comparison with experimental data- that the author struggled to validate the more advanced version of the model.

2.1.3. Work of Pichler, Hellmich, Mang, Ulm, Dormieux

Pichler and co-workers employed micromechanics solutions to model a broad range of problems associated with cement based materials such as early age properties of cement paste, mortar or shotcrete (Pichler et al., 2009a,b; Pichler and Hellmich, 2011) or cracking in partially saturated porous media (Pichler and Dormieux, 2010a,b). While a detailed description of these models is beyond the scope of this review, a significant and worthwhile contribution to modelling the mechanical behaviour of concrete is their combined fracture-micromechanics model for tensile strain softening based on propagation of interacting microcracks (Pichler et al. 2007).

As mentioned by the authors, the scope of the model (Pichler et al. 2007) was to capture the strain softening behaviour associated with uniaxial tensile loading, inside the fracture process zone ahead of a macrocrack. Also, several issues, some of them unsatisfactorily described by more established phenomenological models, were considered in the development of the model: the proposal of a theoretical framework that employed a suitable damage variable and that would appropriately describe the effect of damage on the material stiffness, the development of a criterion for initiation of microcracking and the definition of a damage evolution law. These points were therefore addressed in a model that employed the Eshelby matrix-inclusion homogenization scheme to simulate an elastic matrix weakened by penny-shaped microcracks (inclusions) with identical size and orientation. Since the model was intended for simulating tension induced strain softening crack closure was not considered. The case of both a dilute concentration of non-interacting microcracks and a non-dilute concentration of interacting microcracks based on the Mori-Tanaka estimate was analyzed. As in the case of the models proposed by Kondo and co-workers (Pensée et al., 2002; Zhu et al., 2009; Zhu et al., 2011) the crack density parameter of Budiansky

and O'Connell for the case of penny-shaped microcracks was chosen as a damage variable. Next a linear elastic fracture mechanics based criterion for the onset and propagation of microcracks was formulated which took into account the stress concentrations at the edge of a sharp microcrack. While this linear elastic fracture mechanics based formulation, described in more detail in Chapter 3, provides a more mechanistic rationale for damage initiation and evolution it tends to produce an extremely brittle post peak response and requires unrealistically large values for the microcrack radius. In fact, when the interaction between microcracks is ignored, the predicted post peak response follows an unrealistic path in which stresses decrease with decreasing strains. A possible explanation for this over-brittle predicted response is that the model does not include any mechanism or assumption that would account for the arrest of cracks due to the presence of large pores or aggregate particles.

2.2 Theoretical components of the model

The second part of this chapter contains a description of the theoretical components of the constitutive model developed in this thesis, in particular the two-phase composite theory based on the matrix-inclusion Eshelby solution, microcracking based on the solution of an elastic body containing randomly distributed penny-shaped microracks (Nemat-Nasser and Hori, 1993) and a rough crack closure component based on the crack-plane model proposed by Jefferson (2002). These solutions were originally combined in a constitutive model for concrete proposed by Jefferson and Bennett (2007, 2010) which provided the starting point for the present work.

The model simulates a two-phase composite comprising a matrix phase (m) that represents the mortar and spherical inclusions (Ω) that represent the coarse aggregate particles. The composite incorporates penny-shaped microcracks with various orientations and rough surfaces on which stress can be recovered. It is assumed that the microcracks are initiated at the matrix-inclusion interface and then propagate through the matrix phase. This idealization is illustrated in Fig. 2.1. Furthermore, the two phases are characterised by two elastic properties, namely the Young's modulus E_β and Poisson's ratio υ_β, where subscript $\beta = m$ denotes the matrix phase and $\beta = \Omega$ denotes the inclusion phase respectively.

A representative volume element (RVE) was assumed to represent the average elastic properties of the composite, however its existence becomes highly questionable once macrocracking begins. Gitman (2006) showed that, in the context of cracking, the concept of an RVE becomes meaningless, therefore in this study the term 'representative material element' (RME) is used to define an RVE for elastic properties. It is however well established that cracking even in mode I fracture is distributed over a fracture process zone (FPZ) and it would seem reasonable to define an average strain measure within this region. The author therefore states clearly that the average strains used in the present model for a tensile case are consistent with the average strains in a FPZ. In compression the formation of a distinct FPZ is delayed in comparison with the tensile case but such a zone does ultimately develop and become a discrete crack. A further important point is that once a fully formed crack has occurred the model is not applicable and could only be applied to the material either side of the macrocrack. It is therefore the author's opinion that for a comprehensive description of fracture the model representing the behaviour of a continuum needs to be combined with a model which includes a strong discontinuity.

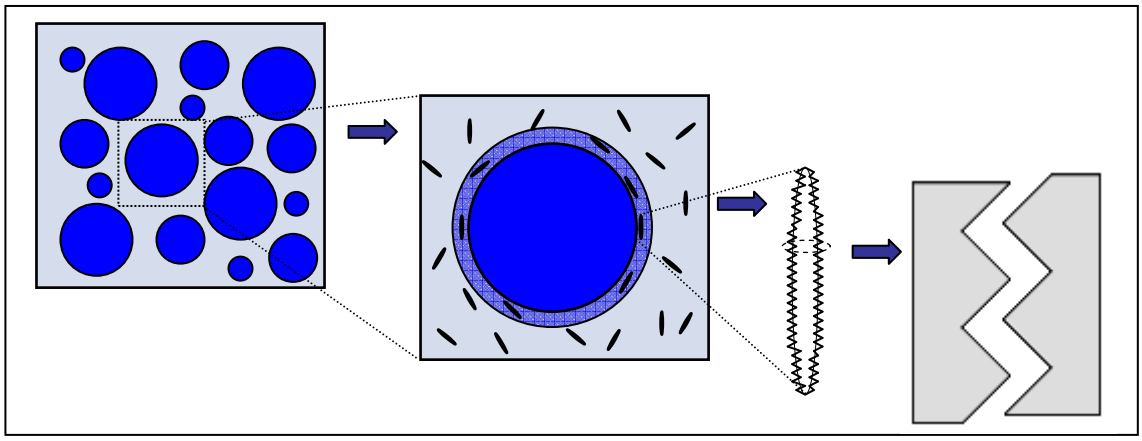

Figure 2.1. Microcracking and rough contact concepts

2.2.1 Elastic two-phase composite

Firstly the elastic properties of the two-phase composite are determined by means of the classical micromechanical solution based on the work of Eshelby (1957) combined with the Mori-Tanaka homogenisation scheme for a non-dilute distribution of inclusions (Nemat-Nasser and Hori 1999).

Eshelby (1957) showed that if a *homogeneous* elastic ellipsoidal subregion in an infinite elastic domain changes its size, shape or both, i.e. undergoes a transformation such as thermal expansion, so that it no longer conforms with its previous space, the state of stress and strain in the subregion is uniform. If the change in strain in the subregion in a stress-free state is denoted by the *'stress-free strain'* tensor ($\boldsymbol{\varepsilon}_t$) – also called *'transformation strain'* or *'eigenstrain'* - then the disturbance strain in the subregion ($\boldsymbol{\varepsilon}_c$) is given by

$$\boldsymbol{\varepsilon}_c = \mathbf{S} : \boldsymbol{\varepsilon}_t \tag{2.7}$$

in which **S** is called the (interior point) Eshelby tensor. The components of **S** depend upon the shape of the inclusion and for isotropic spherical inclusions in an isotropic elastic medium, **S** is a symmetric fourth order tensor with the following non-zero terms (plus symmetric counterparts) (Nemat-Nasser and Hori, 1993)

$$S_{ijkl} = \frac{5\upsilon_m - 1}{15(1-\upsilon_m)}\delta_{ij}\delta_{kl} + \frac{4-5\upsilon_m}{15(1-\upsilon_m)}\left(\delta_{ik}\delta_{jl} + \delta_{il}\delta_{jk}\right) \tag{2.8}$$

where δ_{ij} is the Kronecker delta. It is noted that a direct tensor notation is employed throughout the thesis and the tensor operations are defined in Annex 1.

In modelling composites it is *inhomogeneities* or *inhomogeneous inclusions* embedded in a matrix that are relevant. In this case a solution can be derived using Eshelby's solution for homogeneous inclusions undergoing a transformation strain (equation 2.7). In this approach the inhomogeneous inclusion, which has different elastic properties from the the matrix, is replaced by an *equivalent homogeneous inclusion* which has identical elastic properties to those of the matrix material and into which is introduced an equivalent eigenstrain ($\boldsymbol{\varepsilon}_\tau$) that accounts for the in elastic properties between the two materials. This is done in such a way that the stress in the equivalent homogeneous inclusion is the same as for the inhomogeneous inclusion.

If a uniform far field strain $\boldsymbol{\varepsilon}_0$ is then applied, the strain in the equivalent homogeneous inclusion becomes the sum of the far field strain and the disturbance strain:

$$\boldsymbol{\varepsilon}_\Omega = \boldsymbol{\varepsilon}_0 + \boldsymbol{\varepsilon}_c = \boldsymbol{\varepsilon}_0 + \mathbf{S} : \boldsymbol{\varepsilon}_\tau \tag{2.9}$$

The equivalent transformation strain $\boldsymbol{\varepsilon}_\tau$ accounts for the difference in the elastic properties of the materials and is not associated with any stress, therefore the stress in the equivalent homogeneous inclusion, formed from the matrix material, in obtained by applying Hooke's law to ($\boldsymbol{\varepsilon}_0 + \boldsymbol{\varepsilon}_c - \boldsymbol{\varepsilon}_\tau$) rather than ($\boldsymbol{\varepsilon}_0 + \boldsymbol{\varepsilon}_c$) (Eshelby, 1957):

$$\boldsymbol{\sigma}_\Omega = \mathbf{D}_m : \left(\boldsymbol{\varepsilon}_0 + \boldsymbol{\varepsilon}_c - \boldsymbol{\varepsilon}_\tau\right) \tag{2.10}$$

in which $\mathbf{D}_m$ is the elasticity tensor of the matrix. The stress in the inhomogeneous inclusion is given by:

$$\boldsymbol{\sigma}_\Omega = \mathbf{D}_\Omega : \left(\boldsymbol{\varepsilon}_0 + \boldsymbol{\varepsilon}_c\right) \tag{2.11}$$

where $\mathbf{D}_\Omega$ denotes the elasticity tensor of the inhomogeneity.

The equivalent eigenstrain $\boldsymbol{\varepsilon}_\tau$ is computed such that the stress in the inhomogeneity is equal to the stress in the equivalent homogeneous inclusion. The condition in which (2.10) is made equal to (2.11) is termed the *consistency condition* (Nemat-Nasser and Hori, 1993), which is different from the consistency condition in plasticity, and may be written:

$$\mathbf{D}_\Omega : \left(\boldsymbol{\varepsilon}_0 + \boldsymbol{\varepsilon}_c\right) = \mathbf{D}_m : \left(\boldsymbol{\varepsilon}_0 + \boldsymbol{\varepsilon}_c - \boldsymbol{\varepsilon}_\tau\right) \tag{2.12}$$

Using equation (2.7), equation (2.12) becomes:

$$\mathbf{D}_\Omega : \left[\boldsymbol{\varepsilon}_0 + \mathbf{S} : \boldsymbol{\varepsilon}_\tau\right] = \mathbf{D}_m : \left[\boldsymbol{\varepsilon}_0 + (\mathbf{S} - \mathbf{I}^{4s}) : \boldsymbol{\varepsilon}_\tau\right] \tag{2.13}$$

Rearranging gives:

$$(\mathbf{D}_\Omega - \mathbf{D}_m) : \boldsymbol{\varepsilon}_0 + \left((\mathbf{D}_\Omega - \mathbf{D}_m) \cdot \mathbf{S} + \mathbf{D}_m\right) : \boldsymbol{\varepsilon}_\tau = \mathbf{0} \tag{2.14}$$

Hence

$$\boldsymbol{\varepsilon}_\tau = \mathbf{A}_\Omega : \boldsymbol{\varepsilon}_0 \tag{2.15}$$

where $\mathbf{A}_\Omega = \left((\mathbf{D}_\Omega - \mathbf{D}_m) \cdot \mathbf{S} + \mathbf{D}_m\right)^{-1} \cdot (\mathbf{D}_m - \mathbf{D}_\Omega)$

Introducing (2.15) in (2.9) gives:

$$\boldsymbol{\varepsilon}_\Omega = \left(\mathbf{I}^{4s} + \mathbf{S} \cdot \mathbf{A}_\Omega\right) : \boldsymbol{\varepsilon}_0 \tag{2.16}$$

Using (2.15) in (2.10) or in (2.11) gives the following expressions for the stress in the inclusion:

$$\boldsymbol{\sigma}_{\Omega} = \mathbf{D}_{\mathrm{m}} \cdot \left[\mathbf{I}^{4s} + (\mathbf{S} - \mathbf{I}^{4s}) \cdot \mathbf{A}_{\Omega} \right] : \boldsymbol{\varepsilon}_0 \tag{2.17}$$

$$\boldsymbol{\sigma}_{\Omega} = \mathbf{D}_{\Omega} \cdot \left(\mathbf{I}^{4s} + \mathbf{S} \cdot \mathbf{A}_{\Omega} \right) : \boldsymbol{\varepsilon}_0 \tag{2.18}$$

The above analysis is applicable to an infinite elastic matrix containing a single inclusion. Now an RME is considered in which $\mathrm{f_m}$ is the volume fraction of matrix material and f_{Ω} is the volume fraction of inclusions noting that $f_m + f_{\Omega} = 1$. For each phases the constitutive relationships are given by

$$\begin{aligned} \boldsymbol{\sigma}_{\Omega} &= \mathbf{D}_{\Omega} : \boldsymbol{\varepsilon}_{\Omega} \\ \boldsymbol{\sigma}_{\mathrm{m}} &= \mathbf{D}_{\mathrm{m}} : \boldsymbol{\varepsilon}_{\mathrm{m}} \end{aligned} \tag{2.19a,b}$$

In this composite domain the following expressions for the average stress and average strain respectively hold:

$$\overline{\boldsymbol{\sigma}} = f_{\Omega} \boldsymbol{\sigma}_{\Omega} + f_{\mathrm{m}} \boldsymbol{\sigma}_{\mathrm{m}} \tag{2.20}$$

$$\overline{\boldsymbol{\varepsilon}} = f_{\Omega} \boldsymbol{\varepsilon}_{\Omega} + f_{\mathrm{m}} \boldsymbol{\varepsilon}_{\mathrm{m}} \tag{2.21}$$

So far the effects of the interaction between inclusions have been ignored. However, in the case of concrete, for which the volume fraction of the coarse aggregate has a significant value, the assumption of non-interacting inclusions (dilute concentration) is unrealistic. Several homogenization schemes that take into account the interactions between inclusions are available in the literature i.e. the self-consistent method, the Mori-Tanaka scheme, the Ponte-Castaneda and Willis method etc. In the self-consistent method the effective properties are derived such that $\overline{\mathbf{D}} = \overline{\mathbf{C}}^{-1}$, where $\overline{\mathbf{D}}$ and $\overline{\mathbf{C}}$ denote the effective elasticity and compliance tensors respectively.

In the Mori-Tanaka method the argument is made that when the inclusions are not dilute the 'disturbance' strain may be based on the average matrix strains (or stresses) rather than the far field strain (or stress). If the far field strain is replaced by the average strain in the matrix $\boldsymbol{\varepsilon}_{\mathrm{m}}$, Eqs (2.16) becomes:

$$\boldsymbol{\varepsilon}_{\Omega} = \left(\mathbf{I}^{4s} + \mathbf{S} \cdot \mathbf{A}_{\Omega} \right) : \boldsymbol{\varepsilon}_{\mathrm{m}} = \mathbf{T}_{\Omega} : \boldsymbol{\varepsilon}_{\mathrm{m}} \tag{2.22}$$

Using (2.19a,b) and (2.22) in (2.20) gives:

$$\bar{\boldsymbol{\sigma}} = \left(f_{\Omega}\ \mathbf{D}_{\Omega} \cdot \mathbf{T}_{\Omega} + f_{\mathrm{m}} \mathbf{D}_{\mathrm{m}} \right) : \boldsymbol{\varepsilon}_{\mathrm{m}} \tag{2.23}$$

From (2.21):

$$\boldsymbol{\varepsilon}_{\mathrm{m}} = \left(f_{\Omega} \mathbf{T}_{\Omega} + f_{\mathrm{m}} \mathbf{I}^{4s} \right)^{-1} : \bar{\boldsymbol{\varepsilon}} \tag{2.24}$$

Using (2.24) in (2.23) gives:

$$\bar{\boldsymbol{\sigma}} = \mathbf{D}_{\mathrm{m}\Omega} : \bar{\boldsymbol{\varepsilon}} \tag{2.25}$$

in which $\mathbf{D}_{\mathrm{m}\Omega} = \left(f_{\Omega} \mathbf{D}_{\Omega} \cdot \mathbf{T}_{\Omega} + f_{\mathrm{m}} \mathbf{D}_{\mathrm{m}} \right) \cdot \left(f_{\Omega} \mathbf{T}_{\Omega} + f_{\mathrm{m}} \mathbf{I}^{4s} \right)^{-1}$

2.2.2 Microcracking

Microcracking is a primary source of non-linearity in the mechanical behaviour of concrete (van Mier, 1997) and therefore needs to be addressed with a rigorous formulation. There are a number of micromechanical solutions that can be employed to simulate this mechanism. For example the Eshelby matrix-inclusion theory has been used by Penseé et al. (2002, 2003), Zhu et al. (2009), Gambarotta (2004) and Pichler et al. (2007) to derive the effective moduli of a solid containing ellipsoidal cracks. In this case open microcracks are modelled as flat ellipsoidal inclusions with zero stiffness.

In the present model a micromechanical solution based on the classic work of Budiansky and O'Connell (1976) is employed to compute the additional strains from a dilute distribution of penny shaped cracks. This solution for microcracking in concrete was used in the model in Jefferson and Bennett (2007). Nemat-Nasser and Hori (1993) describe in detail the derivation of the additional compliance from a set of penny-shaped microcracks with the same orientation which gives rise to additional strains. It is assumed that microcracks occur only in the matrix (mortar) phase and therefore the elastic properties of the matrix are used in the following.

The crack opening displacements for a penny-shaped crack of radius a_i lying in the s-t plane and with the centre at the origin of a local coordinate system **r s t** (Fig. 2.2), **r** being the unit vector normal to the microcrack, are given by:

$$\mathbf{u}(a) = \frac{8(1-\upsilon_{\mathrm{m}}{}^2)}{\pi E_{\mathrm{m}}} \sqrt{a_i{}^2 - a^2} \begin{bmatrix} \sigma_{rr} \\ \dfrac{2}{2-\upsilon_{\mathrm{m}}} \sigma_{rs} \\ \dfrac{2}{2-\upsilon_{\mathrm{m}}} \sigma_{rt} \end{bmatrix} \tag{2.26}$$

where a is the radial coordinate and σ_{rr}, σ_{rs} and σ_{rt} are the normal and shear components of the farfield stress, with $\sigma_{rr} > 0$.

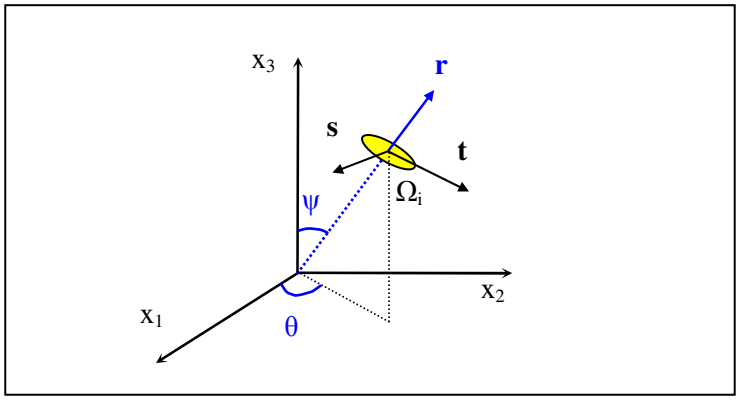

Figure 2.2. Reference system for a penny-shaped microcrack

The additional strains from crack i are next given by

$$\boldsymbol{\varepsilon}_{\mathrm{add}i} = \frac{1}{a_i{}^3} \int_{\Omega_i} \frac{1}{2} \left(\mathbf{r}_i \mathbf{u}(a)^{\mathrm{T}} + \mathbf{u}(a) \mathbf{r}_i{}^{\mathrm{T}} \right) \mathrm{d}\Omega \tag{2.27}$$

It is shown in Nemat-Nasser and Hori (1993) that direct calculation of $\boldsymbol{\varepsilon}_{\mathrm{add}i}$ from Eqs (2.26) and (2.27) yields a result independent of the crack radius. Therefore a single crack radius a_0 is assumed. If a dilute distribution of cracks is assumed then the added strains from a system of cracks is obtained by considering the contribution from each crack to the average additional strain. Based on the above, the non-zero components of the additional strain tensor from a dilute series of cracks with the same orientation, i.e. same normal vector $\mathbf{r}$, are given by:

$$\boldsymbol{\varepsilon}_{\alpha} = \begin{bmatrix} \varepsilon_{\alpha_{rr}} \\ \gamma_{\alpha_{rs}} \\ \gamma_{\alpha_{rt}} \end{bmatrix} = f(\psi,\theta)\frac{16(1-\upsilon_{\mathrm{m}}{}^{2})}{3E_{\mathrm{m}}} \begin{bmatrix} \sigma_{rr} \\ \dfrac{4}{2-\upsilon_{\mathrm{m}}}\sigma_{rs} \\ \dfrac{4}{2-\upsilon_{\mathrm{m}}}\sigma_{rt} \end{bmatrix} \tag{2.28}$$

noting that the engineering shear strain components $\gamma_{\alpha ij}$ are double the tensor shear components $\varepsilon_{\alpha ij}$ $(i \neq j)$. $f(\psi,\theta)$ is the crack density parameter introduced by Budiansky and O'Connell (1976) which for the particular case of penny-shaped cracks is $f = Na_0{}^3$ where N denotes the number of cracks per unit volume. In Jefferson and Bennett (2007) the crack density parameter was expressed more conveniently in terms of a directional damage parameter $\omega(\psi,\theta)$ that grows from 0 (for undamaged state) to 1 (for fully damaged state). The expression relating $f(\psi,\theta)$ and $\omega(\psi,\theta)$ is:

$$f(\psi,\theta) = \frac{3}{16\left(1-\upsilon_{\mathrm{m}}{}^{2}\right)} \cdot \frac{\omega(\psi,\theta)}{1-\omega(\psi,\theta)} \tag{2.29}$$

Eq. (2.28) may now be written as:

$$\boldsymbol{\varepsilon}_{\alpha} = \frac{\omega(\psi,\theta)}{1-\omega(\psi,\theta)}\mathbf{C}_{\mathrm{L}} : \mathbf{s} \tag{2.30}$$

where $\mathbf{C}_{\mathrm{L}}$ is assumed to be the local elastic compliance tensor which can be written in matrix form as $\mathbf{C}_{\mathrm{L}} = \dfrac{1}{E_{\mathrm{m}}} \begin{bmatrix} 1 & 0 & 0 \\ 0 & \dfrac{4}{2-\upsilon_{\mathrm{m}}} & 0 \\ 0 & 0 & \dfrac{4}{2-\upsilon_{\mathrm{m}}} \end{bmatrix}$ and $\mathbf{s} = (\sigma_{\mathrm{rr}}, \sigma_{\mathrm{rs}}, \sigma_{\mathrm{rt}})^{\mathrm{T}}$.

Eq. (2.30) gives the additional strains due to a set of microcracks with the same normal vector $\mathbf{r}(\psi,\theta)$ with respect to the local coordinate system. In general however microcracks do not develop in one direction only but can have various orientations. The total additional strain ($\boldsymbol{\varepsilon}_{\mathrm{a}}$), i.e. from a set of microcracks with arbitrary orientations is obtained by adding the contributions from all possible directions. The local added strains in Eq. (2.30) are first transformed from the local coordinate system **rst** to the

global Cartesian system and the total added strains are then obtained via an integral over a unit sphere which in turn can be reduced to an integral over a hemisphere due to symmetry.

$$\boldsymbol{\varepsilon}_{\mathrm{a}} = \frac{1}{2\pi} \int_{2\pi} \int_{\frac{\pi}{2}} \mathbf{N}(\psi,\theta)^{-1} : \boldsymbol{\varepsilon}_{\alpha} \ \sin(\psi)\, \mathrm{d}\psi \mathrm{d}\theta \tag{2.31}$$

where $\mathbf{N}(\psi,\theta)$ is a transformation tensor given in matrix form in Jefferson (2003). Moreover, the local stress ($\mathbf{s}$) is related to the global stress as follows:

$$\mathbf{s} = \mathbf{N}(\psi,\theta) : \overline{\boldsymbol{\sigma}} \tag{2.32}$$

The matrix forms of the transformation tensor for stresses and strains respectively are given in Annex 2. Introducing Eqs. (2.32) and (2.30) into Eq. (2.31) the expression of the total additional strain due to the presence of microcracks with various orientations becomes:

$$\boldsymbol{\varepsilon}_{\mathrm{a}} = \left(\frac{1}{2\pi} \int_{2\pi} \int_{\frac{\pi}{2}} \mathbf{N}(\psi,\theta)^{-1} \cdot \frac{\omega(\psi,\theta)}{1-\omega(\psi,\theta)} \mathbf{C}_{\mathrm{L}} \cdot \mathbf{N}(\psi,\theta) \ \sin(\psi)\, \mathrm{d}\psi \mathrm{d}\theta \right) : \overline{\boldsymbol{\sigma}} \tag{2.33}$$

Eq. (2.25) describes the elastic constitutive relationship for an elastic two phase composite. When the effect of the presence of microcracks in the matrix is taken into account this expression becomes:

$$\overline{\boldsymbol{\sigma}} = \mathbf{D}_{\mathrm{m}\Omega} : \ \left(\overline{\boldsymbol{\varepsilon}} - \boldsymbol{\varepsilon}_{\mathrm{a}} \right) \tag{2.34}$$

The average stress-strain relationship for a two phase composite containing open penny-shaped microcracks with various orientations is then obtained by introducing Eq. (2.33) in (2.34) and rearranging:

$$\overline{\boldsymbol{\sigma}} = \left(\mathbf{I}^{4s} + \frac{\mathbf{D}_{\mathrm{m}\Omega}}{2\pi} \cdot \int_{2\pi} \int_{\frac{\pi}{2}} \mathbf{N}(\psi,\theta)^{-1} \cdot \frac{\omega(\psi,\theta)}{1-\omega(\psi,\theta)} \mathbf{C}_{\mathrm{L}} \cdot \mathbf{N}(\psi,\theta) \sin(\psi)\, \mathrm{d}\psi \mathrm{d}\theta \right)^{-1} \cdot \mathbf{D}_{\mathrm{m}\Omega} : \ \overline{\boldsymbol{\varepsilon}} \tag{2.35}$$

It is worth noting that a dilute distribution of cracks is assumed in this formulation. The effects of interaction between microcracks are therefore ignored. This assumption is somewhat inaccurate when the crack distribution becomes concentrated.

However, when a solution for a non-dilute distribution of microcracks based on the Mori-Tanaka estimate was employed, little difference in the overall predicted response was observed compared to the predictions obtained using a dilute distribution assumption. Therefore in order to reduce the complexity of the overall model crack interaction effects are ignored throughout.

Eq. (2.35) can be re-written as:

$$\bar{\boldsymbol{\sigma}} = \left(\mathbf{I}^{4s} + \frac{\mathbf{D}_{\mathrm{m}\Omega}}{2\pi} \int_{2\pi} \int_{\frac{\pi}{2}} \mathbf{N}(\psi,\theta)^{-1} \cdot \mathbf{C}_{c\alpha}(\psi,\theta) \cdot \mathbf{N}(\psi,\theta) \sin(\psi)\, \mathrm{d}\psi\, \mathrm{d}\theta \right)^{-1} \cdot \mathbf{D}_{\mathrm{m}\Omega} : \bar{\boldsymbol{\varepsilon}} \qquad (2.36)$$

where $\mathbf{C}_{c\alpha}(\psi,\theta)$ denotes the added local compliance and is given by:

$$\mathbf{C}_{c\alpha}(\psi,\theta) = \frac{\omega(\psi,\theta)}{1-\omega(\psi,\theta)} \mathbf{C}_{\mathrm{L}} \qquad (2.37)$$

Since it is practically impossible to evaluate the integration over the hemisphere in Eq. (2.36) analytically, it is evaluated numerically. Therefore the integral is approximated with a weighted summation over a finite number of integration directions. The weights, as well as the integration directions, are associated with the chosen integration rule. The McLaren rule with 50 integration directions, which reduce to 29 for a hemisphere, is employed for numerical simulations; however, a discussion on the accuracy of these rules is provided in Chapter 5.

2.2.3 Rough Crack Contact Model – stress recovery

Rough crack closure was originally included in the model based on the macroscopic experimental observation (Walraven and Reinhardt, 1981) that cracks can regain contact with normal and shear movement and therefore stress can be transferred across the rough crack surfaces. However, it was argued (Jefferson and Bennett, 2007) that the same observations apply at micro and meso levels. The main principles are presented in Fig. 2.3.

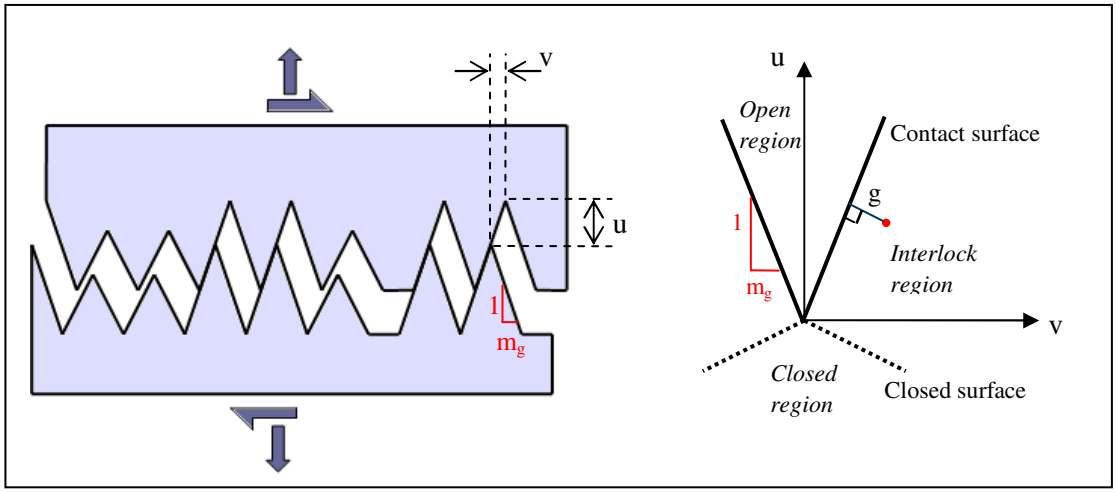

Figure 2.3. Concepts of the contact model

The crack surface is idealised as a sequence of conical teeth (right circular cones) bounded on either side by bands of elastic material. Parameter m_g characterizes the tortuosity of the crack surface and also defines the slope of the contact surface.

In each direction the local stress tensor is written as a sum of the average stress on undamaged material and the recovered stress on microcracks in contact:

$$\mathbf{s} = \mathbf{s}_u + \mathbf{s}_r \tag{2.38}$$

Jefferson and Bennett (2007) employed a set of assumptions to control stress recovery:

a. When local strains $\boldsymbol{\varepsilon}_L$ are in the open region there is no contact and therefore the local recovered stress is 0.
b. The recovered stress depends on a so-called 'embedment strain' (or 'gap strain') **g** which in the interlock region is the distance in strain terms to the contact surface. This assumption implies that the sides of the rough crack surface are frictionless.
c. When the crack surfaces are locked in together, i.e. the local strains are in the closed region, the recovered stress depends directly on the local strain, i.e. $\mathbf{g} = \boldsymbol{\varepsilon}_L$
d. The maximum recovered stress that can be transferred across the crack decreases with increasing crack opening. When the crack opening reaches the point where the crack surfaces have no overlap the transferred stress is null.

e. The recovered stress is related to the local strain vector by the elastic properties of the band of material either side of the crack faces and by a contact matrix (tensor) that depends on the contact state.
f. The local strain vector is that for the idealised band of material from which the additional strains are derived by removing the elastic components
g. In any one direction that is damaged, the proportion of material to which the contact model applies is equal to the damage parameter ω in that particular direction.

Based on these assumptions the expression of the recovered stress can be written in a general way as follows:

$$\mathbf{s}_{\mathrm{r}} = \mathrm{H}_{\mathrm{f}}\,\omega\mathbf{D}_{\mathrm{L}} \cdot \boldsymbol{\Phi} : \mathbf{g} \tag{2.39}$$

where $\boldsymbol{\Phi}$ is the contact tensor that depends upon the state of contact according to Table 2.1.

Table 2.1 Contact formulation

Region	Contact state	Contact tensor
If $\phi_{\mathrm{int}}(\boldsymbol{\varepsilon}_{\mathrm{L}}, m_g) \geq 0$	Open state	$\boldsymbol{\Phi} = \mathbf{0}^{4s}$
If $\phi_{\mathrm{int}}(\boldsymbol{\varepsilon}_{\mathrm{L}}, m_g) < 0$ and $\phi_{\mathrm{cl}}(\boldsymbol{\varepsilon}_{\mathrm{L}}, m_g) > 0$	Shear contact or interlock state	$\boldsymbol{\Phi} = \boldsymbol{\Phi}_{\mathrm{g}}(\boldsymbol{\varepsilon}_{\mathrm{L}}, m_g)$ $\boldsymbol{\Phi}_{\mathrm{g}}(\boldsymbol{\varepsilon}_{\mathrm{L}}, m_g) = \frac{1}{1+{m_g}^2}\left(\left(\frac{\partial\phi_{\mathrm{int}}}{\partial\boldsymbol{\varepsilon}_{\mathrm{L}}}\right)\left(\frac{\partial\phi_{\mathrm{int}}}{\partial\boldsymbol{\varepsilon}_{\mathrm{L}}}\right)^{\mathrm{T}} + \frac{\partial^2\phi_{\mathrm{int}}}{\partial{\boldsymbol{\varepsilon}_{\mathrm{L}}}^2}\right)$
If $\phi_{\mathrm{cl}}(\boldsymbol{\varepsilon}_{\mathrm{L}}, m_g) \leq 0$	Closed state	$\boldsymbol{\Phi} = \mathbf{I}^{4s}$

in which:

$$\phi_{\mathrm{int}}(\boldsymbol{\varepsilon}_{\mathrm{L}}, m_g) = m_g\varepsilon_{\mathrm{Lrr}} - \sqrt{{\varepsilon_{\mathrm{Lrs}}}^2 + {\varepsilon_{\mathrm{Lrt}}}^2} \tag{2.40a}$$

is the contact or interlock surface which separates the open from the closed region and

$$\phi_{\mathrm{cl}}(\boldsymbol{\varepsilon}_{\mathrm{L}}, m_g) = \varepsilon_{\mathrm{Lrr}} + m_g\sqrt{{\varepsilon_{\mathrm{Lrs}}}^2 + {\varepsilon_{\mathrm{Lrt}}}^2} \tag{2.40b}$$

is the closed surface which separates interlock from the closed region.

H_f is a shear contact reduction function that reflects the fact that as the crack opening increases the potential for shear transfer reduces. It is assumed that the value of the H_f function is proportional to A_w/A_b (Fig. 2.4) giving:

$$H_f = \left(1 - \frac{w}{h_t}\right)^2 . \tag{2.41}$$

in which w is the crack opening and h_t is the height of the cone (asperity) taken as the limiting crack opening displacement (or relative-displacement at the end of the softening curve) u_0. Strains are related to displacements by the characteristic length which here is taken as the maximum size of the coarse aggregate particles d_{max}, i.e. $\varepsilon_0 = u_0/d_{max}$. Hence, the contact reduction function can be written in strain terms as

$$H_f = \left(1 - \eta_L\right)^2 \tag{2.42}$$

where $\eta_L = \left(\frac{\varepsilon_{Lrr} - \varepsilon_{tm}}{\varepsilon_0}\right)$ and ε_{tm} is the matrix strain at first uniaxial damage.

However, for numerical reasons, the following exponential function, which provides an adequate match to Eq. (2.42), was preferred in order to avoid the gradient discontinuity when $\eta_L = 1$,

$$H_f = e^{-c_l \eta_L} \tag{2.43}$$

in which c_l is taken to be 3.

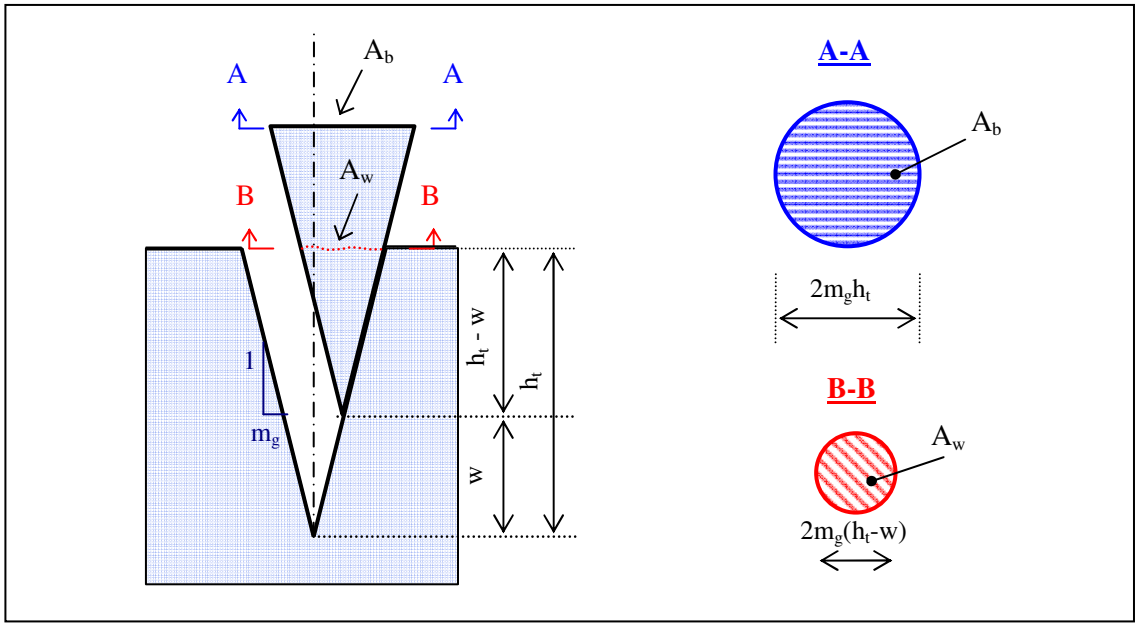

Figure 2.4. Schematic representation of the geometrical assumption for contact reduction

In Jefferson and Bennett (2010), the local recovered stress was based on a single contact surface, however in reality the asperities of a real crack have different heights and contact angles (m_g). To account for these variations the recovered stress is now written as a summation which allows for statistical distributions of the crack roughness parameters, as follows:

$$\mathbf{s}_r = \omega \mathbf{D}_L \cdot \left(\sum_k p_k H_{fk} \mathbf{\Phi}_k \right) : \boldsymbol{\varepsilon}_L \tag{2.44}$$

The asperities heights for each component k are denoted $\lambda_k u_0$.

As will be discussed in Chapter 3, it was found that crack surfaces tend to have a bimodal distribution of asperity heights which are associated with λ values of 1 and 0.1.

The local stress in Eq. (2.38) then becomes:

$$\mathbf{s}_\alpha = \mathbf{s}_u + \mathbf{s}_r = \left[(1-\omega)\mathbf{D}_L : \boldsymbol{\varepsilon}_L \right] + \left[\omega \mathbf{D}_L \cdot \left(\sum_k p_k H_{fk} \mathbf{\Phi}_k \right) : \boldsymbol{\varepsilon}_L \right] \tag{2.45}$$

Removing the elastic compliance from equation (2.45), the added compliance including contact $\mathbf{C}_{c\alpha}$ becomes:

$$\mathbf{C}_{c\alpha} = \left[\left[(1-\omega)\mathbf{I}^{4s} + \omega \left(\sum_k p_k H_{fk} \mathbf{\Phi}_k \right) \right]^{-1} - \mathbf{I}^{4s} \right] \cdot \mathbf{C}_L \tag{2.46}$$

2.3. Summary and concluding remarks

A literature overview of the constitutive models for concrete that are based on micromechanical solutions is presented in the first part of the chapter. The second part details the formulation of a new constitutive model for concrete based on micromechanical solutions. The concept of a representative material element (RME) is employed which essentially defines an elastic representative volume element (RVE). The RME is simulated as a two-phase composite comprising an elastic matrix to simulate the mortar and spherical inclusions to model the coarse aggregate particles embedded in the matrix phase. The elastic properties of the two-phase composite are obtained by employing the Eshelby matrix-inclusion solution and the Mori-Tanaka averaging scheme. The reduction in stiffness due to microcracking is accounted for by considering the matrix phase to be weakened by penny-shaped microcracks that can have various orientations. Furthermore, the model also incorporates a multi-asperity rough crack contact component in order to take into account the recovery of stiffness (normal and shear) when microcracks regain contact.

The formulation of the constitutive model is completed in the following chapter with a new criterion for the initiation and evolution of microcracks based on the assumption that microcracking is initiated at the matrix-inclusion interface.

Chapter 3

Damage initiation and evolution. Numerical predictions

In this chapter, details of the formulation of a microcrack initiation criterion based on the assumption that microcracks are initiated in the interfacial transition zone between coarse aggregate particles and the mortar matrix are presented. A brief discussion of the damage criteria employed in several other micromechanical constitutive models is first presented followed by the formulation of the criterion for the initiation and evolution of microcracking which makes use of the exterior point Eshelby solution. Aspects regarding the geometrical characterization of the morphology of the crack surface are also addressed. Finally, the performance of the proposed constitutive model is assessed in a set of uniaxial, biaxial and triaxial simulations.

3.1. Damage initiation and evolution criteria in micromechanical models

In general the progress of damage is described mathematically via a damage criterion and a damage evolution function. This mathematical characterization stems from damage mechanics and has become a trademark of damage models. In the case of damage models the damage criterion is based upon a damage function written in terms of stresses or strains or an energetic variable. An evolution law governs the expansion or contraction of the damage function with the damage variable. In the case of micromechanical models there are essentially two approaches of describing the progress of damage: one based upon energetic damage mechanics employed by Pensée et al.

(2002), Pensée and Kondo (2003), Zhu et al. (2008, 2009, 2011), Brencich and Gambarotta (2001) and Gambarotta (2004); and the other based upon linear elastic fracture mechanics applied by Pichler et al. (2007) and co-workers.

As mentioned in the section 2.1.1, in the work of Kondo and co-workers, the degree of damage varies with orientation and therefore, in each direction *i,* it is described by an associated damage variables d^i. For current direction *i* the damage function (Eq. 2.1) is expressed in terms of the strain energy release rate (thermodynamic force) obtained by differentiating the free (Helmholtz) energy potential associated to the i^{th} microcrack with respect to the damage variable. Damage is initiated when the thermodynamic force equals the initial crack resistance. The evolution of the damage variable, which in turn governs the expansion of the damage function in strain space, is controlled by an evolution law that employs the normality rule. The crack resistance *R*, which was assumed to depend linearly on the damage variable, i.e. $R(d^i) = c_0 + c_1 \cdot d^i$, is determined phenomenologically. In fact the two parameters featured in the linear expression of the crack resistance curve play an important role in the characterization of damage initiation and evolution. With a small, but non-zero, initial value of the damage variable, c_0 defines the initial damage threshold and c_1 describes the kinematics of damage evolution. The damage criterion is written in terms of energy variables, however it could be similarly expressed in strain terms, with the onset of damage being controlled by a critical strain value. Pensée and Kondo (2003) proposed a comparative damage criterion in which the thermodynamic force was obtained from the free enthalpy (Gibbs energy) and which could similarly be reduced to a stress based one. The stress based formulation employing the Gibbs energy was equivalent to the strain based formulation that made use of the free energy potential for low levels of strain (stress), however at higher strain levels it became unrealistic by not being able to predict a peak stress in uniaxial tension or compression.

Gambarotta and co-workers (Brencich and Gambarotta, 2001; Gambarotta, 2004) employ a damage formulation somewhat similar in concept to the one discussed above and therefore with similar characteristics. In the isotropic model (Brencich and Gambarotta, 2001) the damage function makes use directly of the scalar value of the strain energy release rate whereas the damage function in the anisotropic model (Gambarotta, 2004) is written in terms of the determinant of the matrix associated to the strain energy release rate tensor. In a similar manner to the formulation of Pensée et al.

(2002), damage initiation and evolution is controlled by a phenomenologically based function R referred to as the overall damage toughness which can be interpreted as an overall measure of the crack resistance employed by Pensée et al. (2002).

Pichler et al. (2007) attempted a more mechanistic description of the microcrack initiation and evolution process by proposing a formulation based on linear elastic fracture mechanics. The well known propagation law in linear elastic fracture mechanics theory states that a single crack embedded in an infinite matrix and subjected to uniaxial tensile stresses normal to it starts to propagate when the stress intensity factor that accounts for the stress concentrations at the tip of the crack reaches the fracture toughness of the material or, equivalently, when the energy release rate reaches a critical value. The criterion also describes the nature of propagation once initiated, i.e. if crack growth is quasistatic (stable) or dynamic (unstable). Pichler et al. (2007) employed this criterion that characterizes the propagation of a single crack to describe the onset and propagation of multiple microcracks. For this it was assumed that the far-field strains from the Eshelby matrix-inclusion solution -used to evaluate the homogenized properties of an RME (i.e. an RVE for elastic properties) weakened by a set of penny-shaped microcracks with the same size and orientation- were equal to those caused by the remote uniaxial tensile stresses from formulation of the crack propagation criterion. As mentioned by the authors, this provided the 'missing link' that enabled the use of a linear elastic fracture mechanics solution in a micromechanics framework. Although the formulation is elegant, as mentioned in Chapter 2, it produces an unrealistically brittle response.

An alternative way to consider microcrack propagation was proposed by Karihaloo et al. (1996) and Karihaloo and Wang (1997a) in which the development of periodic crack arrays is shown to produce softening behaviour. This was further developed by the same authors (Karihaloo and Wang, 1997b, Wang et al., 2000) and was shown to be both effective and accurate.

This approach has not been employed in the current multi-phase composite model although this would provide a potential alternative mechanistic approach for the formulation of the microcrack initiation criterion and evolution function.

3.2. Exterior point Eshelby based microcrack initiation criterion

In Jefferson and Bennett (2010), the cracking criterion was based on the average matrix strains, which in fact implies that cracking may be initiated anywhere in the matrix. In an attempt to obtain a better estimate of the cracking stress, microcracks are now assumed, based on experimental evidence, to initiate in the interfacial transition zone surrounding aggregate particles due to tensile stresses, shear stresses or a combination of the two (van Mier 1997). For this purpose, a criterion based on the exterior point Eshelby solution is employed. Before discussing the criterion, this solution will be presented for an elastic two-phase composite.

3.2.1. Exterior point Eshelby. Stress outside an inclusion

According to Ju and Sun (1999), the total strain $\boldsymbol{\varepsilon}_{m\Omega}$ and the total stress $\boldsymbol{\sigma}_{m\Omega}$, at any local point in the matrix domain, defined by the position vector $\mathbf{x}$ relative to the centre of the inclusion (Fig. 3.1), can be written as:

$$\boldsymbol{\varepsilon}_{m\Omega}(\mathbf{x}) = \boldsymbol{\varepsilon}_0 + \mathbf{S}^E(\mathbf{x}) : \boldsymbol{\varepsilon}_\tau^* \tag{3.1}$$

$$\boldsymbol{\sigma}_{m\Omega}(\mathbf{x}) = \mathbf{D}_m : \boldsymbol{\varepsilon}_{m\Omega}(\mathbf{x}) \tag{3.2}$$

where $\boldsymbol{\varepsilon}_0$ is the far-field strain tensor. $\mathbf{S}^E(\mathbf{x})$ is the so-called exterior-point Eshelby tensor. For spheroidal inclusions the explicit components of $\mathbf{S}^E(\mathbf{x})$ are derived in Ju and Sun (1999). Li et al. (2007) particularized Ju and Sun's solution and obtained the explicit components for spherical inclusions in an infinite elastic medium in the following form:

$$\begin{aligned} S^E_{ijmn}(\mathbf{x}) = {} & \frac{\rho^3}{30(1-\upsilon_m)}[(3\rho^3 + 10\upsilon_m - 5)\delta_{ij}\delta_{mn} + (3\rho^3 - 10\upsilon_m + 5)\cdot(\delta_{im}\delta_{jn} + \\ & + \delta_{in}\delta_{jm}) + 15(1-\rho^2)\delta_{ij}\bar{x}_m\bar{x}_n + 15(1-2\upsilon_m-\rho^2)\delta_{mn}\bar{x}_i\bar{x}_j + 15(\upsilon_m-\rho^2)\cdot \\ & \cdot(\delta_{im}\bar{x}_j\bar{x}_n + \delta_{in}\bar{x}_j\bar{x}_m + \delta_{jm}\bar{x}_i\bar{x}_n + \delta_{jn}\bar{x}_i\bar{x}_m) + 15(7\rho^2-5)\bar{x}_i\bar{x}_j\bar{x}_m\bar{x}_n] \end{aligned} \tag{3.3}$$

where υ_m is the Poisson's ratio of the matrix, $\rho = a/|\mathbf{x}|$, $|\mathbf{x}| = \sqrt{x_i x_i}$, a is the radius of the spherical inclusion and $\bar{x}_i$ represent the unit position vector components, i = 1, 2, 3 (Fig. 3.1). The unit position vector $\bar{\mathbf{x}}$ is set to the current sample direction vector.

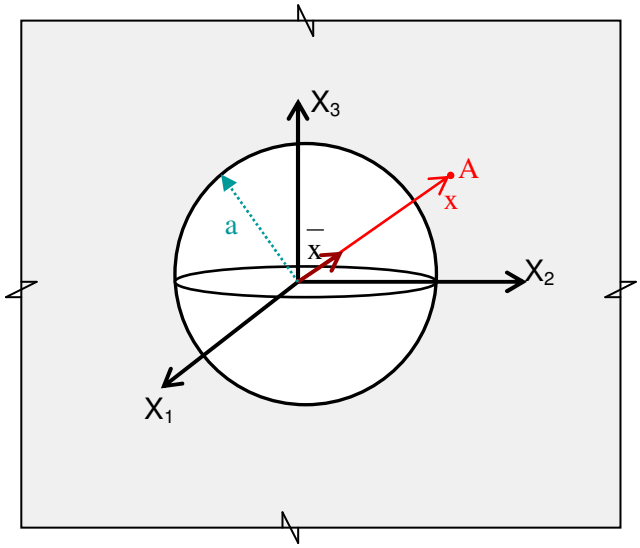

Figure 3.1. Schematic representation of a spherical inclusion contained in an infinite elastic matrix

$\boldsymbol{\varepsilon}_{\tau}^{*}$ in Eq. (3.1) is the eigenstrain given by Ju and Sun (2001):

$$\boldsymbol{\varepsilon}_{\tau}^{*} = -(\mathbf{A} + \mathbf{S}_{\Omega})^{-1} : \boldsymbol{\varepsilon}_{0} \tag{3.4}$$

where $\mathbf{A} = (\mathbf{D}_{\Omega} - \mathbf{D}_{\mathrm{m}})^{-1} \cdot \mathbf{D}_{\mathrm{m}}$ is the fourth-order elastic "phase-mismatch" tensor.

Replacing the eigenstrain in Eq. (3.1) with Eq. (3.4) gives:

$$\boldsymbol{\varepsilon}_{\mathrm{m}\Omega}(\mathbf{x}) = [\mathbf{I}^{4s} + \mathbf{S}^{\mathrm{E}}(\mathbf{x}) : \mathbf{B}_{\Omega}] : \boldsymbol{\varepsilon}_{0} = \mathbf{T}(\mathbf{x}) : \boldsymbol{\varepsilon}_{0} \tag{3.5}$$

where tensor $\mathbf{B}_{\Omega} = -[\mathbf{S}_{\Omega} + (\mathbf{D}_{\Omega} - \mathbf{D}_{\mathrm{m}})^{-1} \cdot \mathbf{D}_{\mathrm{m}}]^{-1}$.

The Mori-Tanaka homogenization scheme for a non-dilute distribution of inclusions is applied in order to account for the interaction between inclusions. According to this scheme, the disturbance strain can be expressed in terms of the average matrix strain rather than the far-field strain. Hence, Eq. (3.5) becomes:

$$\boldsymbol{\varepsilon}_{\mathrm{m}\Omega}(\mathbf{x}) = \mathbf{T}(\mathbf{x}) : \boldsymbol{\varepsilon}_{\mathrm{m}} \tag{3.6}$$

Moreover, it can be shown that the strain in the inclusions $\boldsymbol{\varepsilon}_{\Omega}$ is related to the average matrix strain in a similar fashion:

$$\boldsymbol{\varepsilon}_{\Omega} = \mathbf{T}_{\Omega} : \boldsymbol{\varepsilon}_{\mathrm{m}} \tag{3.7}$$

The overall average strain of the RME before cracking occurs is given by:

$$\overline{\boldsymbol{\varepsilon}} = f_{\Omega}\boldsymbol{\varepsilon}_{\Omega} + f_{\mathrm{m}}\boldsymbol{\varepsilon}_{\mathrm{m}} \tag{3.8}$$

Making use of Eq. (3.7) in Eq. (3.8) and rearranging gives:

$$\boldsymbol{\varepsilon}_{\mathrm{m}} = [f_{\Omega}\mathbf{T}_{\Omega} + f_{\mathrm{m}}\mathbf{I}^{4s}]^{-1} : \overline{\boldsymbol{\varepsilon}} \tag{3.9}$$

Replacing the expression of the average matrix strain in Eq. (3.6):

$$\boldsymbol{\varepsilon}_{\mathrm{m}\Omega}(\mathbf{x}) = \mathbf{T}(\mathbf{x}) : [f_{\Omega}\mathbf{T}_{\Omega} + f_{\mathrm{m}}\mathbf{I}^{4s}]^{-1} : \overline{\boldsymbol{\varepsilon}} \tag{3.10}$$

The stress field in the matrix is subsequently obtained by introducing Eq. (3.10) into Eq. (3.2):

$$\boldsymbol{\sigma}_{\mathrm{m}\Omega}(\mathbf{x}) = \mathbf{D}_{\mathrm{m}} : \mathbf{T}(\mathbf{x}) : [f_{\Omega}\mathbf{T}_{\Omega} + f_{\mathrm{m}}\mathbf{I}^{4s}]^{-1} : \overline{\boldsymbol{\varepsilon}} \tag{3.11}$$

The stress and strain tensors in the matrix on each local plane are then as follows.

$$\mathbf{s}_{\mathrm{m}\Omega}(\mathbf{x}) = \mathbf{N}_i : \boldsymbol{\sigma}_{\mathrm{m}\Omega}(\mathbf{x}) \tag{3.12}$$

$$\boldsymbol{\varepsilon}_{\mathrm{Lm}\Omega}(\mathbf{x}) = \mathbf{C}_{\mathrm{L}} : \mathbf{s}_{\mathrm{m}\Omega}(\mathbf{x}) \tag{3.13}$$

3.2.2. Crack initiation criterion and evolution function

In Fig. 3.2 the lateral stress distribution given by Eq. (3.11) for a spherical inclusion of radius *a* embedded in an infinite elastic matrix subjected to uniaxial compressive stresses is plotted against the distance from the centre of the inclusion along the lateral direction. One can notice very sharp gradients and a tensile stress concentration in the matrix in the proximity of the matrix-inclusion interface. When the distance from the inclusion is large enough, the stress equals the Mori-Tanaka estimate of the mean matrix stress. In Jefferson and Bennett (2010) the onset of microcracking was assumed to occur when this mean matrix stress reached the tensile strength of the matrix. Whilst this formulation was able to simulate the mechanism of lateral tensile splitting in uniaxial compression or cross-cracking, somewhat unrealistic values for the elastic properties needed to be adopted, that artificially increased the lateral tensile stress predictions in the matrix in order to obtain the correct cross-cracking response. It can be readily observed that by employing estimates given by the exterior point Eshelby

solution for a region in the proximity of the matrix-inclusion interface where properties of this interface apply the aforementioned drawbacks can be addressed.

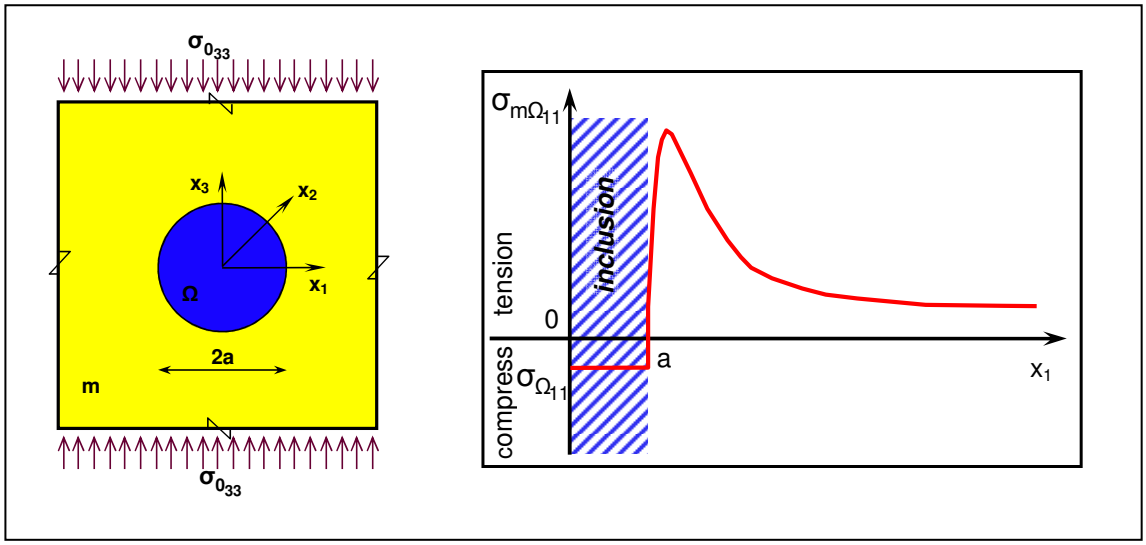

Figure 3.2. Lateral stress distribution given by the exterior point Eshelby solution

Microcracking is therefore assumed to initiate in a band of matrix material (Fig. 3.3) in the ITZ (Interfacial transition zone) when the local principal stress (s_I) within this band – evaluated by employing the exterior point Eshelby based local stresses – exceeds the initial tensile strength of the interface f_{ti}. This then defines the initial damage surface F_s as follows:

$$F_s(s, f_{ti}) = s_I - f_{ti} = 0 \tag{3.14}$$

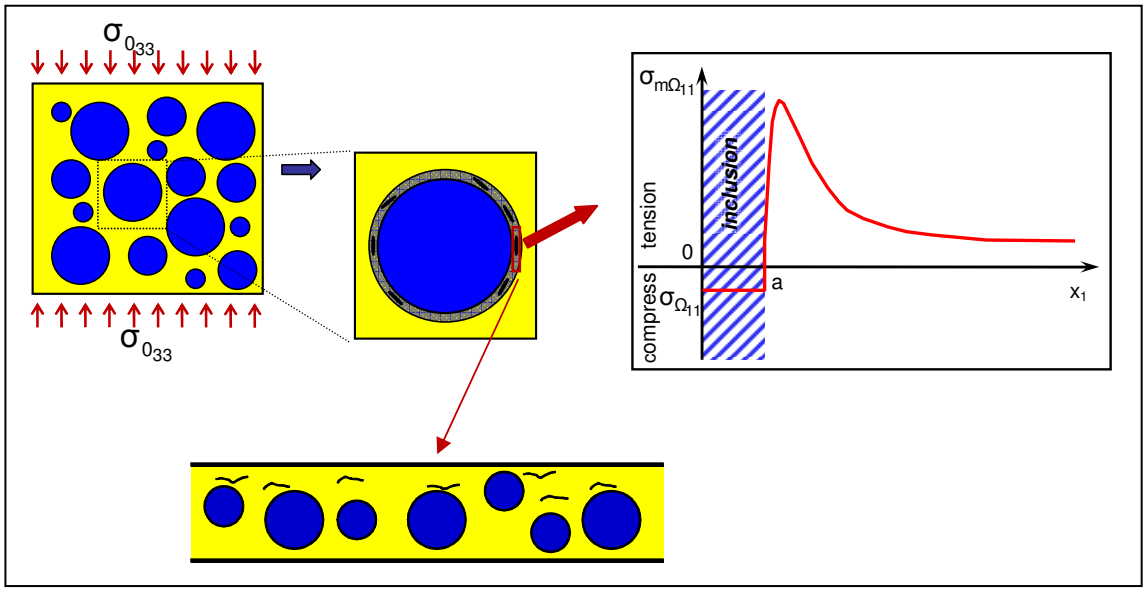

Figure 3.3. Microcrack initiation concept

It is assumed that in this band of material the only non-zero components of the local elastic strain tensor are the rr, rs and rt components. The local elastic constitutive relationship in matrix form reads:

$$\begin{bmatrix} s_{rr} \\ s_{ss} \\ s_{tt} \\ \tau_{rs} \\ \tau_{rt} \\ \tau_{st} \end{bmatrix} = E_m \beta_m \begin{bmatrix} 1 & \alpha_1 & \alpha_1 & 0 & 0 & 0 \\ \alpha_1 & 1 & \alpha_1 & 0 & 0 & 0 \\ \alpha_1 & \alpha_1 & 1 & 0 & 0 & 0 \\ 0 & 0 & 0 & \alpha_2 & 0 & 0 \\ 0 & 0 & 0 & 0 & \alpha_2 & 0 \\ 0 & 0 & 0 & 0 & 0 & \alpha_2 \end{bmatrix} \cdot \begin{bmatrix} \varepsilon_{L_{rr}} \\ 0 \\ 0 \\ \varepsilon_{L_{rs}} \\ \varepsilon_{L_{rt}} \\ 0 \end{bmatrix} \tag{3.15}$$

where $\beta_{\mathrm{m}} = \dfrac{1-\upsilon_{\mathrm{m}}}{(1+\upsilon_{\mathrm{m}})(1-2\upsilon_{\mathrm{m}})}, \alpha_1 = \dfrac{\upsilon_{\mathrm{m}}}{1-\upsilon_{\mathrm{m}}}$ and $\alpha_2 = \dfrac{1-2\upsilon_{\mathrm{m}}}{2(1-\upsilon_{\mathrm{m}})}$. Eq. (3.15) gives the following:

$$\begin{aligned} s_{rr} &= \beta_{\mathrm{m}} E_{\mathrm{m}} \varepsilon_{L_{rr}} \\ s_{ss} &= s_{tt} = \alpha_1 \beta_{\mathrm{m}} E_{\mathrm{m}} \varepsilon_{L_{rr}} = \alpha_1 s_{rr} \end{aligned} \tag{3.16a,b}$$

The principal stresses can be derived as the eigenvalues of the stress tensor. Making use of Eqs. (3.16) and noting that $\tau_{rs} = \tau_{sr}$ and $\tau_{rt} = \tau_{tr}$, the characteristic equation is:

$$\begin{vmatrix} s_{rr} - \lambda & \tau_{rs} & \tau_{rt} \\ \tau_{rs} & \alpha_1 s_{rr} - \lambda & 0 \\ \tau_{rt} & 0 & \alpha_1 s_{rr} - \lambda \end{vmatrix} = 0 \tag{3.17}$$

Expanding the determinant Eq. (3.17) becomes:

$$(\alpha_1 s_{rr} - \lambda)\left[(s_{rr} - \lambda)(\alpha_1 s_{rr} - \lambda) - \left({\tau_{rs}}^2 + {\tau_{rt}}^2 \right) \right] = 0 \tag{3.18}$$

The root obtained by equating the first factor to 0 is not the major principal stress and therefore Eq. (3.18) can be simplified to give:

$$\lambda^2 - \lambda(1+\alpha_1) s_{rr} + \alpha_1 {s_{rr}}^2 - \left({\tau_{rs}}^2 + {\tau_{rt}}^2 \right) = 0 \tag{3.18a}$$

The local major principal stress is obtained as:

$$s_I = s_{rr}\left(\frac{1+\alpha_1}{2}\right)+\sqrt{{s_{rr}}^2\left(\frac{1-\alpha_1}{2}\right)^2+{\tau_L}^2} \tag{3.19}$$

in which $\tau_L = \sqrt{{\tau_{rs}}^2+{\tau_{rt}}^2}$ and $\alpha_L = \left(\frac{\upsilon_m}{1-\upsilon_m}\right)$, noting that **s= $\mathbf{s_{m\Omega}}$**

Before damage is initiated the material is elastic and the local microcrack function (or local damage function) may equivalently be expressed in terms of local strains and an effective local strain history parameter ζ as follows,

$$F_\zeta(\boldsymbol{\varepsilon}_L,\zeta) = \left(\varepsilon_{Lrr}\left(\frac{1+\alpha_L}{2}\right)+\sqrt{{\varepsilon_{Lrr}}^2\left(\frac{1-\alpha_L}{2}\right)^2+{r_\zeta}^2\gamma^2}\right)-\zeta = f_d(\boldsymbol{\varepsilon}_L)-\zeta \tag{3.20}$$

in which $\gamma = \sqrt{{\varepsilon_{Lrs}}^2+{\varepsilon_{Lrt}}^2}$ and $r_\zeta = \left(\frac{\upsilon_m - 1/2}{\upsilon_m - 1}\right)$.

Eq. (3.20) is subject to the standard loading / unloading condition:

$$F_\zeta \le 0; \quad \dot{\zeta} \ge 0; \quad F_\zeta\dot{\zeta} = 0 \tag{3.21 a,b,c}$$

As mentioned earlier microcracking is initiated when the local principal stress in the thin band of material located in the ITZ exceeds the tensile strength of the ITZ. In strain terms this is equivalent to an initial value of the effective local strain history parameter $\zeta_{init} = \varepsilon_{tm} = f_{ti}/E_m$. It is noted that at initiation of damage, and indeed in the elastic domain, the local stress and strain components in Eqs. (3.19) and (3.20) are given by expressions (3.12) and (3.13) respectively for positions determined in Section 3.3.2.

Once formed, microcracks are assumed to extend whenever the above loading condition is satisfied. Also, once damage is initiated, Eqs. (3.10) and (3.11) no longer apply strictly; the development of microcracks disturbs the local stress and strain fields which are no longer linearly related to one another. An exact quantification of this damage induced disturbance is intractable (if all micro-level material variations are taken into account) and hence a simplified approach is adopted. In each direction, as microcracking progresses within the fracture process zone the effect described by the (elastic) stress and strain field given by Eqs. (3.12) and (3.13) is reduced, however, on

average, intact material that can carry stresses remains. The onset of microcracking is therefore controlled by the elastic stress field (Eq. 3.12) and its evolution by a local strain which starts as the concentrated matrix strain but which gradually becomes the elastic portion of the total transformed local strain. Thus $\boldsymbol{\varepsilon}_L$ in Eq (3.20) is taken as the sum of the peak elastic strain in the matrix phase ($\boldsymbol{\varepsilon}_{Lme}$), which is based on $\mathbf{s}_{m\Omega}$ and the local microcracking strain as follows:

$$\boldsymbol{\varepsilon}_L = \boldsymbol{\varepsilon}_{Lme} + \boldsymbol{\varepsilon}_\alpha \tag{3.22}$$

where $\boldsymbol{\varepsilon}_{Lme}$ and $\boldsymbol{\varepsilon}_\alpha$ are given by:

$$\boldsymbol{\varepsilon}_{Lme} = (1-\omega)\mathbf{C}_L : \mathbf{s}_{m\Omega} \tag{3.23}$$

$$\boldsymbol{\varepsilon}_\alpha = \omega \mathbf{N} : \bar{\boldsymbol{\varepsilon}} \tag{3.24}$$

and in which $\mathbf{s}_{m\Omega}$ is calculated from equation (3.11) and (3.12) and remembering that $\omega = \omega(\theta, \psi)$.

It is noted that debonding is not simulated explicitly in the present model which is in contrast to the models of Ju and Lee (2001), Sun et al. (2003) and Viola and Piva (1981); rather, microcracking is simulated by added strains (increased compliance) within the matrix.

The final element of the microcracking theory is the evolution function which links the local damage parameter ω with the effective local strain parameter ζ. Here, an established experimentally derived exponential equation (Willam et al., 1985) is used. This implicitly represents the statistical variations within the heterogeneous material but, as discussed in Section 3.1, an alternative to this function would be one derived by considering the development of period arrays of cracks (Karihaloo et al, 1996).

$$\omega = 1 - \frac{\varepsilon_{tm}}{\zeta} e^{-5\frac{\zeta - \varepsilon_{tm}}{\varepsilon_0 - \varepsilon_{tm}}} \tag{3.25}$$

Several observations can be noted:

- The onset of microcracking in the inclusion-matrix interface could alternatively be modelled by introducing yet another phase around the coarse aggregate

particles to simulate the ITZ. This would however further increase the complexity of the model. The EPE based solution enables the model to set the location of microcrack initiation in a region (within the matrix phase) in the proximity of the matrix-inclusion boundary where ITZ properties are assumed to apply. Thus, in this case the incorporation of an extra phase is not necessary.

- Initiation of damage is stress-controlled however the evolution is strain controlled
- The damage function (Eq. 3.20), evolution conditions (Eqs. 3.21) and evolution function (Eq. 3.25) characterize the onset and propagation of microcracking in each direction. By describing the overall damage by a set of local damage parameters the model has intrinsic anisotropic characteristics.

3.3. Discussion of EPE based crack initiation criterion and rough microcrack characteristics

3.3.1. The interfacial transition zone (ITZ) of a two-phase composite

The motivation for the development of a new crack initiation criterion lies in experimental observations which indicate that damage in normal strength concrete is initiated in the aggregate – hardened cement paste interfacial transition zone (ITZ) and that the onset of cracking is governed by both normal and shear stresses (van Mier 1997). The elasticity solution presented in Section 3.2.2 certifies the existence of a sharp gradient, adjacent to a material discontinuity, in the stress field that generates a peak in the vicinity of the inclusion.

The ITZ is normally considered the weakest link in concrete (van Mier, 1997) and it is generally described as a region around fine and coarse aggregate particles in concrete which has a significantly higher porosity than the bulk cement paste due to the so called “wall” effect (Ollivier et al. 1995, Scrivener and Nemati 1996). Aggregate-cement bond tests (Hsu and Slate, 1963) revealed that this porous transition zone is also characterized by reduced (tensile) strength in comparison with the strength of the cement paste. Experimental observations show that damage is not initiated directly at the aggregate-matrix physical boundary but rather in the porous transition zone (van Mier, 1997).

Studies by Scrivener et al. (2004) and Ollivier et al. (1995) show that the thickness of the ITZ between aggregate particles and hardened cement paste (hcp) is comparable to the size of cement particles, which typically range between 20 and 100 μm. However, the transition zone between mortar (comprising hcp and sand) and coarse aggregate particles is not very well defined in the literature. Caliskan et al. (2002) assumed the transition zone to be the region between the coarse aggregate particles and the part of the mortar matrix which is free of sand particles. According to Monteiro et al. (1985), the transition zones around sand particles interfere with those around coarse aggregate particles and the intensity of this interference determines the final thickness of the transition zone. Moreover, the thickness of the mortar – coarse aggregate interface depends upon the size and shape of the sand rather than cement particles (Caliskan et al. 2002; Monteiro et al. 1985). These observations would suggest that the size of the mortar – coarse aggregate transition zone is considerably greater than the cement paste –aggregate ITZ thickness and has a size which is of the same order as the fine aggregate particle size rather than that of the cement grains.

3.3.2 *Location of microcrack initiation*

As explained in Section 3.2.2, microcracking is initiated when the local principal stress (s_I), which depends upon the local stress field in the matrix, exceeds the tensile strength of the interface f_{ti}. In order to establish the existence and location of a peak in s_I, an analysis was carried out to obtain the variation of the local matrix stress (Eq. 3.12) and local principal stress (Eq. 3.19) with direction and distance from the inclusion. Due to symmetry, and for the purpose of the study, the 29 sample directions of the integration rule were reduced to six representative directions contained in the cross-section plane X_1X_2 and defined by angle ψ (Fig. 3.4), in which X_i denote Cartesian coordinates.

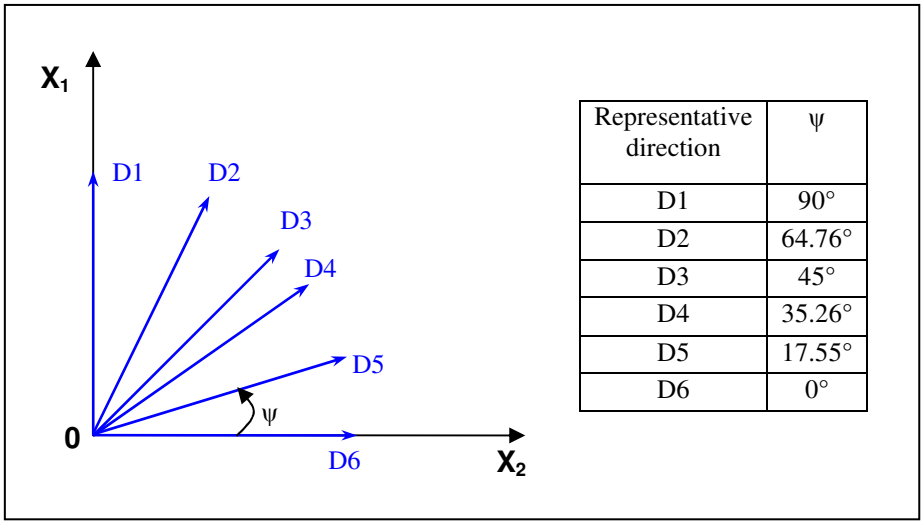

Representative direction	ψ
D1	90°
D2	64.76°
D3	45°
D4	35.26°
D5	17.55°
D6	0°

Figure 3.4. Representative directions

Uniaxial compression and tension cases, with respect to the composite material, were considered for which the loading direction was set to be direction D1 and for which the elastic properties in Table 3.2 (Section 3.6.1) were employed. The results from this analysis are presented in Figs. 3.5a,b.

The value of the compressive stress used to generate these data was chosen to be that which would just initiate cracking in the ITZ in the lateral direction D6, although it is recognised that this would not be the first direction to crack. Fig. 3.5a shows the variation of s_I and also of the normal and shear components of the local matrix stress $\mathbf{s}_{m\Omega}$ with the normalized distance parameter ρ for all six representative directions. The same analysis is performed for uniaxial tension and the results are shown in Fig. 3.5b. A tension positive sign convention is adopted unless otherwise indicated.

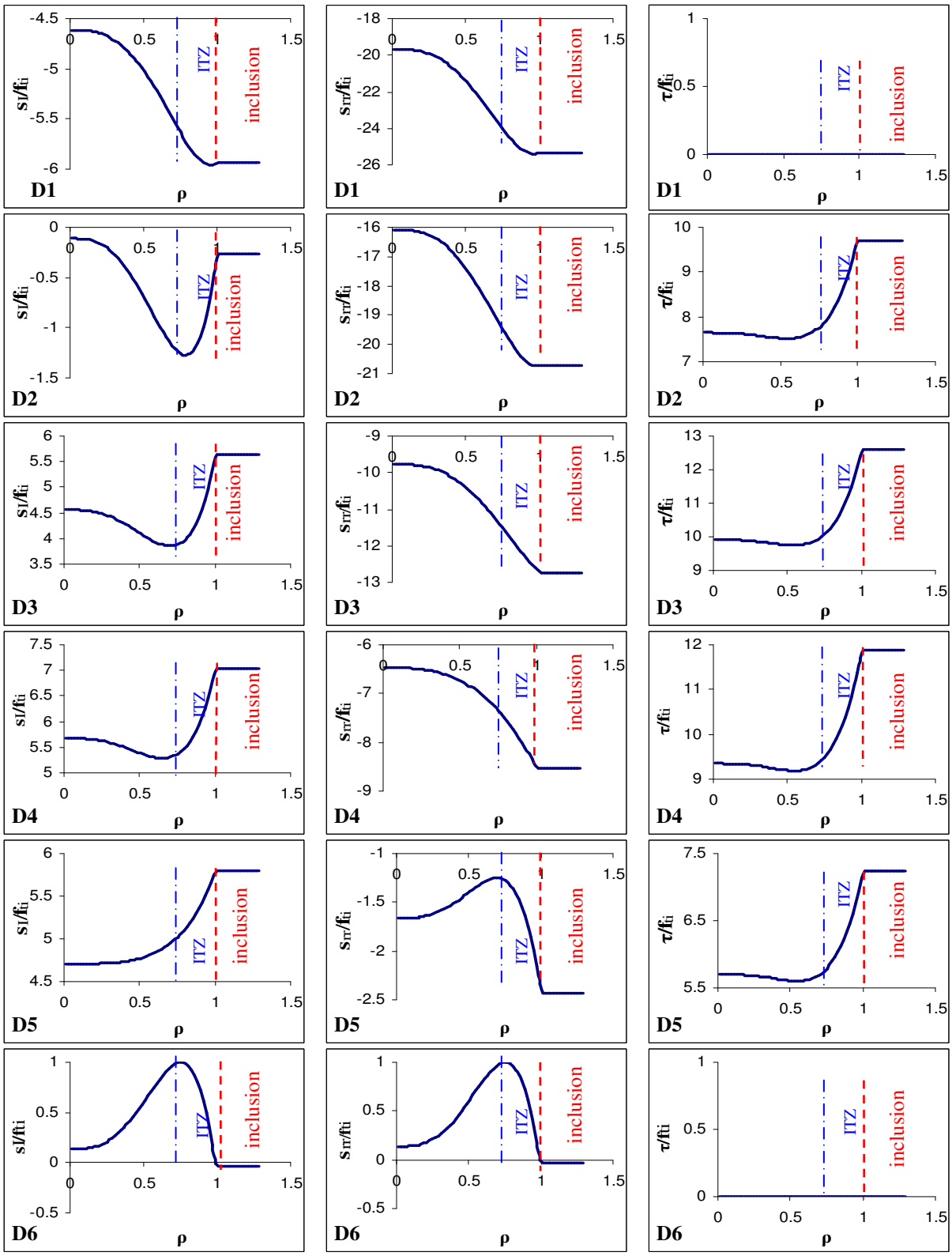

Figure 3.5a. Variation of local principal stress and local stress components in representative directions (uniaxial compression)

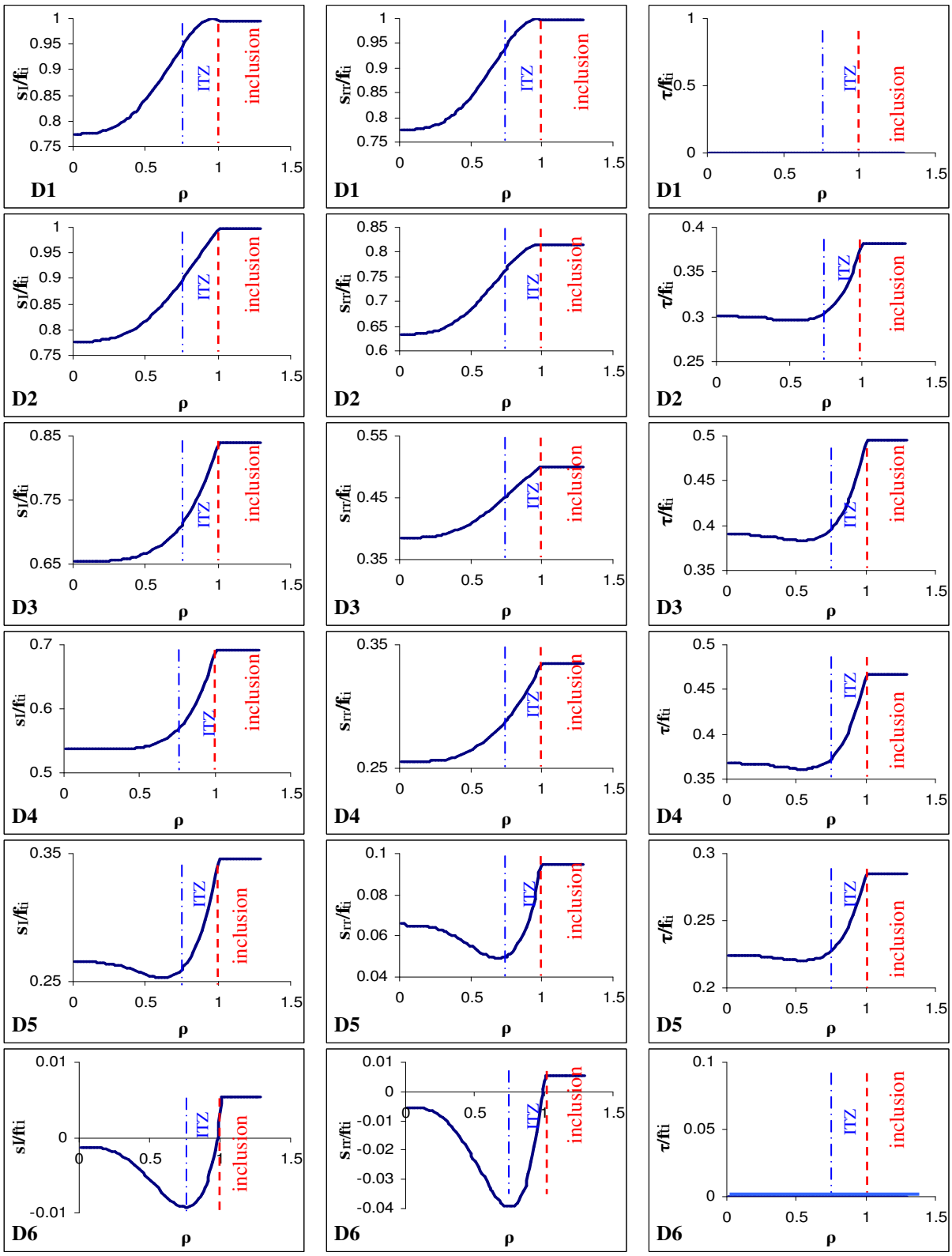

Figure 3.5b. Variation of local principal stress and local stress components in representative directions (uniaxial tension)

No attempt has been made to allow for a variation of elastic properties in the ITZ but it has been shown experimentally, for example by Hsu and Slate (1963) and van Mier (1997, Chapter 2), that the strength of the ITZ is significantly below that of the bulk matrix material. Hsu and Slate suggest the ITZ/matrix tensile strength ratio (r_{im}) varies from 0.33 to 0.67. Thus, when considering the data shown in Figs. 3.5a,b, it is the value of s_I, relative to the material strength at the location under consideration, that is relevant and which governs the assumed cracking criterion.

In uniaxial compression, the peak in s_I occurs at the interface for directions D3 to D5 whilst for direction D6 (with no shear) the peak occurs at approximately at ρ = 0.75. It may be seen that s_I is strongly influenced by the local shear stress and thus initial damage (in uniaxial compression) would occur in direction D4 at the location of the interface (ρ = 1).

In uniaxial tension the location of crack initiation is also at the interface (ρ = 1) and the local principal stress function displays no other maxima.

3.3.3 Parametric study

A parametric study was carried out in order to assess the validity of the findings from EPE analyses for a range of realistic values of elastic properties. A typical mortar mix of normal strength can be characterized by a Young's modulus of E_m = 31 GPa and a Poisson's ratio of υ_m = 0.17. According to van Mier (1997), for frequently used types of coarse aggregate, the values of Young's modulus can vary between 35 and 120 GPa and Poisson's ratio between 0.17 and 0.25. For Young's modulus, the corresponding range of the relative aggregate-mortar ratio E_Ω/E_m is 1.1 - 3.9 and for Poisson's ratio the relative proportion $\upsilon_\Omega/\upsilon_m$ ranges 1 – 1.5. The variation of the local principal stress for direction D6 is shown for the uniaxial compressive case, for the given range of Young's modulus and of Poisson's ratio. It can be observed in Figs. 3.6a, b that the local principal stress peak is present for virtually every value in the realistic range of elastic properties. The peak value depends upon the ratio of the Young's moduli whilst the variation of Poisson's ratio produces but little change in the peak position.

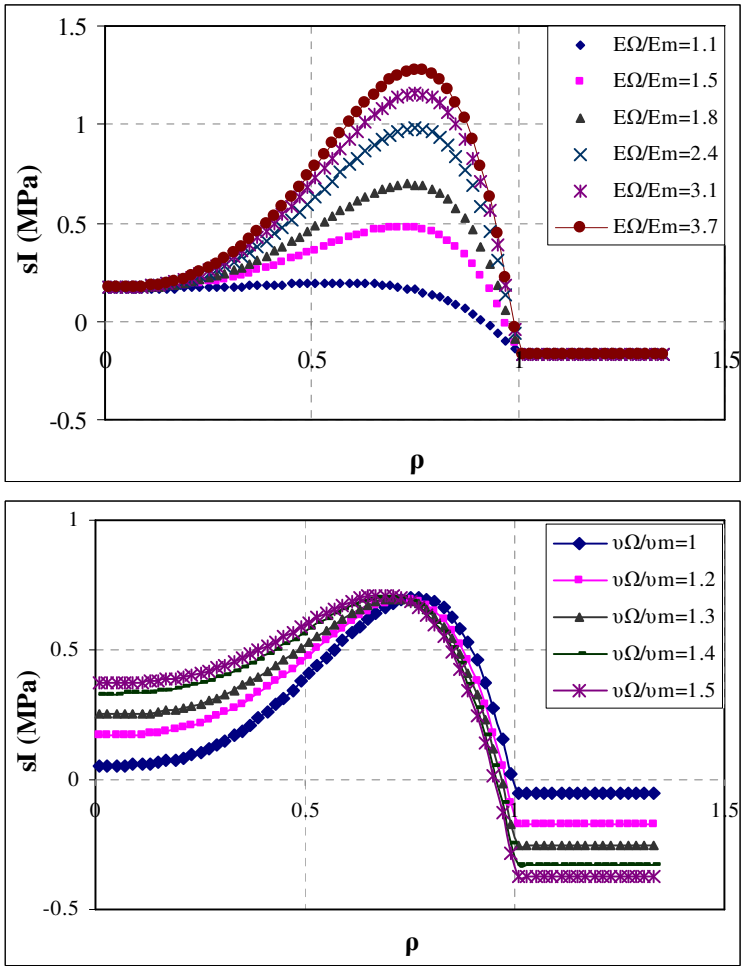

Figure 3.6. s_I vs. ρ for various elastic parameters: a) Young's modulus, b) Poisson's ratio

3.3.4 Summary of findings from EPE study

The following conclusions are drawn from the above investigation of the EPE crack initiation criterion

- Although the current model does not contain a distinctive component to simulate the ITZ, it is concluded that microcracking will always initiate in a region close to the matrix-inclusion boundary where coarse aggregate – mortar interface properties apply.

- The EPE solution adopted is able to capture tensile stress concentrations in the proximity of inclusion – matrix interfaces and in directions lateral to a compressive loading axis. The latter are compatible with the phenomenon of

lateral splitting in uniaxial compression which is considered to be one of the causes of microcrack initiation (van Mier, 1997).

- The crack initiation criterion takes into account the influence of both tensile and shear stresses on interface microcracking.
- The EPE solution enables the use of realistic material properties.

It is noted that this last point is in contrast to the previous model (Jefferson and Bennett, 2010) for which it was necessary to employ somewhat unrealistic elastic properties in order to obtain the correct cross-cracking response.

The EPE microcrack initiation criterion may be summarised as follows.

Loop over sample directions n_i, for i=1 to n_p

Is direction n_i already cracked?

No

Find $(s_I/f_{t*})_{max}$ and associated position ρ

If $(s_I/f_{t*})_{max}>1$, microcracking is initiated. Evaluate initial damage parameter using local stress given by Eq. 3.12

Yes

Update damage parameter using local strain tensor (Eqs. 3.22–3.24).

Note: $f_{t*} = f_{ti}$ if $\rho \geq 0.7$

$f_{t*} = f_{tm}$ if $\rho < 0.7$

where f_{tm} is the tensile strength of the matrix and ρ is defined on page 45.

3.3.5 Roughness of microcrack surface

In the development of the contact model (Jefferson 2002), the author derived a linear expression for the interlock surface:

$$\Phi_{int}(u,v) = m_g u - |v| \tag{3.26}$$

where u is the crack opening and v is the shear displacement at which contact is regained.

This function can be measured directly by forming a crack in a specimen under normal loading, to a certain opening, and then loading the specimen in shear, whilst maintaining the same opening, until significant contact is detected, i.e. the shear and normal compressive stresses start to increase significantly. This can be repeated for different openings and the contact (i.e. 'interlock') surface plotted. For a macrocrack, this is essentially the procedure followed by Walraven and Reinhardt (1981).

The linear function of Jefferson was found to match reasonably, in a particular relative-displacement range, the regression analysis-based relationship of Walraven and Reinhardt (1981):

$$\tau = -\frac{f_{cu}}{30} + \left[1.8u^{-0.80} + \left(0.234u^{-0.707} - 0.20\right)\cdot f_{cu}\right]\cdot v \qquad (3.27)$$

where τ is the shear stress, f_{cu} the compressive strength and in which the dimensions are assumed to be N and mm.

The single value of m_g which gives the best fit to equation (3.27) in the range u = 0 to u_0 is $m_g = 0.25$, as illustrated in Fig. 3.7. However, as is clear from micrographs of real crack surfaces (e.g. van Mier, 1997), asperities do not have all the same height and slope.

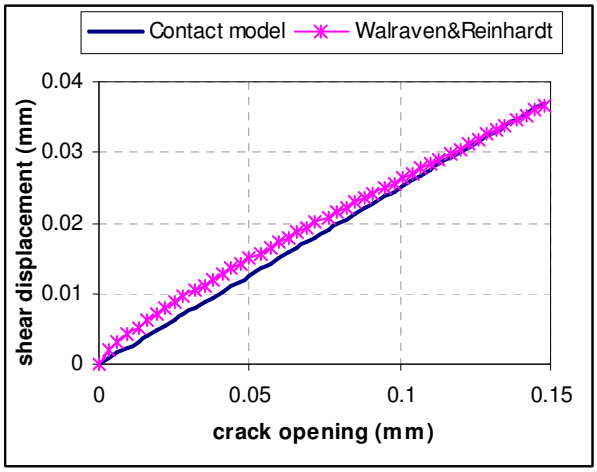

Figure 3.7. Experimental and numerical rough contact surface

In order to explore the variable nature of these surfaces, a study was made of micrographs and images obtained using various non-destructive techniques (In particular, see Plates 4 - 6 in van Mier, 1997; Fig. 15 in Bache and Nepper-Christensen, 1965; Fig. 6 in Elaqra et el., 2007; Fig. 1 in Mouret et al., 1999; Figs. 8 and 9 in Nichols and Lange, 2006). From this study, the following observations are made regarding the roughness characteristics of crack surfaces in normal strength concrete at micro, meso and macro levels.

(i) Fine microcracks in the hardened cement paste phase (hcp) are approximately smooth relative to u_0.

(ii) Microcracks that develop around fine aggregate particles tend to form sinuous paths that bridge-over the fine aggregate particles consequently increasing the roughness of the crack surface (implying that m_g should decrease).

(iii) Excluding the smooth sections of crack surface, the microcrack surfaces may be broadly split into two components which may be alternatively expressed as a bimodal distribution of asperities heights (Table 3.3, Section 3.6.1.):

a) the first component is characterized by asperity heights of the order of u_0 and contact angles ranging from the sharp m_g value suggested by Walraven's function (Eq. 3.27) to 0.8

b) the second component is characterized by asperity heights of $u_0/10$ and somewhat shallower contact angles (m_g in the range 0.5 - 2).

When a rough crack is reloaded, it is assumed that, due to misalignments and loose material becoming lodged between the surfaces, the smooth sections do not regain direct contact.

It is noted that the model represents the roughness around coarse aggregate particles by the variation in the overall microcrack plane orientations ($\mathbf{r}(\theta,\psi)$) and openings, and it is the microcrack roughness (Fig. 2.1) that is being addressed here.

The above observations have been used as a guide to selecting roughness parameters for the model but since the model does not perfectly represent all of the complexities of the contact behaviour between crack surfaces some tuning of the parameters was necessary after reasonable ranges for the parameters were established.

3.4. Summary of micromechanical constitutive model

The development of a constitutive model for concrete, based on micromechanical solutions and geometrical consideration of microcrack morphology, was presented in Chapters 2 and 3. While the theoretical components may appear somewhat complex – this is nevertheless due to the complexity of the material microstructure and damage phenomena which in turn produce a complex mechanical behaviour – the final set of equations, given in Table 3.1, that describe this altogether intricate material is relatively compact.

Table 3.1. Summary of micromechanical constitutive model

$\bar{\boldsymbol{\sigma}} = \mathbf{D}_{\mathrm{m}\Omega} : (\bar{\boldsymbol{\varepsilon}} - \boldsymbol{\varepsilon}_{\mathrm{a}})$	(M1)	Elastic constitutive equation
$\boldsymbol{\varepsilon}_{\mathrm{a}} = \left(\frac{1}{2\pi} \int_0^{2\pi} \int_0^{\pi/2} \mathbf{N}^{-1} : \mathbf{C}_{\mathrm{c}\alpha}(\theta,\psi) : \mathbf{N} \sin(\psi) d\psi d\theta \right) : \bar{\boldsymbol{\sigma}}$	(M2)	Added strains due to microcracking in the matrix.
$\mathbf{C}_{\mathrm{c}\alpha} = \left[\left[(1-\omega)\mathbf{I}^{2\mathrm{s}} + \omega \left(\sum_k p_k H_{fk} \boldsymbol{\Phi}_k \right) \right]^{-1} - \mathbf{I}^{2\mathrm{s}} \right] \cdot \mathbf{C}_{\mathrm{L}}$	(M3)	Local added compliance tensor
$\boldsymbol{\varepsilon}_{\mathrm{Lam}}(\theta,\psi) = \left(1\text{-}\omega(\theta,\psi)\right) \mathbf{C}_{\mathrm{L}} : \mathbf{N} : \boldsymbol{\sigma}_{\mathrm{m}\Omega}(\mathbf{x}_{\mathrm{p}}) + \omega(\theta,\psi) \mathbf{N}_{\varepsilon} : \bar{\boldsymbol{\varepsilon}}$	(M4)	Amplified local strain (used for computing damage variable)
$\boldsymbol{\sigma}_{\mathrm{m}\Omega}(\mathbf{x}) = \mathbf{D}_{\mathrm{m}} \cdot \left[\mathbf{I}^{4s} + \mathbf{S}_{\mathrm{E}}(\mathbf{x}) \cdot \mathbf{B}_{\Omega} \right] \cdot \left[\mathrm{f}_{\Omega} \mathbf{T}_{\Omega} + \mathrm{f}_{\mathrm{m}} \mathbf{I}^{4s} \right]^{-1} : \left(\bar{\boldsymbol{\varepsilon}} - \boldsymbol{\varepsilon}_{\mathrm{a}} \right)$	(M5)	Mori-Tanaka estimate of the EPE based stress field
$\mathrm{F}_{\zeta}(\boldsymbol{\varepsilon}_{\mathrm{Lam}}, \zeta) = \left(\varepsilon_{\mathrm{Lam_{rr}}} \left(\frac{1+\alpha_1}{2} \right) + \sqrt{{\varepsilon_{\mathrm{Lam_{rr}}}}^2 \left(\frac{1-\alpha_1}{2} \right)^2 + {r_\zeta}^2 \gamma^2} \right) - \zeta$	(M6)	Local principal stress based damage function
$\omega(\theta,\psi) = 1 - \frac{\varepsilon_{\mathrm{tm}}}{\zeta(\theta,\psi)} e^{-5 \frac{\zeta(\theta,\psi) - \varepsilon_{\mathrm{tm}}}{\varepsilon_0 - \varepsilon_{\mathrm{tm}}}}$	(M7)	Evolution of the damage parameter, $\omega \in [0,1]$
$\bar{\boldsymbol{\sigma}} = \left(\mathbf{I}^{4\mathrm{s}} + \frac{\mathbf{D}_{\mathrm{m}\Omega}}{2\pi} \int_{2\pi}^{\pi/2} \int \mathbf{N}^{-1} : \mathbf{C}_{\mathrm{c}\alpha}(\theta,\psi) : \mathbf{N} \sin(\psi) d\psi d\theta \right)^{-1} \cdot \mathbf{D}_{\mathrm{m}\Omega} : \bar{\boldsymbol{\varepsilon}}$	(M8)	Final average stress-strain relationship

3.5. Numerical implementation

The constitutive model presented above has been implemented in a MATHCAD sheet using the algorithm in Fig. 3.8.

Enter with $\bar{\boldsymbol{\varepsilon}}$, set of ζ_{prv_i}	*Input strain vector and the previous equivalent strain parameters for each integration direction*
for i=1 to n_s	*Loop over integration directions*
$\bar{\mathbf{x}}_i = \mathbf{n}_i$	*Set unit position vector to current direction vector*
Determine ρ_i	*Determine the position of* $(s_I/f_{t*})_{max}$
$\boldsymbol{\varepsilon}_{m\Omega}(\bar{\mathbf{x}}_i) = \mathbf{T}(\bar{\mathbf{x}}_i) : [f_\Omega \mathbf{T}_\Omega + f_m \mathbf{I}^{4s}]^{-1} : \bar{\boldsymbol{\varepsilon}}$	*Compute average matrix strain at peak position (Eq. 3.10)*
$\mathbf{s}_{m\Omega}(\bar{\mathbf{x}}_i) = \mathbf{N}_i : \mathbf{D}_m : \boldsymbol{\varepsilon}_{m\Omega}(\bar{\mathbf{x}}_i)$	*Compute local cracking stress at peak position (Eq. 3.12)*
If $\omega_i = 0$	*Direction n_i previously uncracked*
If $s_I(\mathbf{s}_{m\Omega})_{max} \geq f_{t*}$	*Condition for microcrack initiation*
$\boldsymbol{\varepsilon}_{Li} = \mathbf{C}_L : \mathbf{s}_{m\Omega}$	*Evaluate initial local strain vector (Eq. 3.23)*
$\zeta_i = f_d(\boldsymbol{\varepsilon}_{Li})$	*Determine effective strain parameter (Eq.3.20)*
Else $\zeta_i = \zeta_{prv_i}$	
Else	*Damage evolution*
Iteration loop	
$\boldsymbol{\varepsilon}_{Li} = (1-\omega_i)\mathbf{C}_L : \mathbf{s}_{m\Omega} + \omega_i \mathbf{N}_{\varepsilon i} : \bar{\boldsymbol{\varepsilon}}$	*Evaluate local strain vector (Eq.3.22-3.24)*
$\zeta_i = f_d(\varepsilon_{L_i})$ *if* $f_d(\varepsilon_{L_i}) > \zeta_{prv_i}$	*Update strain parameter, if exceeds previous max*
Update ω_i	*Update damage parameter (Eq.3.25)*
Close loop	
Evaluate contact matrix $\boldsymbol{\Phi} = \sum_k p_k H_{fk} \boldsymbol{\Phi}_k$	*Determine contact matrix (Table 2.1)*
Evaluate $\mathbf{C}_{c\alpha_i}$	*Evaluate local added compliance matrix (Eq.2.46)*
Close loop	
$\mathbf{C}_{add} = \sum_{i=1}^{n_s} \mathbf{N}_i^{-1} : \mathbf{C} :_{c\alpha_i} \mathbf{N}_i w_i$	*Evaluate the total added compliance*
$\mathbf{D}_{sec} = \left[\mathbf{I}^{4s} + \mathbf{D}_{m\Omega} \cdot \mathbf{C}_{add}\right]^{-1} : \mathbf{D}_{m\Omega}$	*Form secant constitutive matrix (Eq.M8)*
$\bar{\boldsymbol{\sigma}} = \mathbf{D}_{sec} : \bar{\boldsymbol{\varepsilon}}$	*Compute stresses*

Figure 3.8. Algorithm for a specified strain path

3.6. Model parameters and numerical simulations

This section demonstrates that the proposed model is able to emulate many of the characteristic features of the mechanical behaviour of concrete, i.e. pre-peak and post-peak non-linearity, dilatancy and ductility. To illustrate this, uniaxial, biaxial and triaxial simulations are presented and discussed.

If the simulations are considered in terms of a triaxial test, the axial stress and strain are taken as σ_{xx} and ε_{xx}, respectively. The zero stress components are taken as $\sigma_{yy} = \sigma_{zz}$ in the uniaxial simulations and σ_{zz} in the biaxial simulations respectively.

3.6.1 Constitutive parameters

The model has a relatively small number of constitutive parameters, all of which having a clear physical meaning. The material parameters (see Table 3.2) include the elastic properties of the two phases, tensile strength of the ITZ, crack opening at the end of softening curve and the maximum coarse aggregate size. In addition, the model employs geometric contact parameters (contact angles, asperity heights and proportions) as given in Table 3.3. The elastic properties are taken from van Mier (1997), Yang (1998) and Yurtdas et al. (2004) and the tensile strength of the ITZ is based on the experimental data of Hsu and Slate (1963).

Table 3.2. Material properties

Material property	Physical meaning	Value
E_m (MPa)	Young's modulus of mortar	31000
E_Ω (MPa)	Young's modulus of aggregate particles	55000
υ_m	Poisson's ratio of mortar	0.19
υ_Ω	Poisson's ratio of aggregate particles	0.21
f_{ti} (MPa)	Tensile strength of ITZ	1.0
u_0 (mm)	Crack opening at the end of softening curve	0.08
d_{max} (mm)	Maximum aggregate size	10

Table 3.3. Contact parameters

Contact parameter	Physical meaning	Value					
m_g	Tangent of contact angle	0.25	0.4	0.8	0.5	1	2
λ	Height of asperity/u_0	1	1	1	0.13	0.13	0.13
p	Proportion	0.2	0.01	0.05	0.01	0.01	0.01

3.6.2 Example 1. Uniaxial cases

In this example, numerical predictions for uniaxial response are compared with experimental results. The contact parameters in Table 3.3 are used for this simulation. For uniaxial tension, the experimental data of Reinhardt (1984) and Hordijk (1991) are used in comparisons (Fig. 3.9a,b) whereas the numerical predictions for uniaxial compression are compared with the experimental results of Kupfer et al (1969) and van Mier (1986, 1997) (Fig. 3.10).

In the figures, f_t denotes the tensile strength and f_c the uniaxial compressive strength.

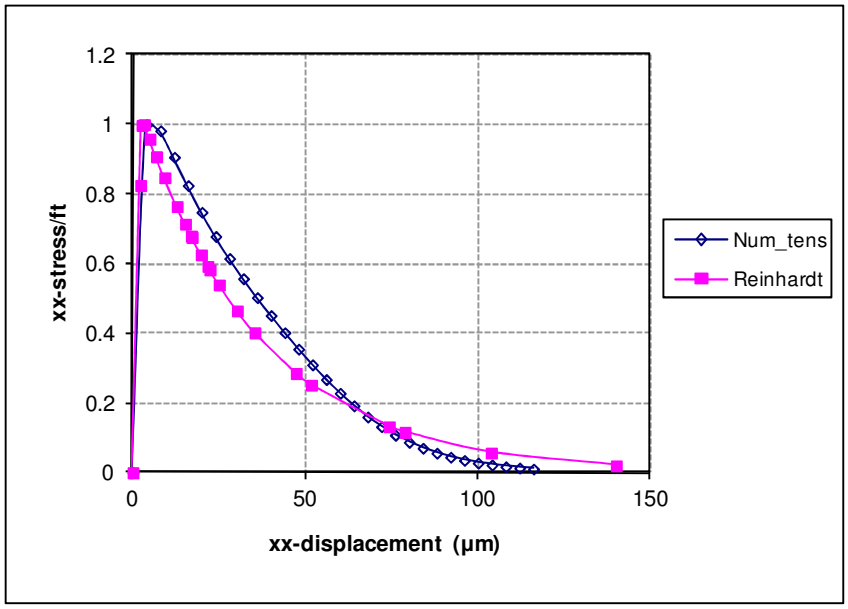

Figure 3.9a. Example 1. Uniaxial tension response

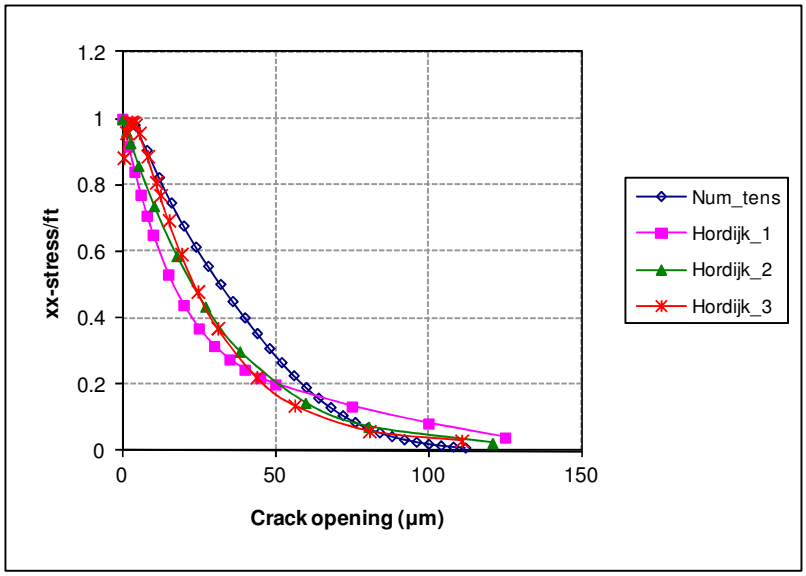

Figure 3.9b. Example 1. Uniaxial tension response. Inelastic response only

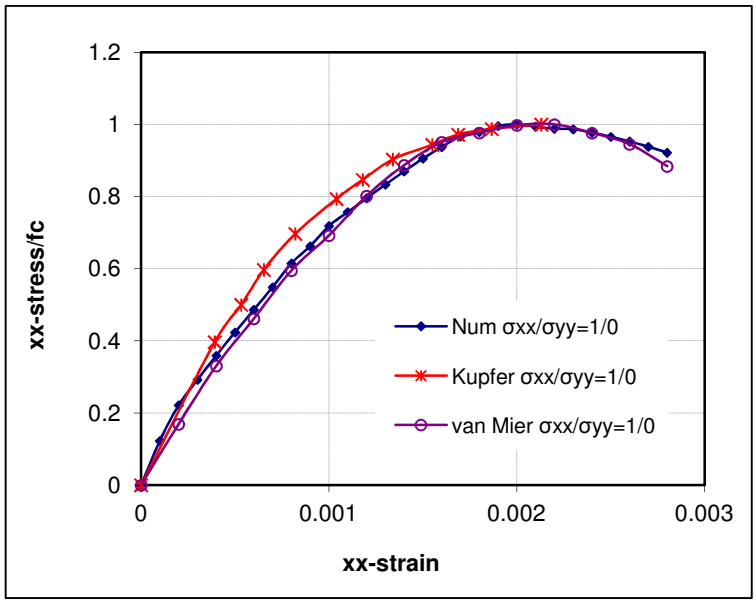

Figure 3.10. Example 1. Uniaxial compression response (compression +ve)

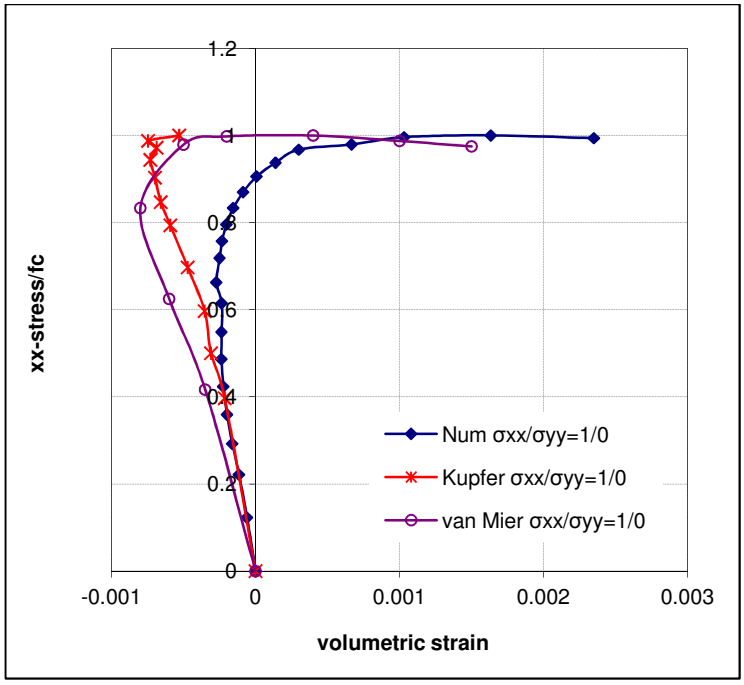

Figure 3.11. Example 1. Normalised stress – volumetric strain curves in uniaxial compression (compression +ve)

These results show that the micromechanical proposed model is able to realistically capture the characteristic features of uniaxial tension and compression behaviour. It is noted in particular that the model predicts the dilatant behaviour observed in uniaxial compression tests (Fig. 3.11).

3.6.3 Example 2. Optimised parameters for uniaxial, biaxial and triaxial simulations

The model does not include friction on the surfaces or plastic embedment of one microcrack surface into another. This is believed to become increasingly important as a specimen is more constrained which implies that the model will become increasingly inaccurate as the confining stress (mean compressive stress) increases. Whilst acknowledging the aforementioned shortcoming, an attempt has nonetheless been made to arrive at a set of parameters (Tables 3.4 and 3.5) which give the best overall response for all uniaxial, biaxial and triaxial mechanical behaviour. It will be seen that these tend to result in a little too much ductility in uniaxial tension in particular.

Table 3.4. Material parameters. Example 2

Material property	Physical meaning	Value
E_m (MPa)	Young's modulus of mortar	31000
E_Ω (MPa)	Young's modulus of aggregate particles	55000
υ_m	Poisson's ratio of mortar	0.19
υ_Ω	Poisson's ratio of aggregate particles	0.21
f_{ti} (MPa)	Tensile strength of ITZ	1.0
u_0 (mm)	Crack opening at the end of softening curve	0.11
d_{max} (mm)	Maximum aggregate size	10

Table 3.5. Contact parameters. Example 2

Contact parameter	Physical meaning	Value					
m_g	Tangent of contact angle	0.25	0.4	0.8	0.5	1	2
λ	Height of asperity/u_0	1	1	1	0.2	0.2	0.2
p	Proportion	0.15	0.02	0.1	0.02	0.02	0.25

Fig. 3.12 presents a comparison between the numerical softening curve in uniaxial tension and experimental curves of Hordijk (1991). The numerical response in this example is slightly more ductile than in the previous example and the tensile strength is overestimated a little (f_t/f_c=0.11).

In Fig. 3.13 the numerical predictions for uniaxial and biaxial compression are compared with experimental data of Kupfer et al. (1969) and van Mier (1984, 1997) and Fig. 3.14 presents the numerical biaxial envelope. The numerical curves show good general agreement with the experimental curves.

In Fig. 3.14 the predicted biaxial failure envelope is shown in comparison with the experimental envelopes of Kupfer et al. (1969) and Gerstle et al. (1978). When comparing the numerical predictions with the widely quoted findings of Kupfer et al. (1969) it would appear that the biaxial compressive strengths are generally overestimated. However, in an international comparative research programme (Gerstle et al., 1978) it was shown that the biaxial strength, as well as the shape of the strength

envelope, can vary considerably depending on the method of testing and size of the specimen. Fig 3.14 includes the inner and outer envelopes from the aforementioned study for tests with low friction loading platens. It is apparent that the predicted biaxial stress ratios lie within the experimental range. It can also be noted that, in agreement with experimental results, the proposed model realistically simulates the envelope in the tension – compression regime.

In Figs. 3.15 and 3.16 the predicted strengths under triaxial confinement are compared with a function empirically derived by Newman (1979) based on a set of triaxial experimental tests on four different concrete and mortar mixes. It can be observed that the increase of strength is a little overestimated, however, the predictions are considerably more realistic than those obtained with the previous model.

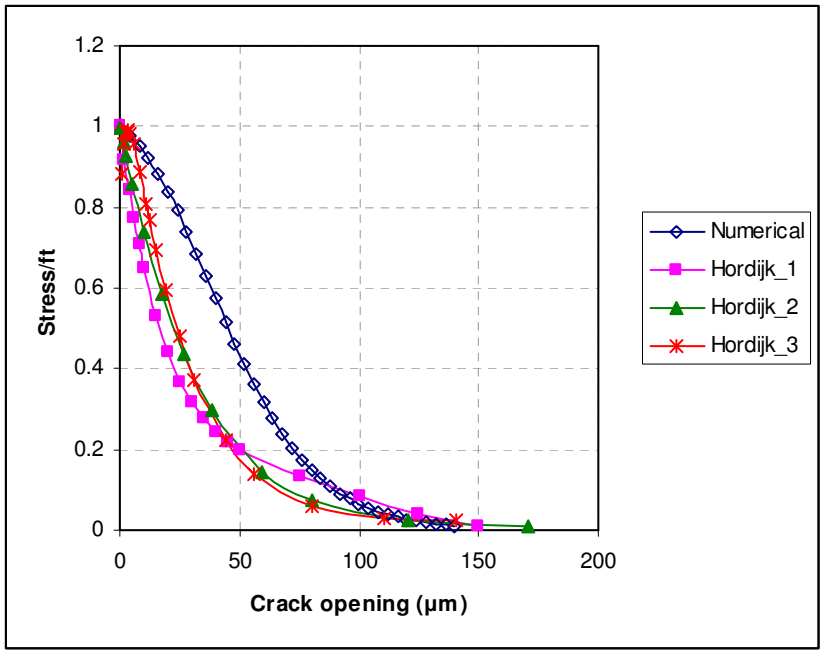

Figure 3.12. Example 2. Inelastic deformations in uniaxial tension

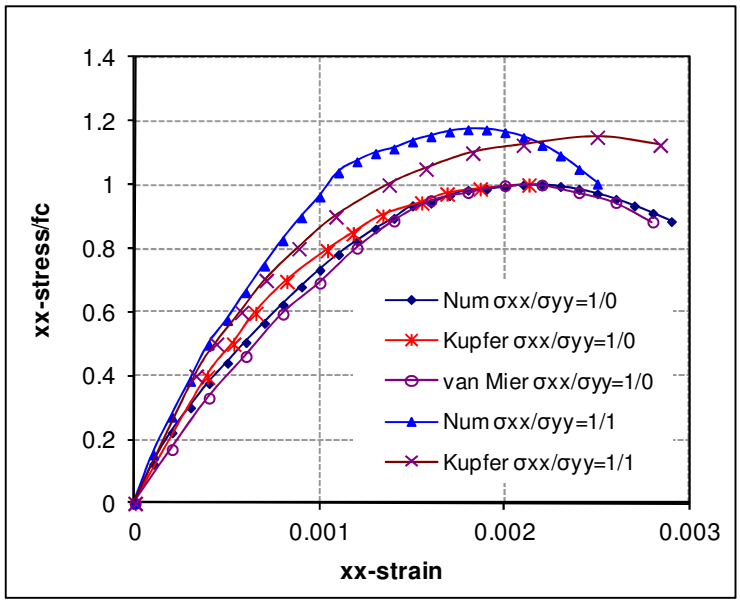

Figure 3.13. Example 2. Uniaxial and biaxial compression responses (compression +ve)

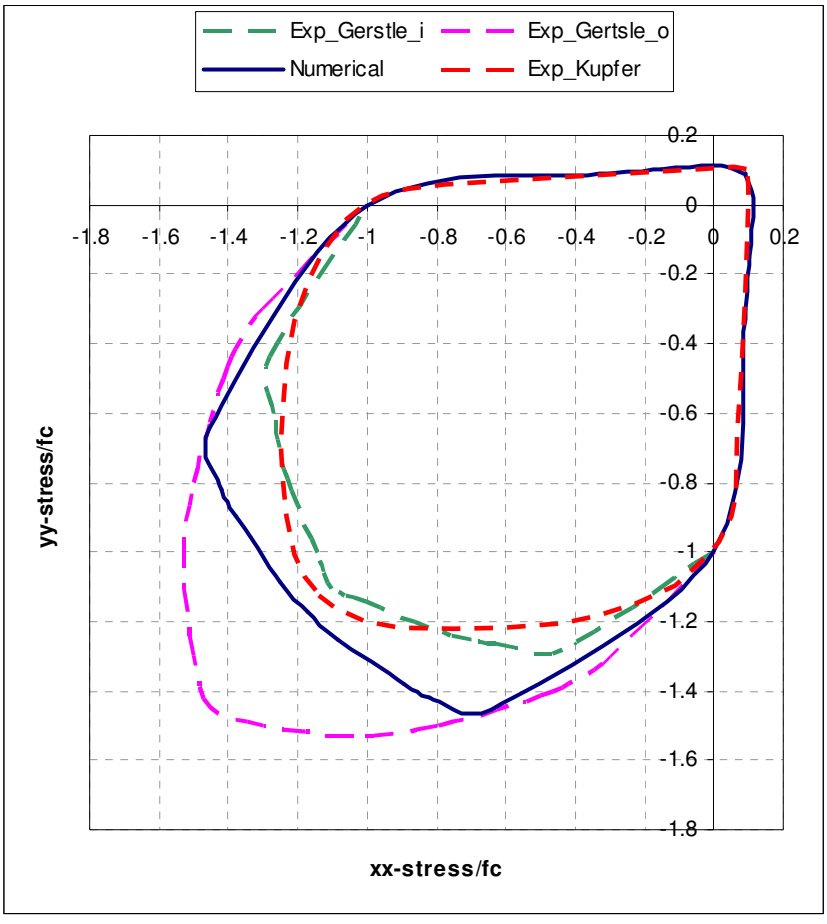

Figure 3.14. Example 2. Biaxial failure envelope

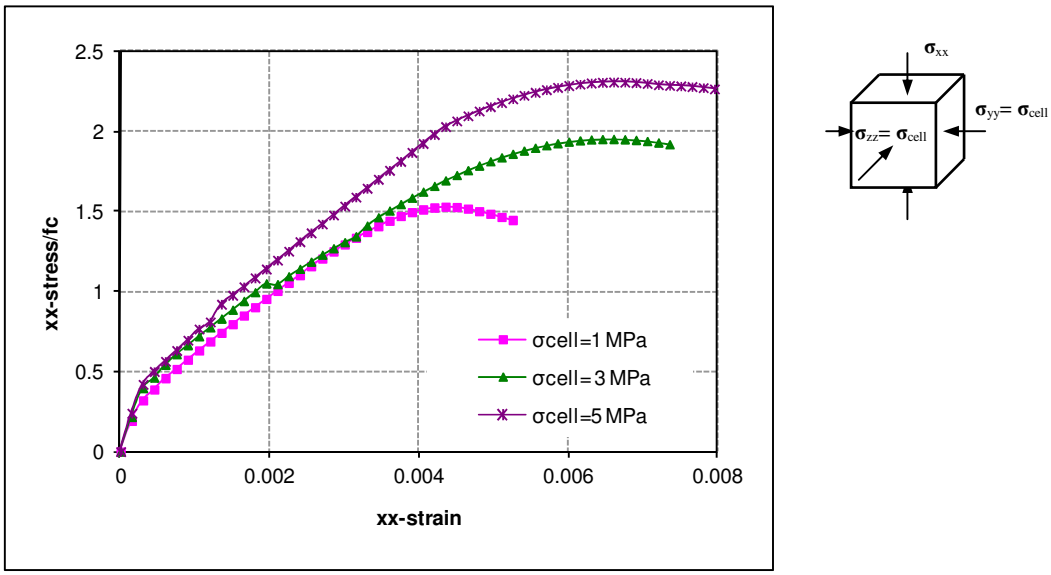

Figure 3.15. Example 2. Triaxial confinement predictions (compressive +ve)

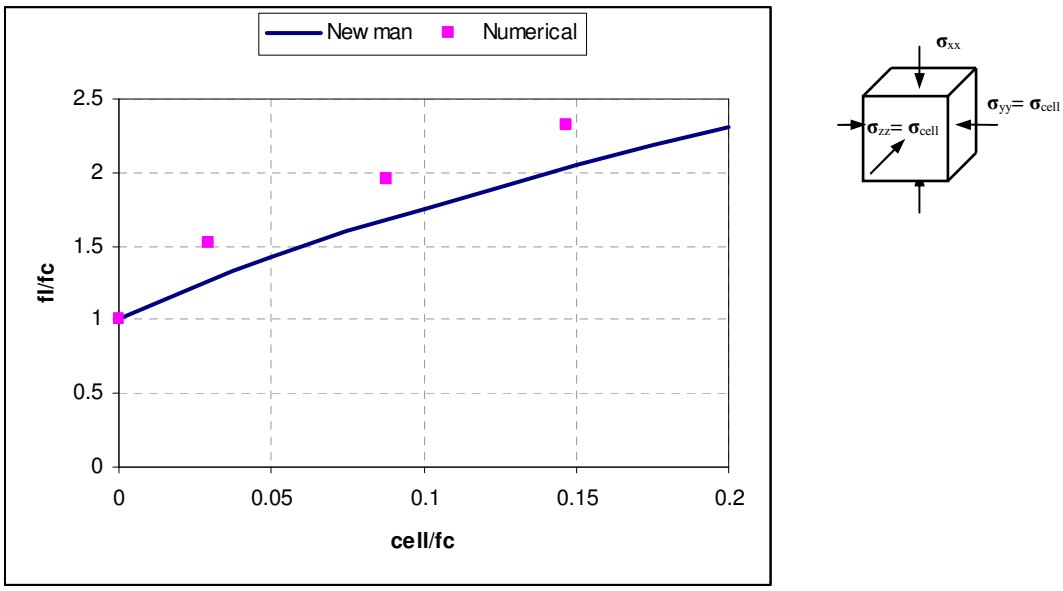

Figure 3.16. Example 2. Triaxial confinement strengths (compressive +ve)

3.6.4 Parametric study on roughness parameters

An initial set of roughness parameters were determined using the observations given in Section 3.3.5 and these were then tuned by undertaking a numerical calibration exercise. In this section, the effect of varying the roughness parameters, within a limited range, is illustrated by considering the effects of changing the parameters on the following values; σ_c , σ_t/σ_c , σ_b/σ_c and ε_c; where σ_c = the peak uniaxial compressive

stress, σ_t = peak tensile strength, σ_b = peak biaxial stress at a principal compressive stress ratio of 1:1 and ε_c = the strain at peak uniaxial compression.

In the study, all parameters not given in Table 3.6 are as per Table 3.4. It may be seen that the same m_g values have been used throughout and the dominant proportions of the regions with large and small asperities have been kept constant.

From Table 3.6 the following observation can be made:

(i) increasing the proportions for the shallower asperities (i.e. increasing p's for the larger m_g values) increases σ_c, decreases σ_b/σ_c ratio and increases the ductility.

(ii) Increasing the asperity heights for the shallower asperities (i.e. increasing the last 3 λ values in Table 3.6) decreases σ_b/σ_c

(iii) Increasing u_0 increases both strength and ductility

Table 3.6. Contact parameters used in parametric study

u_0		**Roughness parameters**						σ_c	σ_t/σ_c	σ_b/σ_c	ε_c
	m_g	0.25	0.4	0.8	0.5	1	2	MPa	-	-	-
0.11	λ	1	1	1	0.1	0.1	0.1	33	0.11	1.33	0.0022
	p	0.15	0.02	0.1	0.02	0.02	0.25				
0.11	λ	1	1	1	0.1	0.1	0.1	33	0.11	1.34	0.0021
	p	0.15	0.02	0.1	0.06	0.02	0.25				
0.11	λ	1	1	1	0.1	0.1	0.1	29	0.12	1.58	0.0016
	p	0.15	0.02	0.02	0.02	0.02	0.25				
0.11	λ	1	1	1	0.1	0.1	0.1	35	0.11	1.4	0.0022
	p	0.15	0.1	0.1	0.02	0.02	0.25				
0.11	λ	1	1	1	0.1	0.1	0.1	33	0.11	1.34	0.00215
	p	0.15	0.02	0.1	0.1	0.02	0.25				
0.13	λ	1	1	1	0.1	0.1	0.1	38	0.10	1.37	0.0025

	p	0.15	0.02	0.1	0.02	0.02	0.25				
0.12	λ p	1 0.15	1 0.02	1 0.1	0.1 0.02	0.1 0.02	0.1 0.25	36	0.11	1.3	0.0023
0.11	λ p	1 0.15	1 0.02	1 0.1	0.2 0.02	0.2 0.02	0.2 0.25	33	0.11	1.17	0.0021

3.7. Concluding remarks

A micromechanical model for cementitious composites was presented which incorporates a new crack initiation criterion based on an exterior point Eshelby solution. It was shown that the presented approach successfully simulates the micromechanisms that lead to failure in the ITZ. The proposed model uses measured micromechanical material properties, i.e. elastic moduli of the individual phases and measured aggregate-mortar interface strength parameters.

By simulating specific physical mechanisms at micro and meso scale; e.g. matrix – spherical inclusion composite, microcrack initiation and propagation, and stress recovery through rough crack closure; the proposed model captures fundamental characteristics of the overall macroscopic behaviour: damage induced anisotropy, volumetric dilatancy under compressive stress states, realistic correlation between tensile and compressive strengths, predictions of ductility consistent with experimental observations, realistic biaxial failure envelope and a more favourable prediction of triaxial behaviour than the previous model.

The final remarks in this chapter make, yet again, reference to the contrast between phenomenological macroscopic models -which generally employ uniaxial compression, uniaxial tension functions and strength envelope equations as direct input- and mechanistic micromechanical models, which combine individual mechanistic components in order to predict a response which is not pre-prescribed. In this context, the model presented here does show considerable promise and, in the author's opinion, provides a significant step towards a comprehensive and accurate mechanistic micromechanical model for the mechanical behaviour of concrete.

Chapter 4

Multi-asperity plastic-contact crack plane model

4.1. Introduction

Cracks in particulate materials exhibit dilatant frictional behaviour when subject to shear relative displacements, or slip, between the crack faces. Due to the geometric irregularities present on the crack surface, i.e. rough asperities, the shear slip is accompanied by a relative displacement in a direction normal to the crack plane termed normal separation or dilation. When such cracks are in compression, this slip is associated with the development of significant shear and normal stresses across the crack plane. 'Aggregate interlock', a term generally used to describe such behaviour in concrete (Paulay and Loeber, 1974), is a fundamental mechanism for the transfer of shear stress across crack faces.

Several models have been proposed to simulate the transfer of stresses across rough cracks. These models use, to varying degrees, combinations of empirically based relationships and mechanistic models to describe the morphology of the crack surfaces and the contact expressions which govern the stress-displacement relationships. (Patton, 1966; Bažant and Gambarova, 1980; Walraven and Reinhardt, 1981; Divakar et al., 1987; Plesha, 1987; Li et al., 1989; Haberfield and Johnston, 1994; Bujadham and Maekawa, 1992; Ali and White, 1999; Jefferson, 2002; Wang et al., 2003). Related models which simulate concrete-rebar interfaces have also been developed (Serpieri and Alfano, 2011).

Following the generally phenomenological approach, Bažant and Gambarova (1980) developed an empirical stress-displacement relationship for cracks in concrete based on the experimental data of Paulay and Loeber (1974). Divakar et al. (1987) proposed a similar model based on data from experimental tests in which pre-cracked concrete specimens were sheared under constant normal stress.

Walraven and Reinhardt (1981) conducted a series of experimental shear tests in which cracked concrete specimens, with both internal and external reinforcement, were subjected to shear loading for different initial crack openings. Based on these data, they developed a rather detailed model in which concrete was represented as a two-phase system of hard spherical inclusions (aggregate particles) embedded in a soft matrix (hardened cement paste). Assuming a probabilistic distribution of aggregate particle sizes, relationships for normal and shear stresses across cracks were derived in terms of crack opening and shear displacement. The model employed two fundamental assumptions: (i) that crack surfaces develop through the matrix and around the circumference of the inclusions and (ii) that the matrix material is characterised by a rigid-plastic stress-strain relationship.

Li et al. (1989) proposed a contact density model for stress transfer in which the crack surface was idealized as a series of infinitely small areas (contact units) with different inclination angles that were described by a trigonometric contact density function. An elastic perfectly-plastic formulation was used to predict the contact stresses that develop on the constituent contact units –the directions of which were assumed to be fixed and normal to the initial contact direction, thus the effect of friction was ignored. The model also employed an effective contact ratio that accounts for the reduction in the contact area due to crack opening and shear. Following the same approach, Ali and White (1999) proposed a model that introduced friction in the contact density function. Additionally, the roughness of the interface was correlated with the fracture energy of concrete in order to enable the prediction of shear friction capacity of normal as well as high strength concrete.

More recently Jefferson (2002) developed a two-dimensional model, based on a type of smooth contact theory, in which the crack surface was modelled as a series of triangular asperities. The model employed a contact function based on the data of Walraven and Reinhardt (1981) which was used to describe three contact states. Much

like in the contact density model of Li et al. (1989) an effective contact proportion function was used to relate the total 'apparent' stresses to the contact stresses, the latter being predicted using an elasto-plastic formulation.

Computational aspects of several crack plane models, used with interface elements in a finite element code, were investigated by Feenstra el al. (1991 a, b). The main focus of their investigation was on numerical performance of the models although a number of simulations of experimental specimens were also presented.

Several models that follow a mechanistic approach have been proposed for rock joints, one of the first of which was due to Patton (1966) in which the asperities of the interface surface were modelled as "saw-teeth". For low compressive normal stresses, the shear response was related to dilation and asperity overriding whereas for high compressive normal stresses asperity shearing behaviour was assumed to be dominant. Employing Patton's saw-tooth asperity surface, as well as a sine-tooth surface, Plesha (1987) developed a two-dimensional dilatant contact model which included a frictional sliding component and a tribological relation for surface degradation due to wear.

In this chapter a new mechanistic model for fully formed cracks that includes contact, friction, crushing -or plastic embedment- along with a three-dimensional geometrical characterization of the crack surface is presented. Whilst elements of this complex mechanism may be found in other models (the mechanistic models developed for concrete tend to make use of complex functions to characterize the crack surface and apply rigid-plastic or elasto-plastic formulations for stress predictions, whereas the models developed for rock joints generally employ a simple two-dimensional geometry -i.e. triangular asperities- and employ a frictional sliding formulation) the present model combines all these aspects in one constitutive law. The model includes multi asperities by simulating the crack surface with a series of conical teeth and corresponding recesses. Plastic embedment of a tooth into the recess wall, as well as frictional sliding on the teeth surfaces, is incorporated into a relative-displacement based plasticity formulation to predict the stresses that develop on the area in contact. Additionally, a geometrically based effective contact function is derived that accounts for the reduction of the contact area with crack opening.

Although the physical mechanisms result in relatively complex behaviour, the proposed model predicts this behaviour simply by considering the contact and plasticity

which occurs between multiple conical asperities on opposing crack surfaces. For this, the plastic surfaces are written in terms of relative displacements. This has the advantage that the form of the function used for the contact surfaces can be used directly to describe the yield and plastic potential functions.

The original motivation for developing the model was to simulate the behaviour of microcracks in a three-dimensional constitutive model for cementitious materials, but, in doing this it was recognized that the behaviour simulated is characteristic of a variety of situations which includes the behaviour of micro, meso and macrocracks in a range of quasi-brittle geomaterials.

4.2. Constitutive model

4.2.1. Concepts and assumptions

The model describes the behaviour of a band of quasi-brittle material which contains a rough crack. The crack plane is defined as the mid surface of this band of material and the orientation of this plane is defined by the local Cartesian coordinates r,s,t, with unit vector **r** being the normal to the crack plane and **s** and **t** being orthogonal in-plane unit vectors (able to be represented by a zero thickness element such that the model could be used to govern the behaviour of a zero thickness interface element in a finite element code.

Conceptually, the crack model comprises a series of conical teeth which form one of the crack faces and conforming conical recesses that form the opposing face. The teeth are characterised by slope m_g and tooth height h_t (Fig. 4.1). The interactions between a tooth and a corresponding recess simulate crushing (or embedment) of a tooth into a recess and friction along the slope of a tooth. Contacts are monitored via the relative movement between the crack faces. A limit is placed on the cone slope m_{g_lim}, and when m_g exceeds this limit the crack surface is assumed to be flat. This part of the crack plane is represented by a frictional contact surface in the s-t plane.

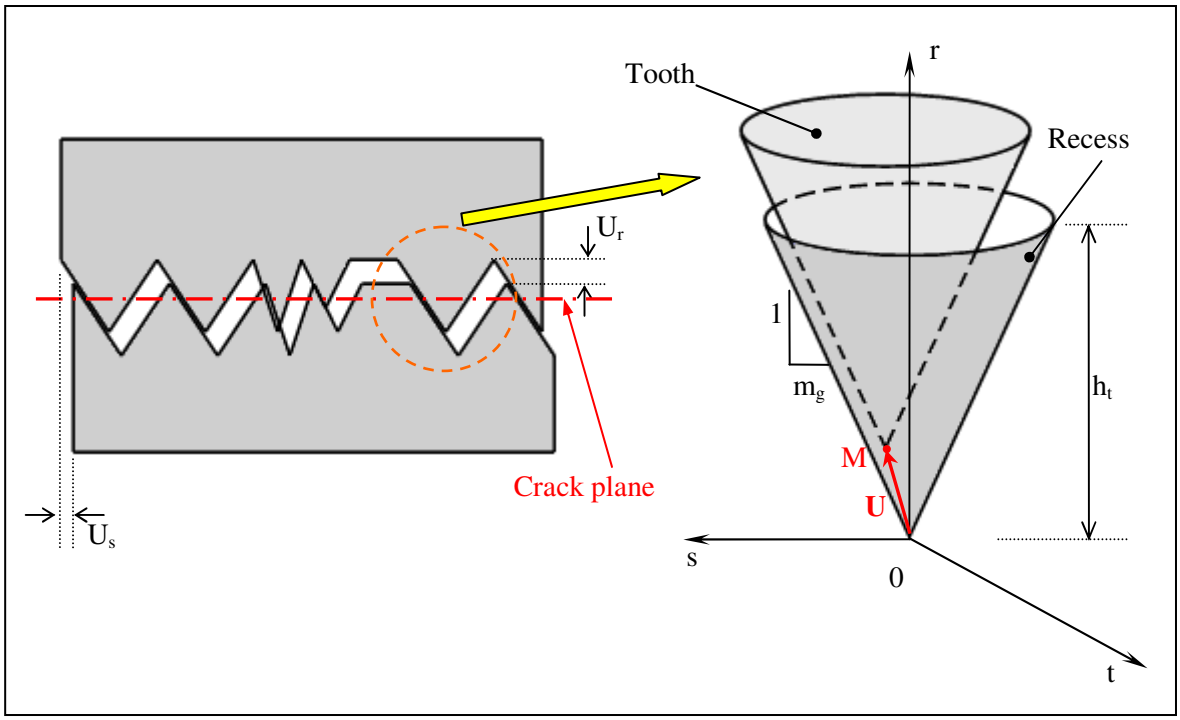

Figure 4.1. Model concepts

The stress tensor which pertains to the crack plane ($\boldsymbol{\sigma}$) can be written in reduced vector form as follows $\boldsymbol{\sigma} = [\sigma_{rr} \quad \sigma_{rs} \quad \sigma_{rt}]^T$. These stresses are computed from the sum of the forces on individual cones, plus the forces acting on the flat parts of the surface, per unit area of crack plane. The associated relative displacement vector is given by $\mathbf{U} = [U_r \; U_s \; U_t]^T$, which is defined as the displacement of the apex of a tooth M relative to the apex of the recess (Fig. 4.1).

The contact stresses are defined relative to the recess wall surface, the orientation of which is defined by the unit normal and tangent direction vectors $\hat{\mathbf{n}}(\alpha)$ and $\hat{\mathbf{m}}(\alpha)$ respectively, as illustrated in Fig. 4.2b; α being the angular coordinate as defined in Fig. 4.2a. Using the simplifying assumption that the contact stresses are constant over the height of the contact zone, these stresses -for a given cone of slope m_g and crack opening U_r - depend upon the angle α and therefore may be denoted $\boldsymbol{\sigma}_c(\alpha) = \left[\sigma_{c_{nn}}(\alpha) \quad \sigma_{c_{nm}}(\alpha)\right]^T$, with $\alpha \in (0, 2\pi)$

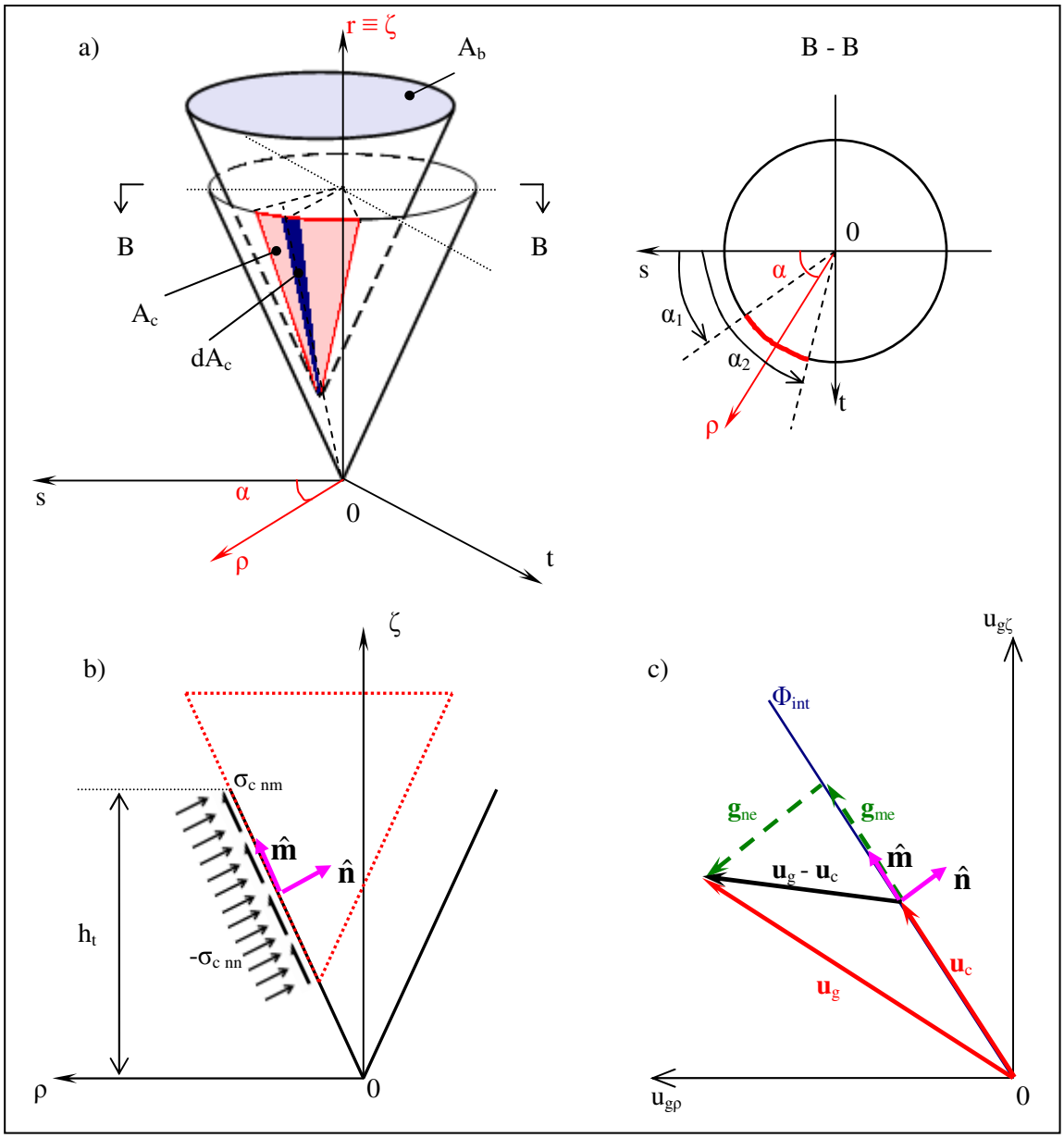

Figure 4.2. Schematic representation a) area of contact; b) contact stresses; c) gap displacements

The contact surface, which defines when a tooth just touches a recess wall, is conveniently described in the cylindrical coordinate system ζ, ρ and α (Fig. 4.2) and the normal and tangential elastic gap displacements ($\mathbf{g}_{ne}$ and $\mathbf{g}_{me}$ respectively), upon which contact stresses depend, are also expressed in these coordinates (Fig. 4.2c). If the elastic normal and shear stiffnesses per unit area of cone wall are denoted k_n and k_m respectively, then the traction vectors associated with the normal and tangential stress components $\sigma_{c\ nn}$ and $\sigma_{c\ nm}$ may be denoted $\mathbf{t}_{cn}$ and $\mathbf{t}_{cm}$ respectively, with the total wall traction vector ($\mathbf{t}_c$) being given by

$$\mathbf{t}_c = \mathbf{t}_{cn} + \mathbf{t}_{cm} = k_n \mathbf{g}_{ne} + k_m \mathbf{g}_{me} \tag{4.1}$$

The stresses at the base of each conical tooth, $\boldsymbol{\sigma}^{cn} = \begin{bmatrix} \sigma_{rr}^{cn} & \sigma_{rs}^{cn} & \sigma_{rt}^{cn} \end{bmatrix}^T$ are then obtained by integrating the tractions over the contact surface, transforming these forces to crack plane coordinates and dividing by the cone base area as follows (See Fig. 4.2a)

$$\boldsymbol{\sigma}^{cn} = \frac{1}{A_b} \int_{2\pi} \mathbf{N}(\alpha)^T \mathbf{t}_c(\alpha) \frac{\partial A_c}{\partial \alpha} d\alpha \tag{4.2}$$

in which $\mathbf{N}(\alpha) = \begin{bmatrix} 1 & 0 & 0 \\ 0 & \cos(\alpha) & \sin(\alpha) \end{bmatrix}$, $A_c(\alpha)$ is the contact surface area and A_b is the base area of a cone. It is also noted that $\mathbf{t}_c = \mathbf{0}$ for angles where there is no contact.

The model accounts for the variability of the crack surface roughness by using a range of asperity slopes (m_g) and tooth heights (h_t), which is accomplished using a probability density function $p(m_g, h_t)$ that describes the relative likelihood of an asperity of given slope and height occurring. Considering firstly the expression for crack plane stress for a discrete distribution of h_t and m_g values:

$$\boldsymbol{\sigma} = \sum_{i=1}^{n_c} \frac{A_{bi} \boldsymbol{\sigma}_i^{cn}}{A} = \sum_{i=1}^{n_c} P(m_{gi}, h_{ti}) \left(\frac{1}{A_{bi}} \int_{2\pi} \mathbf{N}(\alpha)^T \mathbf{t}_c(\alpha, m_{gi}) \frac{\partial A_c(\alpha, m_{gi}, h_{ti}, U_r)}{\partial \alpha} d\alpha \right) \tag{4.3}$$

in which $P(m_{gi}, h_{ti}) = \frac{A_b(m_{gi}, h_{ti})}{A}$, A is the area of the crack plane and n_c = number of discrete pairs (m_g, h_t) considered.

In continuous form, Eq. (4.3) becomes

$$\boldsymbol{\sigma} = \int_0^{\infty} \int_0^{h_{t\max}} p(m_g, h_t) \left(\frac{1}{A_b(m_g, h_t)} \int_{2\pi} \mathbf{N}(\alpha)^T \mathbf{t}_c(\alpha, m_g) \frac{\partial A_c(\alpha, m_g, h_t, U_r)}{\partial \alpha} d\alpha \right) dh_t dm_g \tag{4.4}$$

A further assumption is that the wall of a tooth conforms to the shape of the recess wall during embedment i.e. the tooth deforms such that its shape conforms to the shape of the recess wall. Using the above assumption, the product of the terms relating to the side contact and base areas of the cone in Eq. (4.4) may be written as follows.

$$\frac{1}{A_b} \frac{\partial A_c}{\partial \alpha} = \frac{1}{2\pi} \left(1 - \frac{U_r}{h_t} \right)^2 \frac{\sqrt{1+m_g^2}}{m_g} = \frac{1}{2\pi} c_f(U_r) \frac{\sqrt{1+m_g^2}}{m_g} \tag{4.5}$$

where $c_f(U_r) = \left(1 - \frac{U_r}{h_t}\right)^2$ denotes an effective contact function that accounts for the fact that the contact area reduces as the crack opening increases and which is equivalent to the effective contact ratio K of Li et al. (1989).

Using Eq. (4.5) in (4.4) gives the following expression for the crack plane stress

$$\boldsymbol{\sigma} = \int_0^{\infty} \int_0^{h_{t\max}} p(m_g, h_t) c_f(U_r) \cdot \frac{\sqrt{1+m_g^2}}{m_g} \left(\frac{1}{2\pi} \int_{2\pi} \mathbf{N}(\alpha) \mathbf{t}_c(\alpha, m_g) d\alpha \right) dh_t dm_g \tag{4.6}$$

4.2.2. Constitutive relationships

The tooth displacements in cylindrical coordinates are defined as follows

$$\mathbf{u}(\alpha) = \begin{bmatrix} u_\zeta \\ u_\rho(\alpha) \end{bmatrix} = \mathbf{N}(\alpha)\mathbf{U} \tag{4.7}$$

noting that $u_\zeta = u_r$.

The model considers two types of inelastic behaviour, those due to (i) plastic embedment, which is governed by the plastic displacement vector $\mathbf{u}_p$ and (ii) frictional sliding which requires the stress free displacement $\mathbf{u}_c$.

For a given α, $\mathbf{u}_g$ is defined as follows

$$\mathbf{u}_g = \mathbf{u} - \mathbf{u}_p \tag{4.8}$$

In terms of $\mathbf{u}_g$, the contact surface function (or *interlock function*) may be defined as follows;

$$\Phi_{int}(\mathbf{u}_g, m_g) = m_g \cdot u_{g\zeta} - u_{g\rho} \tag{4.9}$$

the actual surface being defined by $\Phi_{int}(\mathbf{u}_g, m_g) = 0$. For a given direction α, the contact state is illustrated in Fig. 4.2.b,c and defined by the following condition:

If $\Phi_{int}(\mathbf{u}_g, m_g) \le 0$ and $u_{g\zeta} \le h_t$ contact

If $\Phi_{int}(\mathbf{u}_g, m_g) > 0$ or $u_{g\zeta} > h_t$ open (no contact)

By establishing the contact state for each direction, the contact area A_c of a cone is also determined. This comprises the integral of infinitesimal areas dA_c that lie between the contact limits α_1 and α_2 ($A_c = \int dA_c = \int_{\alpha_1}^{\alpha_2} \frac{\partial A_c}{\partial \alpha} d\alpha$) with α_i being defined as the roots of the equation $\Phi_{int}(\mathbf{u}_g(\alpha), m_g) = 0$, which are only evaluated when real roots exist i.e. when contact is detected (Fig. 4.2a).

The total, normal and tangential elastic gap vectors are defined by

$$\mathbf{g}_e = \mathbf{u}_g - \mathbf{u}_c \tag{4.10a}$$

$$\mathbf{g}_{ne} = \mathbf{\Phi}_d \mathbf{u}_g \tag{4.10b}$$

$$\mathbf{g}_{me} = (\mathbf{u}_g - \mathbf{u}_c) - \mathbf{g}_{ne} \tag{4.10c}$$

in which $\mathbf{\Phi}_d = \frac{1}{1+m_g^2} \begin{pmatrix} m_g^2 & -m_g \\ -m_g & 1 \end{pmatrix}$ noting that (4.10a) and (4.10c) may be deduced from vector summations illustrated in Fig. 4.2c and derivation of (4.10b) is given in Jefferson (2002)

Using Eqs. (4.10b,c) in Eq. (4.1) gives the contact traction vector as follows

$$\mathbf{t}_c = k_n \mathbf{\Phi}_d \mathbf{u}_g + k_m \left((\mathbf{I} - \mathbf{\Phi}_d)\mathbf{u}_g - \mathbf{u}_c \right) \tag{4.11}$$

The contact traction vector obtained in Eq. (4.11) is then introduced in Eq. (4.6) to give the effective stress on the crack plane $\boldsymbol{\sigma}$.

4.2.2.1. Crushing

As a tooth embeds into a recess there is assumed to be some crushing of the material in the vicinity of the interface. The yield function, which encloses the elastic domain, is written in terms of the interlock function as follows:

$$F_n(\mathbf{u}_g, \gamma_y) = -\Phi_{int}(\mathbf{u}_g) - \chi_m \cdot \gamma_y \tag{4.12}$$

in which γ_y is a plastic embedment parameter given by $\gamma_y = \frac{\sigma_y}{k_n}$ (Fig. 4.3), $\chi_m = \sqrt{1+m_g^2}$ and noting that Φ_{int} is negative in the contact region. The yield stress is taken as $\sigma_y = 0.95 f_c$ where f_c is the uniaxial compressive strength.

It is also noted that all yield and plastic potential functions are developed in terms of relative displacement variables, rather than the contact stresses, since this leads to a more compact final algorithm. This is possible because the contact stresses are linearly related to the embedment displacements $\mathbf{g}_{ne}$, $\mathbf{g}_{me}$, which in turn are linearly related to the relative displacement variables (for a given slope m_g).

It is assumed that the plastic flow is proportional to the elastic embedment $\mathbf{u}_g$-$\mathbf{u}_c$, which leads to the following flow rule;

$$\dot{\mathbf{u}}_p = \dot{\lambda} \cdot \mathbf{q} \tag{4.13}$$

where $\mathbf{q} = \mathbf{u}_g - \mathbf{u}_c$

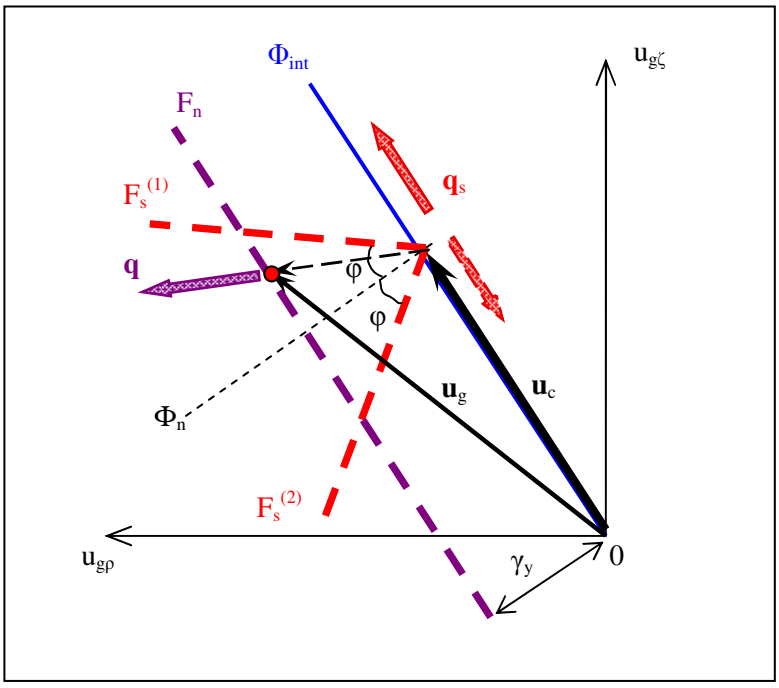

Figure 4.3. Plastic surfaces

4.2.2.2. Frictional sliding

Similarly to the crushing yield surface, the frictional sliding yield surface is developed in terms of $\mathbf{u}_g$. However, permanent sliding is not introduced in the plastic embedment $\mathbf{u}_p$ but rather is controlled by the evolution of the stress free displacement $\mathbf{u}_c$. Sliding is assumed to be governed by Coulomb friction which controls the form of the yield surface and flow rule employed, as illustrated in Fig. 4.3. The frictional yield surface F_s has two parts $F_s^{(1)}$ and $F_s^{(2)}$ which lie either side of the wall normal function $\Phi_n(\mathbf{u}_g, \mathbf{u}_c) = 0$ (see Fig. 4.3), with the active surface being governed by the value of the Heaviside function $H(\mathbf{u}_g, \mathbf{u}_c)$.

$$F_s(\mathbf{u}_g, \mathbf{u}_c) = H(\mathbf{u}_g, \mathbf{u}_c) \cdot F_s^{(1)}(\mathbf{u}_g, \mathbf{u}_c) + \left(1 - H(\mathbf{u}_g, \mathbf{u}_c)\right) \cdot F_s^{(2)}(\mathbf{u}_g, \mathbf{u}_c) \tag{4.14}$$

where

$$F_s^{(*)}(\mathbf{u}_g, \mathbf{u}_c) = \Phi_s^{(*)}(\mathbf{u}_g - \mathbf{u}_c) = \Phi_s^{(*)}(\mathbf{g}_e) \tag{4.15}$$

and

$$\Phi_s^{(*)}(\mathbf{u}) = u_\zeta + m^{(*)} \cdot u_\rho \tag{4.16}$$

$m^{(*)}$ denotes the slopes of the upper (1) and lower (2) sliding yield surfaces and are functions of the friction coefficient $\mu = \tan(\varphi)$, where φ is the local friction angle

$$m^{(1)} = \frac{m_g - \mu}{1 + m_g \mu}$$
$$m^{(2)} = \frac{m_g + \mu}{1 - m_g \mu} \tag{4.17a,b}$$

H is the Heaviside function defined as:

$$H = \begin{cases} 1 & \text{if} \quad \Phi_n(\mathbf{u}_g, \mathbf{u}_c) \geq 0 \\ 0 & \text{if} \quad \Phi_n(\mathbf{u}_g, \mathbf{u}_c) < 0 \end{cases} \tag{4.18}$$

where $\Phi_n(\mathbf{u}_g, \mathbf{u}_c) = \Phi_s^{(0)}(\mathbf{u}_g - \mathbf{u}_c)$ and $\Phi_s^{(0)}(\mathbf{u}) = u_\zeta + m_g \cdot u_\rho$

Sliding is assumed to occur along the face of the wall, which leads to the following flow rule.

$$\dot{\mathbf{u}}_c = \dot{\lambda}_s \cdot \mathbf{q}_s \tag{4.19}$$

where:

$$\mathbf{q}_s = \frac{\Phi_n(\mathbf{u}_g, \mathbf{u}_c)}{\left|\Phi_n(\mathbf{u}_g, \mathbf{u}_c)\right|} \cdot \frac{\partial \Phi_s^{(0)}(\mathbf{u}_g, \mathbf{u}_c)}{\partial \mathbf{u}_g}, \tag{4.20}$$

noting that when $u_\zeta \le 0$ (i.e. the crack is fully closed), further sliding in the sense of crack closure is prevented due to geometric constraints.

4.2.2.3. Flat component

As mentioned in section 2.1, in the region where the slope of asperities m_g is above m_{g_lim}, taken as 5, the surface is assumed to be (locally) flat. The contact criterion for this flat component is given directly by

$$\begin{aligned} &\text{contact} && \text{if } U_r \le 0 \\ &\text{no contact} && \text{if } U_r > 0 \end{aligned}$$

It is furthermore assumed that when in contact (i.e. a crack is fully closed) the compressive deformations in a direction normal to the crack plane are elastic, i.e. crushing does not occur. Coulomb based frictional sliding is assumed on this surface. The expression of the yield function is given in Eq. (4.21):

$$F_{sf}(\mathbf{U}, \mathbf{U}_{cf}) = \sqrt{(U_s - U_{cfs})^2 + (U_t - U_{cft})^2} - \mu(U_r - U_{cfr}) \tag{4.21}$$

An in-plane radial flow rule is assumed for the flat contact plane as follows

$$\mathbf{q}_{sf} = \begin{bmatrix} 0 \\ \partial F_{sf} / \partial U_s \\ \partial F_{sf} / \partial U_t \end{bmatrix} \tag{4.22}$$

The contact stresses associated with the flat component are:

$$\boldsymbol{\sigma}_f = P_f \mathbf{K}_f (\mathbf{U} - \mathbf{U}_c) \tag{4.23}$$

where P_f is the relative proportion of the flat component, $\mathbf{K}_f = \begin{bmatrix} k_{nf} & 0 & 0 \\ 0 & k_m & 0 \\ 0 & 0 & k_m \end{bmatrix}$ and $\mathbf{U}_c$ denotes the flat surface stress free displacement.

The normal stiffness k_{nf} is taken as 10 times the k_n value used for the teeth. The final constitutive relationship then becomes:

$$\boldsymbol{\sigma} = P_f \mathbf{K}_f (\mathbf{U} - \mathbf{U}_{cf}) + \\ + \int_0^{m_{gmax}} \int_0^{h_{tmax}} p(m_g, h_t) c_f(U_r) \frac{\sqrt{1+m_g^2}}{m_g} \left(\frac{1}{2\pi} \int_{2\pi} \mathbf{N}^T(\alpha) \mathbf{t}_c(\alpha) d\alpha \right) dh_t dm_g \tag{4.24}$$

If the angular integral in Eq. (4.24) is evaluated numerically as a weighted summation and a discrete distribution is used for $p(m_g, h_t)$ with n_g discrete probabilities $P(m_{gi}, h_{ti})$, then $\boldsymbol{\sigma}$ is given by:

$$\boldsymbol{\sigma} = P_f \mathbf{K}_f (\mathbf{U} - \mathbf{U}_{cf}) + \sum_{i=1}^{n_g} \left[P(m_{g_i}, h_{t_i}) c_{fi} \frac{\sqrt{1+m_{g_i}^2}}{m_{g_i}} \sum_{j=1}^{n_p} \mathbf{N}(\alpha_j)^T \mathbf{t}_c(\alpha_j) \cdot \varpi_j \right] \tag{4.25}$$

where $P_f + \sum_{i=1}^{n_g} P(m_{gi}, h_{ti}) = 1$. $\mathbf{t_c}(\alpha)$=is obtained from Eq. (4.11) and ϖ_i is the weight for sample direction i, noting that here all weights are $1/n_p$, where n_p is number of evenly spaced sample positions around a circle.

4.3. Stress computation algorithm

The model has been implemented in a constitutive driver program which uses a Newton-Raphson solution to calculate the unknown stress and/or relative displacement components for a prescribed stress and/or relative displacement path.

A Cutting Plane plastic return algorithm (Simo and Hughes, 1998) has been adopted in the present work, which leads to a set of coupled equations for plastic multipliers of the crushing and sliding yield functions.

A trial value of $\mathbf{u}_g$ for iteration r is given by $\mathbf{u}_g^{tr} = \mathbf{u}_g^{r-1} + \Delta\mathbf{u} - \mathbf{u}_p^{r-1}$, where $\Delta\mathbf{u}$ is the change in total relative displacement from the last converged step. Defining a trial value of the yield function as $F^{tr} = F(\mathbf{u}_g{}^{tr})$ and assuming both surfaces are active, the plastic multipliers may be obtained:

$$\begin{aligned} F^{tr} - \frac{\partial F}{\partial \mathbf{u}_g}\delta\mathbf{u}_p &= F^{tr} - \frac{\partial F}{\partial \mathbf{u}_g}\mathbf{q}\delta\lambda = 0 \\ F_s^{tr} - \frac{\partial F_s}{\partial \mathbf{g}_e}\delta\mathbf{u}_p - \frac{\partial F_s}{\partial g_e}\delta\mathbf{u}_c &= F_s^{tr} - \frac{\partial F_s}{\partial \mathbf{g}_e}\mathbf{q}\delta\lambda - \frac{\partial F_s}{\partial \mathbf{g}_e}\mathbf{q}_s\delta\lambda_s = 0 \end{aligned} \tag{4.26a,b}$$

which may be written in matrix form, as follows:

$$\begin{pmatrix} \mathbf{p}^T\cdot\mathbf{q} & 0 \\ \mathbf{p}_s{}^T\cdot\mathbf{q} & \mathbf{p}_s{}^T\cdot\mathbf{q}_s \end{pmatrix}\cdot\begin{pmatrix} \delta\lambda \\ \delta\lambda_s \end{pmatrix} = \begin{pmatrix} F(\mathbf{u}_g^{tr}) \\ F_s(\mathbf{g}_e^{tr}) \end{pmatrix} \tag{4.27}$$

where $\mathbf{p} = \frac{\partial F}{\partial \mathbf{u}_g}$ and $\mathbf{p}_s = \frac{\partial F_s}{\partial \mathbf{g}_e}$, or more compactly as:

$$\boldsymbol{\Xi}\ \delta\boldsymbol{\lambda} = \mathbf{F}^{tr} \tag{4.28}$$

If one of the surfaces is inactive (i.e. F<0), the system in Eq. (4.27) reduces to one equation for the active yield surface. The algorithm for the stress recovery calculations is given in Table 4.1.

Table 4.1. Stress recovery algorithm

$\mathbf{U}^{(k)} = \mathbf{U}^{(k-1)} + \Delta\mathbf{U}$	Update relative-displacement from previous time step k-1
for i=1 to n_g	Loop over asperity geometric components (m_{gi},h_{ti})
for j = 1 to n_p	Loop over sample directions (α_j)
$\mathbf{u}_g^{(k)} = \mathbf{N}(\alpha_j)\cdot\mathbf{U}^{(k)} - \mathbf{u}_p$ $d\mathbf{u} = \mathbf{N}(\alpha_j)\cdot\Delta\mathbf{U}$	Evaluate $\mathbf{u}_g$ and d$\mathbf{u}$ for current step, component and direction
If $\Phi_{int}(\mathbf{u}_g^{(k)}, m_{gi}) \le 0$ & $\Phi_{int}(\mathbf{u}_g^{(k-1)}, m_{gi}) > 0$	First contact
$\mathbf{u}_c^{(k)} = \begin{bmatrix} \dfrac{du_\rho u_{g\xi}^{(k)} - du_\xi u_{g\rho}^{(k)}}{du_\rho - m_{gi} du_\xi} \\ \dfrac{du_\rho u_{g\xi}^{(k)} - du_\xi u_{g\rho}^{(k)}}{du_\rho - m_{gi} du_\xi} m_{gi} \end{bmatrix}$	Evaluate stress-free displacement at first contact
If $\Phi_{int}(\mathbf{u}_g^{(k)}, m_{gi}) \le 0$ and $U_r^{(k)} < h_{ti}$	Current direction in contact
$\mathbf{t}_c$ → ***Table 4.2.***	Evaluate contact traction $\mathbf{t}_c$
If $\Phi_{int}(\mathbf{u}_g^{(k)}, m_{gi}) > 0$ or $U_r^{(k)} > h_{ti}$; $\mathbf{t}_c = \mathbf{0}$	If no contact, traction is 0 for current direction
End direction and geometric loops	
Evaluate $\mathbf{U}_{cf}$ at first contact if applicable	
If $U_r < 0$	Flat component
$\boldsymbol{\sigma}_f$ → ***Table 4.3.***	Evaluate stress for flat component
Else; $\boldsymbol{\sigma}_f = 0$	If no contact, stress for flat component is 0
$\boldsymbol{\sigma} = \boldsymbol{\sigma}_f + \sum_{i=1}^{n_\xi}\left(P_i \cdot c_{fi} \cdot \sum_{j=1}^{n_p} \mathbf{N}(\alpha_j)^T \cdot \mathbf{t}_{cj} \right)$	Compute stress on crack plane(Eq. 4.25)

(k) denotes current time step and (k-1) previous time step

Table 4.2. Algorithm to evaluate contact traction

If $\Phi_{int}(\mathbf{u}_g^{(k)}, m_{gi}) \le 0$ and $U_r^{(k)} < h_{ti}$	If current direction in contact, evaluate contact traction
If $F(\mathbf{u}_g^{(k)}, \gamma_y) > 0$ or $F_s(\mathbf{u}_g^{(k)}, \mathbf{u}_c) > 0$	Check yield condition
Repeat until $\lvert\mathbf{F}\rvert <$ tol	Cutting plane loop
$\delta\boldsymbol{\lambda} = \boldsymbol{\Xi}^{-1} \cdot \mathbf{F}$	Evaluate plastic multiplier vector
$\mathbf{u}_p = \mathbf{u}_p + \delta\lambda \cdot \mathbf{q}$, $\mathbf{u}_g^{(k)} = \mathbf{u}_g^{(k)} - \delta\lambda \cdot \mathbf{q}$, $\mathbf{u}_c = \mathbf{u}_c + \delta\lambda_s \cdot \mathbf{q}_s$	Update $\mathbf{u}_g$ $\mathbf{u}_p$ $\mathbf{u}_c$
$\mathbf{t}_c = k_n \boldsymbol{\Phi}_d \mathbf{u}_g^{(k)} + k_m \left((\mathbf{I} - \boldsymbol{\Phi}_d) \mathbf{u}_g^{(k)} - \mathbf{u}_c \right)$	Evaluate contact traction for current direction (Eq. 4.11)

Table 4.3. Algorithm to evaluate stresses for flat component

If $U_r < 0$	If flat component in contact, evaluate stress
If $F_{sf}(\mathbf{U}, \mathbf{U}_{cf}) > 0$	Cutting plane algorithm for flat component
Repeat until $\lvert F_{sf}\rvert <$ tol	
$\delta\lambda_{sf} = \dfrac{F_{sf}}{\mathbf{p}_{sf}^{\,T} \cdot \mathbf{q}_{sf}}$	Evaluate plastic multiplier, $\mathbf{p}_{sf} = \dfrac{\partial F_{sf}}{\partial \mathbf{U}}$
$\mathbf{U}_{cf} = \mathbf{U}_{cf} + \delta\lambda_{sf} \cdot \mathbf{q}_{sf}$	Update stress-free displacement for flat component
$\boldsymbol{\sigma}_f = P_f \mathbf{K}_f \left(\mathbf{U} - \mathbf{U}_{cf} \right)$	Evaluate stress for flat component

4.4. Model parameters

The constitutive model proposed in this chapter requires the specification of two types of parameters: material properties (i.e. normal and shear interface stiffness k_n, k_m, friction angle φ and uniaxial compressive strength f_c) and geometrical contact parameters (asperity slopes m_g, asperity heights h_t and their relative proportions P).

The normal interface stiffness values can be obtained from the initial response slope of uniaxial compressive tests. It was found that, for the size of the specimens considered here, k_n and k_m are in the range E/150 to E/100 and G/150 to G/100

(MPa/mm) respectively, where E and G are the Young's and shear moduli respectively. The angle of friction is a readily measurable material parameter and for concrete, values between 20° and 60° have been reported (Birkeland and Birkeland, 1966; Jensen, 1975; Wong et al., 2007).

The crack surface geometry is most satisfactorily addressed by analyzing three-dimensional surfaces of actual cracks. Methods similar to those proposed by Boussa et al. (2001) and Haberfield and Johnston (1994) can be employed to obtain asperity angles, heights and their relative proportions.

4.5. Numerical results

A number of examples illustrating the performance of the constitutive model are presented in this section. In examples 1-3, numerical simulations are compared with experimental data from direct shear tests on concrete and rock joint replica specimens.

The material properties for each example are given in Table 4 and the contact parameters that characterize the crack surface are given in Figs. 4.4, 4.7 and 4.12, noting that the relative proportion assigned for the flat component is 0.1.

Table 4.4. Material properties

Parameter	Example 1	Example 2	Example 3
k_n (MPa/mm)	95	310	350
k_m (MPa/mm)	40	130	145
φ (°)	35	40	35
f_c (MPa)	42	75	37.6

For all three examples, discrete distributions $P(m_g, h_t)$ are used. Two groups of asperities are considered to represent the primary and secondary asperities (Plesha, 1987; Yang et al., 2010) which are denoted h_{t_p} and h_{t_s} respectively. Generally, the primary roughness is described by asperities with relatively larger heights and smaller inclinations whereas the secondary roughness is characterized by shorter and sharper asperities (Patton, 1966; Barton, 1973; Plesha, 1987; Yang et al. 2010). This is also

observed in a qualitative examination of several crack profiles (Gentier et al., 2000; Grasselli and Egger, 2003).

The quantification method of Haberfield and Johnston (1994), in which the crack profile is idealised as a series of straight lines of variable lengths and inclinations, is employed for extracting the asperity angles, heights and their relative proportions in the examples for which crack profiles are available (i.e. Examples 1 and 2). This does require a degree of judgement and it is emphasised that it is possible to obtain a range of surface characterisations using this method.

For the application of the model in a finite element code to the simulation of a specific material, for which detailed crack morphology data may not be available, the crack profile data could be extracted from generic statistical distributions. For example, Boussa et al. (2001) provides such a characterisation for concrete surfaces and Lee et al. (2001) for crack surfaces in granite and marble.

4.5.1. Example 1. Data from Grasselli and Egger (2003)

In this example, numerical simulations of direct shear tests carried out at various levels of constant compressive normal stress are presented and compared with the experimental data reported by Grasselli and Egger (2003). In the experimental tests, concrete replicas of tensile rock joints, having a shear plane of 140x140 mm^2, were subjected to shear displacements of 3mm under different values of constant normal stress: 1.275, 2.55, 5.1 and 6.12 MPa.

Three profiles of the crack surface extracted from the same sample are given in the paper, from which the crack surface roughness parameters, given in Fig. 4.4, were extracted in the manner described above.

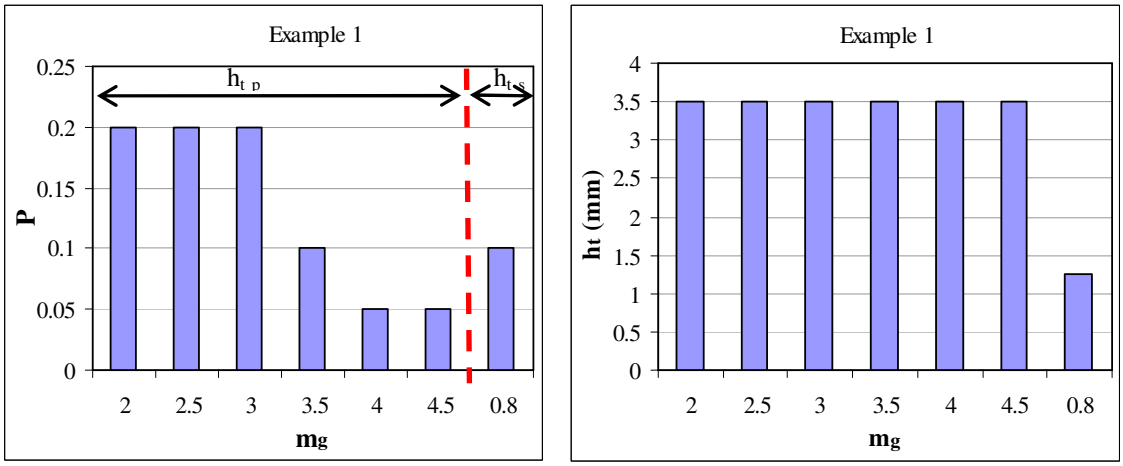

Figure 4.4. Example 1. Geometrical components

The predictions of shear stresses are compared with experimental results in Fig. 4.5. As no experimental data regarding the dilation was provided, no comparison could be made in this case. However, the numerical response is given in Fig 4.6. and it can be noted that the dilation, or normal separation, reduces for higher levels of compressive stresses which is in agreement with other experimental observations (Gentier et al., 2000; Huang et al., 2002)

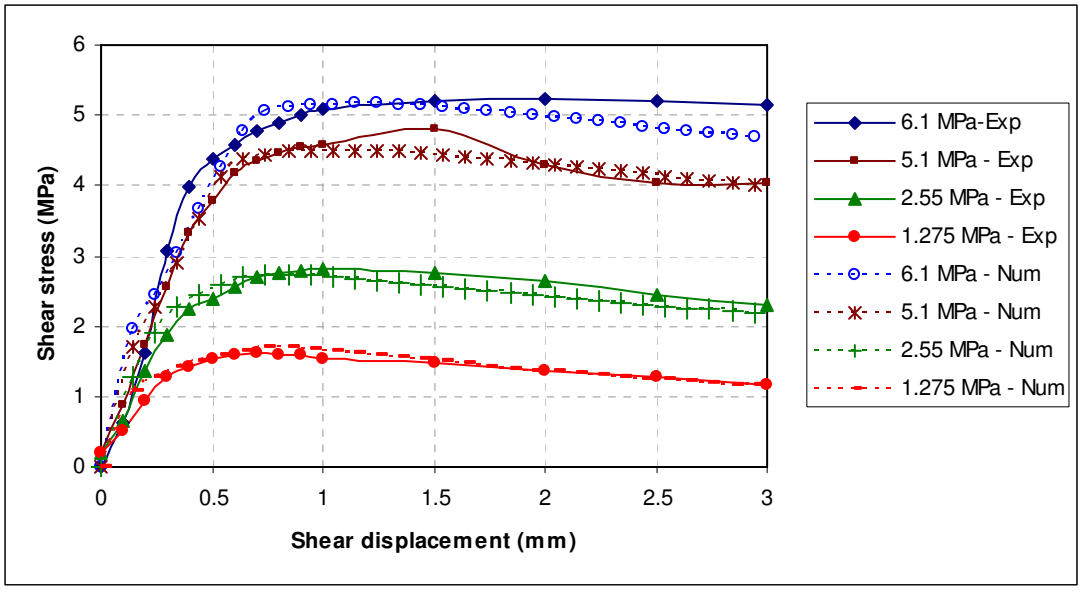

Figure 4.5. Example 1. Shear stress-displacement response

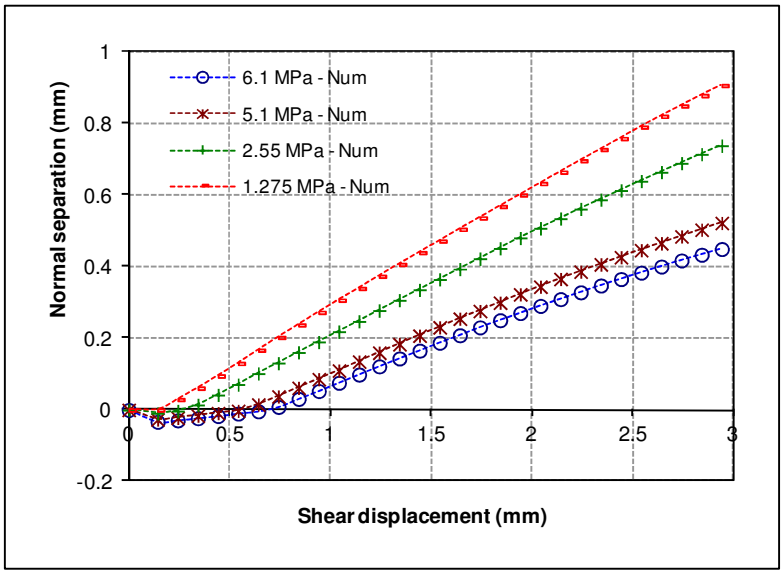

Figure 4.6. Example 1. Numerical prediction of dilation

4.5.2. Example 2. Data from Gentier et al. (2000)

The experimental tests considered in this example were carried out on a set of mortar replicas of a granite sample, each of which had the same surface topography. The circular shear plane was 90 mm in diameter and the shear tests were performed under constant levels of compressive normal stresses of 7, 14 and 21 MPa. Four tests were carried out for each level of normal stress for four different shear directions on the fracture plane.

Schematic two and three-dimensional profiles of the crack surface are provided in Gentier et al. (2000), however additional information is needed in order to quantify them completely. Nevertheless, it did prove possible to make qualitative observations from the data given, from which the geometrical parameters used for the numerical simulation given in Fig. 4.7 were obtained.

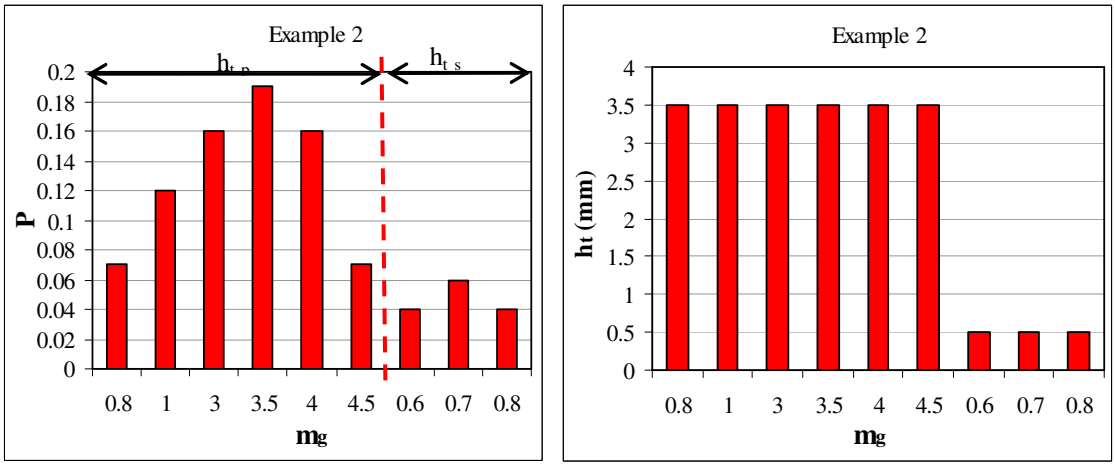

Figure 4.7. Example 2. Geometrical components

The comparison between numerical predictions of shear stresses and the experimental results is shown in Figs. 4.8-10. A comparison for dilation is also performed. The numerical responses generally compare well with the experimental data.

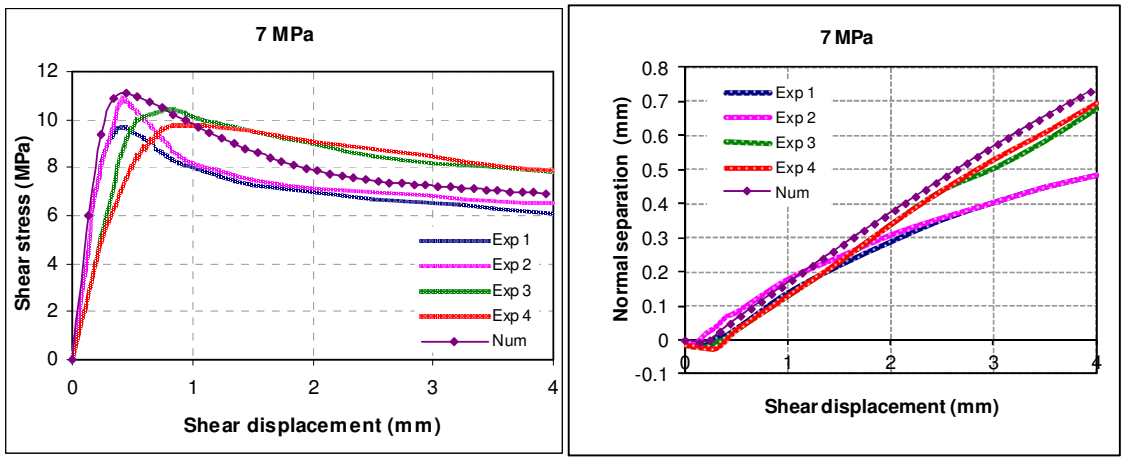

Figure 4.8. Example 2. Shear stress and dilation response under constant normal compression of 7 MPa

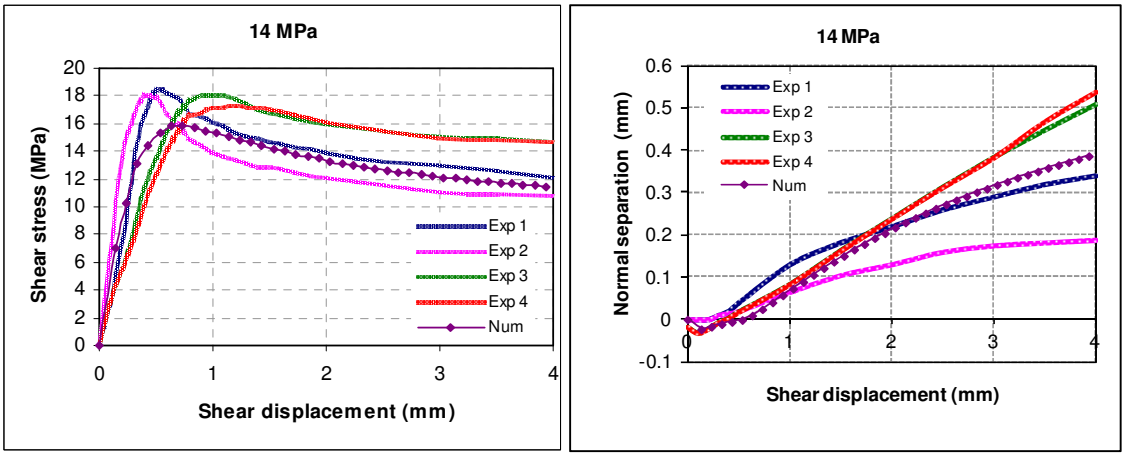

Figure 4.9. Example 2. Shear stress and dilation response under constant normal compression of 14 MPa

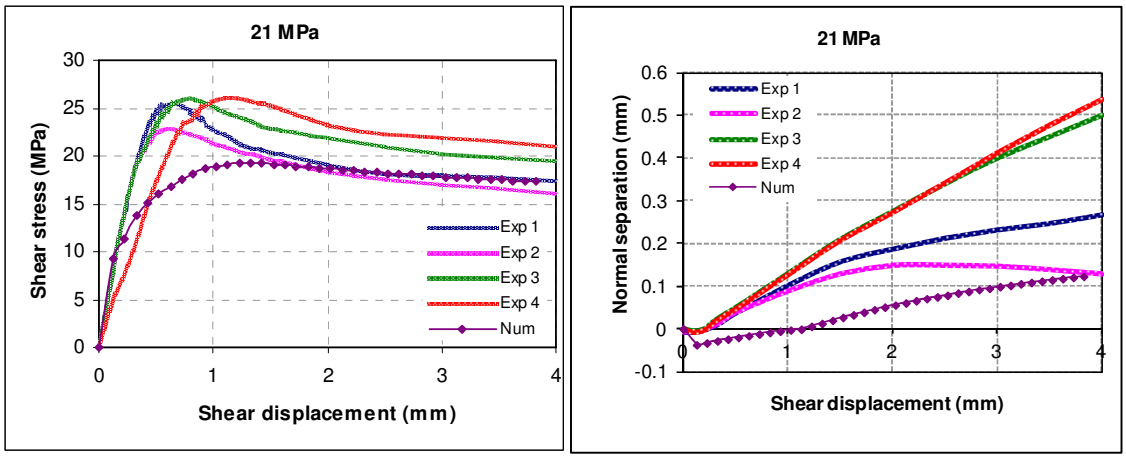

Figure 4.10. Example 2. Shear stress and dilation response under constant normal compression of 21 MPa

4.5.3. Example 3. Data from Walraven and Reinhardt (1981)

The data used for the third example is taken from a series of experiments carried out by Walraven and Reinhardt (1981). Concrete specimens with a shear plane of 300x120 mm^2 were initially pre-cracked in tension and then loaded in shear in a stiff testing frame with external restraint bars to control the opening displacement and on which the normal stress acting on the crack plane could be directly measured. Three different values of initial opening displacement –0.0, 0.2 and 0.4 mm- were applied to the specimens, which were then subjected to shear displacements of up to 2 mm for different restraint stiffness. Walraven and Reinhardt identified each test by the code α/β/γ where α denotes the mix number, β the initial crack opening in mm and γ the normal stress in MPa at an arbitrary crack width of 0.6 mm. Tests 1/0.2/0.4 and

1/0.4/0.3 are considered here. The normal – shear displacement paths, from the experiments which are used in the numerical predictions, are given in Fig. 4.11.

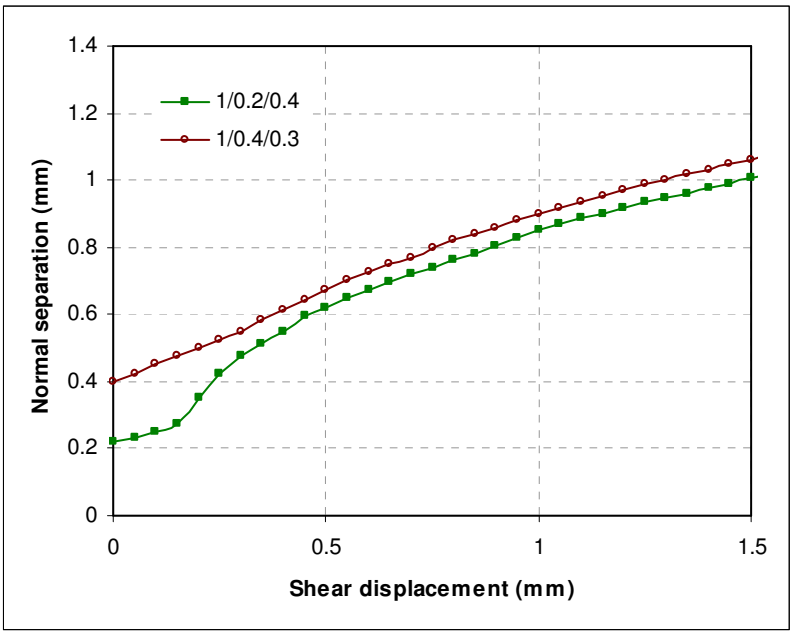

Figure 4.11. Example 3. Normal-shear displacement path

No details are given of the crack surface morphology, however, a reasonable fit of the experimental data is obtained with the geometrical parameters in Fig. 4.12. Numerical predictions of the shear and normal stresses are compared with the experimental results in Figs. 4.13, 4.14.

It may be seen from the experimental normal response, for the case with initial opening of 0.2 that the experimental data shows some normal stress at this initial crack opening value. For a fully formed crack, the normal stress would be expected to be zero until any shear is applied, and this is the case with the numerical response.

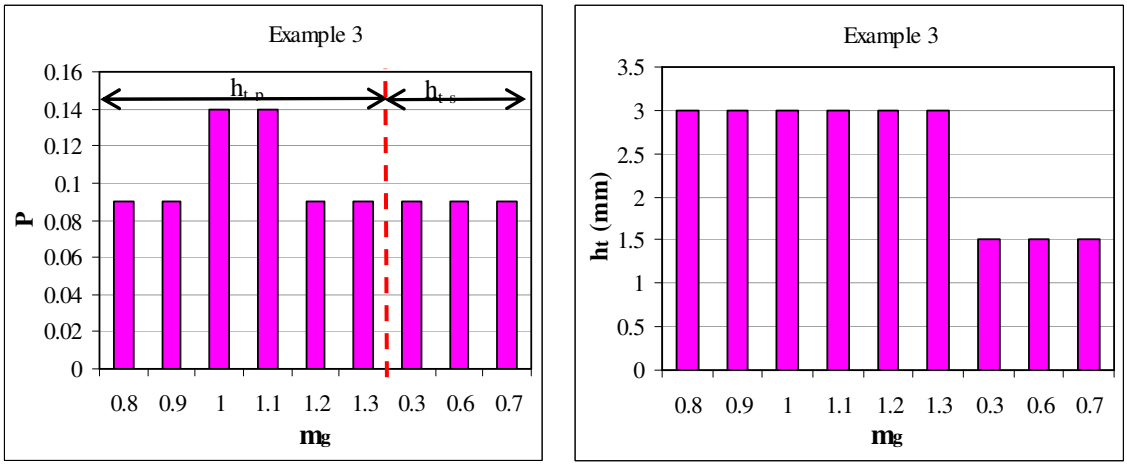

Figure 4.12. Example 3. Geometrical components

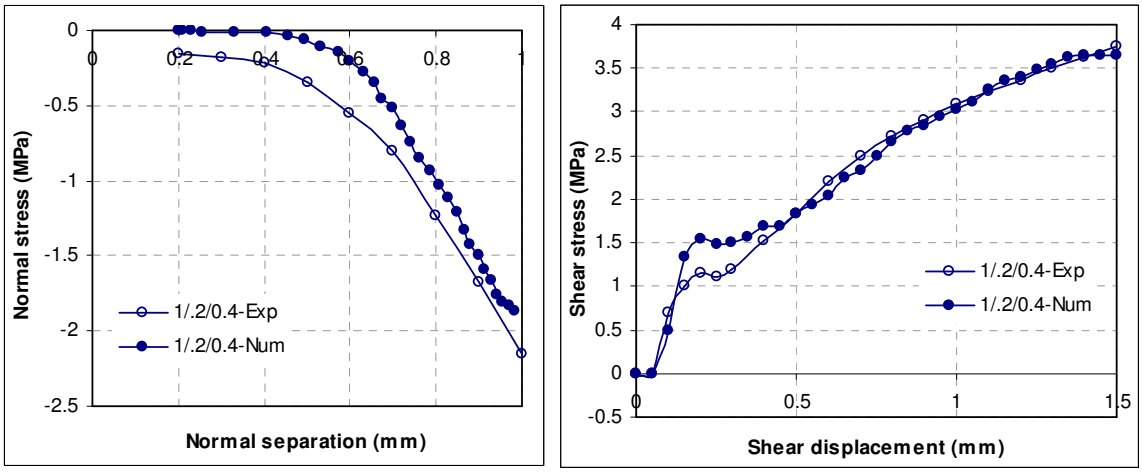

Figure 4.13. Example 3. Normal and shear stress prediction; initial opening 0.2mm

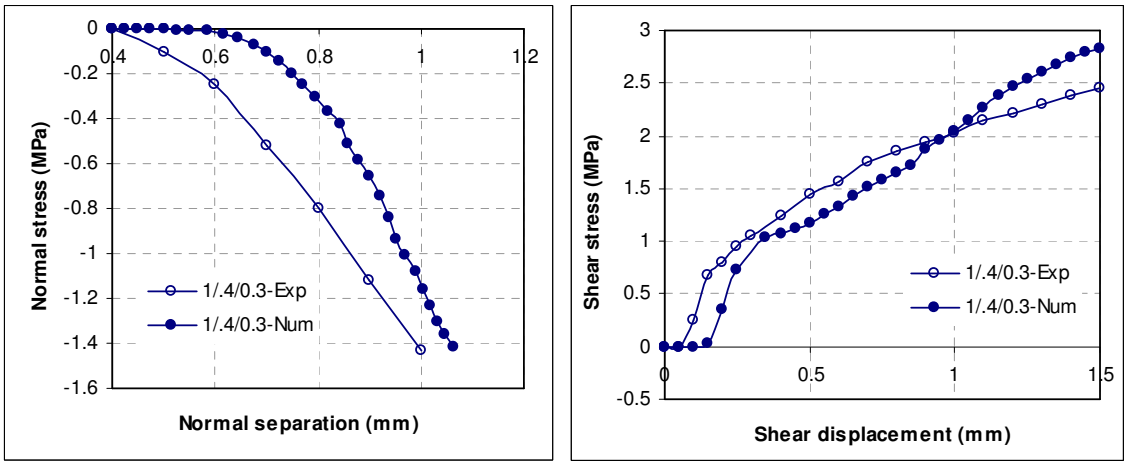

Figure 4.14. Example 3. Normal and shear stress prediction; initial opening 0.4mm

4.5.4. Example 4. Illustrative examples

Finally a set of illustrative examples is carried out employing the model parameters from Walraven and Reinhardt's simulations to illustrate certain features of the model, not present in the above examples. In Example 4a numerical simulations of shear tests under constant crack opening are performed for two different openings 0.2 and 0.4 mm. The shear and normal stress predictions are presented in Fig 4.15. It can be observed that for larger crack openings the stress levels are reduced. This example clearly illustrates the influence of the effective contact function.

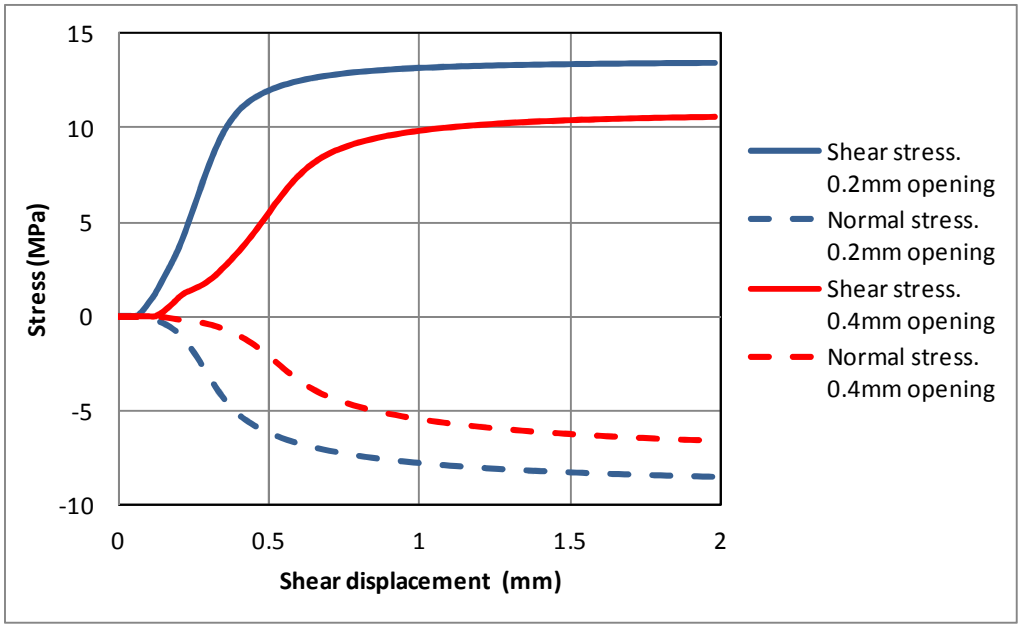

Figure 4.15. Example 4. Normal and shear stress prediction for two different constant openings

In Example 4b, simulations of cyclic shear tests under constant normal compressive stress are performed for two different levels of compressive stress -5 and 10 MPa- and the behaviour under loading and unloading conditions is explored. The shear stress histories and the predicted dilatancy are shown in Fig. 4.16 and 4.17 respectively.

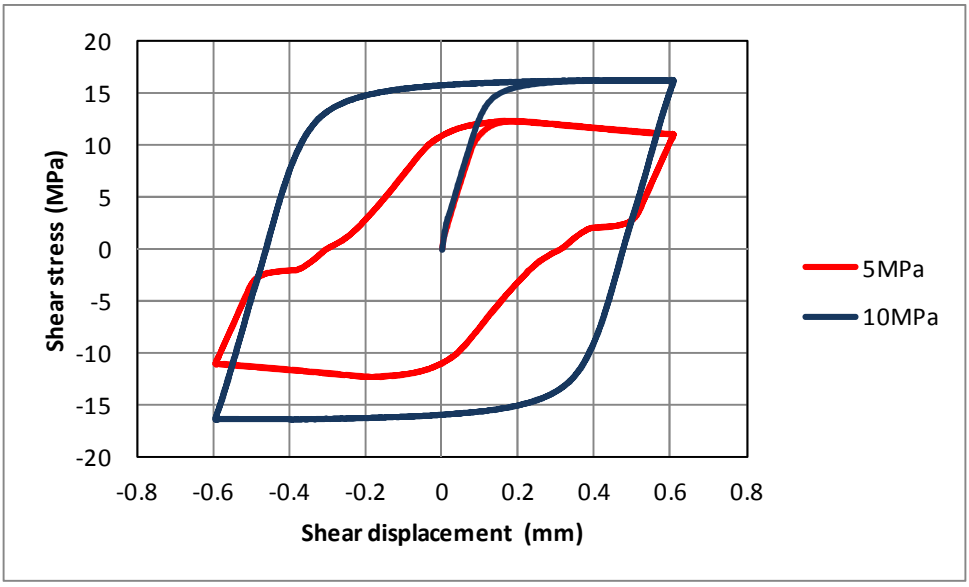

Figure 4.16. Example 4. Shear stress prediction for loading-unloading-reloading cyclic test under constant normal compression

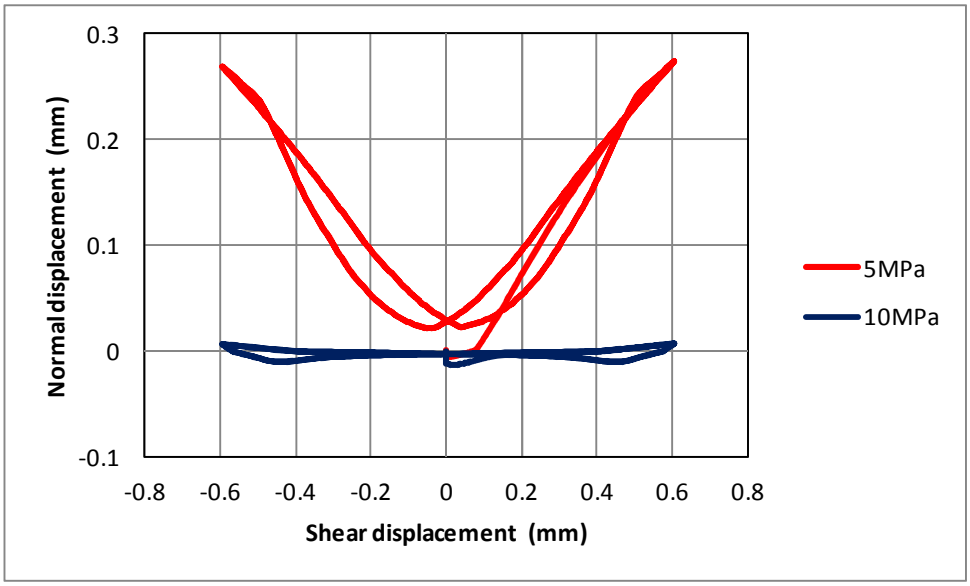

Figure 4.17. Example 4. Prediction of dilatancy for loading-unloading-reloading cyclic test under constant normal compression

It can be noted in the loading stage that the higher the level of compression the higher the predicted shear stresses. For the case of lower compression (5MPa) a reduction in the overall shear stiffness is observed in the unloading stage (section C-D). This occurs due to a delay between gradual unloading of one side and the gradual loading of the opposite side. Increasing the level of normal compression results in a 'lock-in' effect on the asperities, therefore all sample positions are in contact, with the

loading on one side being more advanced than on the opposite side. In this situation the transfer of stresses form one side to the other occurs with no noticeable delay.

4.6. Concluding remarks

A mechanistic constitutive model for simulating the behaviour of fully formed cracks in geomaterials has been proposed. The mechanisms of plastic embedment and frictional sliding between asperities, as well as a three-dimensional multi-asperity characterization of the crack morphology based on simple geometric parameters, were employed in order to predict the contact stresses. An effective contact function was derived and used in relating the contact stresses -that develop on the sides of the asperity teeth- to the stresses on the crack plane.

The proposed model requires a limited number of measurable input parameters. These comprise geometric parameters that describe the roughness of the crack surface (asperity heights, inclinations and their relative proportions) and material properties (compressive strength, friction angle, shear and normal stiffnesses)

Comparisons between numerical and experimental responses show good agreement, with the model being able to simulate key characteristics of observed behaviour, namely:

- shear displacement (slip) at constant normal compressive stress causes dilation
- an increase in the normal compression produces, for the same slip, a higher level of shear stress transferred across the crack plane and reduced dilation
- an increase of the crack opening reduces both normal compressive stress and the shear stress (in displacement-controlled tests)
- non-linear coupled shear and normal responses

Chapter 5

Miscellaneous computational aspects

The present chapter concentrates on several computational issues associated with the constitutive model presented in Chapters 2 and 3. In Section 5.1 the stability of the micromechanical constitutive model with embedded rough contact is considered. Spurious contact chatter behaviour at the constitutive level is reported and a solution proposed which makes use of a single smooth contact state function to replace three discrete existing contact state functions. In section 5.2, a study on the accuracy of the numerical integration methods is carried out for 2D and 3D rules. Finally, the tangent form of the stiffness tensor for the micromechanical model is derived in section 5.3.

5.1. Contact chatter

An aspect of the behaviour of constitutive models for cementitious materials which, in the author's opinion, has not received enough attention in the literature is the numerical difficulties which arise when crack closure and rough crack behaviour is introduced into constitutive models for concrete. It is this issue which is the primary subject of the present chapter. The work is in the context of a micromechanical model for concrete (and other cement-bound materials) but the relationships derived and the conclusions drawn would apply to a rough crack-plane model applied at any scale.

As mentioned in the introduction of Chapter 2 a number of models have been developed in recent years which use micromechanical solutions. These include the

micromechanical model of Penseé et al. (2002, 2003), which incorporated crack closure effects and an energy-based damage criterion; an anisotropic friction-damage model based on the solution of an elastic body containing plane cracks by Gambarotta (2004); and models with both microcrack closure and frictional sliding by Zhu et al. (2008 and 2011). These models do include crack closures effects but do not address contact issues associated with rough crack closure or related numerical difficulties.

It is recalled from Chapters 2 and 3 that the micromechanics based constitutive model, which builds on that proposed by Jefferson and Bennett (2007, 2010), comprises a two phase composite formulation based on the classical Eshelby theory and Mori-Tanaka averaging scheme, a multi-asperity rough microcrack contact component and a micro-damage evolution expression based on an exterior point Eshelby solution. The proposed exterior point Eshelby based microcrack initiation criterion along with the multi-component rough crack contact sub-model facilitated the use of realistic material properties in simulating properly cross-cracking behaviour. This model includes the embedded rough crack component that also plays an important role in capturing dilatant post-peak behaviour in compression but the author has found form the experience of its use that even at the constitutive level when multiple microcrack planes are active, stability problems can arise. It is these problems that gave rise to the study reported here.

Rough crack models have been explored in the past, particularly for discrete crack-plane models, with the emphasis of most of the work being on reproducing experimentally observed behaviour. As presented in Chapter 4 these models use, to varying degrees, combinations of empirically based relationships and mechanistic models to describe the morphology of the crack surfaces and the contact expressions which govern the stress-displacement relationships (Patton, 1966; Bažant and Gambarova, 1980; Walraven and Reinhardt, 1981; Divakar et al., 1987; Plesha, 1987; Li et al., 1989; Bujadham and Maekawa, 1992; Haberfield and Johnston, 1994; Ali and White, 1999; Jefferson, 2002; Wang et al., 2003). A particular exception, with respect to the evaluation of the numerical performance of these models, was the work of Feenstra el al. (1991 a, b) who explored computational aspects of several crack-plane models when applied to interface elements in a finite element code.

The simulation of contact with implicit finite element codes presents considerable numerical challenges and the investigation of these problems is an area of active research (e.g. Wriggers, 2006). Not-surprisingly, certain problems -which occur in macro-contact- also appear when contact is embedded in a constitutive model. These problems will be identified and further discussed in this section.

The aim of the work presented here is to develop a solution to the contact difficulties, at the constitutive level, for the present micromechanical contact model. An additional new development, namely the application of a Gamma probability distribution to describe the morphology of the microcrack surface is also included. Although extraneous in the context of the present chapter, this alternative characterisation of the crack surface roughness was employed in the study of rough contact related numerical instabilities and therefore it is presented here.

5.1.1. Crack morphology description

In numerical simulations presented in Chapter 3 a set of discrete values were used for the crack surface based upon observations of crack roughness at various scales. An attempt was made to characterize the roughness of the microcrack surface by statistical distributions. It was mentioned in Chapter 4 that a number of methods have been proposed (e.g. Haberfield and Johnston, 1994; Boussa et al., 2001) in order to quantify the crack surface morphology and to characterize it by probability density functions. The advantage of such an approach is appealing; the roughness is described by a reduced number of parameters. Nevertheless, substantial experimental data are required for a complete validation and whilst profiles of macro-cracks correlated with experimental results for crack-plane behaviour are scarce, information related to microcrack roughness is almost non-existent.

For the numerical study presented in this section the roughness of the crack surface is represented by a Gamma probability density function (Eqs. 5.1 a,b) applied to two distinct height ranges associated with normalised asperity height values β ($\beta = h_t/u_0$) of 1 and 0.1 which was found to be generally consistent with the experimental data of Boussa et al. (2001). Whilst it is recognised that the data of Boussa et al. (2001) is from a macroscopic crack, it has been assumed that the distribution of the lower height asperities is generally applicable to the present model. However, due to the lack of

comprehensive data on microcrack morphology, the Gamma distribution is proposed tentatively.

The statistical distribution, given in Eq. (5.1 a,b) and Fig. 5.1 is applied as a summation of 5 components for $\beta = 1$ and 3 components for $\beta = 0.1$. It is noted that for $m_g > 3$ the surface of the crack is assumed to be flat.

$$p(t_g) = \frac{1}{\beta_g^{\alpha_g} \cdot \Gamma(\alpha_g)} t_g^{\alpha_g - 1} \cdot e^{-\frac{t_g}{\beta_g}}$$
$$\Gamma(\alpha_g) = \int_0^\infty x^{\alpha_g - 1} \cdot e^{-x} \cdot dx \qquad (5.1a,b)$$

where $t_g = m_g^{-1}$ and $\alpha_g = 0.25$ and $\beta_g = 6$.

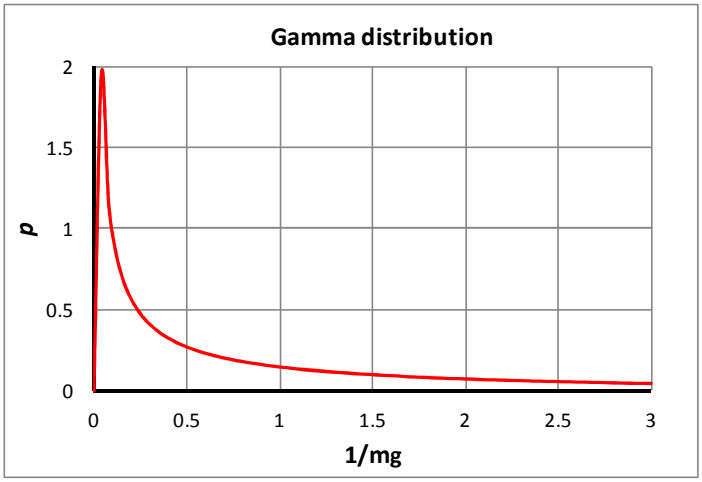

Figure. 5.1. Gamma distribution. $\alpha_g = 0.25$ and $\beta_g = 6$

It is mentioned that the Gamma distribution adopted here gives a relatively high proportion (approximately 25%) of very sharp contact angles (> 65°, i.e. $m_g < 0.45$). Qualitative observations of macro-crack profiles suggest that this is somewhat unrealistic, however reasonable uniaxial tension and uniaxial compression responses are predicted. Indeed, the use of statistical (continuous) distributions or discrete distributions with a lower proportion of sharp contact angles was found to predict rather weak compressive responses. The apparent necessity for sharper contact angles in the micromechanical constitutive model is believed to be due to the fact that friction effects on the side of the asperities are ignored; the use of sharper asperities artificially emulates the friction effects. In fact it can be noticed that in the rough crack plane

model proposed in Chapter 4 in which friction is taken into account the proportion of sharp asperities is considerably lower.

5.1.2. Continuous contact state function

5.1.2.1. Contact chatter

It is well known that contact problems in implicit finite element simulations present considerable numerical challenges (Wriggers, 2006). One such challenge is that models can predict a spurious oscillatory response, which has been termed 'jamming' or 'chatter' (Wriggers, 2006). The present model can, under certain conditions, exhibit this type of behaviour- even in single point stress-strain simulations- when different contact conditions are active on different microcrack planes. This is illustrated for a uniaxial compression path in Fig. 5.2. This solution was obtained with a standard Newton algorithm, although exactly the same response arises with a solution which uses a secant Newton approach. It is recognised that such behaviour can be improved by use of line search algorithms (Crisfield, 1997) but these do not always resolve such difficulties in finite element simulations. Thus, it was decided to remove the discrete separate contact conditions and to develop a single smooth expression which encompassed all three contact states in order to minimise the potential for chatter behaviour at the constitutive level. In doing this two questions were considered;

1. Is smoothed behaviour entirely artificial?
2. Can functions be developed which do not significantly alter apparent macroscopic properties such as the macroscopic tensile and compressive strengths?

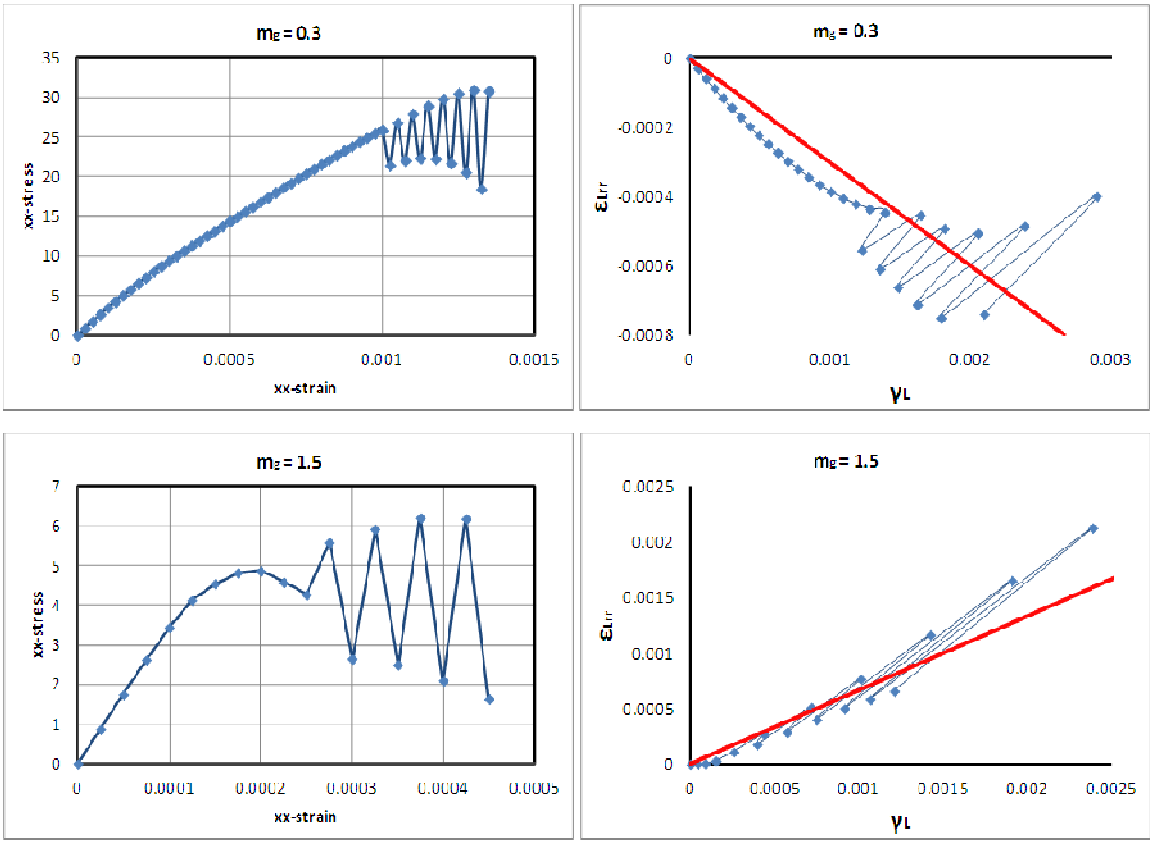

Figure. 5.2. Examples of rough contact related chatter

5.1.2.2. Smoothed contact state function

In order to answer question 1 above, the response from the cyclic test of Reinhardt (1984) is shown in Fig. 5.3. This indicates a smooth crack closure response, although it also shows a hysteresis behaviour which is not included in the present model.

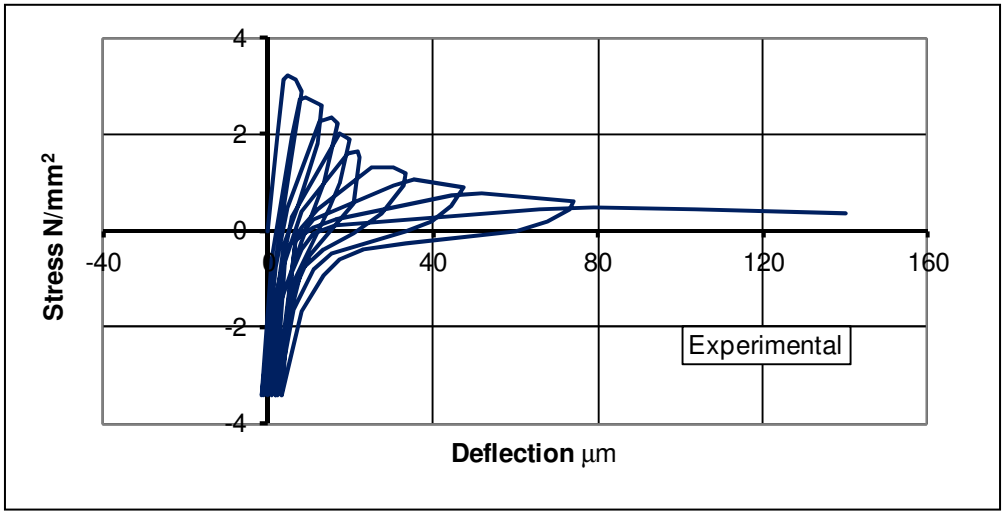

Figure. 5.3. Experimental data of Reinhardt from a cyclic compressive test

Regarding the second question posed above, there is a balance between providing a sufficient degree of smoothing to achieve a stable response and unrealistically altering the computed stress paths which will be explored in the simulations below.

A compound function was therefore sought which allowed both the transition zone between the contact states to be varied and the rate of change of local stress, with respect to a monotonic changing local strain, controlled. The following smoothed contact state function satisfies these criteria and is proposed to replace the separate contact relationships given in Table 2.1.

$$\mathbf{\Phi}(\boldsymbol{\varepsilon}_{\mathrm{L}}, m_g) = \lambda_{\mathrm{cl}}(\boldsymbol{\varepsilon}_{\mathrm{L}}, m_g) \cdot \mathbf{I}^{2s} + \left[1 - \lambda_{\mathrm{cl}}(\boldsymbol{\varepsilon}_{\mathrm{L}}, m_g)\right] \cdot \lambda_{\mathrm{int}}(\boldsymbol{\varepsilon}_{\mathrm{L}}, m_g) \cdot \mathbf{\Phi}_{\mathrm{g}}(\boldsymbol{\varepsilon}_{\mathrm{L}}, m_g) \qquad (5.2)$$

in which the interpolation functions $\lambda_*(\boldsymbol{\varepsilon}_{\mathrm{L}}, m_g), * = \text{'int'} \ \ or \ \ \text{'cl'}$, are essentially modified tanh type functions given by:

$$\lambda_*(\boldsymbol{\varepsilon}_{\mathrm{L}}, m_g) = \frac{e^{(c/2)\cdot\chi_*(\boldsymbol{\varepsilon}_{\mathrm{L}}, m_g)}}{e^{(c/2)\cdot\chi_*(\boldsymbol{\varepsilon}_{\mathrm{L}}, m_g)} + c_\lambda} \qquad (5.3a,b)$$

where $\chi_*(\boldsymbol{\varepsilon}_{\mathrm{L}}, m_g)$ is a normalized signed distance function in local strain space that essentially provides a transition band around the closed and interlock surfaces:

$$\chi_*(\boldsymbol{\varepsilon}_{\mathrm{L}}, m_g) = \frac{1}{a \cdot \varepsilon_{\mathrm{tm}}} \cdot \frac{\phi_*(\boldsymbol{\varepsilon}_{\mathrm{L}}, m_g)}{\left| \dfrac{\partial \phi_*(\boldsymbol{\varepsilon}_{\mathrm{L}}, m_g)}{\partial \boldsymbol{\varepsilon}_{\mathrm{L}}} \right|} \qquad (5.4)$$

where *a, c,* and c_λ are dimensionless parameters that control the shape of the interpolation function λ_* (Fig. 5.4) . It follows directly from Eq. (5.4) that parameter *a* governs the "width" of the transition band around the closed and interlock separating surfaces. Parameter *c* controls the slope of the interpolation function, i.e. the abruptness of the transition between the two contact states (Fig. 5.4a). Finally, parameter c_λ effectively defines the position of the transition band relative to the relevant contact state surface (Fig. 5.4b).

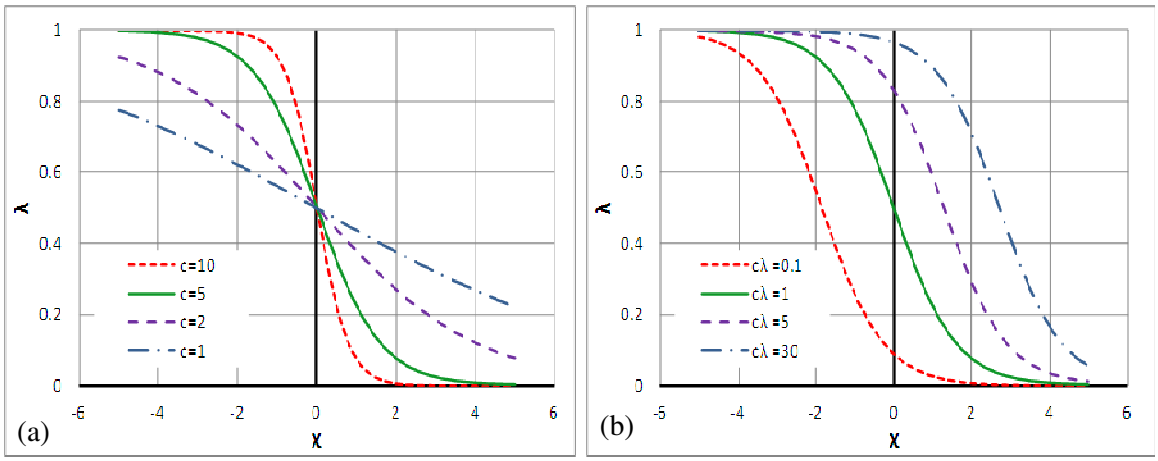

Figure. 5.4. Variation of the interpolation function with smoothing parameters: (a) c and (b) c_λ

5.1.2.3. Parametric study for a single crack-plane

A study is now presented which shows the effects of varying the function parameters a, c and c_λ on the predicted response for a single crack-plane, and which has the overall purpose of guiding the final selection of the values of these parameters.

The study is carried out on a local crack-plane on which the strain path in Figs. 5.5 and 5.6 is prescribed. This path opens a crack under normal strain until the damage parameter $\omega = 0.975$ (phase OA) then applies a shear which results in the build up of normal and shear stresses (phase AB) and finally the path closes the crack (phase BC). Phase OA gives information on the transition between closed and open regions (C-O), phase AB on the open-interlock transition (O-I) and interlock-closed state transition (I-C) is highlighted during phase BC.

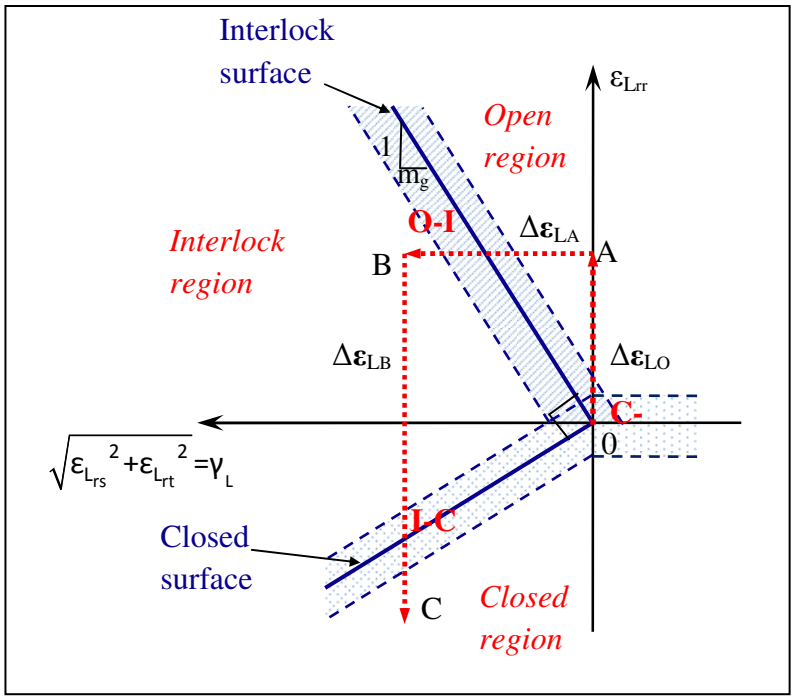

Figure. 5.5. Contact states, transition regions and prescribed strain path

The numerical predictions of the local stress with both smoothed and unsmoothed contact functions are compared. The simulations are carried out (i) with a single component contact sub-model for a range of contact slopes (m_g) between 0.3 and 1.5 and (ii) with a multi-component contact sub-model which uses the Gamma distribution (Eq. 5.1) to define the proportions and slopes of the contact surface.

Three cases are considered in the parametric study as follows:

- Case 1. Parameter a varies, c = 5 and c_λ = 1 fixed.
- Case 2. Parameter c varies, a = 10 and c_λ = 1 fixed
- Case 3. Parameter c_λ varies, a = 10 and c = 5 fixed.

As discussed above, there is a balance between providing a sufficient degree of smoothing to achieve a stable response and unrealistically altering the computed stresses. A particularly undesirable result would be a spurious increase in the apparent tensile strength. This is avoided by using a modified tensile strength parameter as follows

$$f_{t\_mod}=\frac{f_t}{1+\eta_s} \tag{5.5}$$

For a single crack-plane in direct tension, the value of the relative error η_s can readily be calculated by considering the stationary value of the tensile stress with respect to the normal tensile strain. However, when the relationship is used for a microcrack plane in the multi-dimensional model, the solution becomes analytically intractable and thus numerical experimentation was used to determine a final value for η_s for the 2D and 3D models.

Numerical predictions of local normal and shear stress for Cases 1, 2 and 3 respectively are presented in Figs. 5.7-5.9. The stress components are plotted against a monotonically increasing variable, pseudo-time, where 1s = 1 increment of strain change. The variation of the prescribed local strain components with pseudo-time t is schematically illustrated in Fig. 5.6. For all numerical simulations the material properties in Table 5.1 are employed.

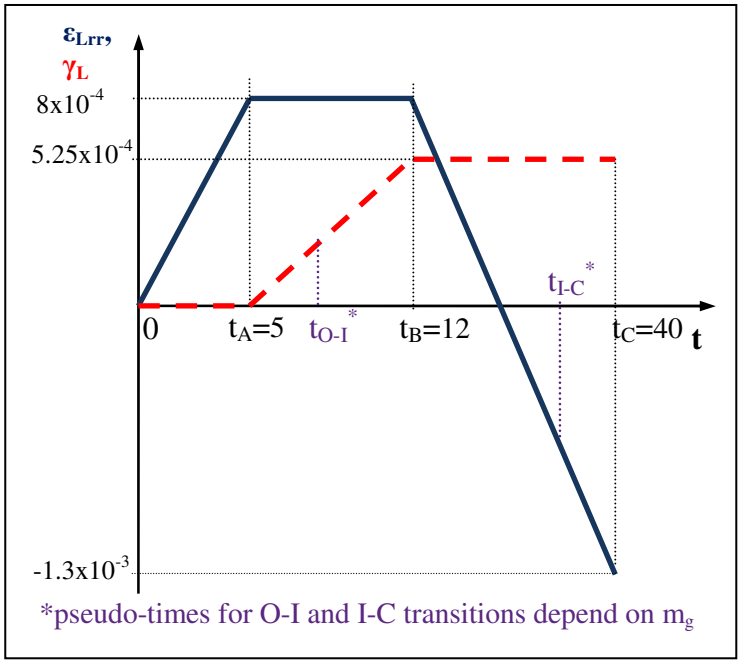

Figure. 5.6. Variation of prescribed strains with pseudo-time

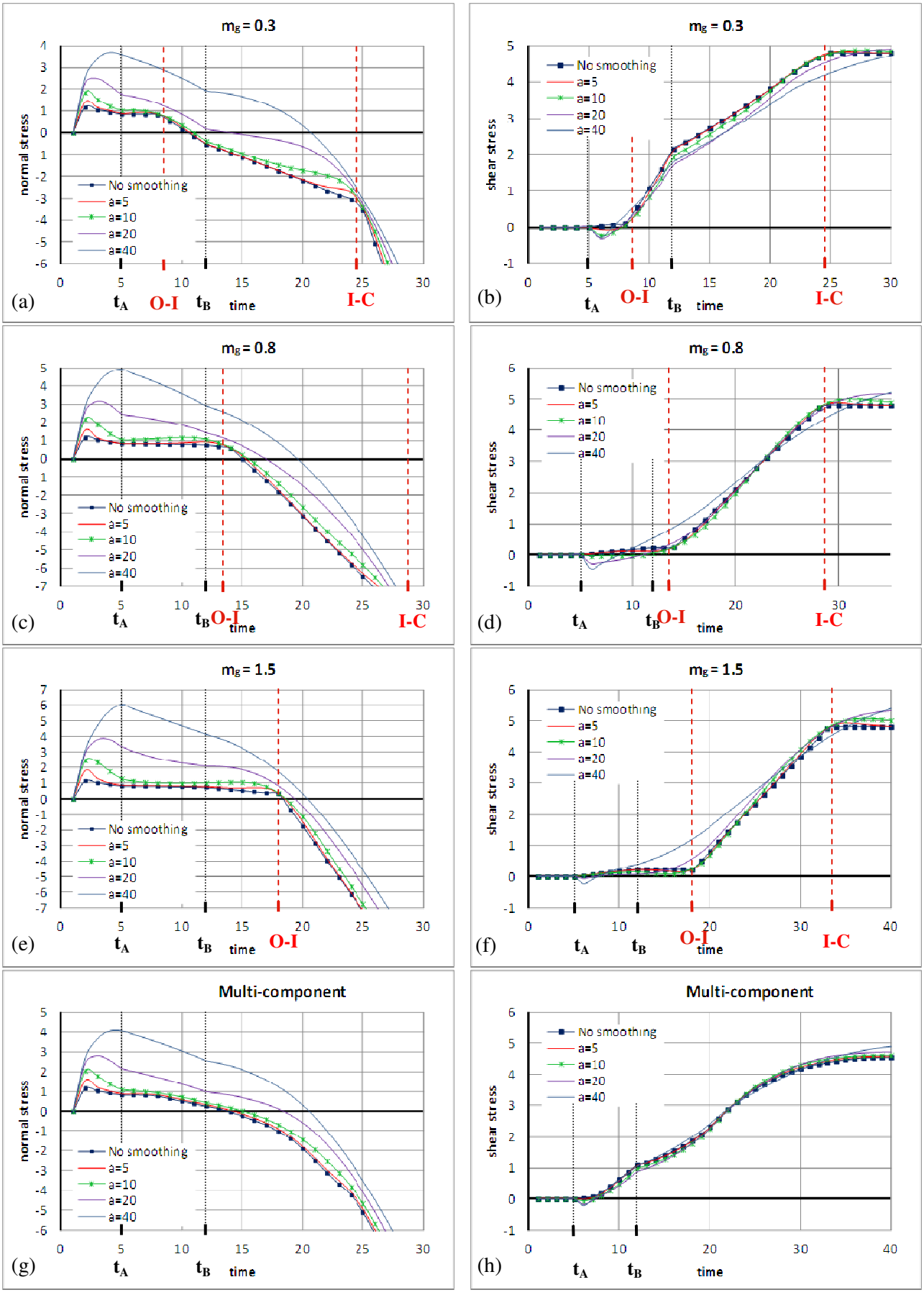

Figure 5.7. Parametric study. Case 1

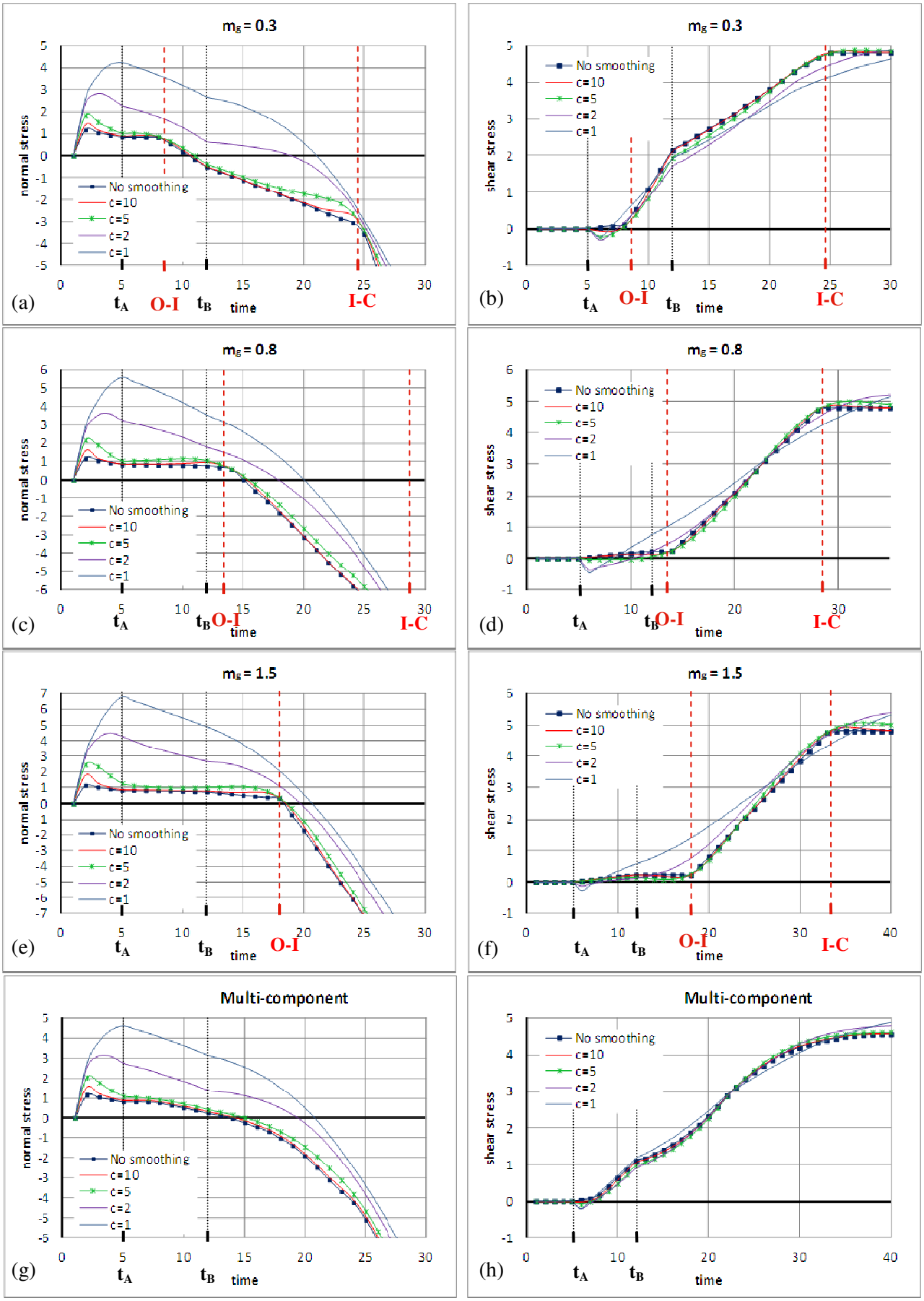

Figure. 5.8. Parametric study. Case 2

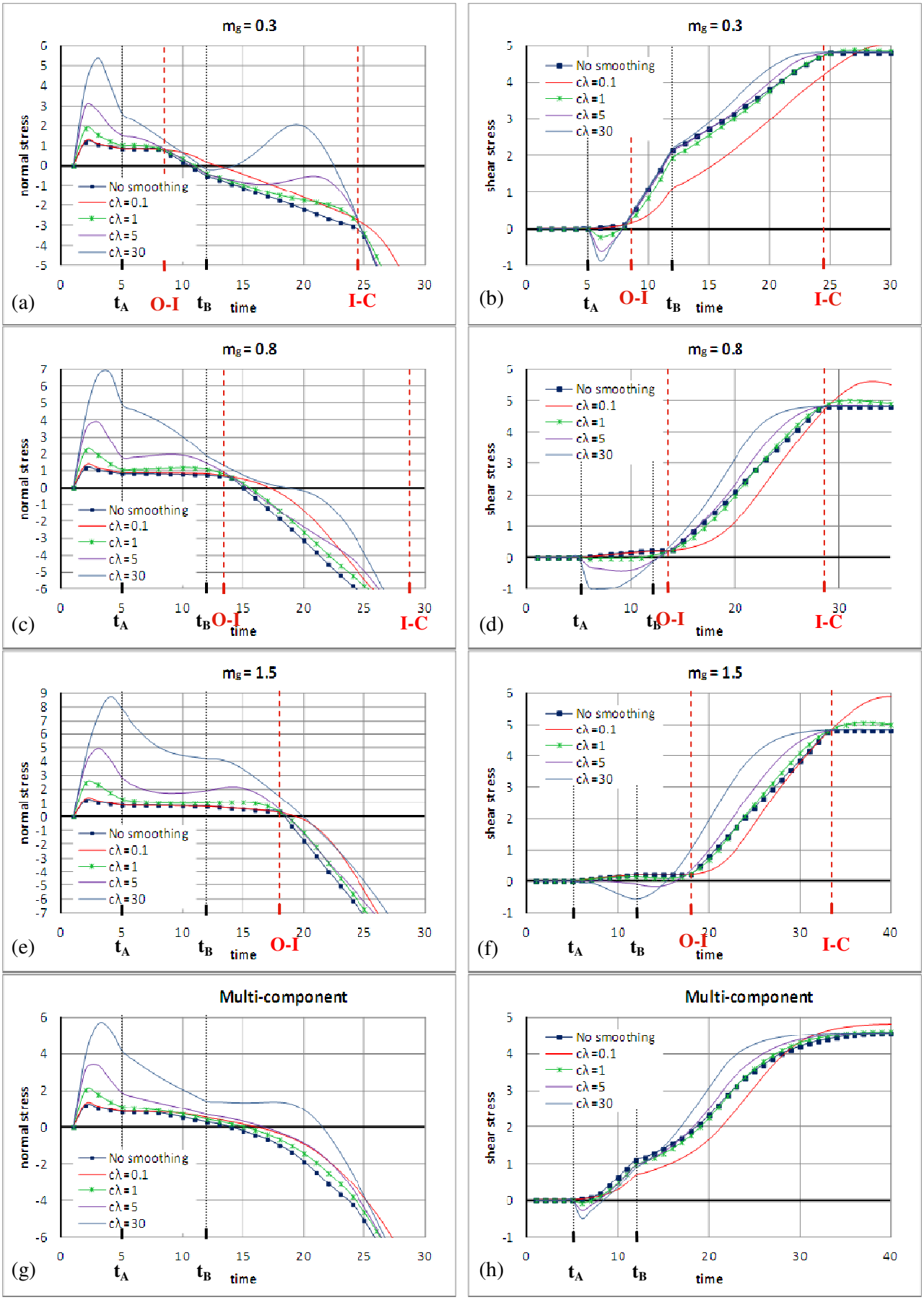

Figure. 5.9. Parametric study. Case 3

Table 5.1. Material properties

E_m (MPa)	E_Ω (MPa)	υ_m	υ_Ω	f_{ti} (MPa)	u_0 (mm)	d_{max} (mm)
31000	55000	0.19	0.21	1.0	0.1	10

Observations from the crack-plane parametric study:

1. From the predictions of the normal component of the local stresses in phase t_O-t_A it can be observed that increasing the value of parameter *a* -i.e. broadening the 'transition band'- can dramatically alter the computed normal (tensile) stresses. (Fig. 5.7. a,c,e,g). The same effect is observed when parameter *c* is decreased (Fig. 5.8. a,c,e,g) or parameter c_λ is increased (Fig. 5.9. a,c,e,g). This has a direct influence on the predicted response in uniaxial tension.
2. The unrealistic overestimation described above is augmented for shallower contact angles (i.e. higher values of m_g).
3. Generally the effect is not as severe as the path crosses the O-I and I-C transition regions for all cases.
4. For small m_g values, shear stresses tend to be underestimated (phase t_B-t_C) when parameter *a* is increased (Fig. 5.7b). However the effect is not as severe in comparison with the overestimation of tensile stress in phase t_O-t_A
5. For all three cases, negative shear stresses can develop in phase t_A-t_B. This undesirable result is generally notable for small m_g values and is particularly pronounced for high values of c_λ. Smoothing parameters will be selected to avoid this occurring.
6. Examples of the most extreme responses may be seen in Figs. 5.7d,f and 5.8d,f with $a = 40$ and $c = 1$ respectively, in which the predicted shear response is very smooth but the response is unduly altered.
7. The multi-component formulation produces an intrinsically smoother response. It can also be noted that the effects of the smoothing function are considerably less pronounced in this case

From these simulations and from the above observations a set of parameter values were selected which are given below in Table 5.2.

Table 5.2. Smoothing parameters

	a	c	c_λ
λ_{int}	10	5	1
λ_{cl}	5	5	1

5.1.3. Comparison between smoothed and unsmoothed response of 2D and 3D constitutive model for a range of micro-roughnesses

The effect of using the single smoothed contact state function in place of the separate functions is now considered for 2D and 3D versions of the model.

It was decided to use a single phase version of the 2D model in order to concentrate on the effect of the smoothing function. Once the conclusions from this 2D study were obtained, the finally proposed form of the function was tested on the full 3D model proposed in Chapters 2 and 3.

(i) Single and multi-component contact results in 2D

Numerical predictions of the 2D plane stress model employing the unsmoothed contact formulation described in Table 2.1 are compared with predictions of the smooth contact formulation (Eqs. 5.2-5.4) in Fig. 5.10 for uniaxial compressive and tensile loading cases. A single contact component formulation (i.e. one m_g value and p=1 for each direction) and multi-component contact formulation using the Gamma distribution of Eq. (5.1) are considered.

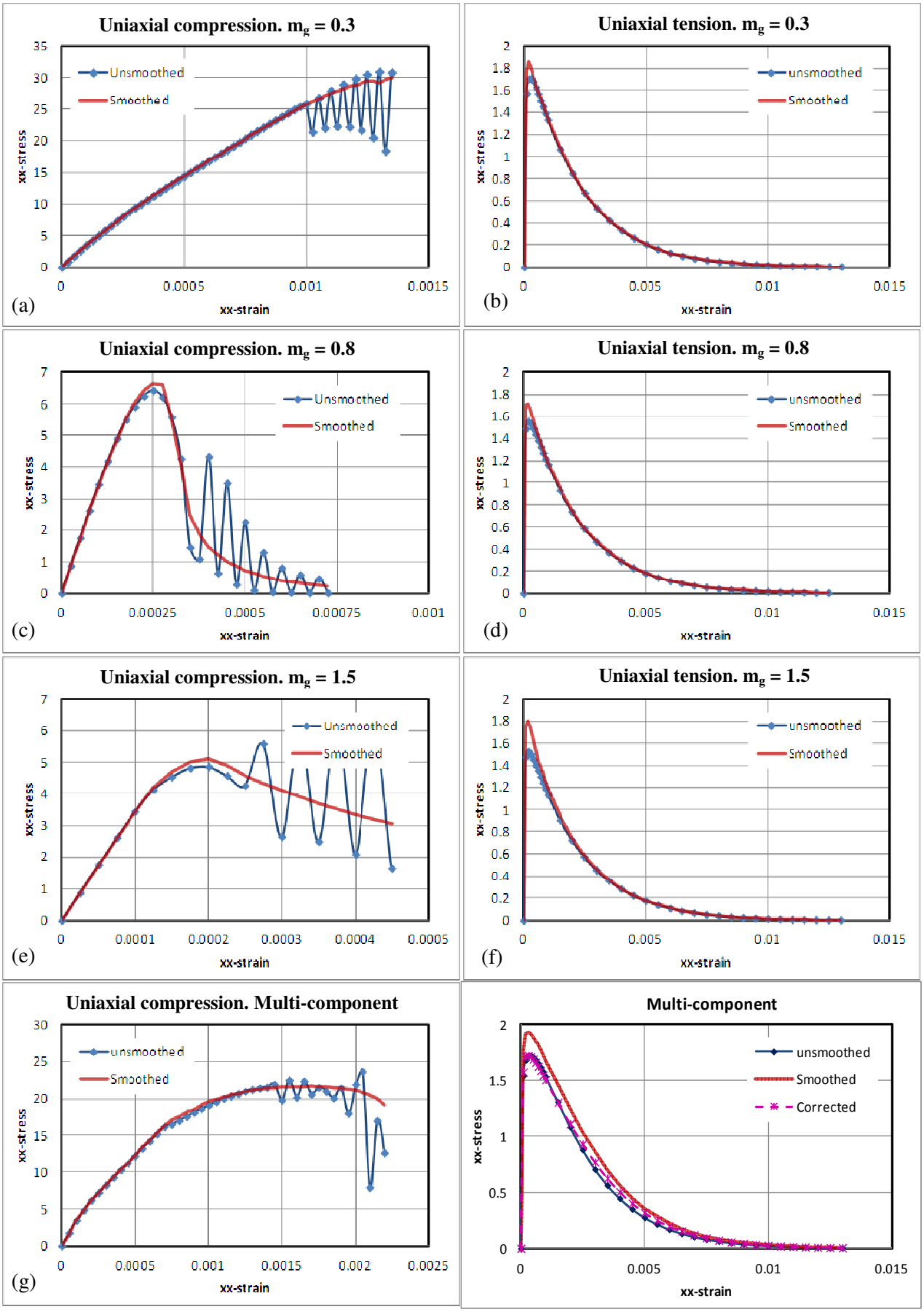

Figure. 5.10. 2D uniaxial tension and compression numerical predictions with unsmoothed and smoothed contact

Observations from 2D study:

- The proposed smoothed contact state function is efficient at removing the rough contact related numerical chatter
- The smoothed contact formulation tends to overestimate the tensile strength. This is the direct result of the problem described in observation 1 from the crack-plane study. However, as mentioned before, this overestimation is corrected by using Eq. (5.5).
- The relative error η_s increases with increasing m_g values which is consistent with the observations from the crack-plane study; for m_g = 0.3 the error is approximately 8% while for m_g = 1.5 the error becomes approximately 15%. Noteworthy is the fact that in this case, i.e. when multiple directions are interacting, the errors are considerably reduced compared to the crack-plane case.
- For multi-component contact formulation the error is further reduced
- The compressive strength is altered insignificantly
- The recommended value for the relative error η_s to be used for correction is 0.1. Fig. 5.10h shows a good correlation between the tensile stresses predicted with the unsmoothed formulation and the corrected tensile stresses

Overall, it is concluded that the use of the smoothed state function with the selected parameters in the 2D model removes chatter but does not appreciably alter the response, particularly when the tensile correction is employed.

(ii) Multiple contact component results in 3D

The effect of the smoothing technique for a multi-component contact formulation is illustrated for a 3D case in Fig. 5.11. The general conclusions from the 2D study apply for the 3D case as well. It can be observed that in 3D the altering effect is further reduced in comparison with the 2D case whilst the chatter is still efficiently eliminated. The recommended value for the relative error η_s to be used for correction is 0.02, which in effect suggests that the correction is hardly needed in 3D.

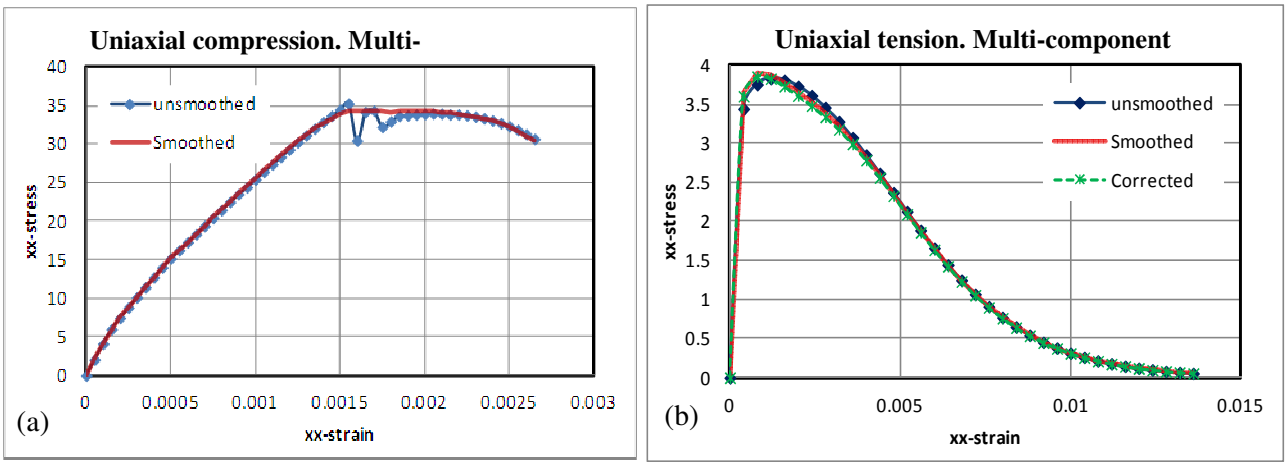

Figure. 5.11. 3D uniaxial tension and compression numerical predictions with unsmoothed and smoothed contact

5.2. Numerical integration rules

A further numerical aspect explored in this study is that of convergence with respect to the spherical integration scheme. Whilst this issue has been investigated for other models which employ spherical integrals (e.g. Bažant and Oh, 1986), previous conclusions regarding the sufficient order of the rule may not be applicable to the present model in which contact plays such a key role.

Integration rules and the optimum number of integration directions were explored for the microplane model by Bažant and Oh (1986). They found that 21 integration directions for an integration rule over a hemisphere were sufficient although with noticeable error. The error however was considered reasonable relative to natural variations in response of real concrete specimens. The accuracy of a specific integration rule however depends upon the type of function that is integrated (Bažant and Oh, 1986) and this issue is therefore explored for the present model which includes the rough contact component. Both 2D (plane stress) and 3D cases are investigated.

5.2.1. Plane stress (2D) case

The convergence properties of a 2D integration rules can be explored in an expedient way using a rule with evenly spaced integration directions. As discussed in Bažant and Oh (1986), centrally symmetric arrangements of integration points i.e. symmetric with respect to the centre of the circle, can be reduced to semicircular

formulae which is a clear advantage over non-symmetric formulae. Therefore only centrally symmetric rules are treated in this study.

In order to illustrate the effect of contact on the accuracy and convergence properties of these formulae, the study is carried out using two versions of the model; one that does not include the contact component and the version that includes the multi-component (smoothed) contact sub-model.

The numerical results for uniaxial compression obtained for the no-contact case are presented in Fig. 5.12 where n_d denotes the number of evenly spaced integration directions used. The rule employing 16 evenly spaced directions is considered to be sufficiently converged for practical purposes but the 5% difference observed in the peak stress with the 12 direction rule, with respect to that of the converged response, is considered a little too great.

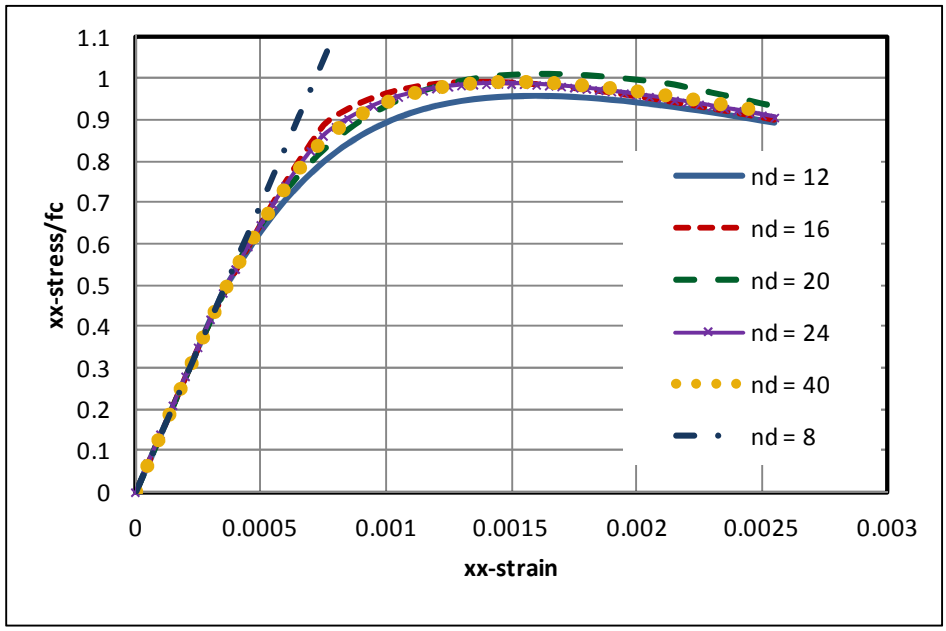

Figure. 5.12. Uniaxial compression predictions for the no-contact 2D model version

The same simulations are next performed with the multi-component (smoothed) contact sub-model and the results are shown in Fig. 5.13. In this case the results converge for $n_d \geq 24$.

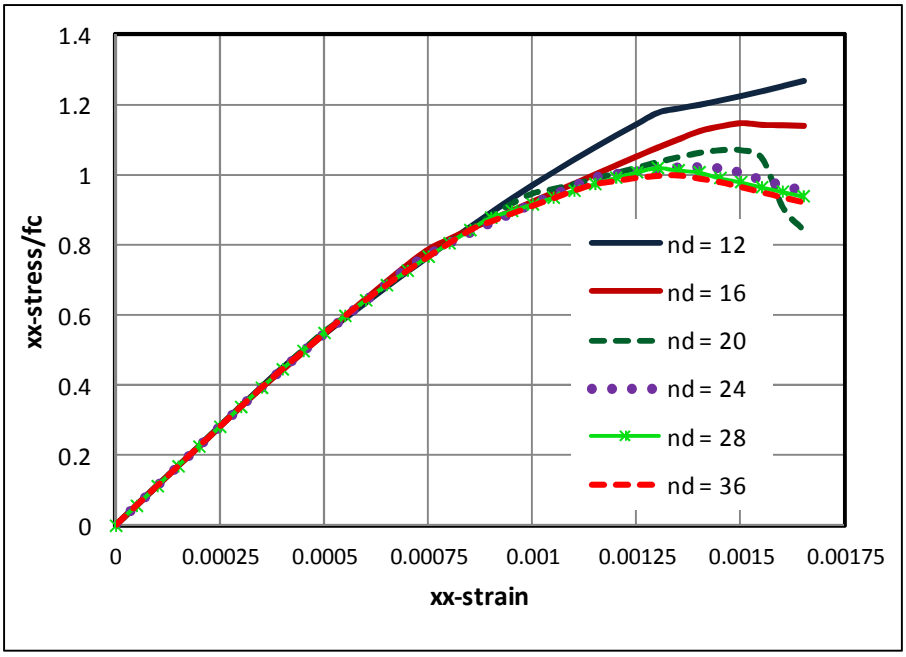

Figure. 5.13. Uniaxial compression predictions for the smoothed contact 2D model version

5.2.2. 3D case

Three centrally symmetric integration rules are again investigated for the multi-component smoothed contact model in 3D as follows:

a. Bažant and Oh's 42-point (2x21), 9th degree rule (Bažant and Oh, 1986)

b. McLaren 50-point, 11th degree rule (Stroud, 1971).

c. Bažant and Oh's 74-point (2x21), 13th degree rule (Bažant and Oh, 1986)

Figure 5.14 presents the stress predictions for the three integration rules. The responses obtained with the 50-point rule and 74 point rule are considered to be sufficiently close for practical purposes and therefore the 74-point rule is considered to be converged with respect to numerical integration.

Notwithstanding the above conclusion, it is recognised that this issue warrants further investigation. In particular, Bažant and Oh (1986) suggest that an additional condition needs to be checked in order to find the optimum integration rule, namely for the given function to be integrated the values of the integrals should be evaluated for all possible body rotations of the set of integration points, associated to the integration formula, about the centre of the unit sphere. The optimum rule is subsequently considered to be the one which gives the smallest difference between the maximum and minimum values of the integral. This has yet to be carried out for the present model and this is therefore recommended in the future work section.

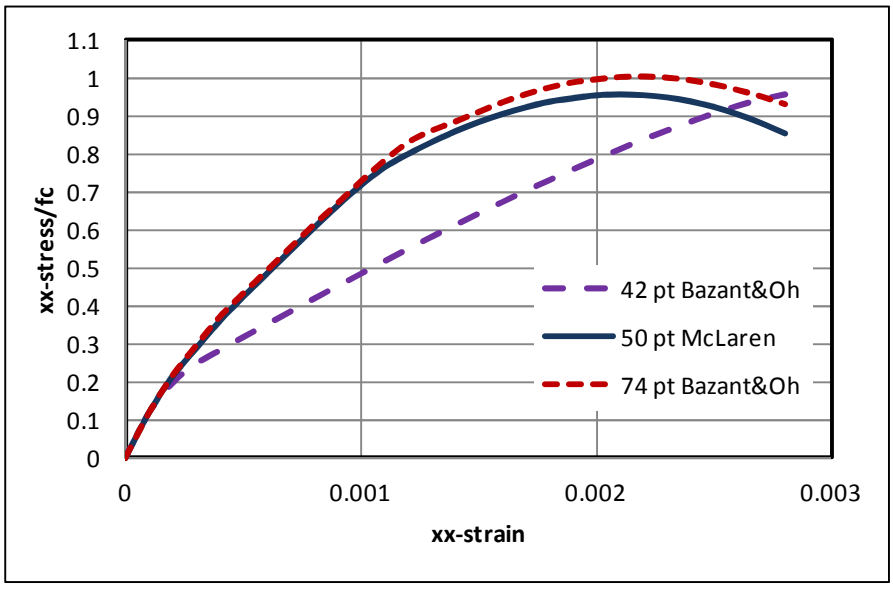

Figure. 5.14. Uniaxial compression predictions for the smoothed contact 3D model version

5.3. Rate formulation. Tangent stiffness

5.3.1. Constitutive driver

In Chapters 2 and 3 a constitutive model for concrete that employed micromechanical solutions and mechanistic assumptions was presented. The model was characterised by a final expression relating the average stresses to average strains (Eq. M8, Section 3.4). In numerical applications a Newton-Raphson based constitutive driver applicable for stress, strain or mixed stress and strain paths is employed and therefore the rate form of the model that makes use of the tangent rather than the secant stiffness is also required. A typical Newton-Raphson based algorithm is presented in Table 5.3.

Table 5.3. Newton-Raphson based constitutive driver algorithm

• Read in title, control data (i.e. No. of increments n and stress model e.g. plane strain) and the material data	
Read in initial conditions $\boldsymbol{\sigma}_{init}$,	
• $\sigma_t = \sigma_{init}$, $\sigma = \sigma_{init}$, $\varepsilon = \mathbf{0}$	Initialise the stress and strain
• Read in the applied stress increment components $\Delta\boldsymbol{\sigma}_a$ and/or strain increment components $\Delta\boldsymbol{\varepsilon}_a$	
• For i = 1 to n	Loop over stress/strain increments
• $\boldsymbol{\sigma}_t = \boldsymbol{\sigma}_t + \Delta\boldsymbol{\sigma}_{a_i}$	Update total stresses (σ_t)
• $\Delta\boldsymbol{\sigma} = \Delta\boldsymbol{\sigma}_{a_i}$	Set initial value of out-of-balance stresses ($\Delta\boldsymbol{\sigma}$) for this increment
• For j = 1 to m	Loop over iterations
• Compute $\mathbf{D_t}$	Compute tangent stiffness ($\mathbf{D_t}$)
• $\Delta\boldsymbol{\varepsilon} = \mathbf{D}_t^{-1}\Delta\boldsymbol{\sigma}$, extract $\Delta\boldsymbol{\sigma}_{rc}$	Compute strain increment ($\Delta\boldsymbol{\varepsilon}$) from out of balance stress and tangent stiffness matrix and extract 'reaction' stress ($\Delta\boldsymbol{\sigma}_{rc}$)
• $\boldsymbol{\varepsilon} = \boldsymbol{\varepsilon} + \Delta\boldsymbol{\varepsilon}$ and $\boldsymbol{\sigma}_t = \boldsymbol{\sigma}_t + \Delta\boldsymbol{\sigma}_{rc}$	Update strains and add reaction stress components to total stresses
• Compute $\boldsymbol{\sigma}$ from existing $\boldsymbol{\sigma}$, $\Delta\boldsymbol{\varepsilon}$ $\boldsymbol{\sigma} = \mathbf{D}_s \cdot \boldsymbol{\varepsilon}$	Use Backward Euler stress recovery algorithm to update the stress
• $\Delta\boldsymbol{\sigma} = \boldsymbol{\sigma}_t - \boldsymbol{\sigma}$	Compute the out of balance stress
• $\varpi = \dfrac{\lvert\Delta\boldsymbol{\sigma}\rvert}{\lvert\boldsymbol{\sigma}_t\rvert}$	Compute the relative error (ϖ) i.e. norm of the out of balance stress
• IF ϖ < tol Exit Iteration Loop	If converged, exit iteration loop
• End j Loop	
• Convergence not achieved, Stop	
• Output results for increment	
• End i Loop	
• Finish	

5.3.3. Tangent stiffness

Next, the formulation for the tangent stiffness tensor is derived in matrix form for the case of a two-phase model incorporating micromechanics based damage evolution and crack closure.

The final constitutive relationship of the model presented in Chapters 2 and 3 can be written as:

$$\bar{\boldsymbol{\sigma}} = \mathbf{D}_{\mathrm{s}} \cdot \bar{\boldsymbol{\varepsilon}} \tag{5.6}$$

For an integration rule with n_d discrete directions the secant stiffness in matrix form has the following expression:

$$\mathbf{D}_{\mathrm{s}} = \left[\mathbf{I}^{4\mathrm{s}} + \mathbf{D}_{\mathrm{m}\Omega} \sum_{i=1}^{n_d} \mathbf{N}_i{}^{\mathrm{T}} \mathbf{C}_{\mathrm{c}\alpha i} \mathbf{N}_i w_i \right]^{-1} \cdot \mathbf{D}_{\mathrm{m}\Omega} \tag{5.7}$$

where w_i is the weight associated with the i^{th} direction and the local added compliance $\mathbf{C}_{\mathrm{c}\alpha\mathrm{i}}$ is given by equation (2.46) $\mathbf{C}_{\mathrm{c}\alpha} = \left[\left[(1-\omega)\mathbf{I}^{2\mathrm{s}} + \omega \left(\sum_k p_k H_{fk} \boldsymbol{\Phi}_k \right) \right]^{-1} - \mathbf{I}^{2\mathrm{s}} \right] \cdot \mathbf{C}_{\mathrm{L}}$.

The following notation is employed:

$$\begin{aligned} \mathbf{A} &= \mathbf{I}^{4\mathrm{s}} + \mathbf{D}_{\mathrm{m}\Omega} \sum_{i=1}^{n_d} \mathbf{N}_i{}^{\mathrm{T}} \mathbf{C}_{\mathrm{c}\alpha i} \mathbf{N}_i w_i \\ \mathbf{B} &= (1-\omega)\mathbf{I}^{2s} + \omega \left(\sum_k p_k H_{fk} \boldsymbol{\Phi}_k \right) \end{aligned} \tag{5.8a,b}$$

Differentiating equation (5.6) gives:

$$\mathrm{d}\bar{\boldsymbol{\sigma}} = \mathbf{D}_{\mathrm{s}} \cdot \mathrm{d}\bar{\boldsymbol{\varepsilon}} + \left(\frac{\partial \mathbf{D}_{\mathrm{s}}}{\partial \bar{\boldsymbol{\varepsilon}}} \mathrm{d}\bar{\boldsymbol{\varepsilon}} \right) \bar{\boldsymbol{\varepsilon}} \tag{5.9}$$

Making use of the expression for the derivative of an inverse, $\frac{\partial \mathbf{Y}^{-1}}{\partial x} = -\mathbf{Y}^{-1} \frac{\partial \mathbf{Y}}{\partial x} \mathbf{Y}^{-1}$, Eq. (5.9) becomes:

$$\mathrm{d}\bar{\boldsymbol{\sigma}} = \mathbf{D}_{\mathrm{s}} \cdot \mathrm{d}\bar{\boldsymbol{\varepsilon}} + \left(-\mathbf{A}^{-1} \cdot \frac{\partial \mathbf{A}}{\partial \bar{\boldsymbol{\varepsilon}}} \cdot \mathrm{d}\bar{\boldsymbol{\varepsilon}} \mathbf{A}^{-1} \cdot \mathbf{D}_{\mathrm{m}\Omega} \right) \bar{\boldsymbol{\varepsilon}} \tag{5.10}$$

in which:

$$\frac{\partial \mathbf{A}}{\partial \bar{\boldsymbol{\varepsilon}}} \mathrm{d}\bar{\boldsymbol{\varepsilon}} = \mathbf{D}_{\mathrm{m}\Omega} \sum_{i=1}^{n_d} \left(\mathbf{N}_i{}^{\mathrm{T}} \left[-\mathbf{B}_i{}^{-1} \cdot \frac{\partial \mathbf{B}_i}{\partial \bar{\boldsymbol{\varepsilon}}} \mathrm{d}\bar{\boldsymbol{\varepsilon}} \cdot \mathbf{B}_i{}^{-1} \mathbf{C}_{\mathrm{L}} \right] \mathbf{N}_i w_i \right) \tag{5.11}$$

For each sample direction i = 1..n_d, $\dfrac{\partial \mathbf{B}}{\partial \bar{\boldsymbol{\varepsilon}}}$ is determined using the chain rule:

$$\frac{\partial \mathbf{B}}{\partial \bar{\boldsymbol{\varepsilon}}} \mathrm{d}\bar{\boldsymbol{\varepsilon}} = \frac{\partial \mathbf{B}}{\partial \omega} \cdot \frac{\partial \omega}{\partial \zeta} \cdot \frac{\partial \zeta}{\partial \boldsymbol{\varepsilon}_{\mathrm{L}}} \cdot \frac{\partial \boldsymbol{\varepsilon}_{\mathrm{L}}}{\partial \bar{\boldsymbol{\varepsilon}}} \mathrm{d}\bar{\boldsymbol{\varepsilon}} + \sum_k \frac{\partial \mathbf{B}}{\partial H_{fk}} \cdot \frac{\partial H_{fk}}{\partial \boldsymbol{\varepsilon}_{\mathrm{L}}} \cdot \frac{\partial \boldsymbol{\varepsilon}_{\mathrm{L}}}{\partial \bar{\boldsymbol{\varepsilon}}} \mathrm{d}\bar{\boldsymbol{\varepsilon}} + \\ + \sum_k \frac{\partial \mathbf{B}}{\partial \boldsymbol{\Phi}_k} \cdot \frac{\partial \boldsymbol{\Phi}_k}{\partial \boldsymbol{\varepsilon}_{\mathrm{L}}} \cdot \frac{\partial \boldsymbol{\varepsilon}_{\mathrm{L}}}{\partial \bar{\boldsymbol{\varepsilon}}} \mathrm{d}\bar{\boldsymbol{\varepsilon}} \tag{5.12}$$

The derivatives that appear in Eq. (5.12) can be evaluated straightforwardly and their expressions are given in Table 5.4.

It is recalled from section 2.2.3 that the embedded strain is expressed as:

$$\mathbf{g} = \boldsymbol{\Phi} \cdot \boldsymbol{\varepsilon}_{\mathrm{L}} \tag{5.13}$$

where the contact matrix $\boldsymbol{\Phi}$ is given in Table 2.1.

Differentiating Eq. (5.13) gives:

$$\mathrm{d}\mathbf{g} = \left(\frac{\partial \boldsymbol{\Phi}}{\partial \boldsymbol{\varepsilon}_{\mathrm{L}}} \mathrm{d}\boldsymbol{\varepsilon}_{\mathrm{L}} \right) \boldsymbol{\varepsilon}_{\mathrm{L}} + \boldsymbol{\Phi} \cdot \mathrm{d}\boldsymbol{\varepsilon}_{\mathrm{L}} \tag{5.14}$$

It can be proven that the differential of the embedded strain for all three contact states is:

$$\mathrm{d}\mathbf{g} = \boldsymbol{\Phi} \cdot \mathrm{d}\boldsymbol{\varepsilon}_{\mathrm{L}} \tag{5.15}$$

Hence, $\dfrac{\partial \boldsymbol{\Phi}}{\partial \boldsymbol{\varepsilon}_{\mathrm{L}}} = 0$ and the third summation in Eq. (5.12) vanishes.

The tangent matrix is then formed in a "column by column" manner so that $\mathrm{d}\bar{\boldsymbol{\varepsilon}}$ is extracted element by element as shown below. Denoting $\mathbf{y} = \mathbf{A}^{-1} \cdot \mathbf{D}_{\mathrm{m}\Omega} \cdot \bar{\boldsymbol{\varepsilon}}$ one can obtain from Eq. (5.11):

$$\frac{\partial \mathbf{A}^{-1}}{\partial \bar{\varepsilon}_j} \mathrm{d}\bar{\varepsilon}_j = -\mathbf{A}^{-1} \cdot \frac{\partial \mathbf{A}}{\partial \bar{\varepsilon}_j} \mathrm{d}\bar{\varepsilon}_j \cdot \mathbf{y} = -\mathbf{A}^{-1} \cdot \frac{\partial \mathbf{A}}{\partial \bar{\varepsilon}_j} \cdot \mathbf{y} \cdot \mathrm{d}\bar{\varepsilon}_j \tag{5.16}$$

Column j, where j = 1, 2, ..6, of matrix $\mathbf{D}_{\mathrm{adt}}$ is hence obtained:

$$\mathbf{D}_{adt}{}^{(j)} = -\mathbf{A}^{-1} \cdot \frac{\partial \mathbf{A}}{\partial \bar{\varepsilon}_j} \cdot \mathbf{y} \tag{5.17}$$

Eq. (5.10) hence becomes:

$$\mathrm{d}\bar{\boldsymbol{\sigma}} = (\mathbf{D}_{\mathrm{s}} + \mathbf{D}_{adt}) \cdot \mathrm{d}\bar{\boldsymbol{\varepsilon}} \tag{5.18}$$

Consequently, $\mathbf{D}_t = \mathbf{D}_s + \mathbf{D}_{adt}$

Table 5.4. Additional derivatives

$$\frac{\partial \mathbf{B}}{\partial \omega} = -\mathbf{I}^{2s} + \sum_k p_k H_{fk} \boldsymbol{\Phi}_k$$

$$\frac{\partial \mathbf{B}}{\partial H_{fk}} = \omega H_{fk} \boldsymbol{\Phi}_k$$

$$\frac{\partial \omega}{\partial \zeta} = \frac{\varepsilon_{tm}}{\zeta} e^{-5\frac{\zeta - \varepsilon_{tm}}{\varepsilon_0 - \varepsilon_{tm}}} \left(\frac{1}{\zeta} - \frac{5}{\varepsilon_0 - \varepsilon_{tm}} \right)$$

$$\frac{\partial \zeta}{\partial \boldsymbol{\varepsilon}_{\mathrm{L}}} = \begin{bmatrix} \dfrac{1+\alpha_L}{2} + \dfrac{\varepsilon_{L_{rr}} \left(\dfrac{1-\alpha_L}{2} \right)^2}{\sqrt{{\varepsilon_{L_{rr}}}^2 \left(\dfrac{1-\alpha_L}{2} \right)^2 + {r_\varsigma}^2 \gamma^2}} \\ \dfrac{\varepsilon_{L_{rs}} {r_\varsigma}^2}{\sqrt{{\varepsilon_{L_{rr}}}^2 \left(\dfrac{1-\alpha_L}{2} \right)^2 + {r_\varsigma}^2 \gamma^2}} \\ \dfrac{\varepsilon_{L_{rt}} {r_\varsigma}^2}{\sqrt{{\varepsilon_{L_{rr}}}^2 \left(\dfrac{1-\alpha_L}{2} \right)^2 + {r_\varsigma}^2 \gamma^2}} \end{bmatrix}^T$$

$$\frac{\partial \boldsymbol{\varepsilon}_{\mathrm{L}}}{\partial \bar{\boldsymbol{\varepsilon}}} = (1 - \omega_{s-1}) \mathbf{C}_L \cdot \mathbf{N} \cdot \mathbf{D}_m \cdot \mathbf{T}(\mathbf{x}_p) \left(f_\Omega \mathbf{T}_\Omega + f_m \mathbf{I}^{4s} \right)^{-1} + \omega_{s-1} \mathbf{N}_\varepsilon \quad *$$

$$\frac{\partial H_f}{\partial \boldsymbol{\varepsilon}_{\mathrm{L}}} = \begin{bmatrix} -\dfrac{c_1}{\lambda \varepsilon_0} e^{-c_1 \frac{\varepsilon_{L_{rr}} - \varepsilon_{tm}}{\lambda \varepsilon_0}} \\ 0 \\ 0 \end{bmatrix}^T$$

* for expediency the damage parameter from the last converged step is used. This simplifying assumption was found to have little influence on the accuracy of the solution.

5.4. Concluding remarks

Chatter behaviour can occur at the constitutive level in the micromechanical model for concrete proposed in Chapters 2 and 3 when multiple microcrack surfaces are active and under different contact conditions.

A single smoothed contact function, which replaces three separate contact state functions, is shown to be effective at removing chatter and smoothing the model response.

The use of the single function can result in unrealistic responses if the smoothing parameters are not properly selected. However, based on a parametric study on a single crack-plane, it is concluded that a set of parameters can be selected which smooth the response, remove chatter and which do not unrealistically alter the predicted response.

Uniaxial tension and compression simulations in 2D and 3D showed that, with the recommended parameters, the use of the smoothed state function efficiently eliminates chatter but does not substantially alter the response.

For a 2D version of the model, it is concluded that a 16 direction integration rule is sufficiently converged for practical purposes. For a 3D version of the model, a 50 direction integration rule is adequate for practical computation although it is acknowledged that in this case further work is required to fully establish the convergence properties of the model.

It is possible to derive a tractable form of the consistent tangent for the model, which can be used when the model is implemented in a finite element program.

Chapter 6

Finite element analysis

The original intention of the work described in this chapter was to assess the performance of the micromechanical constitutive model described in Chapters 2 and 3 when implemented in a finite element code. However, more research time was devoted to exploring the formulation of a microcrack initiation criterion based on the exterior point Eshelby solution, investigating the morphology of the crack surface and to the development of a plastic-contact crack plane model -ultimately aimed to be implemented in the overall constitutive model- and therefore the scope of the chapter is more limited than the original intention. Nevertheless, a simplified 2D version of the constitutive model was successfully implemented in the finite element commercial code LUSAS and its performance is assessed here.

A brief summary of the simplified 2D version is given in section 6.1 followed by implementation details in section 6.2. Section 6.3 presents an initial assessment of the performance of the model using three examples.

6.1. Simplified 2D constitutive model

As mentioned above, the model implemented in the finite element program is a simplified version in 2D of the constitutive model presented in Chapters 2 and 3. Concrete is simulated as an elastic single phase matrix weakened by penny-shaped

microcracks. In this simplified version, microcrack interaction and crack closure effects are not taken into account. It is recalled from Chapter 2 that the model describes a representative material element inside the fracture process zone ahead of a macrocrack. In the 2D formulation, an overall plane-stress assumption is adopted.

The simplified model in a 2D plane-stress formulation is summarised in Table 6.1. The plane-stress specialization of the 3D model is achieved by only considering cracks that occur normal to the out-of-plane dimension, using a plane stress elasticity tensor and by adopting a damage function written in terms of in-plane components only. Implicitly, this means that microcracks only form such that their normal vectors are in-plane.

Table 6.1. Summary of the 2D model version

$\boldsymbol{\sigma} = \mathbf{D} : (\boldsymbol{\varepsilon} - \boldsymbol{\varepsilon}_{\mathrm{a}})$	(6.1)	Elastic constitutive equation
$\boldsymbol{\varepsilon}_{\mathrm{a}} = \left(\frac{1}{2\pi} \int_0^{2\pi} \mathbf{N}^{-1} : \frac{\omega(\theta)}{1-\omega(\theta)} \mathbf{C}_L : \mathbf{N} d\theta \right) : \boldsymbol{\sigma}$	(6.2)	Added strains due to microcracking in the matrix.
$\boldsymbol{\varepsilon}_{\mathrm{L}}(\theta) = \mathbf{N}(\theta) : \boldsymbol{\varepsilon}$	(6.3)	Local strain (used for computing damage variable)
$\mathrm{F}_{\zeta}(\boldsymbol{\varepsilon}_{\mathrm{L}}, \zeta) = \left(\varepsilon_{\mathrm{L_{rr}}} \left(\frac{1+\upsilon}{2} \right) + \sqrt{\varepsilon_{\mathrm{L_{rr}}}^{\,2} \left(\frac{1-\upsilon}{2} \right)^2 + r_{\zeta}^{\,2} \gamma^2} \right) - \zeta$	(6.4)	Local principal stress based damage function, $r_{\zeta} = \frac{G}{E\beta}$, $\beta = \frac{1}{1-\upsilon^2}$
$\omega(\theta) = 1 - \frac{\varepsilon_{\mathrm{t}}}{\zeta(\theta)} e^{-5\frac{\zeta(\theta) - \varepsilon_{\mathrm{t}}}{\varepsilon_0 - \varepsilon_{\mathrm{t}}}}$	(6.5)	Evolution of the damage parameter, $\omega \in [0,1]$
$\boldsymbol{\sigma} = \left(\mathbf{I}^{2s} + \frac{\mathbf{D}}{2\pi} \int_0^{2\pi} \mathbf{N}^{-1} : \frac{\omega(\theta)}{1-\omega(\theta)} \mathbf{C}_L : \mathbf{N} d\theta \right)^{-1} \cdot \mathbf{D} : \boldsymbol{\varepsilon}$	(6.6)	Final average stress-strain relationship

where $\boldsymbol{\sigma}$ and $\boldsymbol{\varepsilon}$ denote the macroscopic stress and strain respectively. $\mathbf{D}$ is the elasticity tensor for a plane-stress case. In matrix form $\mathbf{D} = \frac{E}{1-\upsilon^2} \begin{bmatrix} 1 & \upsilon & 0 \\ \upsilon & 1 & 0 \\ 0 & 0 & \frac{1-\upsilon}{2} \end{bmatrix}$, where E is the Young's modulus and υ the Poisson's ratio.

In the 3D model, microcracking was taken into account by the inclusion of an overall added strain tensor (Eq. 2.33) obtained by summing the local added strains from

all possible directions. As mentioned above, in the plane-stress case, microcracks are assumed to form only in plane (i.e. their normal vectors $\mathbf{r}(\theta)$ are always perpendicular to the normal of the plane). However, locally, these microcracks are considered to be three dimensional penny-shaped ellipsoids. Therefore for the plane-stress case, the local added strain associated with direction θ_i is given by Eq. (2.28) in which the out-of-plane shear component is neglected. Subsequently the local elastic compliance tensor becomes $\mathbf{C}_L = \frac{1}{E}\begin{bmatrix} 1 & 0 \\ 0 & \frac{4}{2-\upsilon} \end{bmatrix}$. Moreover, the integral over a unit sphere from Eq. (2.33) becomes an integral over a unit circle (Eq. 6.2).

Microcracks are then assumed to initiate when the local principal stress associated with the current direction *i* reaches the tensile strength and their development is thereafter assumed strain controlled. The damage function (Eq. 6.4) is subsequently derived in a manner similar to that presented in section 3.2.2. Damage is still assumed to initiate in the coarse aggregate particle-mortar interface; however, in this simplified version, the two phases are no longer modelled separately and the exterior point Eshelby solution that provides tensile stress concentrations in the interface is therefore not applicable. Nevertheless, the mechanistic rationale is maintained and the ratio G/E between the shear and the Young's modulus in the expression of r_ζ is modified to provide the right balance between the overall tensile and compressive strengths.

The integration over the unit circle in Eq. 6.6 is evaluated numerically employing a centrally symmetric integration rule with 16 evenly spaced directions. It was shown in Fig. 5.12 that for this case 16 integration directions provide a converged solution.

The exact tangent stiffness matrix is obtained following the procedure presented in section 5.3.3. In matrix form it reads:

$$\mathbf{D}_t = \mathbf{D}_s + \mathbf{D}_{adt} \tag{6.7}$$

where:

$$\mathbf{D}_s = \left(\mathbf{I}_3 + \mathbf{D} \cdot \sum_{i=1}^{n_d} \mathbf{N}_i{}^T \frac{\omega_i}{1-\omega_i} \mathbf{C}_L \mathbf{N}_i w_i \right)^{-1} \cdot \mathbf{D} \tag{6.8}$$

and $\mathbf{D}_{adt}$ is obtained in a "column by column" manner employing the following notation, $\mathbf{A} = \mathbf{I}_3 + \mathbf{D} \cdot \sum_{i=1}^{n_d} \mathbf{N}_i^T \frac{\omega_i}{1-\omega_i} \mathbf{C}_L \mathbf{N}_i w_i$ and $\mathbf{y} = \mathbf{A}^{-1} \cdot \mathbf{D} \cdot \boldsymbol{\varepsilon}$:

$$\mathbf{D}_{adt}^{(j)} = -\mathbf{A}^{-1} \cdot \frac{\partial \mathbf{A}}{\partial \varepsilon_j} \cdot \mathbf{y} \tag{6.9}$$

where j denotes the column number, j = 1,2,3 and

$$\frac{\partial \mathbf{A}}{\partial \boldsymbol{\varepsilon}} d\boldsymbol{\varepsilon} = \mathbf{D} \cdot \sum_{i=1}^{n_d} \mathbf{N}_i^T \left(\frac{1}{(1-\omega_i)^2} \cdot \frac{\partial \omega}{\partial \zeta} \cdot \frac{\partial \zeta}{\partial \boldsymbol{\varepsilon}_L} \cdot \frac{\partial \boldsymbol{\varepsilon}_L}{\partial \boldsymbol{\varepsilon}} d\boldsymbol{\varepsilon} \right) \mathbf{C}_L \mathbf{N}_i w_i \tag{6.10}$$

6.2. Implementation in LUSAS

The constitutive 2D model presented in the previous section was implemented in the commercial finite element program LUSAS through its material model interface. The finite element method is a well established subject and its theoretical formulation can be found in numerous textbooks (e.g. Hinton and Owen, 1977; Owen and Hinton, 1980). For completeness, key equations are given below and a generic formulation of a nonlinear finite element code showing details regarding the implementation of the constitutive model is presented in Fig. 6.1.

The overall force-displacement relationship reads:

$$\mathbf{f} = \mathbf{K}_g \mathbf{u} \tag{6.11}$$

where **f** denotes a general force vector that includes body forces per unit volume, surface loads per unit area and point loads, $\mathbf{K}_g$ is the global stiffness matrix of the structure and **u** represents the nodal displacement vector. The global stiffness matrix is obtained by assembling the stiffness matrices from each element given by

$$\mathbf{K} = \int_{\Omega} \mathbf{B}^T \mathbf{D}_s \mathbf{B} d\Omega \tag{6.12}$$

where $\mathbf{D}_s$ is the secant **D** matrix relating stresses to strains, in this case given by Eq. 6.6 and Ω represents the element volume. **B** denotes the strain-displacement matrix with

$$\boldsymbol{\varepsilon} = \mathbf{B}\mathbf{u}^e \tag{6.13}$$

where $\boldsymbol{\varepsilon}$ denotes the strains within an element and superscript e denotes an element quantity. It can be shown from the principle of virtual work that the out-of-balance force vector, which is null when equilibrium is satisfied, is given by:

$$\boldsymbol{\psi}^e = \int_\Omega \mathbf{B}^T \boldsymbol{\sigma}^e d\Omega - \mathbf{f}^e = 0 \tag{6.14}$$

For nonlinear problems, the stiffness varies continually and Eq. (6.14) is not satisfied at any stage of the computation. For each load increment $\Delta\mathbf{f}^e$ the corresponding displacement increment is obtained by solving the following:

$$\Delta\mathbf{f}^e = \mathbf{K}_t \Delta\mathbf{u}^e \tag{6.15}$$

where $\mathbf{K}_t$ is the tangent stiffness matrix given by:

$$\mathbf{K}_t = \int_\Omega \mathbf{B}^T \mathbf{D}_t \mathbf{B} d\Omega \tag{6.16}$$

Convergence is achieved when the norm of the global out-of-balance force vector normalized by the norm of the total force vector becomes less than the chosen tolerance:

$$\frac{|\boldsymbol{\psi}|}{|\mathbf{f}|} \leq tol \tag{6.17}$$

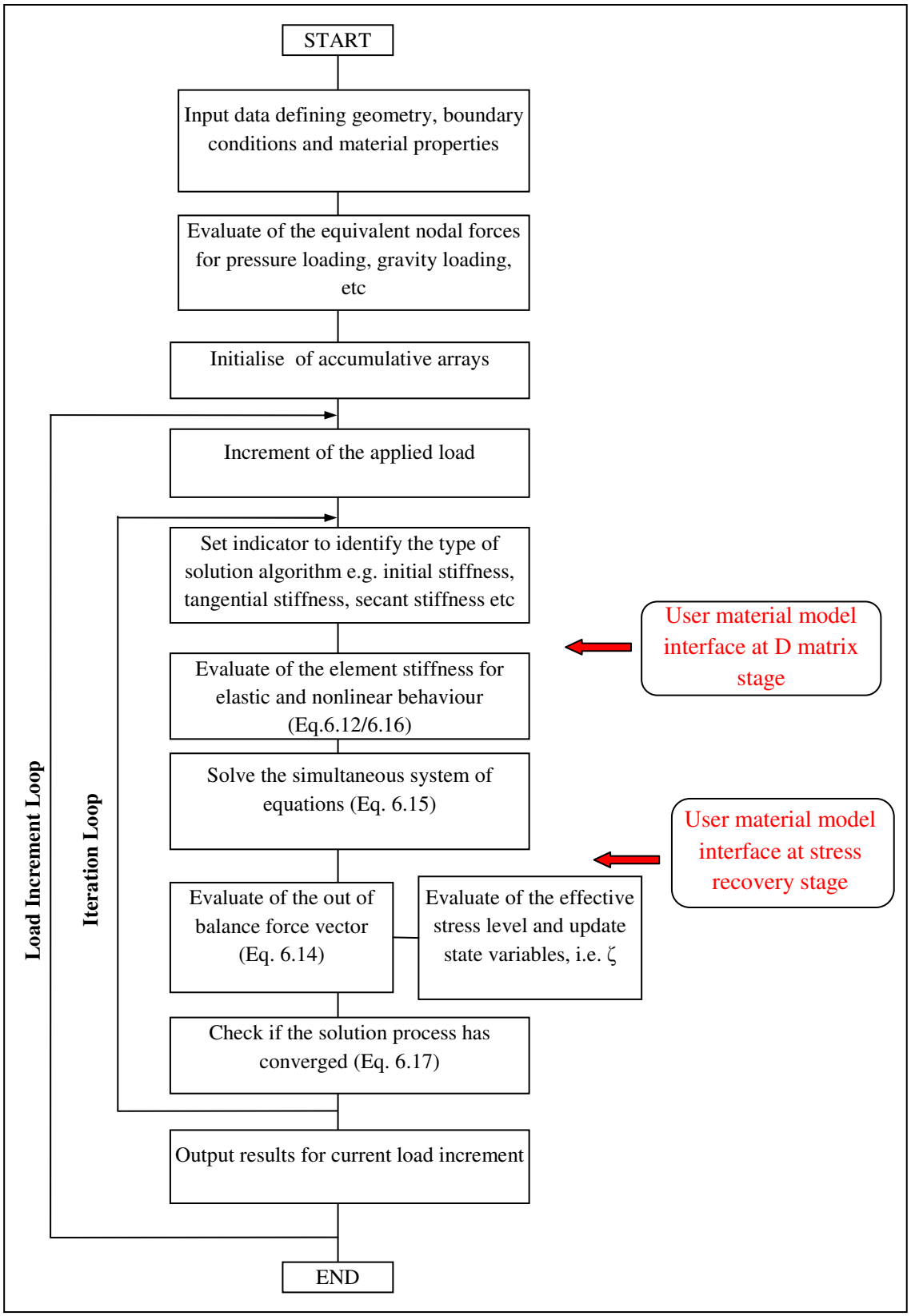

Figure 6.1. Generic formulation of a nonlinear finite element code showing

The strain softening issue, briefly discussed in the introduction chapter of this thesis, is addressed in the finite element program LUSAS according to the fracture

energy crack band approach proposed by Bažant and Oh (1983) in which the softening curve is adjusted with the characteristic element size in order to maintain the fracture energy.

6.3. Numerical examples

As an initial assessment of the performance of the constitutive model, three numerical examples are presented in this section. 8-noded quadrilateral elements with quadratic interpolation are used throughout. For all three analyses, the LUSAS inbuilt automatic step selection procedure was employed in which the load (or displacement) increment is adjusted according to the number of iterations required for convergence.

6.3.1. Example 1. Direct fracture test

In the first example numerical results from a plane-stress analysis of the direct fracture test carried out by Petersson (1981) are presented and compared to the experimental results. In the experimental test the un-reinforced concrete specimen shown in Fig. 6.2 was loaded in direct tension under displacement control.

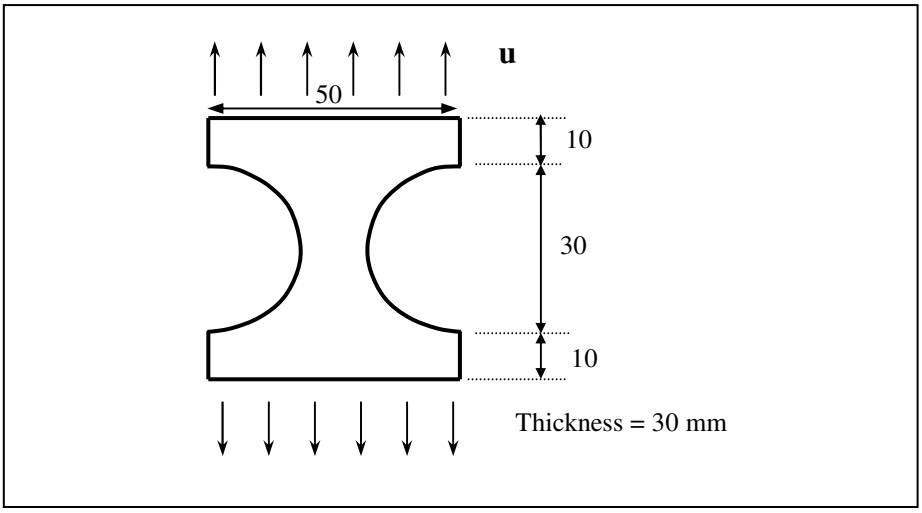

Figure 6.2. Example 1. Geometrical dimensions (mm) and test arrangement

Due to symmetry, only half of the specimen is analysed. The mesh employed for the analysis and a magnified deformed mesh are presented in Fig. 6.3 and the material properties are given in Table 6.2. The load-displacement numerical response is

compared against the experimental response in Fig 6.4. It is noted the numerical deformations correspond to half of the specimen and are therefore doubled in Fig 6.4. Plots of the strain and stress profiles at different stages: Stage A. elastic, Stage B. at peak stress and Stage C. softening regime, as indicated on Fig 6.4, are presented in Figs 6.5-6.7.

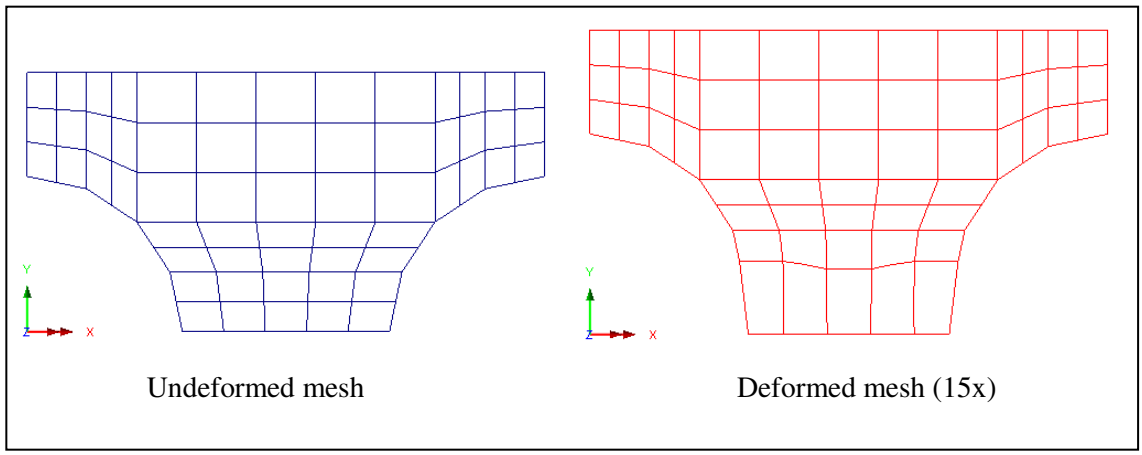

Figure 6.3. Finite element meshes

Table 6.2. Example1. Material properties

Material property	Value
E (N/mm^2)	35000
υ	0.2
f_t (N/mm^2)	1.6
G_f (N/mm)	0.035

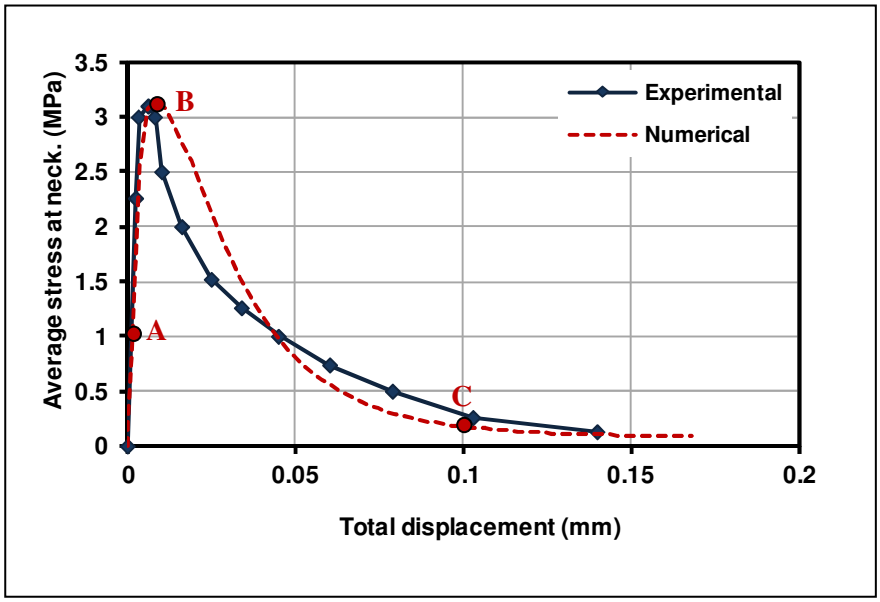

Figure 6.4. Example 1. Load-displacement response

The numerical predictions compare well against the experimental data which indicates that the constitutive model performs well under tensile loading and shows that it is capable of predicting a reasonable tensile softening response. The strain profile at stage C indicates that the strains and consequently damage have localised in the band of elements adjacent to the line of symmetry which is consistent to the experimental observations reported by Petersson (1981).

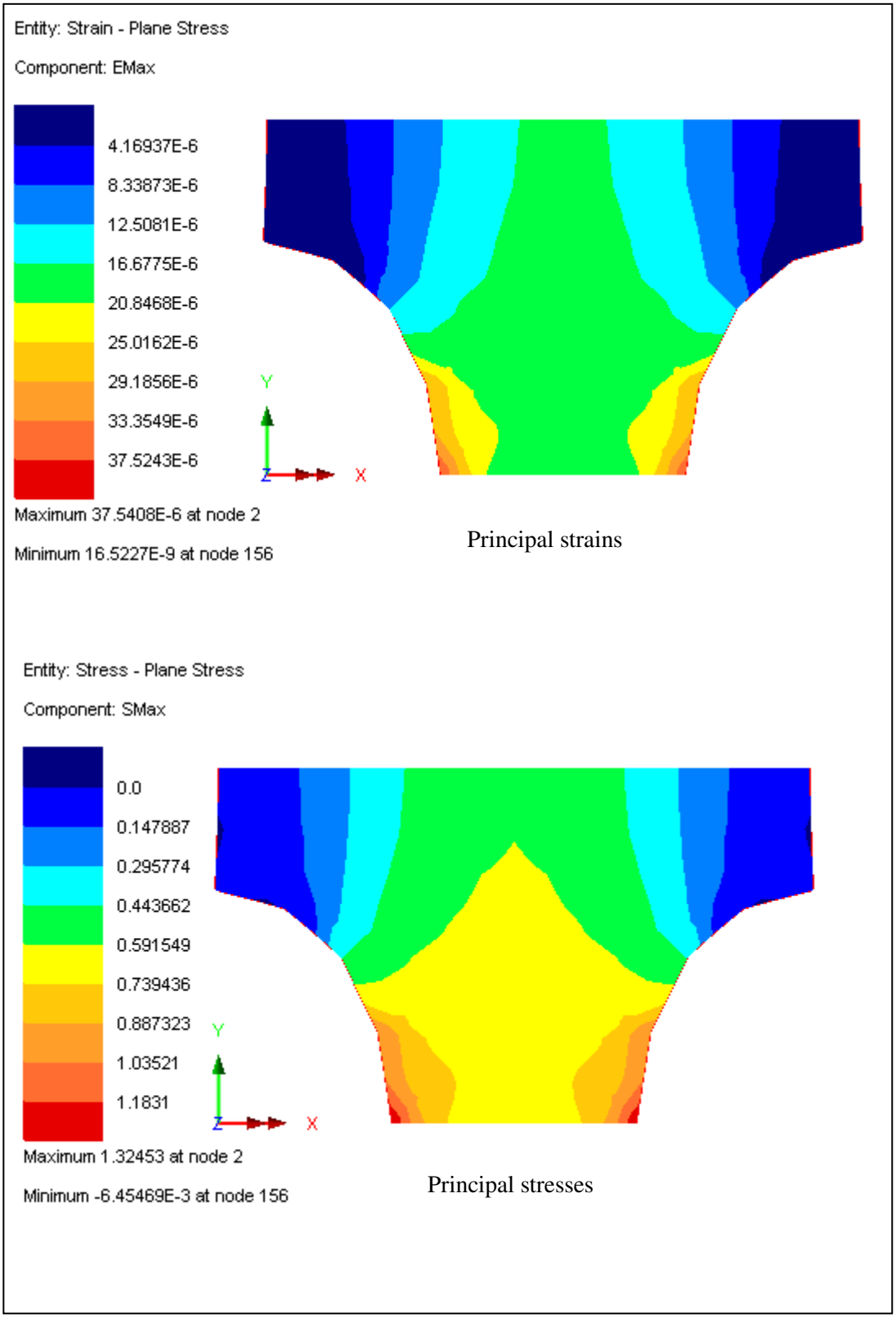

Figure 6.5. Example 1. Principal strain and stress contours at stage A

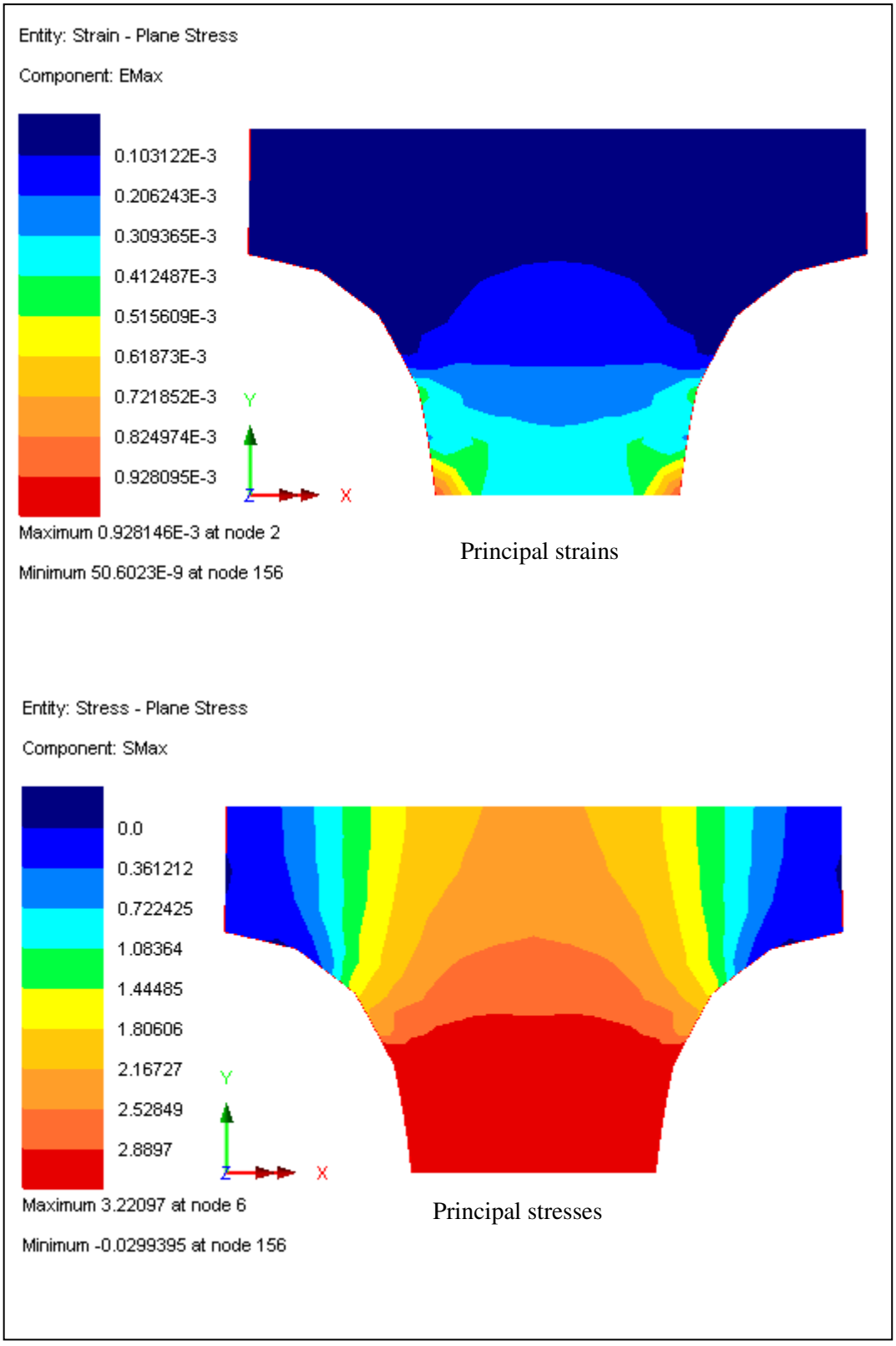

Figure 6.6. Example 1. Principal strain and stress contours at stage B

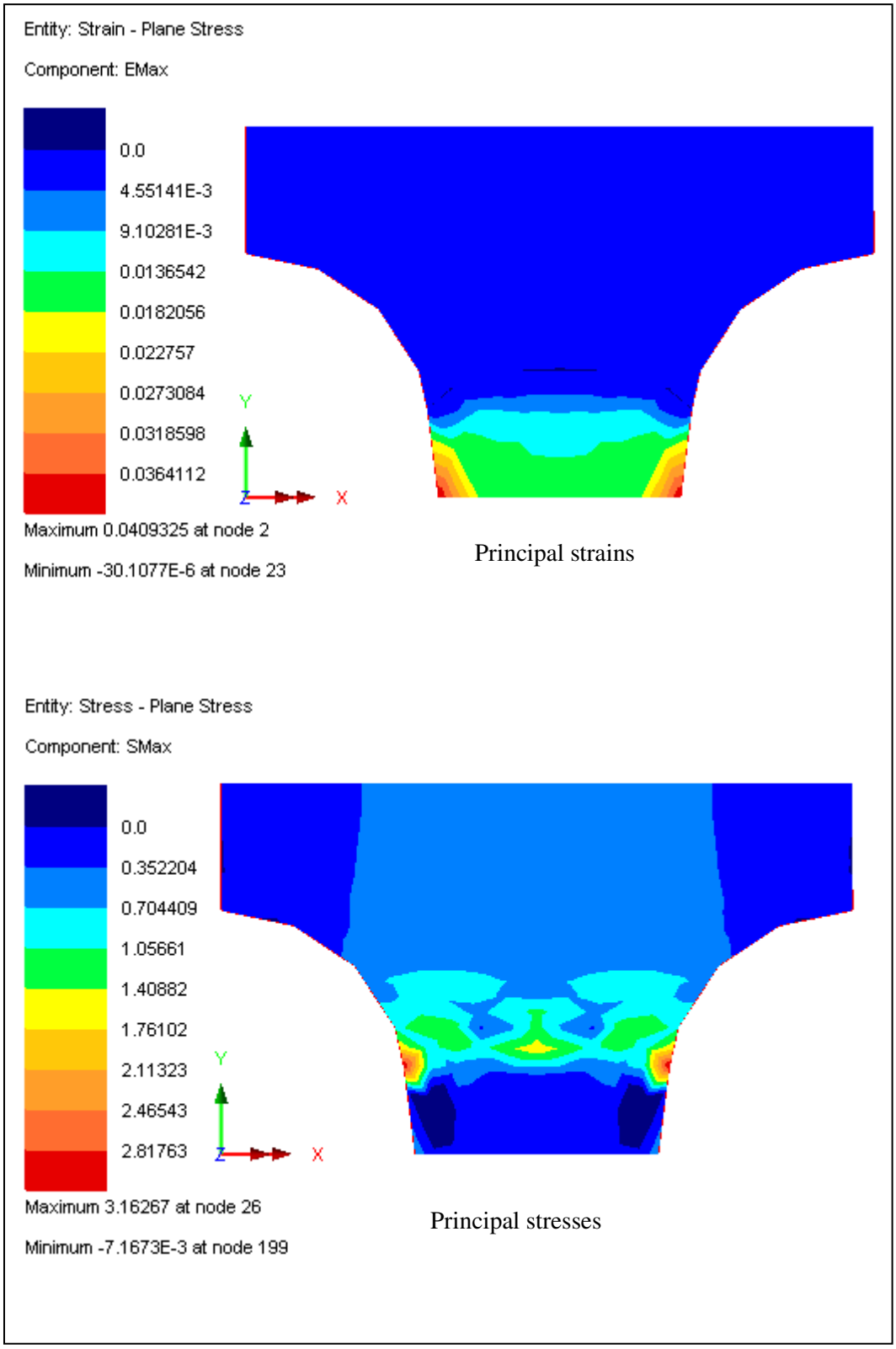

Figure 6.7. Example 1. Principal strain and stress contours at stage C

6.3.2. Example 2. Reinforced concrete beam

The second example presents results from the analysis of a reinforced concrete beam. The specimen, experimentally tested by Bresler and Scordelis (1963), contained only longitudinal reinforcement anchored at both ends with steel plates. A three-point bend test was carried out under load control in which the point load was applied through a steel plate to avoid local crushing. The dimensions of the beam and details regarding the experimental arrangement are shown in Fig 6.8.

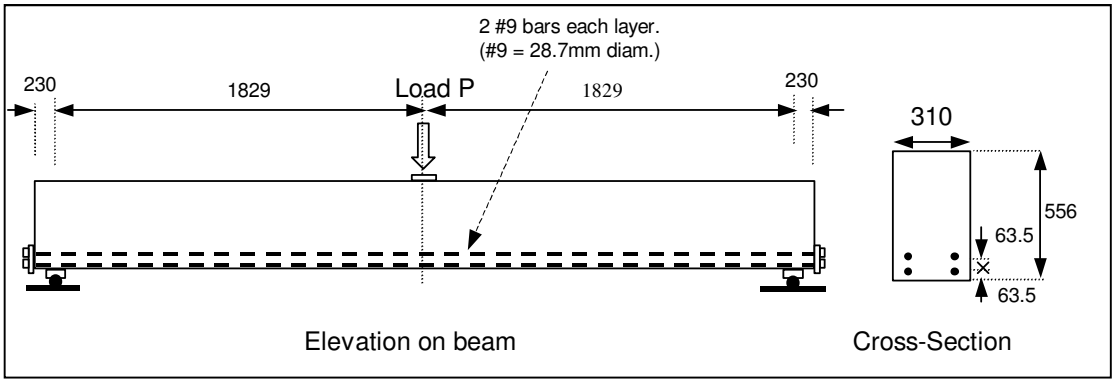

Figure 6.8. Example 2. Geometrical dimensions (mm) and test arrangement

As the specimen, the supports and the load are symmetric with respect to the centre line, only half the beam is analysed. Plots of the mesh employed for the finite element analysis and of the deformed mesh are shown in Fig. 6.9. Boundary conditions are employed such that the support is restrained in Y direction while the nodes on the centre line are restrained in X direction. The material properties employed in the analysis are given in Table 6.3.

Table 6.3. Example 2. Material properties

Material property	**Value**
Concrete	
E (N/mm^2)	20000
υ	0.2
f_t (N/mm^2)	1.6
G_f (N/mm)	0.02
Reinforcement	
E_s (N/mm^2)	205000
υ_s	0.3

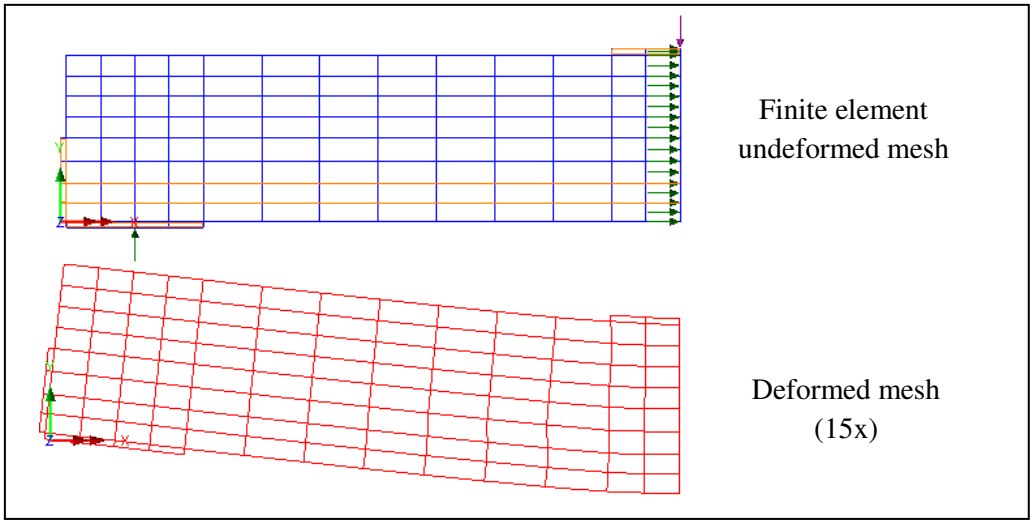

Figure 6.9. Example 2. Finite element meshes

The numerical load-deflection response is compared with the experimental response in Fig 6.10. Plots of the strain contour at different stages, indicated on the load-deflection graph, are presented in Figs 6.11-6.13.

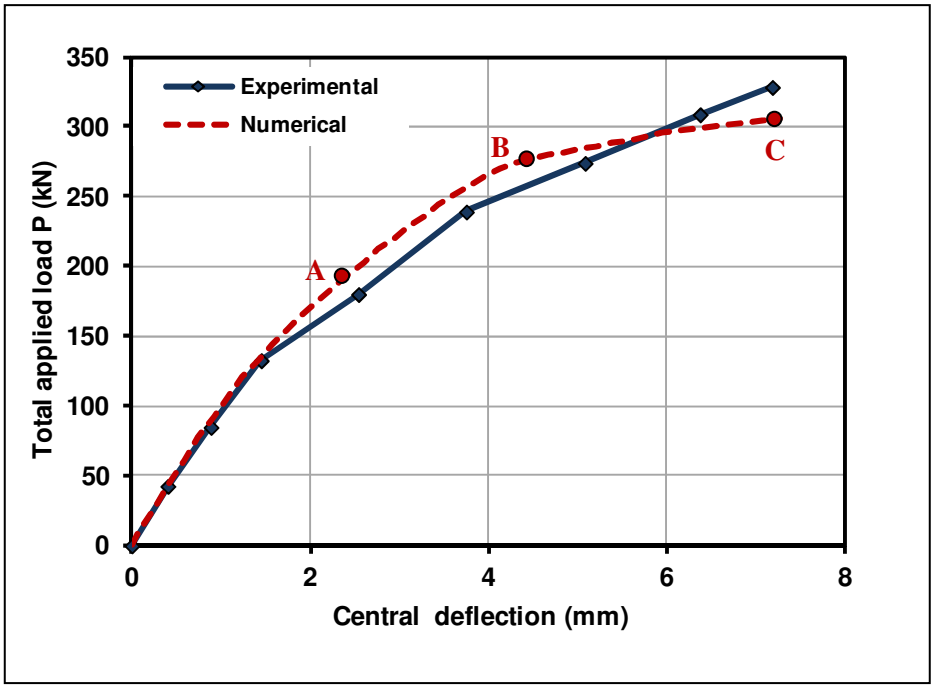

Figure 6.10. Example 2. Load-deflection response

It can be observed from Fig 6.10 that the constitutive model captures the nonlinear behaviour prior to failure of a reinforced concrete beam in a three-point bend test. This suggests that the approach is at least reasonable for modelling a specimen subject to both significant shear and bending.

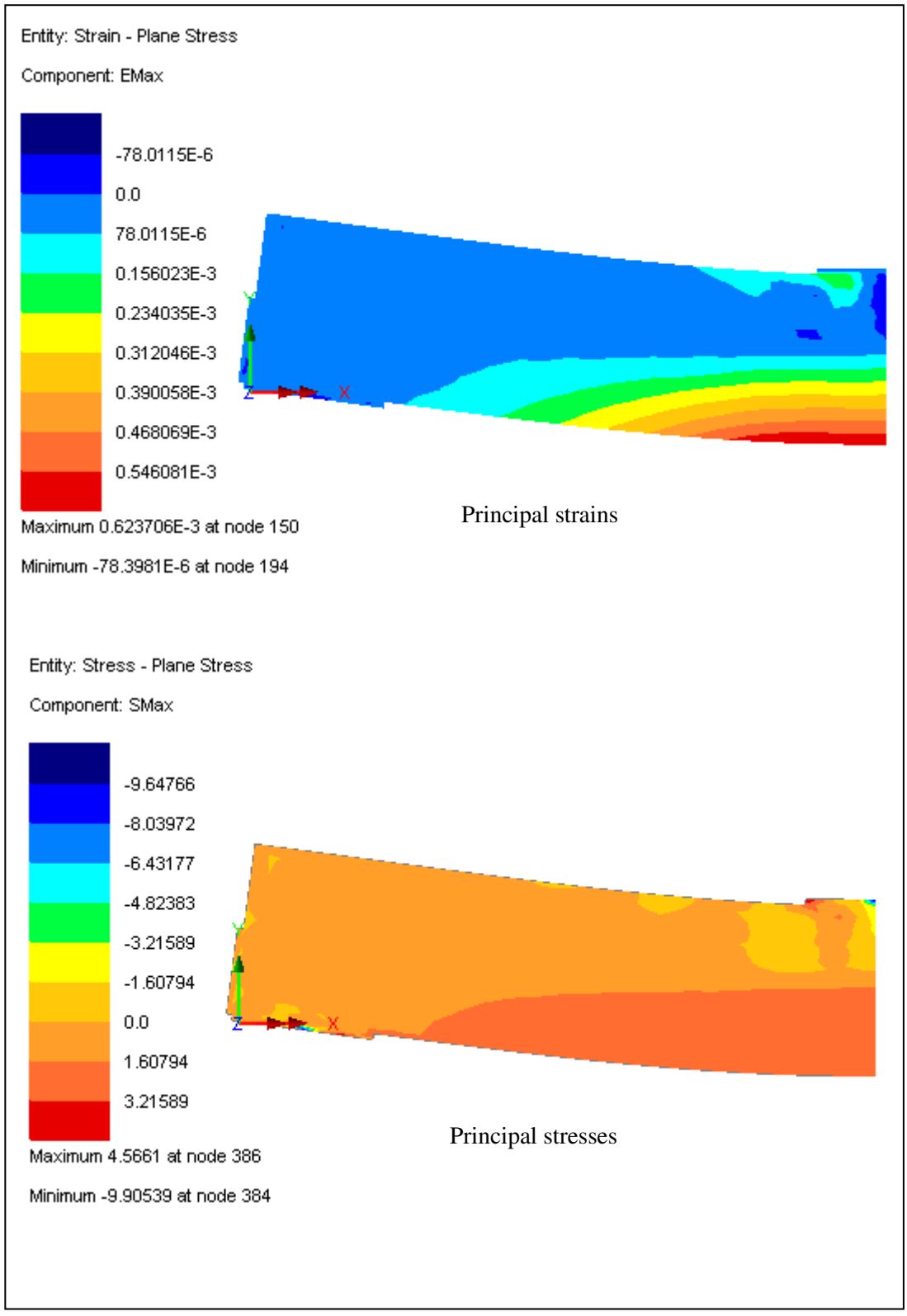

Figure 6.11. Example 2. Principal strain and stress contours at stage A

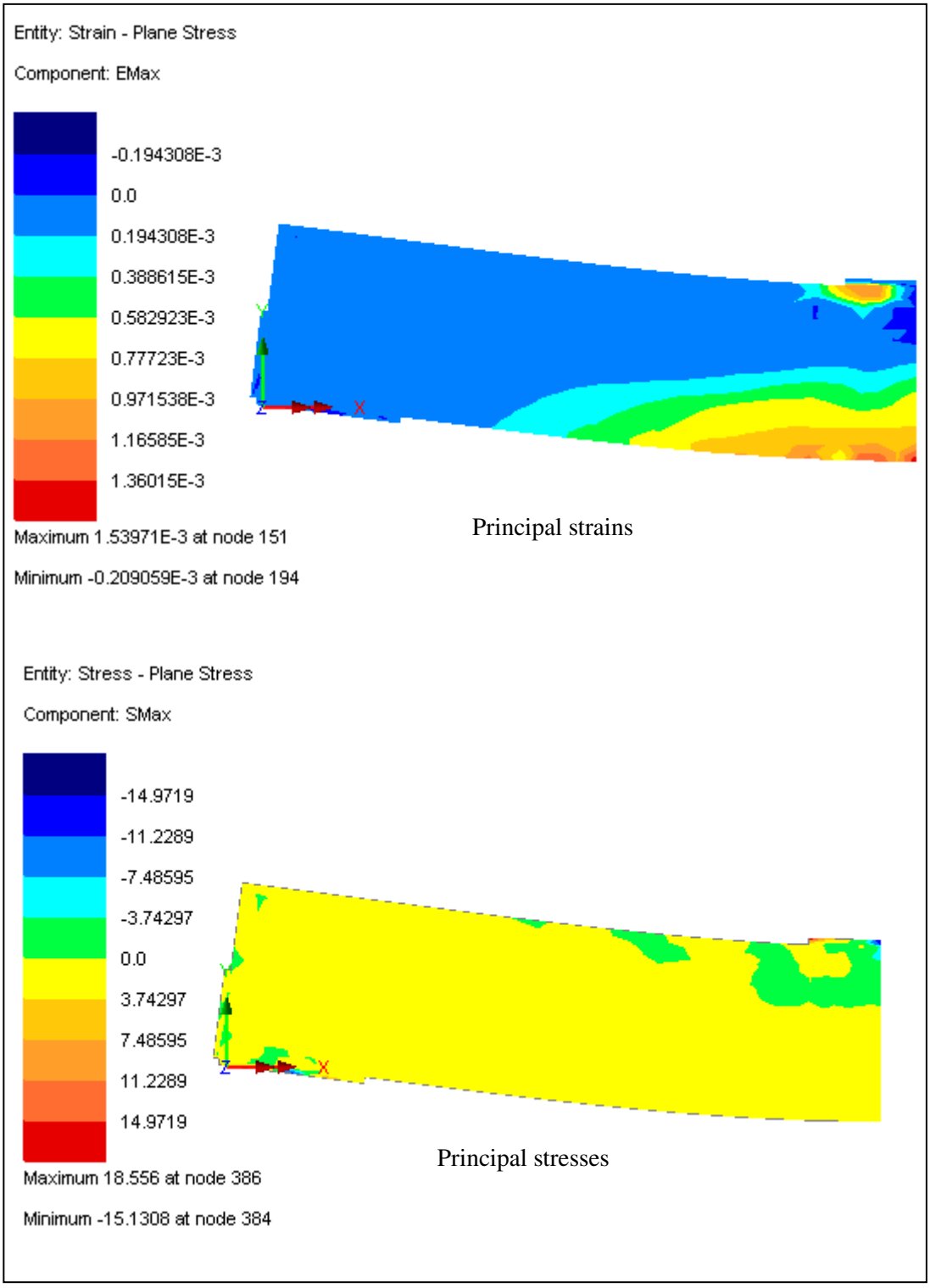

Figure 6.12. Example 2. Principal strain and stress contours at stage B

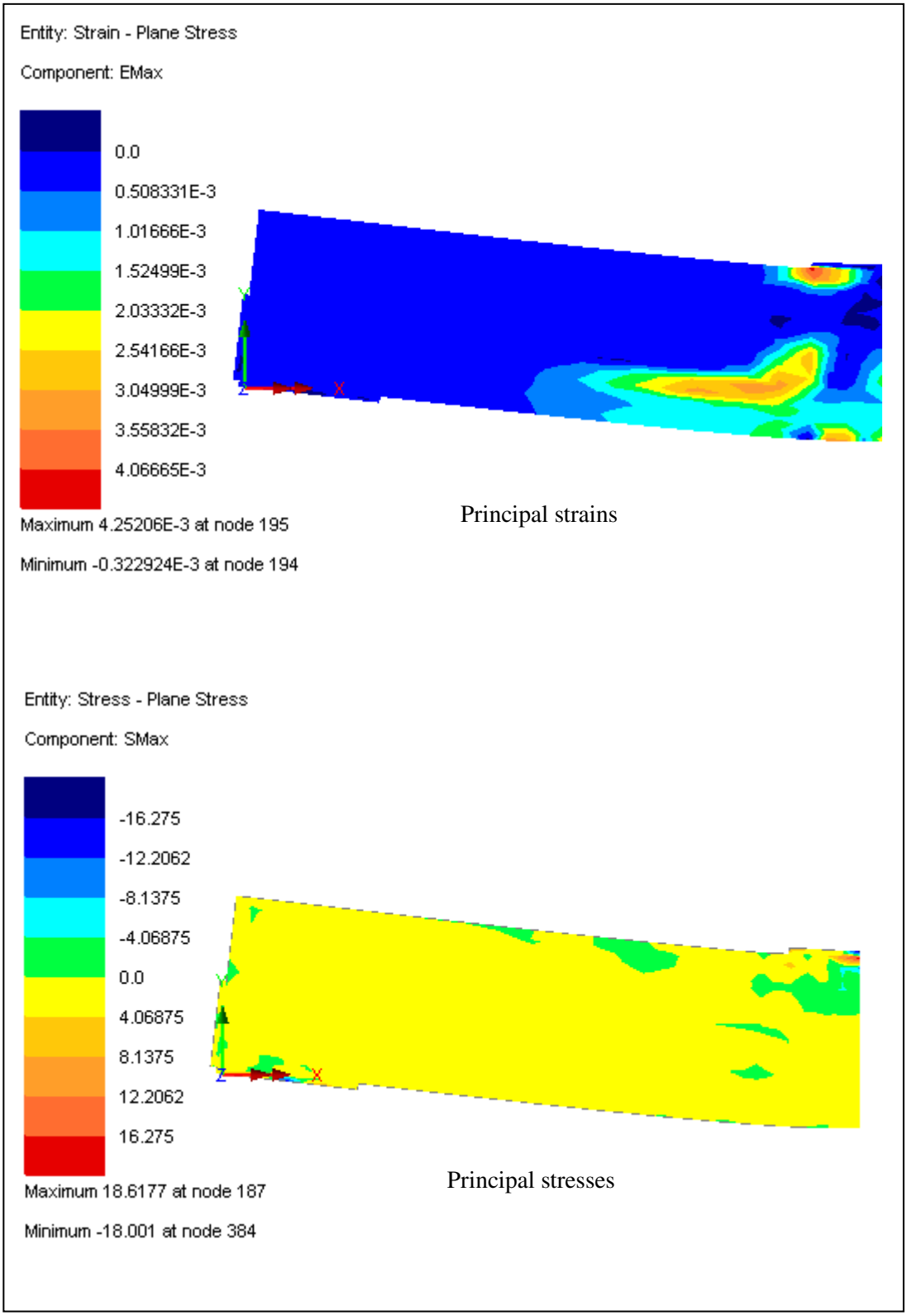

Figure 6.13. Example 2. Principal strain and stress contours at stage C

6.3.3. Example 3. L-shaped panel

In the final example, the analysis of an un-reinforced L-shaped panel experimentally tested by Winkler et al. (2001) is presented. Details regarding the geometry and test arrangement are given in Fig 6.14. The base of the specimen was fully restrained and load F was applied incrementally under displacement control.

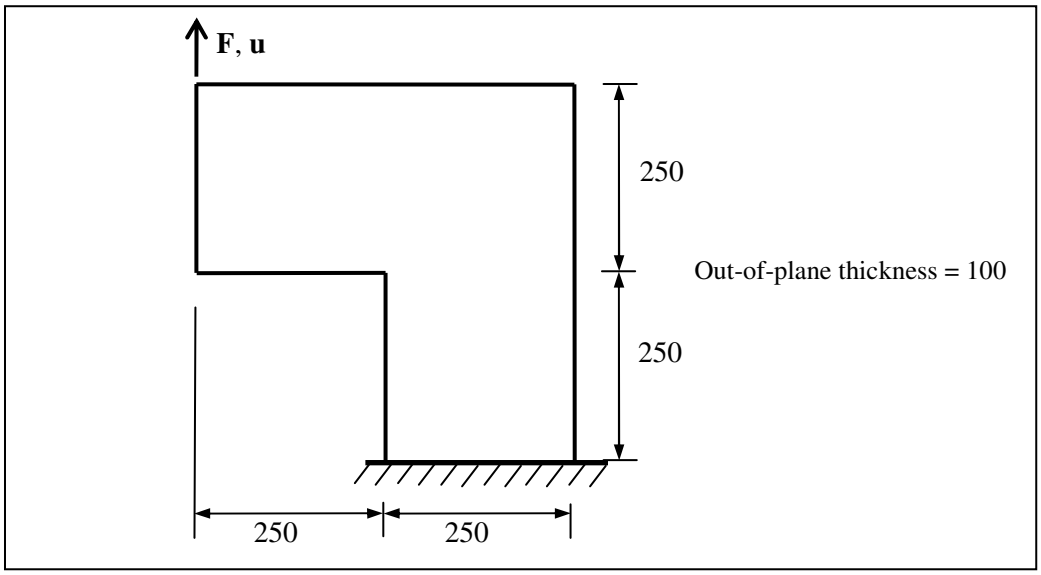

Figure 6.14. Example 3. Geometrical dimensions (mm) and test arrangement

The material properties applied in this example are given in Table 6.4. The mesh employed in the numerical analysis as well as a plot of the deformed mesh is shown in Fig 6.15.

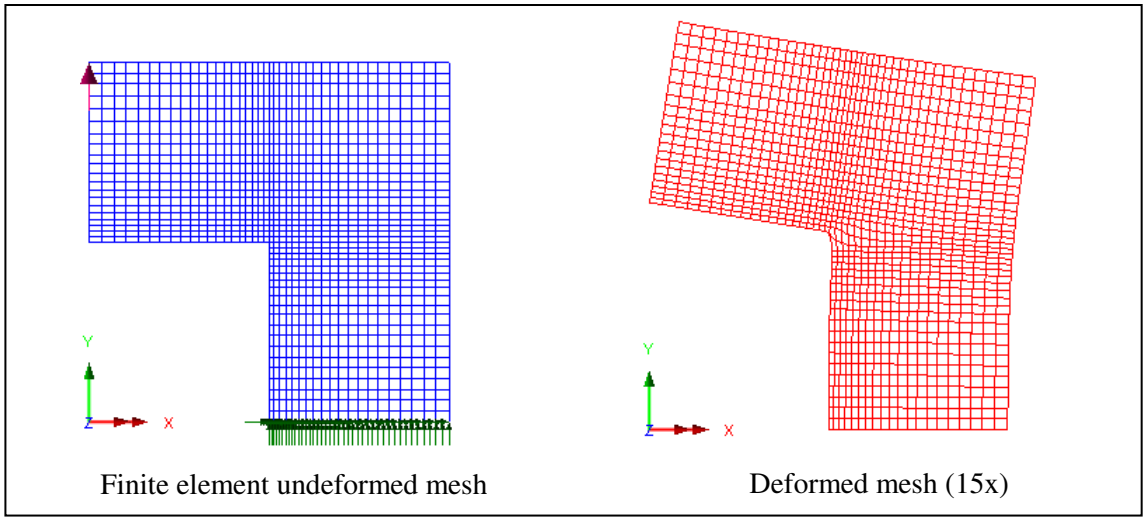

Figure 6.15. Example 3. Finite element meshes

Table 6.4. Example 3. Material properties

Material property	Value
E (N/mm^2)	24500
υ	0.21
f_t (N/mm^2)	1.25
G_f (N/mm)	0.0175

The experimental and numerical load-displacement responses are compared in Fig 6.16. and plots of the strain profile at different stages: A. elastic, B. peak load and C. Softening regime are presented in Figs. 6.17-6.19. The numerical prediction compares reasonably well with the experimental response. It can be observed from Fig 6.18 that around the peak load strains begin to localize which may be taken as the position of a macro-crack. The development of this crack follows a trajectory that is in agreement with crack path reported by Winkler et al. (2001).

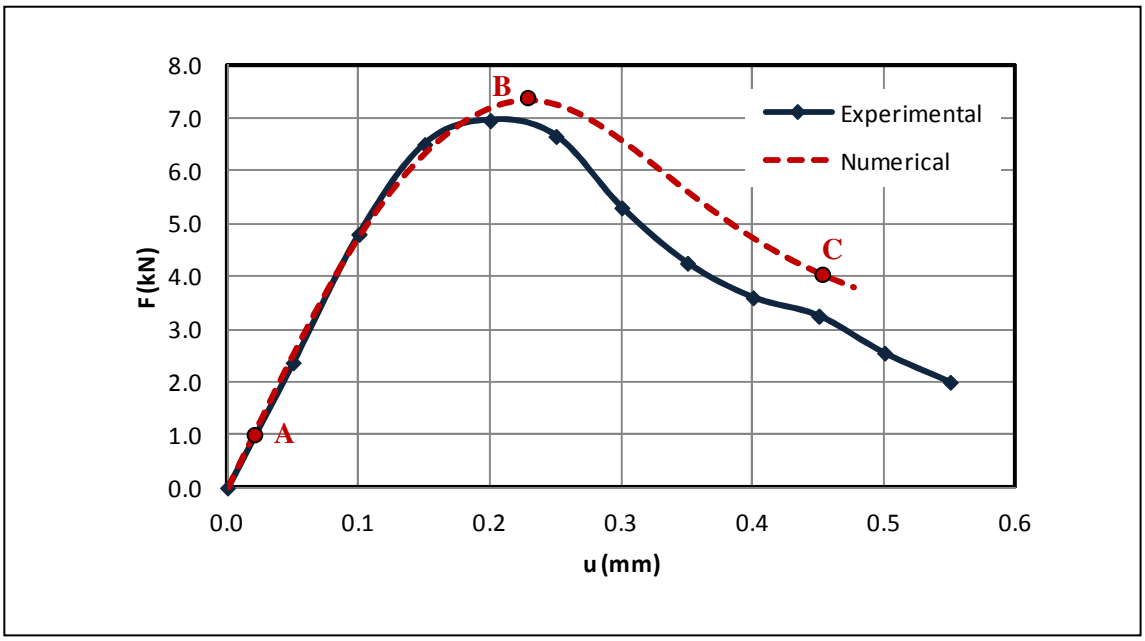

Figure 6.16. Example 3. Load-displacement responses

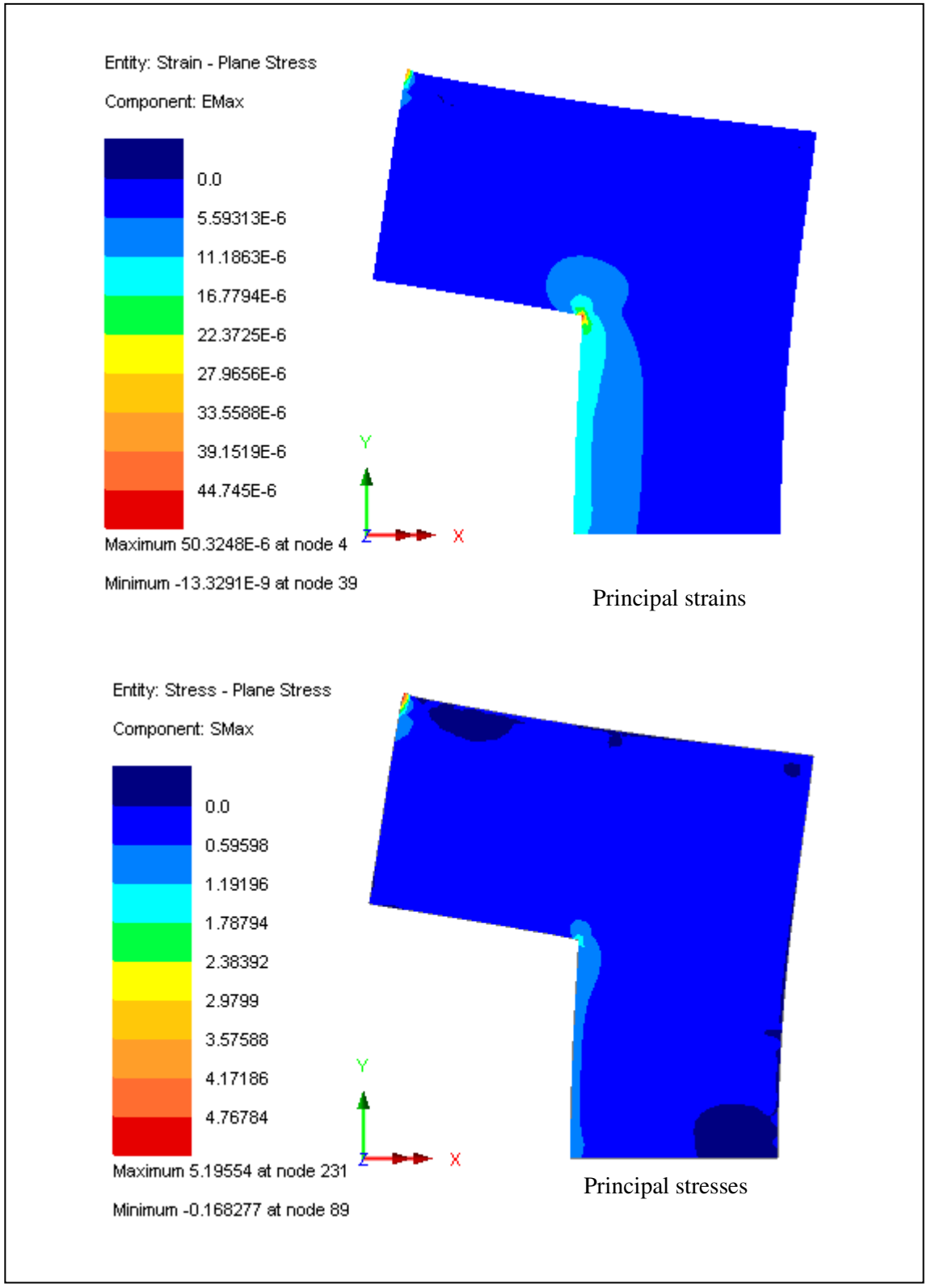

Figure 6.17. Example 3. Principal strain and stress contours at stage A

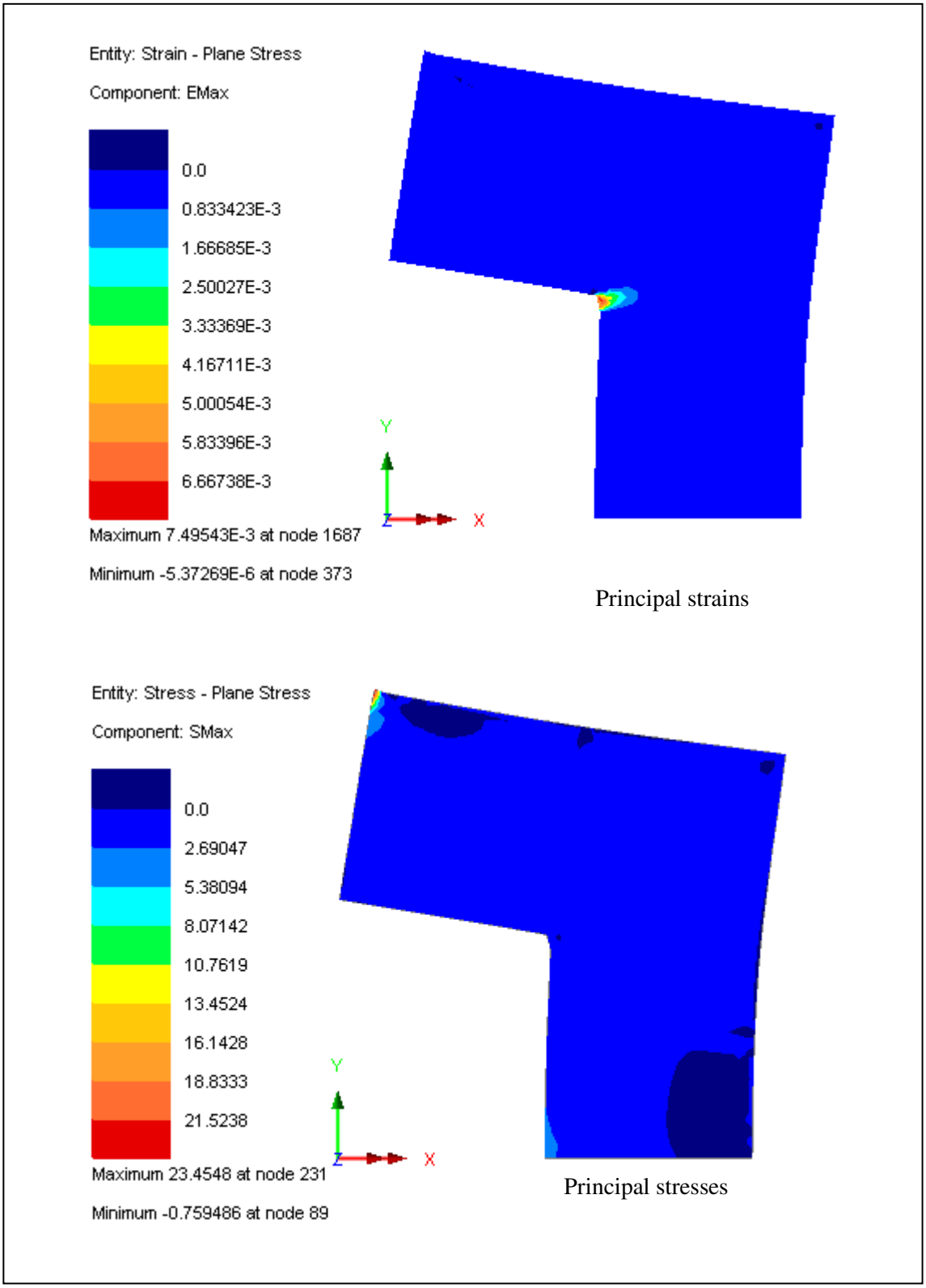

Figure 6.18. Example 3. Principal strain and stress contours at stage B

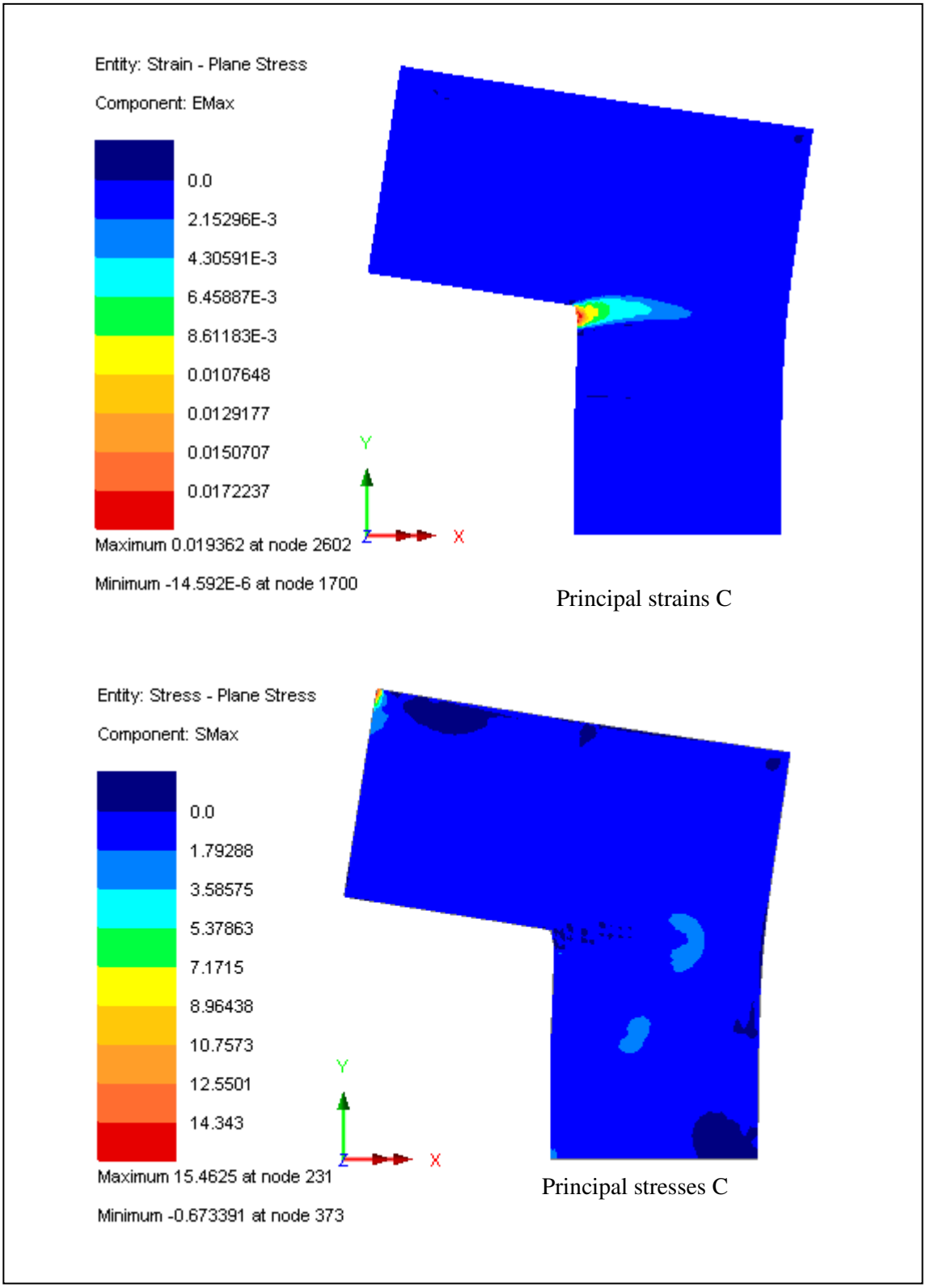

Figure 6.19. Example 3. Principal strain and stress contours at stage C

6.4. Summary and concluding remarks

A 2D simplified version of the micromechanical constitutive model proposed in Chapters 2 and 3 was implemented in the finite element commercial program LUSAS via its material model interface.

A set of finite element simulations of experimental tests was carried out in which the performance of the constitutive model was assessed under various stress states of tension and compression combined with shear. As mentioned in the introduction, this is not an in-depth study but merely constitutes an initial evaluation. Further investigation is required to achieve a comprehensive assessment. Nevertheless, the study presented here clearly demonstrates the potential of the micromechanical model in finite element simulations.

Chapter 7

Discussion and conclusions. Recommendations for future work

7.1. Discussion and conclusions

As discussed in the introduction to this thesis, despite the considerable research efforts of the last five decades, a universal formulation for an accurate and robust mathematical model for concrete, able to capture all facets of the complex behaviour of this material, has not yet been developed. The aim of the work presented in this thesis was to address this long-standing problem and to make progress towards the development of a reliable constitutive model based on micromechanical solutions.

The central focus of this research was the formulation of a constitutive model for concrete, and other cementitious composites based on micromechanical solutions. And to this end, particular attention was paid to developing new mechanistic formulations for micro-crack initiation, evolution and post-crack rough contact.

The approach developed assumes the existence of a representative material element (RME) which is simulated as a two-phase composite comprising a matrix phase –that models the mortar- and spherical inclusions –that represent the coarse aggregate particles. The elastic properties of this composite are derived using an Eshelby solution and the homogenisation scheme adopted is that due to Mori and Tanaka. Microcracking is accounted for by the addition of circular microcracks embedded in the matrix phase.

Finally, the model incorporates a rough microcrack contact component that accounts for the fact that once open, microcracks can regain contact and that shear and normal stresses can be transferred across the crack plane.

The microcrack initiation criterion makes use of the tensile stress concentrations at the matrix-inclusion boundary captured by the exterior point Eshelby solution. Therefore microcracks can be assumed to initiate in the interfacial transition zone between coarse aggregate particles and mortar which is in agreement with experimental observations. In this way, the initiation of damage can be realistically modelled and based on a strong mechanistic rationale. Moreover, the two-phase composite approach enables the realistic simulation on lateral splitting cracks in uniaxial compression. This approach was employed in a previous version of the model proposed by Jefferson and Bennett (2010) however at that time somewhat unrealistic elastic properties needed to be employed to obtain the correct cross cracking response as microcrack initiation was based on the mean matrix stress. The exterior point Eshelby based microcrack initiation criterion facilitated the use of realistic material properties (i.e. measured elastic properties for the two phases and measured mortar-aggregate interface strength parameters) for a correct response. An important and noteworthy aspect of the overall model is that it requires a limited number of measurable parameters and, as shown in section 3.6, the model captures key features of the macroscopic behaviour, namely:

- damage induced anisotropy
- volumetric dilatancy under compressive stress states
- realistic correlation between tensile and compressive strengths, i.e. realistic f_t/f_c ratio
- predictions of ductility consistent with experimental observations
- realistic biaxial failure envelope
- a more favourable prediction of triaxial behaviour than the previous model.

This clearly shows the potential of micromechanical and, in broader terms, mechanistic models which, by simulating simple physical mechanisms at micro and meso-scales, can realistically predict a wide range of characteristic responses.

It should be mentioned however that the formulation presented in Chapters 2 and 3 is not definitive and requires further development. Indeed, whilst the model is capable of reproducing in a realistic manner uniaxial and biaxial tensile and compressive

characteristic responses as well as a very reasonable prediction of triaxial behaviour for low and moderate degrees of confinement, it cannot yet predict the response of all conceivable triaxial stress-strain paths.

Nevertheless, two significant aspects are neglected in the formulation of the rough crack contact model which have a direct effect on the microcrack plane behaviour and ultimately on the overall behaviour, namely friction and crushing on the sides of the asperities.

In order to address this, the multi-asperity plastic-contact crack plane model detailed in Chapter 4 was developed following yet again a mechanistic approach. In this model, a 3D characterization of the crack morphology is employed in which the crack surface is idealised as a series of conical teeth, and corresponding recesses, of variable height and slope. Based on this geometrical characterization, an effective contact function was derived to relate the contact stresses that develop on the sides of the teeth to the net stresses on a crack plane. Plastic embedment and frictional sliding are simulated using a local plasticity model in which the plastic surfaces are expressed in terms of the contact surface function in cylindrical relative displacement space. Additional focus in developing the crack plane model was given to the quantification of the crack surface roughness. A relatively straightforward quantification procedure proposed by Haberfield and Johnston (1994) was employed however a rigorous description of the surface morphology proved difficult due to the lack of comprehensive experimental data. Nevertheless it did prove possible to use direct measurements of crack surface roughness in the model to obtain close matches with the associated experimental mechanical test data without the need for extensive 'parameter fitting'. The main characteristics of non-linear crack plane behaviour which the model can accurately simulate are:

- shear displacement (slip) at constant normal compressive stress causes dilation
- an increase in the normal compression produces, for the same slip, a higher level of shear stress transferred across the crack plane and reduced dilation
- an increase of the crack opening reduces both normal compressive stress and the shear stress (in displacement-controlled tests)
- non-linear coupled shear and normal responses

It should be emphasised that, as the model was developed with mechanistic components, a reduced number of parameters with physical meaning and readily measurable is required.

Several computational aspects regarding the overall constitutive model proposed in Chapters 2 and 3 were discussed in Chapter 5. It was shown that instability problems or chatter behaviour can occur at the constitutive level when multiple microcrack surfaces are active and under various contact conditions. To address this issue, a single smoothed contact function that employs two tanh type interpolation functions was proposed to replace the three separate functions for open, interlock and closed contact states. The smoothed contact state function was shown to be effective at removing chatter and smoothing the model response with the proviso that care was required when selecting the smoothing parameters to ensure that unrealistic responses did not result from the smoothing process. A set of parameters were selected based on a parametric study that did not significantly alter the predicted response while being efficient in smoothing the response and removing chatter.

The accuracy of the integration methods applied to the micromechanical constitutive model was next addressed. 2D and 3D rules were investigated and it was concluded that the integration rules were sufficiently converged for any practical numerical analysis.

In the final part of Chapter 5, the consistent tangent stiffness was derived. The availability of this tangent is important for the efficient numerical performance of the model. The exact tangent was derived for the two phase composite model but it did prove necessary to introduce a slight approximation with respect to the part of the tangent matrix which controls the evolution of the concentrated stresses in the exterior point Eshelby solution. Checks however suggest that this approximation has minimal effect on numerical performance.

Finally, in Chapter 6 an initial assessment of the micromechanical model when implemented in the commercial finite element code LUSAS was presented. In this study a simplified 2D version of the micromechanical model was employed in which concrete was simulated as an elastic matrix weakened by a dilute distribution of penny-shaped microcracks with various orientations. Three analyses of experimental tests were performed in which the performance of the model was assessed in various situations:

direct tension of an unreinforced specimen, tension combined with compression (i.e. bending) and shear in the analysis of a reinforced concrete beam and tension combined with shear in the analysis of an L shaped unreinforced specimen. The results showed that the model could predict realistic responses that compared well against the experimental responses. The author recognizes that more work is needed to fully evaluate the numerical performance of the models in finite element codes but the study presented undoubtedly demonstrates the potential of micromechanical mechanistic models.

As a final conclusion, the work of this thesis demonstrates the potential of the micromechanical approach in achieving a robust and comprehensive constitutive model for concrete. The study presented does, in the author's opinion, certainly demonstrate the capability of the models developed and represent significant progress in the use of micromechanical theories in the constitutive modelling of concrete. Nevertheless further research is required to meet the ultimate objective and, in this regard, recommendations are made below.

7.2. Recommendations for future work

Several aspects that require further research work have already been identified throughout this study and in fact it is the intention of the author to address them during a subsequent post-doctoral research project.

Regarding the further development of the constitutive model, a number of recommendations are made as follows:

- The investigation of several homogenization schemes that would take into account microcrack interaction effects. Although in the present formulation this aspect is believed to have little effect on the overall results a more comprehensive study is considered necessary
- The implementation of the multi-asperity plastic-contact crack-plane model in the overall constitutive model for a more realistic characterization of the crack-plane behaviour. In the author's opinion, the ability of the crack-plane model to realistically predict the crack-plane characteristic behaviour will have a significant and positive effect in obtaining a more favourable triaxial response

- A study on the integration rules for the full constitutive model in order to determine the optimum rule
- A more rigorous geometric quantification of the crack surface morphology based on experimental data obtained from realistic specimens although, as mentioned before, this largely depends on the availability of such data. If profiles of macro-cracks correlated with experimental results for crack-plane behaviour are scarce, information related to microcrack roughness is almost non-existent. The situation however is not without hope as qualitative observations from micrographs and hypotheses based on back-analysis of experimental tests can be of great benefit.
- The employment of statistical distributions to characterize the crack surface roughness. This was done tentatively in Chapter 5. Again experimental data is needed to ultimately validate the proposed probability density functions

Regarding the implementation in a finite element program and the actual finite element analyses employing the constitutive model, the following actions are recommended and intended:

- Implement the proposed 3D model, as well as an enhanced version of model that incorporates the plastic-contact crack-plane formulation, in the finite element code. Of special interest is the investigation of the effect of contact on the robustness of the code. It was shown in Chapter 5 that contact related instability is present, even at a constitutive level, and an interesting aspect would be to investigate the efficiency of the smoothed contact state function in a finite element context.
- Implement the model with a more rigorous regularisation scheme than the crack-band approach used to date.
- Provide a means of transition to fully formed cracks by means of coupling the approach to elements with embedded strong discontinuities

Finally the author would like to mention that the above work will form part of a new Knowledge Transfer Partnership with the company that have sponsored this research (LUSAS), which should mean that the above future work becomes a reality and does not just remain on an indeterminate wish list.

Bibliography

Ali, M.A., White, R.N., 1999. Enhanced contact model for shear friction of normal and high strength concrete. *ACI Structural Journal* 96 (3), 348-360

Andrieux S, Bamberger Y, Marigo JJ., 1986. Un modèle de matériau microfissuré pour les roches et les bétons. *J Mécan Théor Appl*, 5(3), 471–513.

Askes H., Aifantis E.C., 2002. Numerical modelling of size effects with gradient elasticity: Formulation, meshless discretization and examples. *International Journal of Fracture* 117, 347-358

Bache H.H., Nepper-Christensen P., 1965. Observations on strength and fracture in lightweight and ordinary concrete. *The structure of Concrete and its behaviour under load: Proceedings of an International Conference, London. Cement and Concrete Association*, 1968. 93-108

Barton, N., 1973. Review of a shear strength criterion for rock joints. *Engineering Geology* 7, 287-332

Batdorf S.B., Budianski B., 1949. A mathematical theory of plasticity based on the concept of slip. *Thechnical Note No. 1871, National Advisory Committee for Aeronautics,* Washington D.C.

Bažant Z.P., Caner F.C., Carol I., Adley M.D., Akers S.A., 2000. Microplane model M4 for concrete. I: Formulation with work-conjugate deviatoric stress. *Journal of Engineering Mechanics, ASCE*, 126(9), 944–953.

Bažant Z.P., Caner F.C., 2005. Microplane model M5 with kinematic and static constraints for concrete fracture and anelasticity. I: Theory. *Journal of Engineering Mechanics, ASCE*, 131(1), 31–40.

Bažant Z.P., Caner F.C., 2005. Microplane model M5 with kinematic and static constraints for concrete fracture and anelasticity. II: Computation. *Journal of Engineering Mechanics, ASCE*, 131(1), 41–47.

Bažant, Z.P., Gambarova, P., 1980. Rough cracks in reinforced concrete. *Journal of the Structural Division, Proceedings of the ASCE* 106 (4), 819-842

Bažant Z.P., Oh B.H., 1983. Crack band theory for fracture of concrete. *Materials and Structures* 16, 155-177

Bažant Z.P., Oh B.H., 1984. Microplane model for progressive fracture of concrete and rock. *Journal of Engineering Mechanics, ASCE*, 111(4), 559-582

Bažant Z.P., Oh B.H., 1986. Efficient numerical integration on the surface of a sphere. *Zeitschrift für angewandte Mathematik und Mechanik* (ZAMM, Berlin), 66 (1), 37–49.

Bažant Z.P., Ožbolt J., 1990. Nonlocal microplane model for fracture, damage and size effect in structures. *Journal of Engineering Mechanics, ASCE*. 116(11), 2485-2504

Bažant Z.P., Pijaudier-Cabot G., 1988. Nonlocal continuum damage, localization instability and convergence. *Journal of Applied Mechanics, ASME* 55, 287-293

Bažant Z. P. and Prat P., 1988. Microplane model for brittle plastic materials. I: Theory, II: Verification. *Journal of Engineering Mechanics, ASCE*, 114, 1672-1702.

Belytschko T., Black T., 1999. Elastic crack growth in finite elements with minimal remeshing. *International Journal for Numerical Methods in Engineering* 45, 601-620

Belytschko T., Moës N., Usui S., Parimi C., 2001. Arbitrary discontinuities in finite elements. *International Journal for Numerical Methods in Engineering* 50, 993-1013

Bernard O., Ulm F-J., Lemarchand E., 2003. A multiscale micromechanics-hydration model for the early-age elastic properties of cement-based materials. *Cement and Concrete Research*, 33(9), 1293-1309

Birkeland P.W., Birkeland, H.W., 1966. Connections in precast concrete construction. *Journal of the American Concrete Institute*, 345-368

Boussa H., Tognazzi-Lawrence C., La Borderie C., 2001. A model for computation of leakage through damaged concrete structures. *Cement & Concrete Composites* 23, 279-287

Brencich A., Gambarotta L., 2001. Isotropic damage model with different tensile-compressive response for brittle materials. *International Journal of Solids and Structures*, 38, 5865-5892

Bresler B., Scordelis A.C., 1963. Shear strength of reinforced concrete beams. *Journal of the American Concrete Institute*, January, 51-72

Budiansky B., O'Connell R.J., 1976. Elastic moduli of a cracked solid. *International Journal of Solids and Structures* 42, 81-97

Bujadham B., Maekawa K., 1992. The universal model for stress transfer across cracks concrete. *Procurment of the Japan Society of Civil Engineers* 17(451), 277-287

Caliskan S., Karihaloo B.L., Barr B.I.G., 2002. Study of rock-mortar interfaces. Part I: surface roughness of rock aggregates and microstructural characteristics of interface. *Magazine of Concrete Research* 54(6), 449-461

Caner F.C., Bažant Z.P., 2000. Microplane model M4 for concrete. II: Algorithm and calibration. *Journal of Engineering Mechanics, ASCE*, 126(9), 944–953.

Carol I., Jirasek M., Bažant Z.P., 2001. A thermodynamically consistent approach to microplane theory. Part I. Free energy and consistent microplane stresses. *International Journal of Solids and Structures* 38, 2921-2931

Carol I., Prat P.C., Bažant Z.P., 1992. New explicit microplane model for concrete: Theoretical aspects and numerical implementation. *International Journal of Solids and Structures* 29(9), 1173-1191

Chaboche J.L., 1979. Le concept de contrainte effective appliquee a l'elasticite ea a viscoplasticite en presence d'un endommagement anisotrope. *Colloquium Euromech 115, Grenoble*

Cicekli U., Voyiadjis G.Z., Abu Al-Rub R.K., 2007. A plasticity and anisotropioc damage model for plain concrete. *International Journal of Plasticity* 23, 1874-1900

Comi C., Perego U., 2001. Fracture energy based bi-dissipative damage model for concrete. *International Journal of Solids and Structures* 38, 6427-6454.

Contrafatto L., Cuomo M., 2006. A framework of elastic-plastic damaging model for concrete under multiaxial stress states. *International Journal of Plasticity* 22, 2272-2300

Crisfield M.A., 1997. Non-linear Finite Element Analysis of Solids and Structures. Volume 2. Advanced topics. Wiley

de Borst R., 2002. Fracture in quasi-brittle materials: a review of continuum damage-based approaches. *Engineering Fracture Mechanics* 69, 96-112

Deeb R., Ghanbari A., Karihaloo B.L., 2011. Development of self-compacting high and ultra high performance concretes with and without steel fibres. *Cement and Concrete Composites*, In Press, Corrected Proof. doi:10.1016/j.cemconcomp.2011.11.001

Desmorat R., Gatuingta F., Ragueneaua F., 2007. Non-local anisotropic damage model and related computational aspects for quasi-brittle materials. *Engineering Fracture Mechanics* 74(10), 1539-1560

di Prisco M., Mazars J., 1996 Crush-crack: a non-local damage model for concrete. *Mechanics of Cohesive Frictional Materials* 1, 321-347

Divakar M.P., Fafitis A., Shah S.P., 1987. Constitutive model for shear transfer in cracked concrete. *Journal of Structural Engineering, ASCE* 113 (5), 1046-1062

Dormieux L., Kondo D., Ulm F.-J., 2006. Microporomechanics. John Wiley & Sons Ltd. West Sussex, UK

Elaqra H., Godin N., Peix G., R'Mili M., Fantozzi G., 2007. Damage evolution analysis in mortar during compressive loading using acoustic emission and X-ray tomography: Effects of the sand/cement ratio. *Cement and Concrete Research* 37, 703-713

Este G., Willam K., 1994. Fracture energy formulation for inelastic behaviour of plain concrete. *Journal of Engineering Mechanics ASCE* 120(9), 1983-2011

Farhat F.A., Nicolaides D., Kanellopoulos A., Karihaloo B.L., 2007. CARDIFRC-performance and application to retrofitting, *Engineering Fracture Mechanics* , 74, 151-167

Faria R., Oliver J., Cervera M., 1998. A strain-based plastic viscous-damage model for massive concrete structures. *International Journal of Solids and Structures* 35(14), 1533-1558

Feenstra P.H., de Borst R., 1995. A plasticity model and algorithm for mode-I cracking in concrete. *International Journal for Numerical Methods in Engineering* 38, 2509-2529

Feenstra P.H., de Borst R., Rots J.G., 1991a. Numerical study on crack dilatancy. I: Models and stability analysis. *Journal of Engineering Mechanics, ASCE* 117(4), 733-753

Feenstra P.H., de Borst R., Rots J.G., 1991b. Numerical study on crack dilatancy. II: Applications. *Journal of Engineering Mechanics, ASCE* 117(4), 754-769

Gambarotta L., 2004. Friction-damage coupled model for brittle materials. *Engineering Fracture Mechanics* 71, 824-836

Gambarotta L., Lagomarsino S., 1993. A microcrack damage model for brittle materials. *International Journal of Solids and Structures*, 30, 177-198

Gentier S., Riss J., Archambault G., Flamand R., Hopkins D., 2000. Influence of fracture geometry on shear behaviour. *International Journal of Rock Mechanics and Mining Sciences* 37, 161-174

Gerstle K.H., Linse D.L., Bertacchi P., Kotosovos M.D., Ko H-Y, Newman J.B., Rossi P., Schickert G., Taylor M.A, Traina L.A., Zimmerman R.M. and Bellotti R., 1978. Strength of concrete under multiaxial stress states, in *Proceedings Douglas McHenry International Symposium on 'Concrete and Concrete Structures'*, ACI SP 55, American Concrete Institute, Detroit, Mi, 103-131

Gitman I.M., 2006. Representative volumes and multi-scale modelling of quasi-brittle materials. *PhD Thesis,* Delft University of Technology: TU Delft, the Netherlands

Gitman I.M., Askes H., Sluys L.J., 2007 Representative Volume: existence and size determination, *Engineering Fracture Mechanics*, **74**, 2518-2534.

Gitman I.M., Askes H., Sluys L.J., 2008. Coupled-volume multi-scale modelling of quasi-brittle material. *European Journal of Mechanics A/Solids* 27, 302-327

Grasselli G., Egger P., 2003. Constitutive law for the shear strength of rock joints based on three-dimensional surface parameters. *International Journal of Rock Mechanics and Mining Sciences* 40, 25-40

Grassl P., Jirásek M., 2006. Damage-plastic model for concrete failure. *International Journal of Solids and Structures* 43, 7166-7196

Grassl P., Lundgren K.G., Gylltoft K., 2002. Concrete in compression: a plasticity theory with a novel hardening law. *International Journal of Solids and Structures* 39, 5205-5223

Haberfield C.M., Johnston I.W., 1994. A mechanistically-based model for rough crack joints. *International Journal of Rock Mechanics Mining Sciences & Geomechanics Abstracts* 31 (4), 279-292

Han D.J., Chen W.F., 1985. A nonuniform hardening plasticity model for concrete materials. *Mechanics of Materials* 4, 238-302

Hasegawa T., Bažant Z.P., 1993. Nonlocal microplane concrete model with rate effect and load cycles. I: General formulation. *Journal of Material in Civil Engineering*, 5(3), 394-410.

Hellmich Ch., Barthélémy J-F., Dormieux L.,2004. Mineral-collagen interactions in elasticity of bone ultrastructure - A continuum micromechanics approach. *European Journal of Mechanics- A/Solids* 783-810.

Hinton E., Owen D.R.J., 1977. Finite Element Programming. *Academic Press,* London, UK

Hordijk D.A., 1991. Local approach to fatigue of concrete, PhD Thesis Delft University of Technology, The Netherlands

Hofstetter K., Hellmich C., Eberhardsteiner J., 2005. Development and experimental verification of a continuum micromechanics model for the elasticity of wood. *European Journal of Mechanics- A/Solids* 24,1030-1053.

Hsu T.T.C., Slate F.O., 1963. Tensile bond strength between aggregate and cement paste or mortar. *Journal of the ACI* 60(4), 465-486

Huang T.H., Chang C.S., Chao C.Y., 2002. Experimental and mathematical modelling for fracture of rock joint with regular asperities. *Engineering Fracture Mechanics* 69, 1977-1996

Huang S., Zhou L., Zhou J., Ge Z., 2012. Study on waste concrete as reclaimed fine aggregate. *Applied Mechanics and Materials* 121-126, 2942-2945

Jefferson A.D., 2002. Constitutive modelling of aggregate interlock in concrete. *International Journal for Numerical and Analytical Methods in Geomechanics* 26, 515-535

Jefferson A.D., 2003. Craft – a plastic–damage–contact model for concrete. I. Model theory and thermodynamic Considerations. *International Journal of Solids and Structures* 40, 5973–5999

Jefferson A.D., Bennett T., 2007. Micro-mechanical damage and rough crack closure in cementitious composite materials. *International Journal for Numerical and Analytical Methods in Geomechanics* 31(2), 133-146

Jefferson A.D., Bennett T., 2010**.** A model for cementitious composite materials based on micro-mechanical solutions and damage-contact theory. *Computers and Structures* 88, 1361-1366

Jefferson A.D., 2010. Finite element material models for concrete. *Proceedings of The Tenth International Conference on Computational Structures Technology (CST2010)*, Valencia, Review Paper

Jennings H.M., Bullard J.W., 2011. From electrons to infrastructure: Engineering concrete from the bottom up. *Cement and Concrete Research* 41(7), 727-735

Jensen B.C., 1975 Lines of discontinuity for displacements in the theory of plasticity of plain and reinforced concrete. *Magazine of Concrete Research* 27(92), 143-150

Jirasek M., Zimmermann T., 1998. Rotating crack model with transition to scalar damage. *Journal of Engineering Mechanics, ASCE,* 124, 277-284

Ju J.W., Chen T,M., 1994. Micromechanics and effective elastoplastic behavior of two-phase metal matrix composites. *Journal of Engineering Materials and Technology, ASME,* 116, 310-218

Ju J.W., Lee H.K., 2001. Micromechanical damage model for effective elastoplastic behaviour of partially debonded ductile matrix composites. *International Journal of Solids and Structures* 38, 6307-6332

Ju J.W., Sun L.Z., 1999. A Novel Formulation for the Exterior-Point Eshelby's Tensor of an Ellipsoidal Inclusion. *Journal of Applied Mechanics* 66, 570 – 574

Ju J.W., Sun L.Z., 2001. Effective Elastoplastic Behaviour of Metal Matrix Composites Containing Randomly Located Aligned Spheroidal Inhomogeneities. Part I: Micromechanics-Based Formulation. *International Journal of Solids and Structures* 38, 183-201

Ju J.W., Tseng K.H., 1996. Effective elastoplastic behaviour of two-phase ductile matrix composites: a micromechanical framework. *International Journal of Solids and Structures* 33(29), 4267-4291

Kang H.D., Willam K.J., 1999. Localization characteristics of triaxial concrete model. *Journal of Engineering Mechanics, ASCE.* 125(8), 941-950

Karihaloo B.L., Wang J., 1997a. On the solution of doubly periodic array of cracks. *Mechanics of Materials*, 26, 209-212

Karihaloo B.L., Wang J., 1997b. Micromechanical modelling of strain hardening and tension softening in cementitious composites. *Computational Mechanics,* 19, 453-462

Karihaloo B.L., Wang J., Grzybowski, M., 1996. Doubly periodic arrays of bridged cracks and short fibre-reinforced cementitious composites. *Journal of the Mechanics and Physics of Solids,* 44(10), 1565-1586

Karihaloo B.L., Xiao Q.Z., 2003. Modelling of stationary and growing cracks in FE framework without remeshing: a state-of-the-art review. *Computers and Structures* 81, 119-129

Kim B.R., Lee H.K., 2009. An RVE-based micromechanical analysis of fiber-reinforced

composites considering fiber size dependency. *Composite Structures*, 90(4), 418-427

Kupfer H.B., Hilsdorf H.K., Ruch H., 1969. Behaviour of concrete under biaxial stresses. *Journal of the ACI*. 66(8), 656-666

Krajcinovic D., Fonseka G.U., 1981. The continuous damage theory of brittle materials. Part I: General theory. *Journal of Applied Mechanics ASME* 48, 809-815

Komnitsas K., Zaharaki D., 2007. Geopolymerisation: A review an prospects for the minerals industry. *Minerals Engineering*, 20, 1261-1277

Lee H.S., Park I.J., Cho T.F., You K.H., 2001. Influence of asperity degradation on the mechanical behavior of rough rock joints under cyclic shear loading. *International Journal of Rock Mechanics and Mining Sciences* 38, 967-980

Lee J., Fenves G.L., 1998. Plastic-damage model for cyclic loading of concrete structures. *Journal of Engineering Mechanics, ASCE* 124(8) 892-900

Lemaitre J., Desmorat R., 2005. Engineering Damage Mechanics. Ductile, Creep, Fatigue and Brittle Failures. Springer-Verlag Berlin Heidelberg, The Netherlands

Li B., Maekawa K., Okamura, H., 1989. Contact density model for stress transfer across cracks in concrete. *Journal of the Faculty of Engineering, the University of Tokyo* 40 (1), 9-52

Li S., Sauer R.A., Wang G., 2007. The Eshelby Tensors in a Finite Spherical Domain – Part I: Theoretical Formulations. *Journal of Applied Mechanics* 74, 770 – 783

Li S., Wang G., 2008. Introduction to Micromechanics and Nanomechanics. *World Scientific Publishing*, Singapore

Lopez C.M., Carol I., Aguado A., 2007. Meso-structural study of concrete farcture using interface elements. I: Numerical model and tensile behaviour. *Journal of Materials and Structures*, 41(3), 583-599

Lubliner J., Oliver J., Oller S., Oñate E. 1989. A plastic damage model for concrete. *International Journal of Solids and Structures* 25(3), 299-326

Maekawa K., Okamura H., 1983. The deformational behaviour and constitutive equation of concrete using the elasto-plastic and fracture model. *Journal of the Faculty of Engineering of Tokyo*, Series B37, 253.

Marfia S., Rinaldi Z., Sacco E., 2004. Softening behaviour of reinforced concrete beams under cyclic loading. *International Journal of Solids and Structures* 41, 3293-3316

Mazars J., 1984. Application de la méchanique de l'endommagement au comportement

non linéare et à la rupture du béton de structure. *PhD thesis*. Université Paris VI

Mazars J., 1986. A description of micro- and macroscale damage of concrete structures. *Engineering Fracture Mechanics* 25(5/6), 729-737

Mazars J., Pijaudier-Cabot G., 1989. Continuum damage theory – application to concrete. *Journal of Engineering Mechanics, ASCE* 115(2), 345-365

Moës N., Dolbow J., Belytschko T., 1999. A finite-element method for crack growth without remeshing. *International Journal for Numerical Methods in Engineering* 46, 131-150

Monteiro P.J.M., Maso J.C, Ollivier J.P., 1985. The aggregate-mortar interface. *Cement and Concrete Research* 15(6), 953-958

Mouret M., Bascoul A., Escadeillas G., 1999. Microstructural features of concrete in relation to initial temperature – SEM and ESEM characterization. *Cement and Concrete Research* 29, 369-375

Mura T., 1987. Micromechanics of Defects in Solids. Second, revised edition *Kluwer Academic Publishers*, Dordrecht, the Netherlands

Nanthagopalan P., Santhanam M., 2011. Fresh and hardened properties of self-compacting concrete produced with manufactured sand. *Cement and Concrete Composites* 33 (3), 353-358

Nemat-Nasser S., Hori M., 1993. Micromechanics: Overall properties of heterogeneous materials. North-Holland.

Newman J.B., 1979. Concrete under complex stress, in: Lydon, F.D., Developments in concrete technology – 1. *Applied Science Publishers*, London

Ngo D., Scordelis A.C., 1967. Finite element analysis of reinforced concrete beams. *Journal of the American Concrete Institute* 64, 152-163

Nguyen G.D., 2005. A thermodynamic approach to constitutive modelling of concrete using damage mechanics and plasticity theory. *PhD thesis,* University of Oxford, Oxford, UK

Nguyen G.D., Korsunsky A.M., 2008. Development of an approach to constitutive modelling of concrete: Isotropic damage coupled with plasticity. *International Journal of Solids and Structures* 45, 5483-5501

Nichols A.B., Lange D.A., 2006. 3D surface image analysis for fracture modelling of cement based materials. *Cement and Concrete Research* 36, 1098-1107

Oliver J., Husepe A.E., Pulido M.D.G., Chaves E., 2002. From continuum mechanics to fracture mechanics: the strong discontinuity approach. *Engineering Fracture Mechanics* 69, 113-136

Oliver J., Husepe A.E., Samaniego E., 2003. A study on finite elements for capturing strong discontinuities. *International Journal for Numerical Methods in Engineering* 56, 2135-2161

Oliver J., Huespe A.E., Samaniego E. Chaves W.V., 2004. Continuum approach to the numerical simulation of material failure in concrete. *International Journal for Numerical and Analytical Methods in Geomechanics* 28, 609–632.

Oliver J., Huespe A.E., 2004. Continuum approach to material failure in strong discontinuity settings. *Comput Methods in Applied Mechanics and Engineering* 193, 3195–3220.

Ollivier J.P., Maso J.C., Borduette B., 1995. Interfacial transition zone in concrete. *Advanced Cement Based Materials* 2, 30-38

Ortiz M., 1985. A constitutive theory for the inelastic behaviour of concrete. *Mechanics of Materials* 4, 67-93

Ouyang C., Mobasher B., Shah S., 1990. An R-curve approach for fracture of quasi-brittlematerials. *Engineering Fracture Mechanics*, 37, 901-913

Owen D.R.J., Hinton E., 1980. Finite Elements in Plasticity: Theory and Practice. *Pineridge Press Limited,* Swansea, UK

Ožbolt J., Bažant Z.P., 1992. Microplane model for cyclic triaxial behavior of concrete, *Journal of Engineering Mechanics, ASCE*. 118(7), 1365-1386

Patton F.D., 1966. Multiple modes of shear failure in rock. *Proceedings of the 1st Congress of the International Society of Rock Mechanics*, Lisbon, 509-513

Paulay T., Loeber P.J., 1974. Shear transfer by aggregate interlock. *Special Publication SP42, American Concrete Institute*, 1-15

Peerlings R.H.J., de Borst R., Brekelmans W.A.M., de Vree J.H.P., 1996. Gradient enhanced damage for quasi-brittle materials. *International Journal for Numerical and Analytical Methods in Geomechanics* 39, 3391-3403

Peerlings R.H.J., de Borst R., Brekelmans W.A.M., Geers M.G.D., 1998. Gradient-enhanced damage modelling of concrete fracture. *Mechanics of Cohesive-Frictional Materials* 3, 323-342

Peerlings R.H.J., Geers M.G.D., de Borst R., Brekelmans W.A.M., 2001. *International Journal of Solids and Structures* 38, 7723-7746

Pensée V., Kondo D., 2003. Micromechanics of anisotropic brittle damage: comparative analysis between a stress based and a strain based formulation. *Mechanics of Materials* 35, 747-761

Pensée V., Kondo D., Dormieux L., 2002. Micromechanical analysis of anisotropic damage in brittle materials. *Journal of Engineering Mechanics, ASCE*. 128(8), 889-897

Petersson P., 1981. Crack Growth and development of failure zones in plain concrete and similar materials. *PhD thesis,* Lund Institute of Technology, Sweden

Pichler B., Dormieux L., 2010a. Cracking risk of partially saturated porous media-Part I: Microporoelasticity model. *International Journal for Numerical and Analytical Methods in Geomechanics* 34 (2), 135-157

Pichler B., Dormieux L., 2010b. Cracking risk of partially saturated porous media- Part II: Application to drying shrinkage. *International Journal for Numerical and Analytical Methods in Geomechanics* 34 (2), 159-186

Pichler B., Hellmich C., 2011. Upscaling quasi-brittle strength of cement paste and mortar: A multi-scale engineering mechanics model. *Cement and Concrete Research* 41(5), 467-476

Pichler B., Hellmich C., Eberhardsteiner J., 2009a. Spherical and acicular representation of hydrates in a micromechanical model for cement paste: Prediction of early-age elasticity and strength. *Acta Mechanica* 203 (3-4), 137-162

Pichler B., Hellmich C., Mang H.A., 2007. A combined fracture-micromechanics model for tensile strain-softening in brittle materials, based on propagation of interacting microcracks. *International Journal for Numerical and Analytical Methods in Geomechanics* 31, 111-132

Pichler B., Scheiner S., Hellmich C., 2009b. From micron-sized needle-shaped hydrates to meter-sized shotcrete tunnel shells: Micromechanical upscaling of stiffness and strength of hydrating shotcrete. *Acta Geotechnica* 3 (4), 273-294

Pichler C., Lackner R., Mang H.A., 2007. A multiscale micromechanics model for the autogenous-shrinkage deformation of early-age cement-based materials. *Engineering Fracture Mechanics*, 74(1-2), Pages 34-58

Pijaudier-Cabot G., Bažant Z.P., 1987. Nonlocal damage theory. *Journal of Engineering Mechanics, ASCE* 113(10), 1512-1533

Plesha M.E., 1987. Constitutive models for rock discontinuities with dilatancy and surface degradation. *International Journal for Numerical and Analytical Methods in Geomechanics* 11 (4), 345-362

Ponte-Castaneda P., Willis J.R., 1995. The effect of special distribution on the behaviour of composite materials and cracked media. *Journal of the Mechanics and Physics of Solids* 43, 1919-1951

Qiu Y., 1999. An investigation into the microplane constitutive model for concrete. *PhD Thesis,* University of Sheffield, UK.

Rashid Y.R., 1968. Ultimate stress analysis of prestressed concrete pressure vessels. *Nuclear Engineering and Design*, 7(4), 334-344

Reinhardt H.W., 1984. Fracture mechanics of an elastic softening material like concrete. Heron, 29(2), Delft, The Netherlands, 1-42

Ru C.Q., Aifantis E.C., 1993. A simple approach to solve boundary-value problems in gradient elasticity. *Acta Mechanica* 101, 59-68

Sakulich A.R., Li V.C., 2011. Nanoscale characterization of Engineered Cementitious Composites (ECC), *Cement and Concrete Research*, 41, 169-175

Salari M., Saeb S., Willam K.J., Patchet S., Carrasco R., 2004. A coupled elastoplastic damage model for geomaterials. *Computer Methods in Applied Mechanics and Engineering* 193, 2625-2643

Scrivener K.L, Nemati K.M., 1996. The percolation of pore space in the cement paste/aggregate interfacial zone of concrete. *Cement and Concrete Research* 26(1), 35-40

Scrivener K.L., Crumbie A.K, Laugesen P., 2004. The interfacial transition zone (ITZ) between cement paste and aggregate in concrete. *Interface Science* 12, 411-421

Serpieri R., Alfano G., 2011. Bond-slip analysis via a thermodynamically consistent interface model combining interlocking, damage and friction. *International Journal for Numerical Methods in Engineering* 85, 164-186

Simo J.C., Hughes T.J.R., 1998. Computational Inelasticity, Vol 7 of Interdisciplinary Applied Mathematics, Springer-Verlag, New York

Simo J.C., Ju J.W., 1987. Strain- and stress-based continuum damage models-I. Formulation. *International Journal of Solids and Structures* 23(7), 821-840

Simo J.C., Ju J.W., 1987. Strain- and stress-based continuum damage models-I. Computational aspects. *International Journal of Solids and Structures* 23(7), 841-869

Stroud A.H., 1971. Approximate calculation of multiple integrals. Prentice-Hall, Inc

Sun L.Z., Ju J.W, Liu H.T., 2003. Elastoplastic modelling of metal matrix composites with evolutionary particle debonding. *Mechanics of Materials* 35, 559-569

Taylor G.I., 1938. Plastic strains in metals. *J Inst. Metals* 62, 307-324

The Concrete Centre, 2010. Concrete Credentials: Sustainability http://www.concretecentre.com/sustainability/energy_efficiency.aspx [Accessed 15/12/2011]

Ulm F.-J., 2010. Nanoengineering green concrete or C-Crete: From atoms to concrete structures. http://www.concretetechnologyforum.org/2010cscproceedings/documents/Ulm%20Presentation%204-15-10.pdf [Accessed 20/12/2011]

Vandeperre L.J., Liska M., Al-Tabbaa A., 2008. Microstructures of reactive magnesia cement blends, *Cement & Concrete Composites*, 30, 706-714

van Mier J.G.M. 1986. Fracture of concrete under complex stress, Heron, 31(3): 1-90

van Mier J.G.M., 1997. Fracture processes of concrete. CRC Press

Viola V. and Piva E., 1981. Fracture behaviour by two cracks around an elliptic rigid inclusion, *Engineering Fracture Mechanics* 15, 303-325,

Voyiadjis G.Z. and Kattan P.I., 2006. Advances in damage mechanics: Metals and metal matrix composites with an introduction to fabric tensors. Second edition. Elsevier

Walraven J.C., Reinhardt H.W., 1981. Theory and Experiments on the Mechanical Behaviour of Cracks in Plain and Reinforced Concrete Subjected to Shear Loading. Heron. 26(1A)

Wang J., Fang J., Karihaloo B.L., 2000. Asymptotics of multiple carck interactions and prediction of effective modulus. *International Journal of Solids and Structures*, 37, 4261-4273

Wang J.G., Ichikawa Y., Leung C.F., 2003. A constitutive model for rock interfaces and joints. *International Journal of Rock Mechanics & Mining Sciences* 40, 41-53

Wells G.N., Sluys L.J., 2001. A new method for modelling cohesive cracks using finite elements. *International Journal for Numerical Methods in Engineering* 50, 2667-2682

Wiktor V., Jonkers H.M., 2011. Quantification of crack-healing in novel bacteria-based self-healing concrete. *Cement and Concrete Composites*, 33(7), 763-770

Willam, K., Hurlburt, B., Sture, S., 1985. Experimental and constitutive aspects of concrete failure. *Finite Element Analysis of Concrete Structures*. *Proceedings of Tokyo Seminar*, Japan., ASCE, 226-254

Willam K.J., Warnke E.P., 1975. Constitutive models for triaxial behaviour of concrete. *Proceedings of the International Association of Bridge Structural Engineering*, Report 19, Zurich, Switzerland, 1-30

Winkler B.J., Hofstetter G., and Niederwanger G., 2001, Experimental verification of a constitutive model for concrete cracking, *Proceedings of the Institution of Mechanical Engineers Part L-Journal of Materials-Design and Applications*, 215(L2), 75-86.

Wong R.C.K., Ma S.K.Y., Wong R.H.C., Chau K.T., 2007. Shear strength components of concrete under direct shearing. *Cement and Concrete Research* 37, 1248-1256

Wriggers P., 2006. Computational Contact Mechanics, 2nd edition. Springer

Wu M., Johannesson B., Geiker M., 2012. A review: Self-healing in cementitious materials and engineered cementitious composite as a self-healing material. *Construction and Building Materials*, 28(1), 571-583

Xie N., Zhu Q.Z., Xu L.H., Shao J.F., 2011. A micromechanics-based elastoplastic damage model for quasi-brittle rocks. *Computers and Geotechnics*, 38, 970–977

Yang C.C., 1998. Effect of the transition zone on the elastic moduli of mortar. *Cement and Concrete Research* 28(5), 727-736

Yang Z-Y., Taghichian A., Li W-C., 2010. Effect of asperity order on the shear response of the three-dimensional joints by focusing on damage area. *International Journal of Rock Mechanics & Mining Sciences* 47, 1012-1026

Yurtdas I., Burlion N., Skoczylas F., 2004. Experimental characterization of the drying effect on uniaxial mechanical behaviour of concrete. *Materials and Structures* 37, 170-176

Zhang J., Hou D., Han Y., 2012. Micromechanical modeling on autogenous and drying shrinkages of concrete. *Construction and Building Materials,* 29, 230–240

Zhu Q.Z., Kondo D., Shao J.F., 2008. Micromechanical analysis of coupling between anisotropic damage and friction in quasi brittle materials: Role of homogenization scheme. *International Journal of Solids and Structures* 45, 1358-1405

Zhu Q.Z., Kondo D., Shao J.F., 2009. Homogenization-based analysis of anisotropic damage in brittle materials with unilateral effect and interactions between

microcracks. *International Journal for Numerical and Analytical Methods in Geomechanics* 33, 749-772

Zhu Q.Z., Shao J.F., Kondo D., 2011. A micromechanics-based thermodynamic formulation of isotropic damage with unilateral and friction effects. *European Journal of Mechanics A/Solids* 30, 316-325

Annex 1

Direct tensor notations

The notations for tensor operations followed by Voyiadjis and Kattan (2006) are employed in this thesis and are defined in Table A.1 in which α denotes a scalar, **a** and **b** represent first order tensors (i.e. vectors), **A**, **B** and **C** are second-order tensors and **P**, **Q** and **R** denote fourth-order tensors respectively.

Table A.1. Direct tensor notation

Direct tensor notation	Notation based on Einstein summation convention (summation of repeated indices)
$\alpha = \mathbf{a} \cdot \mathbf{b}$	$\alpha = a_i b_i$
$\mathbf{A} = \mathbf{a} \otimes \mathbf{b}$	$A_{ij} = a_i b_j$
$\alpha = \mathbf{A} : \mathbf{B}$	$\alpha = A_{ij} B_{ij}$
$\mathbf{C} = \mathbf{A} \cdot \mathbf{B}$	$C_{ik} = A_{ij} B_{jk}$
$\mathbf{P} = \mathbf{A} \otimes \mathbf{B}$	$P_{ijkl} = A_{ij} B_{kl}$
$\mathbf{C} = \mathbf{P} : \mathbf{A}$	$C_{ij} = P_{ijkl} A_{kl}$
$\mathbf{B} = \mathbf{A} : \mathbf{P}$	$B_{kl} = A_{ij} P_{ijkl}$
$\mathbf{R} = \mathbf{P} \cdot \mathbf{Q}$	$R_{ijmn} = P_{ijkl} Q_{klmn}$

Annex 2

Transformation tensors

Details of the stress and strain transformation between global and local coordinate systems are presented. It is recalled from Chapter 2 that the local coordinate system is associated with a family of microcracks and is defined by the unit vectors $\mathbf{r}_d$, $\mathbf{s}_d$ and $\mathbf{t}_d$ (Fig A.1) with $\mathbf{r}_d$ being normal to the microcrack plane and $\mathbf{s}_d$ and $\mathbf{t}_d$ being the in-plane vectors.

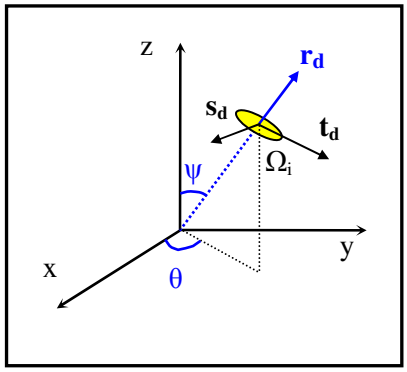

Figure A.1. Local coordinate system of a microcrack family

The local stresses associated to the i^{th} microcrack family characterized by the normal vector $\mathbf{r}_{di}$ are related to global stresses as follows:

$$\mathbf{s}_i = \mathbf{N}_{\sigma i}\boldsymbol{\sigma} \tag{A.1}$$

Where the local and global stresses are given in vector form by:

$$\mathbf{s} = \begin{bmatrix} \sigma_{rr} & \sigma_{rs} & \sigma_{rt} \end{bmatrix}^T \tag{A.2}$$

$$\boldsymbol{\sigma} = \begin{bmatrix} \sigma_{xx} & \sigma_{yy} & \sigma_{zz} & \tau_{xy} & \tau_{xz} & \tau_{yz} \end{bmatrix}^T \tag{A.3}$$

$$\mathbf{N}_\sigma = \begin{bmatrix} r_{d1}{}^2 & r_{d2}{}^2 & r_{d3}{}^2 & 2r_{d1}r_{d2} & 2r_{d2}r_{d3} & 2r_{d1}r_{d3} \\ r_{d1}s_{d1} & r_{d2}s_{d2} & r_{d3}s_{d3} & r_{d2}s_{d1}+r_{d1}s_{d2} & r_{d3}r_{d2}+r_{d2}r_{d3} & r_{d1}s_{d3}+r_{d3}s_{d1} \\ r_{d1}t_{d1} & r_{d2}t_{d2} & r_{d3}t_{d3} & r_{d2}t_{d1}+r_{d1}t_{d2} & r_{d3}t_{d2}+r_{d2}t_{d3} & r_{d1}t_{d3}+r_{d3}t_{d1} \end{bmatrix} \tag{A.4}$$

where subscripts 1, 2 and 3 denote the x, y, z components of the unit normal vectors $\mathbf{r}_d$, $\mathbf{s}_d$ and $\mathbf{t}_d$ respectively.

In tensor form the transformation of both stresses and strains employ the same transformation tensor. However, in matrix form the strain transformation matrix differs from the stress transformation matrix in that it takes into account that the engineering shear strain components employed in matrix form are twice the tensor shear strain components. For clarity, the following notation is employed: $\mathbf{N}$ denotes the transformation tensor (for both stresses and strains), $\mathbf{N}_\sigma$ denotes the stress transformation matrix and $\mathbf{N}_\varepsilon$ denotes the strain transformation matrix. Therefore for the transformation of strains the following equivalent expressions are employed where $\boldsymbol{\varepsilon}_L$ denotes the local strain and $\boldsymbol{\varepsilon}$ the global strain vector respectively:

$$\boldsymbol{\varepsilon}_{Li} = \mathbf{N}_{\varepsilon i}\boldsymbol{\varepsilon} \tag{A.5}$$

$$\boldsymbol{\varepsilon}_L = \begin{bmatrix} \varepsilon_{rr} & \gamma_{rs} & \gamma_{rt} \end{bmatrix}^T \tag{A.6}$$

$$\boldsymbol{\varepsilon} = \begin{bmatrix} \varepsilon_{xx} & \varepsilon_{yy} & \varepsilon_{zz} & \gamma_{xy} & \gamma_{xz} & \gamma_{yz} \end{bmatrix}^T \tag{A.7}$$

$$\mathbf{N}_\varepsilon = \begin{bmatrix} r_{d1}{}^2 & r_{d2}{}^2 & r_{d3}{}^2 & r_{d1}r_{d2} & r_{d2}r_{d3} & r_{d1}r_{d3} \\ 2r_{d1}s_{d1} & 2r_{d2}s_{d2} & 2r_{d3}s_{d3} & r_{d2}s_{d1}+r_{d1}s_{d2} & r_{d3}r_{d2}+r_{d2}r_{d3} & r_{d1}s_{d3}+r_{d3}s_{d1} \\ 2r_{d1}t_{d1} & 2r_{d2}t_{d2} & 2r_{d3}t_{d3} & r_{d2}t_{d1}+r_{d1}t_{d2} & r_{d3}t_{d2}+r_{d2}t_{d3} & r_{d1}t_{d3}+r_{d3}t_{d1} \end{bmatrix} \tag{A.8}$$

The general transformation of the local stresses and strains into the global coordinate system, in tensor form, is obtained as follows:

$$\boldsymbol{\sigma}_{gi} = \mathbf{N}_i{}^{-1}\mathbf{s}_i \tag{A.9}$$

$$\boldsymbol{\varepsilon}_{gi} = \mathbf{N}_i^{-1} \boldsymbol{\varepsilon}_{Li} \tag{A.10}$$

$\boldsymbol{\sigma}_{gi}$ and $\boldsymbol{\varepsilon}_{gi}$ represent the contributions to the global stress and strain tensors respectively from the current local direction. The global stresses ($\boldsymbol{\sigma}$) and strains ($\boldsymbol{\varepsilon}$) are obtained by summing the contributions from all possible directions.

In matrix form Eqs. (A.9-10) read:

$$\boldsymbol{\sigma}_{gi} = \mathbf{N}_{\varepsilon i}^{T} \mathbf{s}_i \tag{A.11}$$

$$\boldsymbol{\varepsilon}_{gi} = \mathbf{N}_{\sigma i}^{T} \boldsymbol{\varepsilon}_{Li} \tag{A.12}$$